Influences of turbulence and combustion regimes on explosions of gas-dust hydrid mixtures

Nicolas Cuervo Rodriguez

UNIVERSITÉ DE LORRAINE

École Doctorale
Ressources Procédés
Produits Environnement

Influences of turbulence and combustion regimes on explosions of gas-dust hydrid mixtures

Thesis

Presented and defended publicly on:
December 11th 2015
for obtaining a:

PhD title from The University of Lorraine
in Process and Product Engineering

by:
Nicolas CUERVO RODRIGUEZ

Compostion of the Jury

Rapporteurs:

Almerinda Di BENEDETTO	Professor	Università degli Studi di Napoli Federico II
Michel MOLIÈRE	Doctor Engineer (HDR)	Université de Technologie de Belfort-Montbéliard

Examinateurs:

Philippe GILLARD	Professor	Université d'Orléans
Alexis VIGNES	Doctor Engineer	INERIS
Olivier DUFAUD	Professor	Université de Lorraine (Thesis Co-Director)
Laurent PERRIN	Professor	Université de Lorraine (Thesis Director)

LRGP Laboratoire Réactions et Génie des Procédés

CNRS

Laboratoire Réactions et Génie des Procédés — **UMR CNRS 7274** — Nancy

Acknowledgements

I've noticed that for many people, pursuing new enterprises and starting a completely new live far from their loved ones is a very difficult and heart-breaking thing to do. In my case, although it has not been the easiest thing, it has been mostly a very pleasing and rewarding experience. If this has been the case, it is only because of all the people that I have been privileged to be surrounded by. These are the people that I want to thank here.

To my folks and sisters[1]

Not only have you not gotten in my way, as is sometimes the case in other families, but you have paved it and guided me through it. You have inspired me, given me strength and made me who I am. You have sacrificed so many things to give me a good life and to give me a good education; that you sacrificed a part of yourselves by not only letting me leave you, but also by encouraging me to do it; knowing that even if it would be painful for us it would also be good for me. Thank you for your encouragement, your support and specially for all your sacrifice.

To Olivier and Laurent

You were supposed to be my thesis advisers, but you were willingly more than that. I came to France knowing little about the culture or the language and with your excellent human qualities you made my transition experience very easy and rewarding. Thank you, specially for your patience, but also for your guidance and your help in so many things that sometimes were not really part of your duties. Thank you, because I know that anything that you may have done in order to help

[1] A mis viejos y hermanas: ustedes no solamente no me han bloqueado el camino, como suele suceder en otras familias, sino que han sido quienes lo construyeron y quienes me guiaron por él. Ustedes han sido mi fuente de inspiración y fortaleza, y me han hecho quién soy. Además, han tenido que sacrificar tantas cosas para darme una buena vida y una buena education, que terminaron sacrificando una parte de ustedes; no solo al dejarme ir, sino al alentarme a hacerlo porque sabían que aunque sería doloroso, sería también bueno para mí. Gracias por el ánimo, el apoyo y sobretodo por todos sus sacrificios.

me, you have done it selflessly and you have helped me to become a better researcher and a better person.

To the members of the team SAFE

It is rare to find such a friendly work environment as the one I found in the team SAFE. I thank all the team SAFE for their conversations and coffee breaks. Thanks to the PhD students who I had so many laughs with. I want to thank particularly those who directly intervened in this work: Manon POUPEAU, David TORRADO, Marie LAUTARD, Delphine JOURDAIN, Pierre AUZOLE, Roberto OLCESE, Carlos MURILLO, every hour I invested working with you was largely recompensed latter by becoming essential pieces of this work. Either because you made me question what we were doing or because the work you did is reflected everywhere in this document, your hard-work and good company contributed largely to the completion of this work.

To my friends

Andrea, this journey started because you and Carlos, held me in such a high regard and you expressed it around you, thank you, to you both.

Aurore, Felipe and Mathilde, your patience and everyday company were an important support for finishing this work, thank you for feeding me at times and forcing me to abandon the computer at other times.

Alberto, Eduardo and Ricardo, talking with you around a meal or an spirited beverage about this work certainly helped to push it forward. Clearly, your friendship has been some of the most rewarding things of this experience as is certainly the friendship of so many people that I am sorry for not mentioning here. You're the only lucky ones because your input outside the lab, eventually helped me to finish this work.

Chiara, your smile, your patience, your support and your company, helped me to complete this work and those, are among the things that I consider most rewarding of this whole experience. Hopefully, I will be able to make it up to you for the times we could not spend together and the holidays I could not travel with you.

Contents

List of Figures

List of Tables

Nomenclature

Roman Symbols

A_p	Projected area of a particle in the plane perpendicular to the flow direction	m^2
C_D	Drag coefficient of a particle travelling through a fluid	–
$C_\circ$	Discharge coefficient for gas expansion through an orifice	–
$\tilde{C}_P$	Specific heat capacity at constant pressure	$\frac{\mathrm{J}}{\mathrm{mol\,K}}$
$\tilde{C}_V$	Specific heat capacity at constant volume	$\frac{\mathrm{J}}{\mathrm{mol\,K}}$
d_{50}	Mass median particle diameter	µm
d_c	Critical diameter of ignition kernel	m
d_p	Diameter of dust particle	m
$\left(\frac{\mathrm{d}P}{\mathrm{d}t}\right)_\mathrm{max}$	Maximum Rate of Pressure Rise	$\frac{\mathrm{bar}}{\mathrm{s}}$
g	Acceleration of gravity 9.8 $\frac{\mathrm{m}}{\mathrm{s}^2}$	$\frac{\mathrm{m}}{\mathrm{s}^2}$
h_conv	Convection coefficient	
V_i	Volume of i	m^3
I_t	Turbulence intensity. **Equation 3.28**	–
K	Stretching factor	$\frac{1}{\mathrm{s}}$
k_D	Constant for modelling oxygen diffusion limitation during combustion in the initial kernel. **Equation 1.10**	$\frac{\mathrm{W}}{\mathrm{m\,K}}$
k_D	Constant for modelling surface kinetic limitation during combustion in the initial kernel. **Equation 1.12**	$\frac{\mathrm{W}}{\mathrm{m\,K}}$
K_St	Deflagration index of dust.	$\frac{\mathrm{bar\,m}}{\mathrm{s}}$
LEL	Lower Explosive Limit or Lower Flammability Limit of gas	–
m_i	Mass of substance i	kg
$\dot{m}_\mathrm{c}$	Mass reaction rate	$\frac{\mathrm{kg}}{\mathrm{s}}$
MEC	Minimal Explosive Concentration of dust	$\frac{\mathrm{g}}{\mathrm{m}^3}$
$\tilde{M}_i$	Molar mass of substance i	$\frac{\mathrm{kg}}{\mathrm{mol}}$

MIE	Minimum Ignition Energy	J
m_p	Mass of a particle	kg
n_i	Moles of i	mol
N_p	Number of dust particles inside a given volume	–
P_i	Pressure at point or time i	bar
R	Ideal gas constant, 8.314 $\frac{\mathrm{J}}{\mathrm{mol\,K}}$	$\frac{\mathrm{J}}{\mathrm{mol\,K}}$
r	Ratio of the product of flammability limits and enthalpy of combustion of gas and dust. **Equation 1.18**	–
$\dot{R}_i$	Rate of reaction of component i	$\frac{\mathrm{kg}}{\mathrm{s}}$
$\dot{r}_j$	Rate of reaction j	$\frac{\mathrm{kg}}{\mathrm{s}}$
S_u	Burning flame speed	$\frac{\mathrm{m}}{\mathrm{s}}$
S_u	burning velocity of flame	$\frac{\mathrm{cm}}{\mathrm{s}}$
S_u^0	Unstretched burning velocity of flame	$\frac{\mathrm{cm}}{\mathrm{s}}$
S_ul	Laminar burning velocity	$\frac{\mathrm{m}}{\mathrm{s}}$
t	Time	s
T_ad	Adiabatic flame temperature	K
T_i	Temperature at point or time i	K
T_u	Temperature of unburnt mixture	K
t_v	Ignition time delay	ms
$\overline{u}$, $\overline{v}$, $\overline{w}$	Mean value of velocity in the x, y and z directions.	$\frac{\mathrm{m}}{\mathrm{s}}$
u', v', w'	Velocity fluctuation from mean value in the x, y and z directions. **Equation 3.26**	$\frac{\mathrm{m}}{\mathrm{s}}$
u'_rms, v'_rms, w'_rms	Root-Mean-Square of turbulent velocity fluctuation in the x, y and z directions.	$\frac{\mathrm{m}}{\mathrm{s}}$
v_0	Initial vertical velocity of a particle falling in a fluid media	$\frac{\mathrm{m}}{\mathrm{s}}$
v_choked	Speed of air during choked regime, equivalent to to the speed of sound at the conditions of the flow	$\frac{\mathrm{m}}{\mathrm{s}}$
v_p	Velocity of particle falling in a fluid media relative to the velocity of the media. **Equation 3.24**	$\frac{\mathrm{m}}{\mathrm{s}}$

Greek Symbols

$\Delta_\mathrm{c}\hat{H}$	Enthalpy of combustion	$\frac{\mathrm{J}}{\mathrm{kg}}$
δ_M	markstein length	mm
ε	Porosity of solid.	
ε_v	Volatile fuel content of solid. **Equation 1.26**	$\frac{\mathrm{g}}{\mathrm{g}}$
γ	Heat capacity ratio $\frac{\tilde{C}_P}{\tilde{C}_V}$	–
κ	Permeability	m^2
Λ	Any combustible component (*e.g.* Methane, starch, acetone).	
λ	Thermal conductivity	$\frac{\mathrm{W}}{\mathrm{m\,K}}$
μ	Viscosity	$\frac{\mathrm{kg}}{\mathrm{m\,s}}$
$\nu_i, \nu_{i,j}$	Stoichiometric coefficient of i (in reaction j)	

σ_{p}	Terminal velocity of a particle travelling in a fluid media. **Equation 3.22**	$\frac{\mathrm{m}}{\mathrm{s}}$
ϕ	Fuel equivalence ratio, fuel-richness of a mixture. **Equation 1.22**	–
Φ	Normalized fuel equivalence ratio, fuel-richness of a mixture. **Equation 1.23**	–
ρ_i	Mass concentration or density of component i	$\frac{\mathrm{kg}}{\mathrm{m}^3}$
u_r	Gas speed in the radial direction	$\frac{\mathrm{kg}}{\mathrm{m}^3}$
$\overline{\rho}_{\mathrm{b}}$	Mean density of burnt material	$\frac{\mathrm{kg}}{\mathrm{m}^3}$
ρ_{g}	Density of gas	$\frac{\mathrm{kg}}{\mathrm{m}^3}$
ρ_{p}	Solid density of dust particle	$\frac{\mathrm{kg}}{\mathrm{m}^3}$
$\overline{\rho}_{\mathrm{u}}$	Mean density of unburnt cloud	$\frac{\mathrm{kg}}{\mathrm{m}^3}$
τ_{choked}	Characteristic time for the isentropic expansion of an ideal gas in choked (subsonic) regime. **Equation 3.11**	s
τ_{p}	Characteristic time of particle settling. **Equation 3.23**	s
τ_{subsonic}	Characteristic time for the isentropic expansion of an ideal gas in subsonic regime	s
Υ_{Λ_i}	Fraction of oxygen demand of component Λ_i. **Equation 1.25**	

Accents

$\tilde{a}, \tilde{A}, \tilde{\alpha}$	Denotes molar based intensive properties
$\hat{a}, \hat{A}, \hat{\alpha}$	Denotes mass based intensive properties
$\dot{a}, \dot{A}, \dot{\alpha}$	Denotes a flow of matter
$\overline{a}, \overline{A}, \overline{\alpha}$	Denotes a mean value

Subscripts

ad	Adiabatic
b	Burnt material
dust	Dust
eq	Equivalent to volatile mass content or to the concentration ratio of stoichiometric to maximum deflagration conditions. **Equation 1.27**
gas	Gas
hyb	Hybrid mixture
$\vert_{\mathrm{st}}$	defined at stoichiometric conditions
u	Unburnt material

Introduction

On December 16th of 1999, aiming to improve the safety of workers who are exposed to explosive environments (*Atmosphères Explosives* ATEX), the European directive 1999/92/CE was released. In France, this legislation was implemented through the decrees 2002-1553 and 2002-1554 from December 24th and the notices from July 8th and 28th 2003. These regulations impose on different industrial sectors, several restrictions on the handling of combustible products. Including also, a large variety of powdered solids who are capable of burning or even exploding when dispersed in the form of clouds. Because of these guidelines, industries and researchers have been encouraged to study different characteristics related to the inflammation and explosion of granulated powders. Therefore the norms have helped on their purpose of improving the safety of industrial processes.

Hybrid mixtures were defined by the norm NF EN 1127-1 norm as mixtures of air with flammable compounds in different states of mater; mixtures of powdered charcoal, methane and air are a good example. However, at the time when these regulations were designed the understanding of the so called hybrid mixtures was limited. Unfortunately, the risk their explosions represent is nonetheless prevalent because of both, their probability of occurrence and the severity of their consequences. In fact, hybrid mixtures are encountered in various industries such as paint factories (pigments and solvents), the mining sector (dusts and gas), grain elevators (small grains and fermentation gases) or pharmaceutical industries (Glor, 2003). Furthermore accidents caused by their explosions are neither scarce nor minor (1994 – Groß-Umstadt, Germany) (1906 – Courrieres, France: methane explosion leading to secondary coal dusts explosions: 1100 fatalities).

Because of the limited availability of knowledge, the safety guidelines could do nothing but to suggest the treatment of these mixtures through the analysis of its individual components. For this reason the interest on dust explosions from researchers has been extended. Hybrid mixtures on the contrary, have been studied with less intensity, and consequently, the characteristics of their flammable and explosive behaviour have been poorly referenced. The research that has been developed on this subject suggests however, that hybrid mixtures should be treated with a more critical approach than the one stipulated by the norms. Indeed it has been shown that dusts and gases can generate through their mutual interactions, explosions that could not be predicted to happen through the analysis of the

separate components. Some of the particularities on severity and inflammability among others, exhibited by theses mixtures are described in the first chapter of this document.

The present work has been the therefore, the result of an effort to help in reducing the lack of understanding of these kinds of mixtures. The explosions of organic dusts have served here as the obvious starting point. Indeed, during the explosion of an organic dust cloud, different successive steps occur: the particle heating, its devolatilization/pyrolysis and then, the oxidation of the pyrolysis gases or the solid itself. The characteristic times of these phenomena can be greatly different, and a rate-limiting step can then be defined. For small particles with diameters lower than 10 to 30 µm, the pyrolysis step is fast, and the combustion kinetics can be reduced to the oxidation phase as it has been previously shown by Hertzberg et al. (1987) and Di Benedetto and Russo (2007). This is not the case for larger particles and the heat transfer or the oxygen diffusion can become rate-limiting. Understanding and underlining the role of the pyrolysis step in organic dusts explosions has several aims: i) the results can be used as input into a predictive model based on a simplified kinetic scheme representing the pyrolysis and the oxidation, ii) increasing the effect of the rate-limiting step can lead to the development of adequate protective measures (Dufaud and Perrin, 2010), iii) the study of the combustion process is compulsory to understand the turbulence/combustion interactions in the front flame (influence of the Lewis number, presence of flame pockets), iv) Amyotte et al. (1993) and later Dufaud et al. (2008) have pointed that the mixtures of dusts and its pyrolysis gases can be regarded as a hybrid mixture. In this document on **Chapter 2**, the peculiar case of wheat starch has been studied. Firstly, an experimental setup has been developed to pyrolyze starch and analyse the gases produced. Based on these experiments, the explosive behaviour of organic dusts, its pyrolysis gases and their mixtures has been studied. Furthermore, a one dimensional finite-volume scheme has been developed to represent the pyrolysis of a single biomass particle. Both experimental and computational results shall lead to the improvement of a global model representing the explosive of dusts and gas/dusts hybrid mixtures.

Particle image velocimetry (PIV) was used to quantitatively characterise the turbulence inside a 7 cm×7 cm vertical tube. The analysis should allow to understand the effect of turbulence when studying the ignitability of dusts in particular and hybrid mixtures in general by means of the when the Mike apparatus. The way this equipment creates a dust cloud is through the sudden expansion of a pressurised gas that drags with it a deposited layer of dusts. Consequently the mean velocity of the particles, was estimated by developing a model that accounts for the gas expansion and the drag and gravity forces on the particles. Because of its theoretic foundations, the model shall certainly prove its usefulness in different applications related to the sudden expansion of a gas.

Finally the structural behaviour of propagating hybrid mixture flames was analysed. This was performed in the context of developing a technique that would allow to import into the study of dust and hybrid mixture explosions, a theory that was developed for gas flames. Although the technique, was proven not to work the way it was conceived; the results presented here lay the ground for a development of transform the technique into one that will be useful in the characterization of dust and hybrid mixture flames through their burning velocities and Markstein length.

Furthermore a model in Simulink® was developed by means of the Computer Vision Toolbox of Matlab® to automatically analyse the videos of explosions and interpret the morphological changes the flame exhibits. Because of the way it works, this model can be easily adapted to the use in the technical development to come.

In the present study the focus has been mostly limited to mixtures of wheat starch and methane. Theses components have been chosen because of the broad knowledge available of each one individually and also because of how simple they are: starch particles being quasi-spherical and methane being a small molecule. As a consequence, they can be considered as model compounds and the approaches developed in this document could be (easily) extrapolated to other fuel-air mixtures.

Chapter 1

Specificities of Dust-Gas Hybrid Mixtures

Contents

1.1. Introduction

This chapter introduces varied evidence explaining the particular behaviours of dust-gas hybrid mixtures. It is divided in three parts, the first part shows the particularities for the ignition of hybrid mixtures and especially how the Minimal Ignition Energy of dusts is reduced with the presence of small quantities of gas. The explosive concentration limits are shown to be also affected in a disproportionated fashion with respect to the limits of the pure compounds, which seems to be explained by difference in the adiabatic temperatures of the mixture's components. The second part of the chapter, shows the analysis on the severity of different hybrid mixtures, as well as the interactions that sometimes make them dissimilar from their components. Finally, a novel approach to analyse the data for severity is presented, that may prove to be very useful in identifying the particularities of hybrid mixtures, proposing empirical predicting models, and more importantly reducing the amount of tests necessary to characterize the mixtures.

1.2. Inflammability of Hybrid Mixtures

1.2.1. Minimum Ignition Energy MIE

The minimum ignition energy (MIE), is empirically defined as the lowest energy necessary to ignite a combustible vapour or dust cloud with an electric spark at ambient temperature and atmospheric pressure (Laurent, 2011; IEC standard 1241-2-1, 1994). In the particular case of solid-gas hybrid mixtures, the MIE has been found to be considerably reduced by the presence of small concentrations of combustible gases in dust clouds. Particularly, Franke (1978), Pellmont (1979), and Pellmont (1980) have already shown three decades ago that the MIE of carbon black, cellulose and PVC is drastically reduced in the presence methane or propane in concentrations of just 1 to 3 %vol. This is not (as) surprising when one considers that, for example, for the case of propane the stoichiometric concentration is 4 %vol and that its Lower Explosive Limit (LEL) is 2%. Therefore those seemingly low concentrations of combustible gas may be actually considerably high with regard to the other characteristic parameters of the compound, like the molar weight, that could make an important difference in the actual fuel richness of 2 mixtures with similar concentrations of different gases. For these reasons caution should be taken when analysing the behaviour of hybrid mixtures because apparently low concentrations of a combustible vapour in an otherwise dust charged atmosphere may considerable affect the mixture's properties as its ignitability. In this context, some authors have proposed to estimate the minimum ignition energy of hybrid mixtures $\mathrm{MIE}_{\mathrm{hyb}}$ through the use of a relation between the minimum ignition energies and the concentration ratios of the gaseous and solid components (Bartknecht, 1989; Britton, 1998):

$$\mathrm{MIE}_{\mathrm{hyb}} = (\mathrm{MIE}_{\mathrm{gas}})^{\frac{y_{\mathrm{gas}}}{y_{\mathrm{gas}_0}}} (\mathrm{MIE}_{\mathrm{dust}})^{1-\frac{y_{\mathrm{gas}}}{y_{\mathrm{gas}_0}}} \tag{1.1}$$

Where y_{gas} is the volume concentration of the gas and y_{gas_0} is the gas concentration that accounts for the smallest $\mathrm{MIE}_{\mathrm{gas}}$.

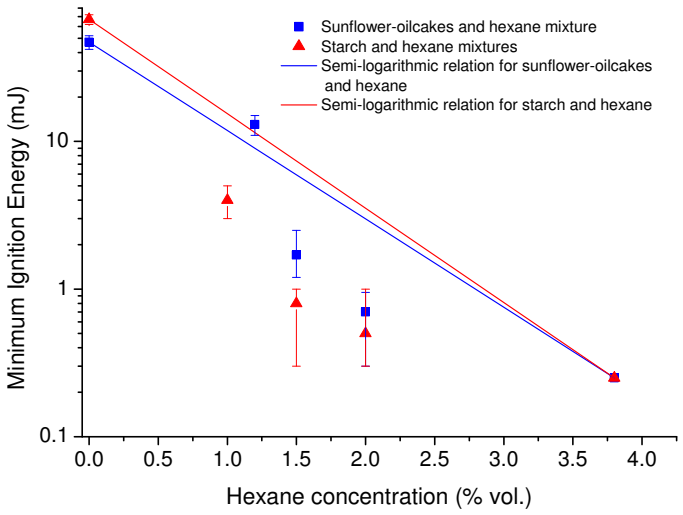

Figure 1.1. Behaviour of the Minimum Ignition Energy of hybrid mixtures of sunflower-oilcakes/hexane and starch (d_{50} = 70 µm)/hexane according to the hexane content (Khalili et al., 2012)

Figure 1.1 shows the comparison of **Equation 1.1** to experimental values of the minimum ignition energy of mixtures of hexane with sunflower-oilcakes and starch (d_{50} = 70 µm). The value for the MIE_{gas} of hexane, 0.25 mJ, used in this figure was obtained from the literature (Lees, 2012). Error bars are considerably large for MIE_{hyb} below 1 mJ because this is the minimum energy the modified Hartmann tube can deliver and therefore the values obtained below that point are just estimative. A considerable decrease of the MIE is observed with hexane concentrations as low as 1% ($y_{gas}|_{st}$=2.16% [1], LEL=1.1 %). For example starch's MIE decreases from 67 mJ for pure dust to 4 mJ when hexane is present at 1 %vol. Furthermore, in agreement with previous general works of Franke (1978) and Pellmont (1979), mixtures containing sunflower-oilcakes the addition of just 1.5 %vol. of hexane reduces the MIE from 47 mJ to 1.7 mJ. Notice that the addition of 1.5 %vol and 2 %vol of hexane to starch and sunflower-oilcakes respectively decreases the MIE below 1 mJ. Consequently, the energy of a brush discharge would be sufficient to ignite these mixtures, whereas, in practice no evidence exists to consider pure dust clouds sensitive to this kind of discharge (Glor, 2003). This helps to underline the risks that hybrid mixtures represent as some industrial context, that are thought to be harmful *exclusively because* of the presence of high concentrations of dust may hide a more sensitive risk that would otherwise be neglected in the absence of this kind of evidence. Therefore, such empirical relations are useful tfor risk analysis. Furthermore, although **Equation 1.1** gives a good estimation for the order of magnitude of the MIE_{hyb} it does not adjust properly to the experimental results; it rather overestimates the MIE_{hyb} (consequently, underestimating the risk). Thus, for example **Equation 1.1** predicts the MIE_{hyb} to be higher than 1 mJ for hexane concentrations below 2.7 %vol which is not the case as previously mentioned.

[1] $y_{gas}|_{st}$: stoichiometric gas concentration in air

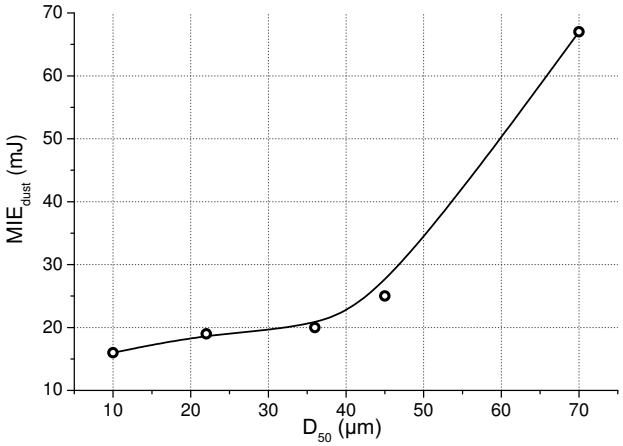

d_{50} (µm)	$\mathrm{MIE_{dust}}$ (mJ)
10	16
22	19
36	20
45	25
70	67

Figure 1.2 and Table 1.1 Minimal Ignition energies of sieved samples of starch (Khalili et al., 2012)

One of the phenomena that explain this specific behaviour of hybrid mixtures may be the modification of the limiting stage of the combustion, besides the interactions between turbulence and combustion, the modification of the initial turbulence dispersing the dust phase, etc. Indeed, various works on nanoparticles have shown that the reduction of the size of the particles induces a transition from a diffusion controlled combustion to one limited by the chemical kinetics of the smaller particles (Van der Wel, 1993; Bouillard et al., 2010; Di Benedetto et al., 2010)

1.2.1.1. The role of particle size in defining the phenomenon that limits the propagation of the combustion kernel

Measuring the minimal ignition energies for sieved samples of starch allows to estimate the particle size at which propagation of the kernel transits from being limited by the diffusion of oxygen to being limited by the chemical kinetics inside the particle. **Figure 1.2** and **Table 1.1** show how the MIE decreases from 67 mJ to 16 mJ in a non linear fashion.

This behaviour can be explained through a complementary definition of the MIE that involves the *critical combustion kernel diameter*. A definition of MIE is used (Ballal and Lefebvre, 1979; Van der Wel, 1993; Bouillard et al., 2010; Khalili et al., 2012) in terms of the energy necessary to heat to the ignition temperature the smallest spherical volume of unburnt mixture that can produce a self-propagating burning kernel. This is achieved when the heat generated in the kernel, is equivalent to the heat exchanged with the unburnt mixture surrounding it. This means that the ratio of volume to surface area of the resulting kernel is high enough for the heat generated to compensate the heat exchanged. By supposing that the heat capacity of burnt and the unburnt mixture is constant (which is valid for both solids and ideal gases), the MIE could be therefore described in terms of the mean heat capacities of **burnt (b)** and **unburnt (u)** mixtures as:

$$\mathrm{MIE} = m_\mathrm{b}\overline{\hat{C}}_{P_\mathrm{b}}T_\mathrm{ad} - m_\mathrm{u}\overline{\hat{C}}_{P_\mathrm{u}}T_\mathrm{u} \tag{1.2}$$

where T_{ad} is the adiabatic flame temperature at constant pressure. Considering a mean value for the heat capacity $\overline{\hat{C}}_P$ $(\frac{\mathrm{J}}{\mathrm{kg\,K}})$ on the control volume for the temperature range in question as:

$$\overline{\hat{C}}_P = \frac{\overline{\hat{C}}_{P_\mathrm{b}} T_{\mathrm{ad}} - \overline{\hat{C}}_{P_\mathrm{u}} T_\mathrm{u}}{T_{\mathrm{ad}} - T_\mathrm{u}} \tag{1.3}$$

and considering that mass is conservative then the MIE equals:

$$\mathrm{MIE} = \overline{\rho}_\mathrm{b} V_\mathrm{b} \overline{\hat{C}}_P \left(T_{\mathrm{ad}} - T_\mathrm{u}\right) = \overline{\rho}_\mathrm{u} V_\mathrm{u} \overline{\hat{C}}_P \left(T_{\mathrm{ad}} - T_\mathrm{u}\right) \tag{1.4}$$

Finally, if the ratio of burnt to unburnt densities varies according to the ideal gas law:

$$\frac{\overline{\rho}_\mathrm{b}}{\overline{\rho}_\mathrm{u}} = \left(\frac{P\tilde{M}_\mathrm{b}}{RT_{\mathrm{ad}}}\right)\left(\frac{RT_\mathrm{u}}{P\tilde{M}_\mathrm{u}}\right) = \frac{T_\mathrm{u}}{T_{\mathrm{ad}}}\frac{\tilde{M}_\mathrm{b}}{\tilde{M}_\mathrm{u}} \approx \frac{T_\mathrm{u}}{T_{\mathrm{ad}}} \tag{1.5}$$

An expression is then derived for the MIE depending on the properties of the mixture and the critical diameter of the kernel d_c:

$$\mathrm{MIE} = \frac{\pi}{6}\overline{\rho}_\mathrm{u}\overline{\hat{C}}_P\frac{T_\mathrm{u}}{T_{\mathrm{ad}}}\frac{\tilde{M}_\mathrm{b}}{\tilde{M}_\mathrm{u}}\left(T_{\mathrm{ad}} - T_\mathrm{u}\right){d_\mathrm{c}}^3 \approx \frac{\pi}{6}\overline{\rho}_\mathrm{u}\overline{\hat{C}}_P\frac{T_\mathrm{u}}{T_{\mathrm{ad}}}\left(T_{\mathrm{ad}} - T_\mathrm{u}\right){d_\mathrm{c}}^3 \tag{1.6}$$

As the propagation of the kernel depends on whether enough heat is produced to compensate for the one released to the environment, if conduction is assumed to be the major reason of heat exchange, its size can be described by:

$$d_\mathrm{c} = \frac{\dot{m}_\mathrm{c}\Delta_\mathrm{c}\hat{H}}{2\pi\lambda\left(T_{\mathrm{ad}} - T_\mathrm{u}\right)} \tag{1.7}$$

where $\dot{m}_\mathrm{c}$ is the mass reaction rate, $\Delta_\mathrm{c}\hat{H}$ is the heat of combustion and λ is the thermal conductivity. This leads to the following expression of the MIE:

$$\mathrm{MIE} \approx \frac{\pi}{6}\overline{\rho}_\mathrm{u}\overline{\hat{C}}_P\frac{T_\mathrm{u}}{T_{\mathrm{ad}}}\frac{1}{\left(T_{\mathrm{ad}} - T_\mathrm{u}\right)^2}\left(\frac{\dot{m}_\mathrm{c}\Delta_\mathrm{c}\hat{H}}{2\pi\lambda}\right)^3 \tag{1.8}$$

The mass reaction rate can be defined in terms of the speed of the reduction of the particle volume $\frac{\mathrm{d}\left({d_\mathrm{p}}^3\right)}{\mathrm{d}t}$ as:

$$\dot{m}_\mathrm{c} = -\frac{\overline{\rho}_\mathrm{b}}{\nu_{\mathrm{dust}}}\frac{\pi}{6}\frac{\mathrm{d}\left({d_\mathrm{p}}^3\right)}{\mathrm{d}t} \tag{1.9}$$

where ν_{dust} is the stoichiometric coefficient of the dust.

The classic shrinking core models (Levenspiel, 1989) have been used to describe the evolution of the particle diameter in time. During the initial moments of the ignition when **combustion is limited by the diffusion of oxygen** to the walls

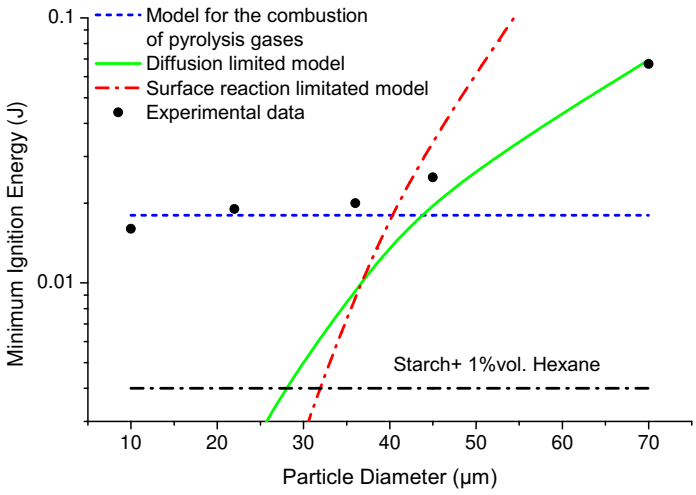

Figure 1.3. Influence of the particle size on the MIE of starch samples (Khalili et al., 2012)

of the particle the mass reaction rate can be represented as:

$$\dot{m}_c = \frac{8\pi}{9} d_{p_0} \tilde{M}_b k_D C_{O_2} \tag{1.10}$$

where k_D is a constant that behaves according the Arrhenius law.

Combining **Equations 1.8** and **1.10**, the classical evolution of the MIE as a function of particle diameter that had been reported by Kalbert (Eckhoff, 2003) is obtained (Bouillard et al., 2010):

$$\text{MIE} \propto {d_{p_0}}^3 \tag{1.11}$$

When **combustion is limited by the kinetics of the reaction at the surface of the particle**, during a pyrolysis stage for example, the mass reaction rate changes as a function of the square of d_{p_0}:

$$\dot{m}_c = \frac{\pi}{3} {d_{p_0}}^2 \tilde{M}_b k_R C_{O_2}^n \tag{1.12}$$

where k_R is a kinetic constant following the Arrhenius law and n is the order of the reaction related the oxygen concentration.

In the case of a very **fast vaporization of solid particles** or higher rates of pyrolysis than surface combustion, which is the case for very small organic particles (Di Benedetto and Russo, 2007), $\dot{m}_c$ can be considered to be constant in time and is therefore independent of size of the particles.

Figure 1.3 shows the evolution of the MIE of different starch samples as a function of d_{50}. The models previously mentioned are adapted through numerical optimization of the activation energies and pre-exponential factors for the Arrhenious behaving constants k_D and k_R. The optimization was constrained for the parameters to have a real physical meaning, obtaining activation energies between 50 and 200 $\frac{\text{kJ}}{\text{mol}}$ (Di Blasi, 2008). It is evident that the model representing a combustion

mechanism limited by the reaction kinetics at the surface of the particles does not represent adequately the experimental data in no interval of particle diameter. On the contrary the model representing the diffusional limitation is in good agreement for particles larger than 36 µm. Below this point the particle size becomes almost irrelevant for the MIE as it stays constant at approximately 20 mJ. A model for a combustion reaction in homogeneous phase might therefore become relevant below that point. It is important to underline that the value of 36 µm shall not be considered to be a fixed and exact value for any other component. Further testing at smaller diameter might help to better define the transition point from the invariability of the MIE because of the small particle size, to a MIE dependent on the particle diameter because of diffusional limitations. Bouillard et al. (2010) have shown for example, that the transition point may be found at particle diameters of 3 µm to 20 µm depending on the chemical nature of the dust analysed.

Relating these results to the discussion of page 10, it seems that the combustion of the starch particles studied in **Figure 1.3** is limited by the diffusional of oxygen to the particle. Thus, the addition of 1%vol. of hexane probably modifies the limiting stage of combustion as the $\mathrm{MIE}_{\mathrm{dust}}$ of 4 mJ could not possibly be the result of a combustion mechanism that is limited by the diffusion of oxygen reaching particles with 36 µm or more, nor is it the result of the combustion in homogeneous phase of the pyrolysis gases of smaller particles. Hexane is therefore playing a significant role in the combustion of the mixtures, most especially during the ignition and later development of the initial kernel.

Using **Equation 1.6** it is possible to deduce the critical kernel diameters from the experimental values of the $\mathrm{MIE}_{\mathrm{hyb}}$. **Figure 1.4** shows the evolution of the critical diameter of the ignition kernel d_{c}, as a function of the mean particle diameter (d_{50}) of starch. Values ranging from 4.5 mm to 7.3 mm where obtained for d_{c}, which in good agreement to the 7 mm reported by Proust (2006a) for starch with d_{50} =28 µm. Similar calculations where performed for mixtures of sunflower-oilcakes and hexane (**Figure 1.5**). The critical ignition kernel diameter decreases from 7 mm for sunflower to 1.2 mm for hexane at 3.8 %. Additionally ignitions of this mixture were observed using a CCD ultrafast camera (Phantom V91) and the size of the initial kernel was measured for pure components. This size resulted to be 7.2 mm for pure sunflower-oilcakes at 100 mJ; which is in good agreement with calculations previously mentioned for both sunflower and starch. For the case of hexane d_{c} was found to be 1.8 mm which is between the values found in the literature ranging between 2 and 3.5 mm (Bjerketvedt et al., 1997; Kondo et al., 2003). Proust (2006a) also proposed a relation for the MIE and d_{c}:

$$\mathrm{MIE} = \lambda_{\mathrm{b}} \frac{{d_{\mathrm{c}}}^2 T_{\mathrm{ad}}}{2 S_{\mathrm{ul}}} \tag{1.13}$$

Using this expression for hexane and considering the following values from the literature (Lees, 2012): $2.34 \cdot 10^{-2}\ \frac{\mathrm{W}}{\mathrm{m\,K}}$ for λ_{b}, 2238 K for T_{ad} and $0.385\ \frac{\mathrm{m}}{\mathrm{s}}$ for the Laminar burning speed S_{ul}, a value for d_{c} of 1.9 mm is found to agree with the results already mentioned. A relation for $d_{\mathrm{c}_{\mathrm{hyb}}}$ was proposed by Khalili et al. (2012) depending on $d_{\mathrm{c}_{\mathrm{dust}}}$ and $d_{\mathrm{c}_{\mathrm{gas}}}$ that is analogous to **Equation 1.1**:

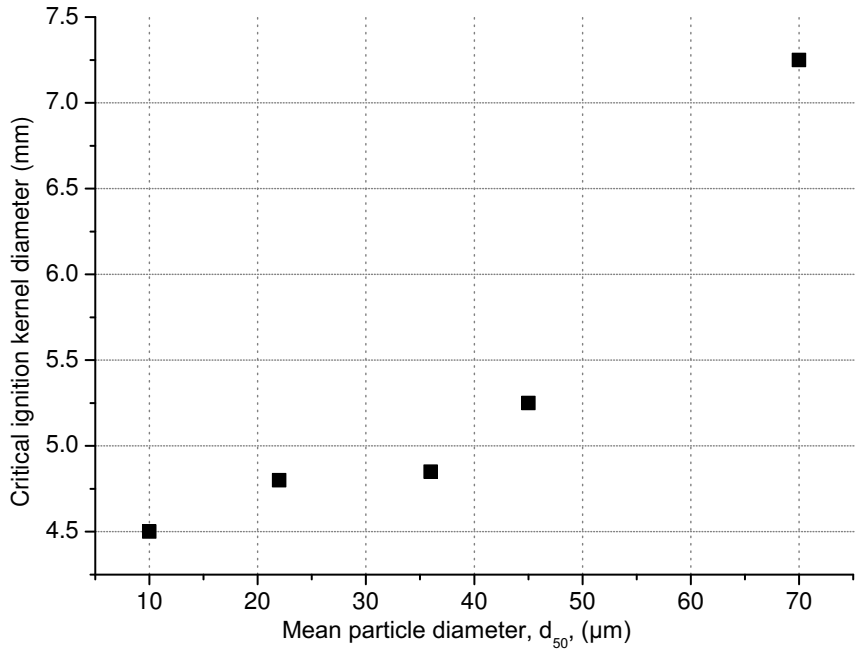

Figure 1.4. Estimated critical kernel sizes vs. starch particle diameter using **Equation 1.6** and the data from **Table 1.1** (Khalili et al., 2012)

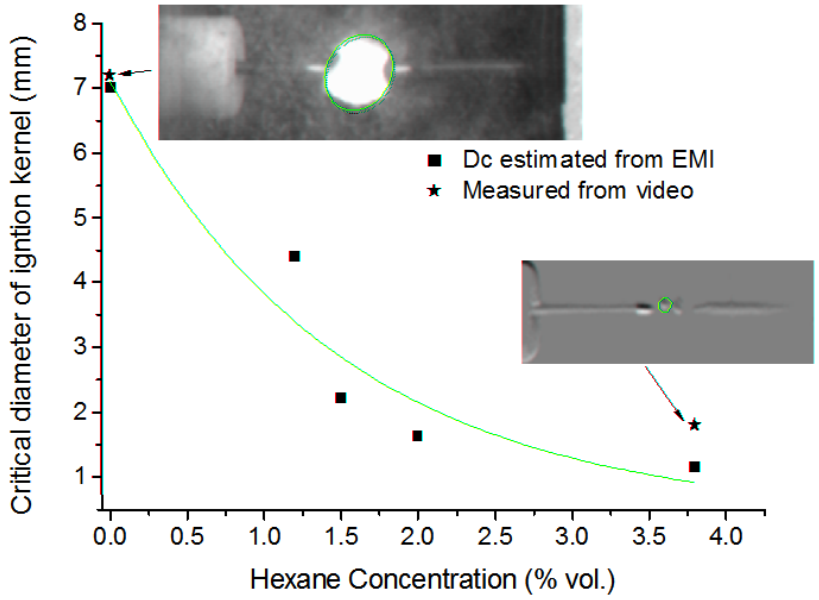

Figure 1.5. Estimated critical kernel sizes of sunflower-oilcakes and hexane mixtures using **Equation 1.6** (Khalili et al., 2012)

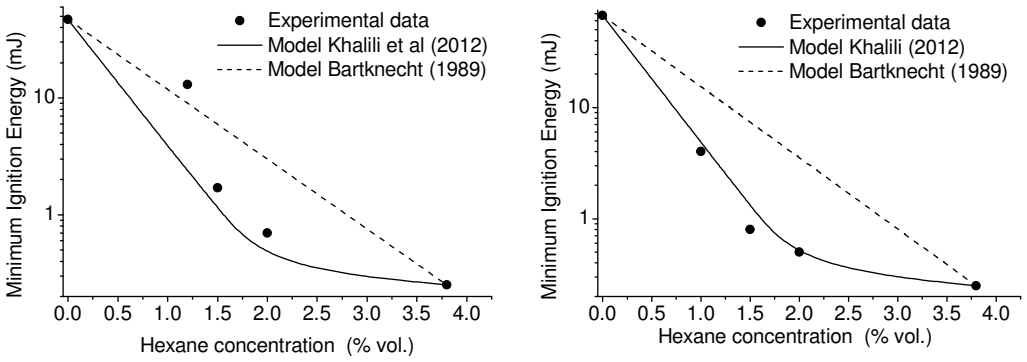

(a) Sunflower-oilcakes and hexane

(b) Starch and hexane

Figure 1.6. Minimum Ignition Energy for sunflower-oilcakes and starch with hexane compared to Bartknecht's (1989) and Khalili's (2012) models, **Equations 1.1** and **1.15** respectively

$$d_{c_{hyb}} = \left(d_{c_{gas}}\right)^{\frac{y_{gas}}{y_{gas_0}}} \left(d_{c_{dust}}\right)^{1-\frac{y_{gas}}{y_{gas_0}}} \tag{1.14}$$

This equation is actually complementary to the model proposed by Khalili et al. (2012) for the MIE_{hyb} that depends only on parameters of each mixture's component and the gas concentration:

$$MIE_{hyb} = MIE_{gas} + (MIE_{dust} - MIE_{gas}) \left(\frac{d_{c_{hyb}}^3 - d_{c_{gas}}^3}{d_{c_{dust}}^3 - d_{c_{gas}}^3} \right) \tag{1.15}$$

This model is compared in **Figure 1.6** to the experimental results for hexane with either sunflower-oilcakes or starch, as well as Bartneckt's model (**Equation 1.1**). It can be observed that the values of the MIE_{hyb} are better predicted through the use of **Equation 1.15** for the mentioned mixtures of organic solids with hydrocarbon gases, especially for methane-starch mixtures. The model was also successfully tested for Pellmont's (1979) work on cellulose ($d_{50} = 27\,\mu m$) and propane (Bartknecht, 1989) with a maximal difference of 5 mJ.

These results are encouraging data for the use of this model in the prediction of the MIE_{hyb}, at least for similar mixtures. This affirmation is not only based upon the good agreement of the model with experimental data, but also because no further tests are required for its use, besides those already in place for the estimation of the MIE_{gas} and the MIE_{dust}. In fact, the complementary values required, $d_{c_{dust}}$ and $d_{c_{gas}}$, can be obtained simultaneously with the minimum ignition energies through the use of a high speed camera.

1.2.2. Ignititability Limits of Hybrid Mixtures

While considering the MIE is of great importance for evaluating the risk of a hybrid mixture explosion, there are more parameters that must be considered. The minimum explosive concentration of the dust (MEC) and the lower explosive limit of the LEL gas must also be accounted. However, considering that the concentration's

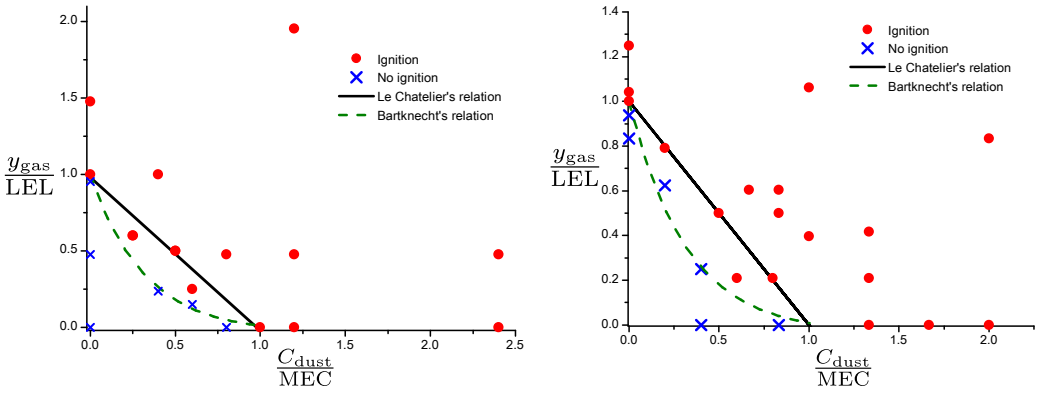

(a) Ethanol and magnesium stearate

(b) Methane and starch

Figure 1.7. Representation of hybrid mixture explosive limits, using Bartknecht and Le Chatelier models

flammable domain is simply framed by the MEC of the dust and the LEL of the gas is a mistake. In fact, mixtures containing concentrations of dust and gas below the LEL and MEC are still sensitive to flammability (Dufaud et al., 2008; Dufaud et al., 2009). Furthermore, the Le Chaterlier's mixing rule, as described by **Equation 1.16**, is often inappropriate for predicting the concentration explosive limits of dust-gas mixtures.

$$\frac{y_{gas}}{LEL} = 1 - \frac{C_{dust}}{MEC} \tag{1.16}$$

Indeed, **Figure 1.7** represents the ignitability domains for mixtures of magnesium stearate with ethanol and starch with methane. These results show that ignition can be observed below the line described by the Le Chatelier's mixing rule: on the one hand, for the case of magnesium stearate with ethanol, explosions with maximum overpressure and rate of pressure rise reaching 0.6 bar and 10 $\frac{bar}{s}$ are observed at concentrations as low as 15 $\frac{g}{m^3}$ of dust and 0.525 %vol of gas. On the other hand, mixtures of 0.96 %vol of methane and 90 $\frac{g}{m^3}$ of starch reach overpressures of 3.4 bar and 26 $\frac{bar}{s}$ for the rate of pressure rise. (Find de corresponding values of MEC and LEL in **Table 1.2**)

In this context, the quadratic expression proposed by Bartknecht (1989) for PVC and methane (**Equation 1.17**) seems to be more adequate to describe the minimal ignition limits of hybrid mixtures.

$$\frac{C_{dust}}{MEC} = \left(1 - \frac{y_{gas}}{LEL}\right)^2 \tag{1.17}$$

This empirical approach was proposed for the explosive concentration limits of PVC and methane mixtures and results in a conservative estimation of the combustibility limits. Although this might be a desired property for predictive models from a safety point of view, it becomes overconservative for some mixtures. This is the case for the mixtures of sunflower-oilcakes and hexane whose explosive concentration limits are represented in **Figure 1.8**. In this cases, **Equation 1.17** is not

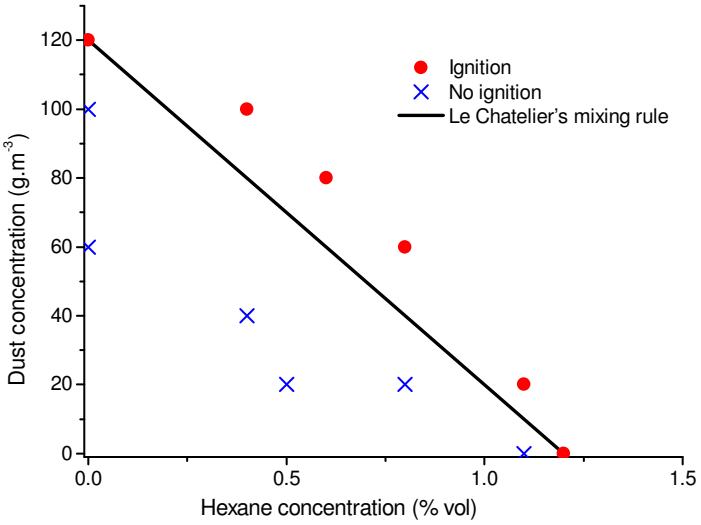

Figure 1.8. Explosive limits of sunflower-oilcakes and hexane

representative of the actual explosive concentration limits of the mixture. In fact the simpler Le Chatelier's mixing rule is more accurate while providing conservative predictions for that particular mixture.

Cases like the previously mentioned allow to highlight the importance of developing a more comprehensive model for dust-gas mixtures or at least of discerning the validity of using a predictive model for a specific mixture. An approach in this direction has already been done by Garcia-Agreda et al. (2011), who justified the use of the Le Chatelier's mixing rule for mixtures of nicotinic acid and methane. Their work illustrates that the Le Chatelier's mixing rule was developed under the assumption that the adiabatic temperatures of the components are rather similar

Table 1.2. Lower explosive limits, Adiabatic temperatures at constant pressure and at constant volume

Compound	LEL (%vol)	MEC ($\frac{g}{m^3}$)	$T_{ad}\|_V$ † (K)	$T_{ad}\|_P$ † (K)
Magnesium stearate	-	25 ‡	1235	1010
Starch	-	150 ‡	2156	1789
Nicotinic acid	-	60 §	1840	1509
Ethanol	2.1 ‡	-	1359	1111
Methane	4.8 ‡	-	1753	1437
Hydrogen	4 ‖	-	741	625

† Estimated at the LEL or MEC with the CEA software (*NASA Chemical Equilibrium with Applications (CEA)*; Gordon and McBride, 1994; Gordon and McBride, 1996)
‡ Khalili et al. (2012)
§ Dufaud et al. (2008)
‖ Coward et al. (1952)

and using it is therefore adequate as long as this condition is ensured. Indeed, the adiabatic temperatures presented in **Table 1.2** for niacin and methane show that the ratio between both is 0.95. In contrast, with methane-starch and ethanol-magnesium stearate, T_{ad} ratios of 0.82 and 1.1 are obtained. Consequently, this would suggest that using the Le Chatelier's mixing rule is valid for mixtures with adiabatic temperatures differing in not more than 5 %.

1.2.2.1. Towards an encompassing model for the explosivity limits of hybrid mixtures

Certainly, the simplicity of Le Chatelier's model is consequent with a proportional contribution of comparable masses of both components on the capacity of the initial kernel to be self-propagating. Therefore, Le Chatelier's model neglects the thermodynamic contribution of the components characterised by the enthalpy of combustion ($\Delta_c \hat{H}$) that determines the adiabatic flame temperature.

This concept is acknowledged on the model proposed by Khalili et al. (2012), that considers the flammability limits of the components and their enthalpy of combustion, using energy balances for dust combustion, gas combustion and hybrid mixture combustion. Khalili et al. tested the applicability of this model for different ratios of the product of the flammability limits and the enthalpy of combustion as expressed in **Equation 1.18**:

$$r = \frac{\mathrm{LEL}}{\mathrm{MEC}} \frac{\rho_g \Delta_c \hat{H}_{gas}}{\Delta_c \hat{H}_{dust}} \tag{1.18}$$

Although this particular aspect of the work was preliminary, it showed that the model is able to estimate flammability values on or below Le Chatelier's line. This is the case for mixtures like ethanol with magnesium stearate and methane with starch

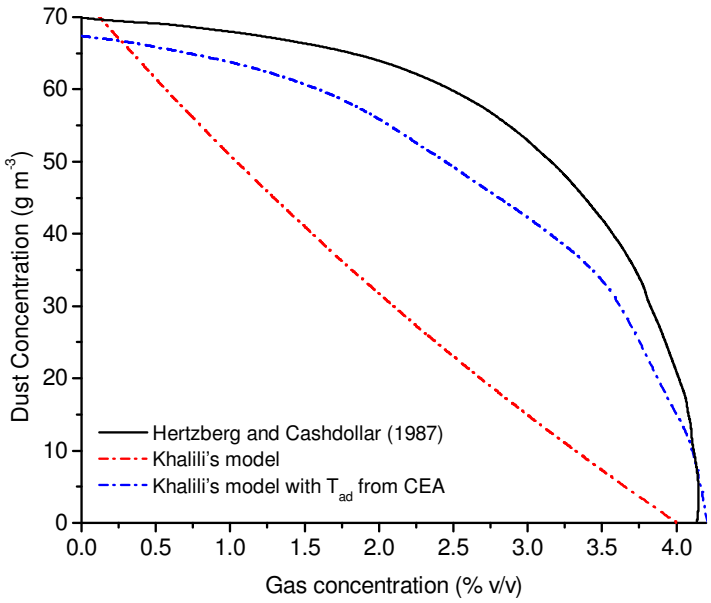

Figure 1.9. Lower concentration flammability limits of hydrogen and corn-starch

(**Figure 1.7**). Nevertheless, the model would be inadequate for predicting flammability limits over Le Chatelier's line like sunflower-oilcakes with hexane. Moreover, it would certainly be incapable of predicting values for mixtures with considerably low ratios of adiabatic flame temperature, as is the case for hydrogen-starch with $\frac{T_{\mathrm{ad}_{\mathrm{gas}}}}{T_{\mathrm{ad}_{\mathrm{dust}}}} = 0.34$. Indeed, **Figure 1.9** presents a comparison between Khalili's model and the lower flammability concentration values, reported by Hertzberg and Cashdollar (1987). The comparison of both, evidences that the mixture can not be described with Khalili's model that behaves, for this particular mixture, almost as Le Chatelier's proportionality line. The reason for this is that Khalili's model estimates the adiabatic flame temperature of the hybrid mixture $T_{\mathrm{ad}_{\mathrm{hyb}}}$ through **Equation 1.19**:

$$T_{\mathrm{ad}_{\mathrm{hyb}}} = \left(T_{\mathrm{ad}_{\mathrm{gas}}}\right)^{\frac{y_{\mathrm{gas}}}{\mathrm{LEL}}} \left(T_{\mathrm{ad}_{\mathrm{dust}}}\right)^{1-\frac{y_{\mathrm{gas}}}{\mathrm{LEL}}} \tag{1.19}$$

therefore, prioritizing the influence of y_{gas} over C_{dust}. Whereas the influence of C_{dust} is more relevant in this case as the value of r for this mixture (**Equation 1.18**), equals the ratio of its adiabatic temperatures: 0.34. Thus, **Equation 1.19** could be modified to depend on C_{dust} as in **Equation 1.20** and therefore improve the whole model.

$$T_{\mathrm{ad}_{\mathrm{hyb}}} = \left(T_{\mathrm{ad}_{\mathrm{dust}}}\right)^{\frac{C_{\mathrm{dust}}}{\mathrm{MEC}}} \left(T_{\mathrm{ad}_{\mathrm{gas}}}\right)^{1-\frac{C_{\mathrm{dust}}}{\mathrm{MEC}}} \tag{1.20}$$

Both equations where tested for hydrogen-starch mixtures against values of $T_{\mathrm{ad}_{\mathrm{hyb}}}|_P$ calculated on the CEA software[2] with the experimental concentration values from Hertzberg and Cashdollar (1987). However, as shown in **Figure 1.10** neither **Equation 1.19** nor **Equation 1.20** are able to describe the behavior of the adibatic temperature for this mixture. In fact, both equations seem to behave almost linearly as opposed to the behaviour of the $T_{\mathrm{ad}_{\mathrm{hyb}}}$ estimated by the CEA. This could explain the similarities of Khalili's model with Le Chatelier's mixing rule when applied to this mixture.

Nonetheless, the calculations performed by the CEA are, to a great extend, mass and energy balances involving extended reaction mechanisms. If those mechanisms where to be simplified, the energy balance of the reaction for a hybrid mixture at its concentration limits could be summarized in **Equation 1.21**.

$$T_{\mathrm{ad}_{\mathrm{hyb}}}\left(y_{\mathrm{gas}}, C_{\mathrm{dust}}\right) = T_0 - \frac{C_{\mathrm{dust}}\Delta_{\mathrm{c}}\hat{H}_{\mathrm{dust}} + y_{\mathrm{gas}}\rho_{\mathrm{gas}}\Delta_{\mathrm{c}}\hat{H}_{\mathrm{gas}}}{\rho_{\mathrm{air}}\tilde{C}_{P\mathrm{air}} + y_{\mathrm{gas}}\rho_{\mathrm{gas}}\tilde{C}_{P\mathrm{gas}} + C_{\mathrm{dust}}\tilde{C}_{P\mathrm{dust}}} \tag{1.21}$$

Hence, with the purpose of testing if the replacement of **Equation 1.19** is sufficient for improving Khalili's model, the $T_{\mathrm{ad}_{\mathrm{hyb}}}$ values from the CEA where fitted in the form of a 6^{th} order polynomial: $T_{\mathrm{ad}_{\mathrm{hyb}}} = \sum_{i=0}^{6} a_i \left(C_{\mathrm{dust}}\right)^i$ and replaced in **Equation 1.21**. In such a way, the variation of y_{gas} from 0 to LEL, allows to obtain corresponding values of C_{dust}. The results of this test are represented by the blue line in **Figure 1.9**. It can be seen that this modification to Khalili's model con-

[2] *NASA Chemical Equilibrium with Applications (CEA)*; Gordon and McBride, 1994; Gordon and McBride, 1996.

siderably approaches its predictions to the experimental values, with a maximum deviation reaching 15%. The bumps in the curve are caused by the modelling of $T_{\mathrm{ad}_{\mathrm{hyb}}}$ through the polynomial function. While such polynomial may not be the best equation to describe $T_{\mathrm{ad}_{\mathrm{hyb}}}$, it achieves the goal of showing the importance of an accurate description of $T_{\mathrm{ad}_{\mathrm{hyb}}}$ for the model. Moreover, the bumps it causes also help to elucidate how sensible the model is to $T_{\mathrm{ad}_{\mathrm{hyb}}}$. Such, sensitivity is also noticed when using values for the adiabatic temperature at constant volume $T_{\mathrm{ad}}|_V$, as no convergence is possible when doing so. This is important as the sensitivity tests for gas and dusts are usually performed at constant pressure and as consequence adiabatic flame values considerably differ from each other depending on the constant condition (**Table 1.2**).

Because of preliminary results, the author proposes that the solution for an encompassing model for the lower explosive limits of hybrid mixtures may be found in an appropriate description of $T_{\mathrm{ad}_{\mathrm{hyb}}}$ together with **Equation 1.21**. Such a model would probably be in the form:

$$T_{\mathrm{ad}_{\mathrm{hyb}}} = f\left(\frac{y_{\mathrm{gas}}}{\mathrm{LEL}}, \frac{C_{\mathrm{dust}}}{\mathrm{MEC}}, T_{\mathrm{ad}_{\mathrm{gas}}}|_P, T_{\mathrm{ad}_{\mathrm{dust}}}|_P, r\right)$$

where r is expressed by **Equation 1.18**. Additionally, taking into account the volumetric expansion of the hotter isobaric gas in **Equation 1.21** may also reduce the deviation observed in the preliminary test presented here.

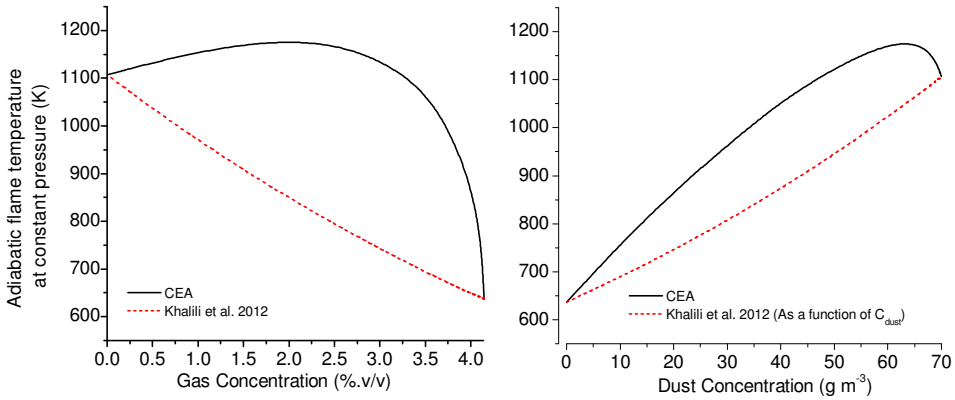

Figure 1.10. Adiabatic flame temperature at constant pressure for mixtures of hydrogen-starch. The black line represents values calculated with the CEA software using gas and dust concentrations reported by Hertzberg and Cashdollar (1987) and presented in **Figure 1.9**†. The red pointed line at the left represents Khalili's model in **Equation 1.19** and the right one represents **Equation 1.19**

†Notice that the black lines on both sides are projections of the the same line on different coordinate systems.

1.3. Severity of Hybrid Mixtures

1.3.1. Severity and Explosion Regimes in Hybrid Mixtures According to Their Composition

The ignitability limits of both, solid and gas have been used by Garcia-Agreda et al. (2011) and Sanchirico et al. (2011) to define **explosion regimes** for hybrid mixtures according to their composition. **Figure 1.11** illustrates how the definition of such regimes is given by the explosivity limits of gas (LEL), dust (MEC) and the hybrid mixture. Thus, depending on the concentration of gas and dust in the mixture, the kinetics of the resulting explosion is expected to be driven mainly by either (or both) components. Explosions of mixtures whose concentrations of gas and dust are over the LEL and the MEC are **dual fuel driven**, while **dust** and **gas-driven regimes** are those in which either the gas or the dust are below the LEL or the MEC respectively. Finally, explosions of mixtures whose concentrations of gas and dust are below the LEL and the MEC are **synergic**.

Garcia-Agreda et al. (2011) and Sanchirico et al. (2011) also proposed, to plot the experimental severity values of the mixture as a function of their compositions over the corresponding position on the axes from **Figure 1.11**. The magnitude of the severity would then be represented by the diameter of the point in the graph. According to the author of the present document, this is a considerable improvement over the $\left(\frac{\mathrm{d}P}{\mathrm{d}t}\right)_{\max}$ *vs.* y_{gas} representation obtained from the hybrid mixture module provided by the KSEP software of the 20l sphere.

In fact $\left(\frac{\mathrm{d}P}{\mathrm{d}t}\right)_{\max}$ *vs.* y_{gas} or $\left(\frac{\mathrm{d}P}{\mathrm{d}t}\right)_{\max}$ *vs.* C_{dust}, is the way that most authors present their results on explosion severity of hybrid mixtures. Although, this view is still valuable as it allows to comprehend the magnitude of the standard deviation,

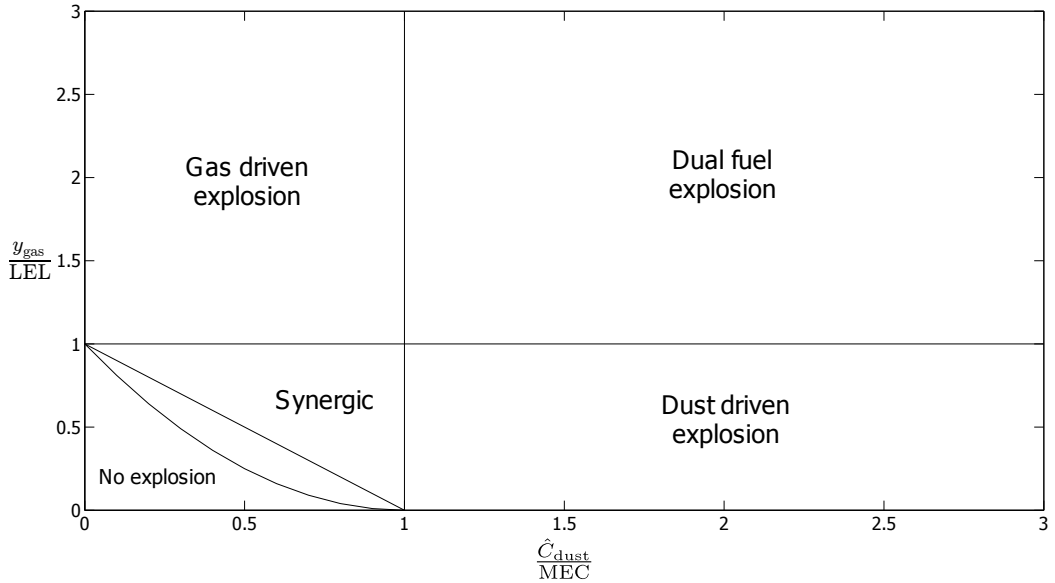

Figure 1.11. Explosion regimes of hybrid mixtures according to their composition as proposed by Garcia-Agreda et al. (2011) and Sanchirico et al. (2011)

it lacks of the space efficiency (in terms of the amount of information delivered to the reader) obtained from the method proposed by Garcia-Agreda et al. (2011) and Sanchirico et al. (2011). Unfortunately, that representation prevents the superposition of a predictive model over the data, or even a tendency curve/surface. This can be done with a contour-graph while efficiently transmitting the information. This has been done by Traore (2007) and Dufaud et al. (2009), but it is still necessary to consider the position of the experimental points. This is important because it allows to visualize empty areas where more experimental data might be necessary to confidently assert the behaviour of the severity parameters in terms of the concentration values.

For this reason the author proposes here another alternative that seeks to combine the advantages of these methods while trying to avoid another disadvantage common to the methods mentioned: Maximum Explosive Concentration of dusts are ever hardly found (or looked for); this happens because at high concentrations the dust rapidly settles, decreasing the concentration do the dust cloud. For this reason, increasing the dust concentration after a maximum K_{St} is achieved, does not seem to considerably decrease the severity of the explosion. Consequently, the comparison of the explosion severity values for a given mixture results in a graphical disparity between dust and gas that will be explained as some important definitions related to the stoichiometry of combustion are presented next.

1.3.2. Stoichiometry of Combustion

1.3.2.1. Fuel Equivalence Ratio and Normalized Fuel Equivalence Ratio

As any other reaction, fuel combustion, depends largely on the composition of the reacting mixture, particularly the ratio between the fuel and the oxidizer. Therefore, for the complete combustion of an organic fuel Λ composed of C, H and O, in the presence of oxygen as described by:

$$+\,\nu_{\mathrm{O_2}}\mathrm{O_2} \longrightarrow \nu_{\mathrm{CO_2}}\mathrm{CO_2} + \nu_{\mathrm{H_2O}}\mathrm{H_2O}$$

the ratio of fuel to oxygen at stoichiometric conditions is $\frac{\nu_\Lambda}{\nu_{\mathrm{O_2}}}$. Accordingly, burning n_Λ moles of fuel requires $n_{\mathrm{O_2}}|_{\mathrm{st}} = \frac{\nu_{\mathrm{O_2}}}{\nu_\Lambda} n_\Lambda$ moles of oxygen to fit stoichiometric proportion, which is the molar **oxygen demand** of the fuel. In these terms, the fuel richness of a mixture can be expressed through the **equivalence ratio** ϕ, defined as the ratio of the ratios of moles of fuel-to-oxygen at actual and stoichiometric conditions. This definition is defined by **Equation 1.22**:

$$\phi = \frac{n_\Lambda / n_{\mathrm{O_2}}}{\left(n_\Lambda / n_{\mathrm{O_2}}\right)|_{\mathrm{st}}} = \frac{\nu_{\mathrm{O_2}}}{\nu_\Lambda}\frac{n_\Lambda}{n_{\mathrm{O_2}}} \tag{1.22}$$

According to this definition a mixture with $\phi = 1$ is called *stoichiometric*, whereas mixtures whose limiting reactant is the fuel $0 < \phi < 1$ are called *fuel-lean mixtures*. Therefore, *fuel-rich mixtures* are those whose limiting reactant is oxygen, $1 < \phi < \infty$. This implies that the domain of ϕ is asymmetrical for fuel-rich and fuel-lean mixtures. To avoid this asymmetry the **normalized fuel equivalence ratio** Φ, is

also used to describe the richness of a mixture (Law, 2006) and is defined in terms of ϕ as:

$$\Phi = \frac{\phi}{1+\phi} \tag{1.23}$$

With this definition mixtures with $\Phi = 0.5$ are considered stoichiometric, whereas for fuel-lean mixtures $0 < \Phi < 0.5$ and $0.5 < \Phi < 1$ for fuel-rich mixtures.

On the other hand, when the fuel is composed of N organic compounds Λ_i, where $i = 1, 2, 3, ..., N$, the set of reactions for complete combustion could be represented as follows:

$$\nu_{\Lambda_1}\Lambda_1 + \nu_{O_2,1}O_2 \longrightarrow \nu_{CO_2,1}CO_2 + \nu_{H_2O,1}H_2O$$

$$\nu_{\Lambda_2}\Lambda_2 + \nu_{O_2,2}O_2 \longrightarrow \nu_{CO_2,2}CO_2 + \nu_{H_2O,2}H_2O$$

$$\vdots$$

$$\nu_{\Lambda_N}\Lambda_N + \nu_{O_2,N}O_2 \longrightarrow \nu_{CO_2,N}CO_2 + \nu_{H_2O,N}H_2O$$

In that case, the definition of ϕ extends to:

$$\phi = \left(\frac{\sum_{i=1}^{N} n_{\Lambda_i}}{n_{O_2}}\right)\left(\frac{\sum_{i=1}^{N} n_{\Lambda_i}}{\sum_{i=1}^{N}\left(\nu_{O_2,i}/\nu_{\Lambda_i}\right) n_{\Lambda_i}}\right)^{-1} = \frac{1}{n_{O_2}}\sum_{i=1}^{N}\frac{\nu_{O_2,i}}{\nu_{\Lambda_i}} n_{\Lambda_i} \tag{1.24}$$

This definition is only related to the content of combustible and oxygen in the mixture and is therefore independent of the combustion products. It means that the definition of ϕ and Φ are still valid even if the products of the *complete* combustion of Λ_i are not exclusively CO_2 and H_2O or even if CO_2 and H_2O are not combustion products for Λ_i .

Although the author of the present work is aware of the limited use that is usually given to the normalized fuel equivalence ratio (Law, 2006), this parameter is recurrently used in this document to represent the content of fuel in the mixture. The decision to adopt this variable is based on the observation of the particular behaviour of different combustion parameters of dust. Indeed, in contrast to gas behaviour, some combustion parameters (*e.g.* $\left(\frac{dP}{dt}\right)_{max}$) do not show considerable changes with large variations in dust concentration for fuel-rich mixtures. Thus, the author considers that the symmetry of the domain of Φ permits to better visualize the data and combustible behaviour of gas and dust.

Finally, a further modification of these concepts of ϕ and Φ is incorporated in this study, that will be called here the **(normalized) fuel equivalence ratio at equivalent volatile mass content** , ϕ_{eq} and Φ_{eq}. This concept was developed on the work by Garcia-Agreda et al. (2011) and Sanchirico et al. (2011) and is further explained in page 26.

1.3.2.2. Fraction of Oxygen Demand

While the fuel equivalence ratio allows to understand the behaviour of a combustible compound according to its stoichiometry with oxygen; the analysis of hybrid mixtures also requires a variable that allows to differentiate the effect of each of the combustible components in the mixture. In the case of mixtures of combustible gases, the molar fraction is usually preferred, whereas for combustible dust mixtures the mass fraction or the mass concentration would normally be chosen. Unfortunately, for the case of dust-gas hybrid mixtures, choosing between either way has a "polluting" effect on the graphic representation of results as either compound tends to be overrepresented in the graph. This usually happens when the density or the molar mass of the compounds differ in various orders of magnitude. That is frequently the case, in the pharmaceutical industry, where particles of solids with high molecular weights can be found in atmospheres with considerably smaller molecules of combustible vapours. Therefore, another parameter has been chosen and defined (as the fuel equivalence ratio) on the oxygen consumption of each fuel in the mixture.

For a hybrid mixture composed of N combustible components Λ_i with $i = 1, 2, ...N$, the oxygen demand of each combustible would be $n_{\mathrm{O}_2,i}|_{\mathrm{st}} = \frac{\nu_{\mathrm{O}_2,i}}{\nu_{\Lambda_i}} n_{\Lambda_i}$. Consequently the **fraction of oxygen demand of** Υ_i is defined here as the molar oxygen demand of Λ_i divided by the oxygen demand of the whole mixture:

$$\Upsilon_{\Lambda_i} = \frac{n_{\mathrm{O}_2,i}|_{\mathrm{st}}}{\sum_{j=1}^{N} n_{\mathrm{O}_2,j}|_{\mathrm{st}}} = \frac{\nu_{\mathrm{O}_2,i}}{\nu_{\Lambda_i}} n_{\Lambda_i} \left(\sum_{j=1}^{N} \frac{\nu_{\mathrm{O}_2,j}}{\nu_{\Lambda_j}} n_{\Lambda_j} \right)^{-1} \tag{1.25}$$

Υ_{Λ_i} varies therefore from 0 (meaning that there is no Λ_i present in the combustible mixture) to 1 (meaning Λ_i is the only combustible component in the mixture). A value of $\Upsilon_{\Lambda_i} = 0.5$ for a binary mixture means that both components are present in equivalent quantities according to the oxygen they would require to undergo complete combustion.

1.3.2.3. Volatile Content of Dust

The combustion of solids can be simplified as a process that follows two different reaction paths: heterogeneous combustion, in which oxygen diffuses to the surface of the solid particle where oxidation takes place; and homogeneous combustion, consisting on the thermal decomposition of the solid particle into simpler gas molecules that will then mix in the gas phase to be oxidised. Consequently, the predominance of either path depends on the rates at which oxygen diffusion and heat transfer happen. This process is ultimately dependent on the size of the particle, or more precisely on the ratio between surface area where heterogeneous reaction occurs and the volume of the particle to be heated up until volatilisation.

Dufaud et al. (2012b) have shown that a *limiting particle size* exists (30 µm for wheat starch) below which, the volatilisation of the particle is so fast that reducing its size has no effect in lowering the MIE. That study together with Dufaud et al., 2012a, highlight the importance of this pyrolysis step in the study of organic dust explosions. Not only it has a noticeable effect on the MIE but also in the propagation of the flame and thus on the severity of the dust explosion. Furthermore,

the volatilization process leads to the creation of a hybrid mixture of the dust and its pyrolysis gases. Therefore the understanding of this process may also be helpful on the study of hybrid mixtures. For this reason this subject is further addressed in **Chapter 2** (page 41).

The importance of the volatilization step is also acknowledged by Di Benedetto and Russo (2007), who showed that in the case of small particles, the explosion can be modelled as the explosion of its volatiles. This approach has been taken further and incorporated to the analysis of hybrid mixtures by Garcia-Agreda et al. (2011) through their work on mixtures of nicotinic acid with acetone. They analysed the severity of explosions relative to the **dust concentration equivalent to combustible volatiles content** $\hat{C}_{\text{eq}}$, defined in terms of the experimental dust concentration $\hat{C}_{\text{dust}}$ and the combustible **mass fraction of combustible volatiles**, ε_{v} as:

$$\hat{C}_{\text{eq}} = \varepsilon_{\text{v}} \hat{C}_{\text{dust}} \tag{1.26}$$

For estimating the ε_{v} of nicotinic acid, they used the CEA software[3] and found it to be around 0.26 for a temperature range of 700-1800 K. Consequently, they found that the resulting values of $\hat{C}_{\text{eq}}$ for dust concentration at maximum deflagration index $\hat{C}_{\text{dust}}\Big|_{\max\left(K_{\text{St}}\right)}$ are remarkably similar to the expected stoichiometric values of $\hat{C}_{\text{dust}}$:[4]

$$\hat{C}_{\text{eq}}\Big|_{\max\left(K_{\text{St}}\right)} = \varepsilon_{\text{v}} \hat{C}_{\text{dust}}\Big|_{\max\left(K_{\text{St}}\right)} \approx \hat{C}_{\text{dust}}|_{\text{st}} \tag{1.27}$$

These results allow, in principle, to think about $\hat{C}_{\text{eq}}$ as the concentration of dust that actually contributes to or participates in the generation of energy during the explosion. This work was expanded by Sanchirico et al. (2011) who redefined the fuel equivalence ratio to consider ε_{v}. Such redefinition is called **(normalized) fuel equivalence ratio at equivalent volatile mass content of dust** Φ_{eq} and ϕ_{eq}, given by **Equations 1.28** and **1.29**:

$$\Phi_{\text{eq}} = \frac{\phi_{\text{eq}}}{1 + \phi_{\text{eq}}} \tag{1.28}$$

$$\phi_{\text{eq}} = \frac{1}{n_{\text{O}_2}} \sum_{i=1}^{N} \frac{\nu_{\text{O}_2,i}}{\nu_{\Lambda_i}} \varepsilon_{\text{v}_i} n_{\Lambda_i} \tag{1.29}$$

Notice that, as opposed to the definition given by Sanchirico et al., **Equation 1.29** allows ε_{v} to be different than 1 also for gaseous compounds. Indeed, for most gases $y_{\text{gas}}\Big|_{\max\left(K_{\text{St}}\right)} = y_{\text{gas}}|_{\text{st}}$ and therefore ε_{v} is always 1. Nevertheless, this

[3] *NASA Chemical Equilibrium with Applications (CEA)*; Gordon and McBride, 1994; Gordon and McBride, 1996.

[4] Notice that the subscript $_{\text{St}}$ in K_{St} has its origins in the german word for dust *Staub*, that is not related to the notation used in this document for defining values found at stoichiometric conditions $|_{\text{st}}$

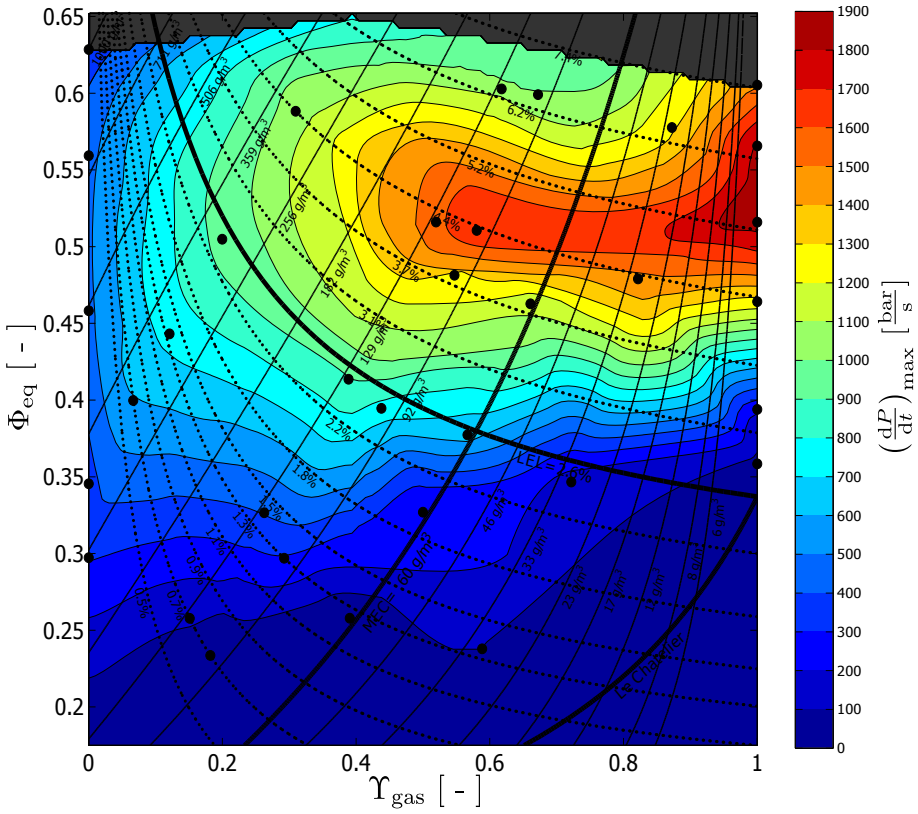

Figure 1.12. Rate of pressure rise map for the niacin/acetone mixtures with t_v =60 ms. Υ_{gas} and Φ_{eq} are defined by **Equations 1.25** and **1.28** respectively. y_{gas} and C_{dust} are represented by the pointed and solid lines respectively. (Sanchirico et al., 2011)

might not be the case for various organic solvents whose boiling point at 1 bar is close to 20 °C allowing the formation of two phases. Consequently, during the preparation of the tests in the 20 l sphere, the solvent is completely vaporized prior the dispersion of the dust (0.6 bar), but after the dispersion the sphere reaches 1 bar driving the condensation of a portion of the solvent. As a result, there is an effective concentration of the solvent that is actually contributing to the explosion that can be estimated through **Equation 1.27**.

1.3.3. Representation of the explosion severity in terms of Φ_{eq} and Υ_{gas}

Using the definitions of Υ_{gas} and Φ_{eq} from **Equations 1.25** and **1.28** a contour-graph can be plotted as a function of both of them. **Figure 1.12** presents such a graph for the rate of pressure rise of niacin-acetone mixtures from Sanchirico's work. **Table 1.3** shows the values of ε_v and the complete combustion reaction of the pure components of this mixture as well as other components of mixtures analysed later in this chapter.

In regard to the representation of **Figure 1.12**, on the one hand, it allows to

Table 1.3. Dust and gas fractions combustion reactions and estimated fractions of oxygen demand

Fuel	Complete combustion reaction	ε_v
Starch	$(C_6H_{10}O_5)_n + 6nO_2 \longrightarrow 6nCO_2 + 5nH_2O$	0.30
Nicotinic acid	$C_6H_5NO_2 + \frac{25}{4}\,O_2 \longrightarrow 6\,CO_2 + \frac{5}{2}\,H_2O + \frac{1}{2}\,N_2$	0.28
Telithromycin	$C_{43}H_{65}N_5O_{10} + \frac{217}{4}\,O_2 \longrightarrow 43\,CO_2 + \frac{65}{2}\,H_2O + \frac{5}{2}\,N_2$	0.35
Methane	$CH_4 + 2\,O_2 \longrightarrow CO_2 + 2\,H_2O$	1
Diisopropyl ether	$(C_3H_7)_2O + 9\,O_2 \longrightarrow 6\,CO_2 + 7\,H_2O$	1
Acetone	$(CH_3)_2CO + 4\,O_2 \longrightarrow 3\,CO_2 + 3\,H_2O$	1
Toluene	$C_7H_8 + 9\,O_2 \longrightarrow 7\,CO_2 + 4\,H_2O$	0.26

separate fuel-lean from fuel-rich mixtures by an horizontal line at $\Phi_{eq} = 0.5$. On the other hand, a vertical line at $\Upsilon_{gas} = 0.5$ separates dust-richer mixtures from gas-richer mixtures ones according to the oxygen they would consume if both underwent complete combustion. Tracing dust and gas concentrations lines on the top of it, allows to still comprehend the exact amount of dust or gas present in the mixture. Moreover, the concentration explosivity limits define the regimes described in **Section 1.3.1** in page 21 with a balanced representation of each one on the surface of the graph. Finally the presence of the experimental points allows to detect areas with low density of experimental data that might be necessary to address in order to state appropriate conclusions about the mixture's behaviour.

1.3.4. Analysis of the severity map of various dust-gas hybrid mixtures

The observations Sanchirico et al. (2011) made in their work, are still evident when observing **Figure 1.12**. For example, once the Φ_{eq} is fixed the explosion severity is decreased by replacing gas with dust. Indeed, this might seem generally true as the maximum severities of pure gas explosions are usually greater than those of most dusts (with counted exceptions of dusts classed 3 as aluminium that can reach $\left(\frac{dP}{dt}\right)_{max}$ of 1900 $\frac{bar}{s}$, that overpasses most gases mentioned in **Table 1.3**). Therefore, if a proportional behaviour in the severity of the mixtures is expected, the severity of the mixture should be framed by that of its components at equivalent fuel content. This is the case for niacin-acetone mixtures as stated by Sanchirico et al. Any point over any horizontal line in **Figure 1.12**, at $\Phi_{eq} = 0.5$ for example, would always be in a higher or similar severity zone as a point at its left over the same line. This kind of situation would imply that the interactions between gas and dust are minimum or non existent during the explosion. Nevertheless, it might seem that in such an environment the severity of the explosion would decline steadily and consequently find at ($\Upsilon_{gas} = 0.5, \Phi_{eq} = 0.5$) values of $\frac{1900+300}{2} = 1100\ \frac{bar}{s}$ instead of 1600 $\frac{bar}{s}$. Of course this is not the case because of the thermal interactions between acetone and niacin: explosions of 4% acetone would reach 1200 $\frac{bar}{s}$ while 130 $\frac{g}{m^3}$ niacin would not even surpass 100 $\frac{bar}{s}$. Mainly because the niacin is not able to achieve complete combustion by its own, as reflected on its ε_v =0.26. But because of the heat inertia caused by the combustion of acetone, a larger portion of dust can

react and release more energy that adds up to magnify the severity, specially in the dual-driven regime.

Beyond thermal interactions, chemical ones may also be found. Those kinds of interactions that unlike acetone/niacin mixtures would result in severity values that are not framed by those of the pure components. This kind of behaviour *seems* to be exhibited by telithromycine/acetone, telithromycine/toluene and niacin/diisopropyl-ether mixtures whose severity maps can be observed in **Figures 1.13** to **1.15**. Data for these figures comes from the thesis work of Traore (2007), some of which was published by Dufaud et al. (2009). The emphasis given before to the word "seems", arises from the fact that the data was originally presented, only as a contour plot without the presence of the experimental points over it. For this reason one may think that in all of these mixtures, maximum severity is achieved in the dual-driven region instead of the vertical line at $\Upsilon_{\text{gas}} = 1$. Consequently suggesting, that the secondary reactions of the pure components release sub-products whose interactions increase the combustion velocity of the whole mixture.

Whereas, **Figure 1.13** lacks of the most important experimental points that would allow to confidently make that claim. First of all, the four points at $\Upsilon_{\text{gas}} = 1$ are not enough to characterise that line nor to assert that the maximum rate of pressure rise that acetone can achieve is $1300\,\frac{\text{bar}}{\text{s}}$. In fact, importing the severity values obtained by Sanchirico et al. (2011) for acetone into this graph one could see: that the data are complementary to each other, in the sense that a typical paraboloid-like curve is obtained for acetone from both sets of data; and that the maximum rate of pressure rise for acetone is $1900\,\frac{\text{bar}}{\text{s}}$. These data were not grouped here because the values obtained by Sanchirico et al. (2011) were obtained with continued electric ignition and Traore (2007) used chemical igniters. Second of all, a huge space empty of data (almost $\frac{1}{2}$ of the figure) exists at the right of the line for $C_{\text{dust}} = 110\,\frac{\text{g}}{\text{s}}$. The lack of data in this region, that might turn out to be the most interesting for these mixture in terms of risk management, is the reason for doubting that in fact synergistic chemical interactions are present as it is possible that with sufficient information, a plot as the one from **Figure 1.12** could be obtained. However, there is not enough information over the line $\Phi_{\text{eq}} = 0.5$, particularly below the point that reaches a maximum severity of $1800\,\frac{\text{bar}}{\text{s}}$ arround $\Upsilon = 0.5$. It would be expected for a point there to be reach a higher $\left(\frac{\text{d}P}{\text{d}t}\right)_{\text{max}}$. Consequently the possibility for a chemically interacting mixture, is left as an open question.

In the case of telithromycine/toluene in **Figure 1.14**, the data for pure gas is better characterized with maximum severity at $1500\,\frac{\text{bar}}{\text{s}}$. On the other hand, according to the experimental data available, the mixtures reach maximum severity of $\left(\frac{\text{d}P}{\text{d}t}\right)_{\text{max}} = 1900\,\frac{\text{bar}}{\text{s}}$, on the dual-driven region at $\Phi_{\text{eq}} = 0.5$ and $\Upsilon_{\text{gas}} = 0.7$. Although experimental values would be desirable on the for dust concentrations below $120\,\frac{\text{g}}{\text{m}^3}$, there is little doubt that in this case, the thermal interactions are not enough to explain this behaviour. This mixture is behaving in a way that would not be expected by observing its components separately and is a good example of the need to address hybrid mixtures as a particular class. Moreover, only two experimental points are found over the line for $\Phi_{\text{eq}} = 0.5$ (besides the one for gas); which means that, over this line it would still be possible for this mixture to have a point

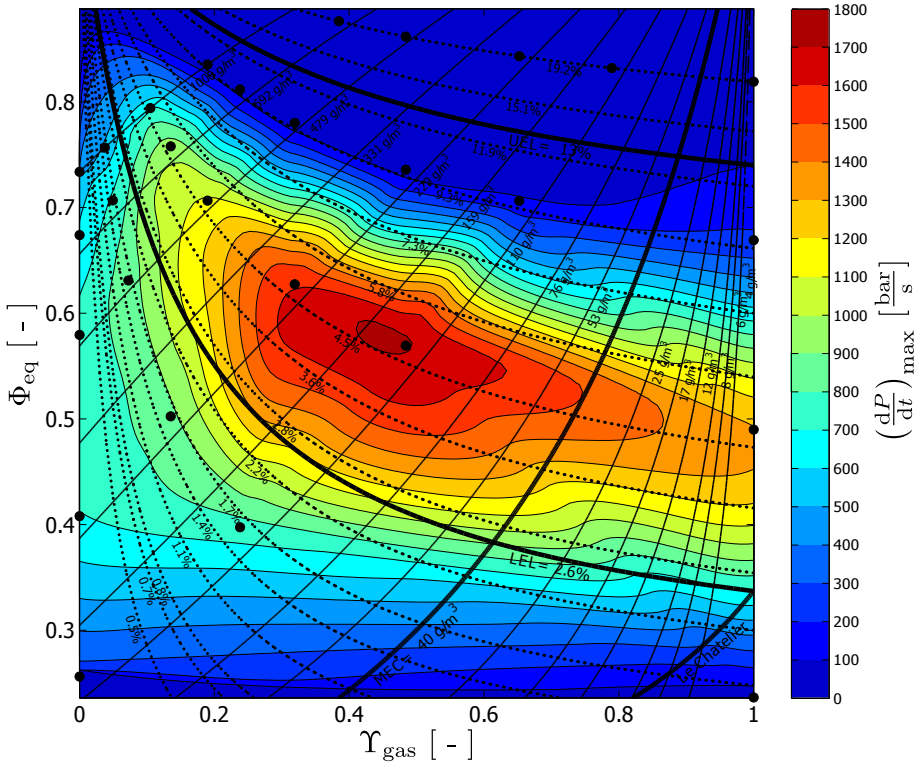

Figure 1.13. Rate of pressure rise map for the telithromycine-acetone mixtures. Υ_{gas} and Φ_{eq} are defined by **Equations 1.25** and **1.28** respectively. y_{gas} and C_{dust} are represented by the pointed and solid lines respectively. (Traore, 2007)

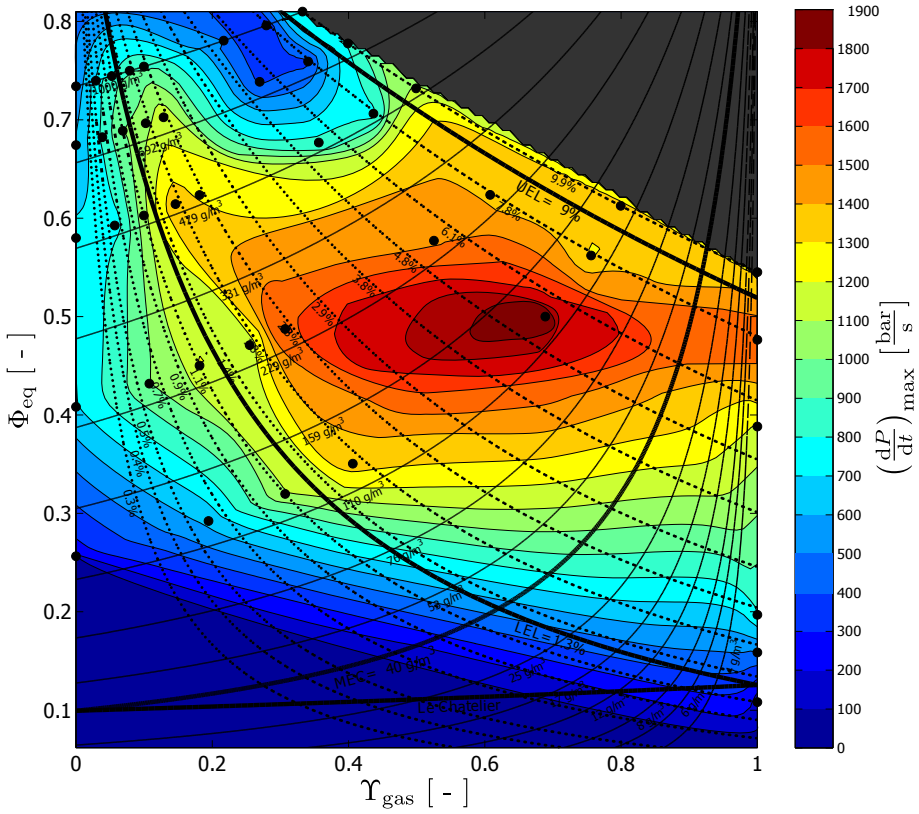

Figure 1.14. Rate of pressure rise map for the telithromycine/toluene mixtures. Υ_{gas} and Φ_{eq} are defined by **Equations 1.25** and **1.28** respectively. y_{gas} and C_{dust} are represented by the pointed and solid lines respectively. (Dufaud et al., 2009)

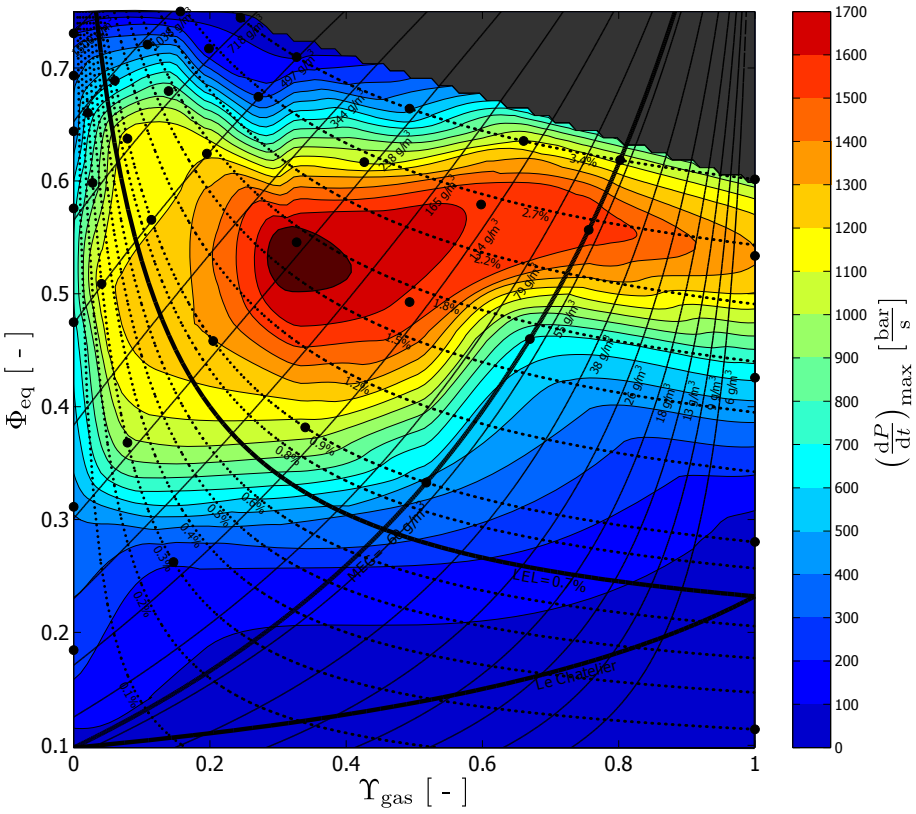

Figure 1.15. Rate of pressure rise map for the niacine/diisopropyl-ether mixtures. Υ_{gas} and Φ_{eq} are defined by **Equations 1.25** and **1.28** respectively. y_{gas} and C_{dust} are represented by the pointed and solid lines respectively. (Dufaud et al., 2009)

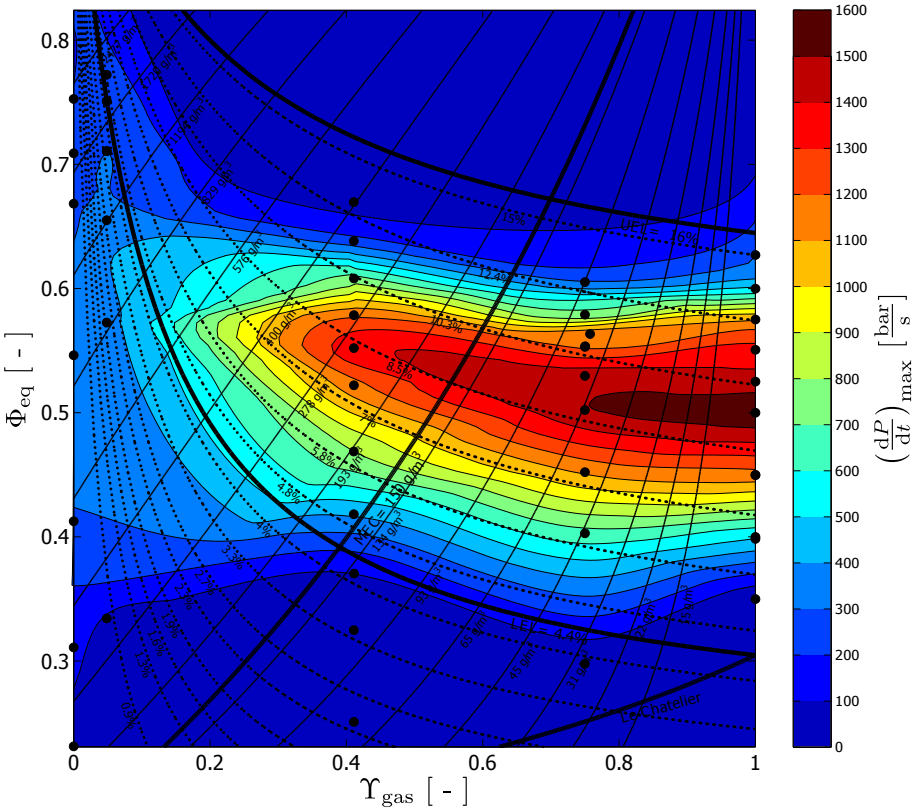

Figure 1.16. Rate of pressure rise map for the starch/methane mixtures. Υ_{gas} and Φ_{eq} are defined by **Equations 1.25** and **1.28** respectively. y_{gas} and C_{dust} are represented by the pointed and solid lines respectively

with higher $\left(\frac{\mathrm{d}P}{\mathrm{d}t}\right)_{\max}$ anywhere between $0.3 \leq \Upsilon_{\mathrm{gas}} < 1$.

Similar claims can be done for nicotinic acid/diisopropylether mixtures in **Figure 1.15**. The gas is fairly well characterised. More points are desirable for $C_{\mathrm{dust}} < 60\,\frac{\mathrm{g}}{\mathrm{m}^3}$. The highest $\left(\frac{\mathrm{d}P}{\mathrm{d}t}\right)_{\max}$ the gas reaches is $1300\,\frac{\mathrm{bar}}{\mathrm{s}}$ while its mixtures with nicotinic acid reach $1700\,\frac{\mathrm{bar}}{\mathrm{m}^3}$. This last value could eventually be even higher if more data where available for $0.2 \leq \Upsilon_{\mathrm{gas}} < 1$. Therefore, this behaviour could not be explained exclusively from the thermal interactions between dust and gas, but rather a kinetic explanation, for interacting subproducts of combustion may be more appropriate.

1.3.4.1. Experimental Study for Starch-Methane Hybrid Mixtures

Mixtures of methane/starch were also mapped for their severity values (**Figure 1.16**) using a wide range of dust and gas concentrations. The tests were performed at the LRGP and the University of Naples Federico II for mixtures of starch and methane (See pages A-3 to A-7 in **Appendix A** for further detail). The experimental testing was designed for characterising the behaviour of mixtures in sets with constant values of Υ_{gas} (0, 0.05, 0.4, 0.75 and 1), meaning that an equivalent ratio of gas/dust is present for each set of mixtures tested at different values of Φ_{eq}. In fact, each of the sets tested can be classified as belonging to either a pure compound or a *"superior" regime*[5]: pure dust ($\Upsilon_{\mathrm{gas}} = 0$), dust-driven regime ($\Upsilon_{\mathrm{gas}} = 0.05$), dual-driven regime ($\Upsilon_{\mathrm{gas}} = 0.4$), gas-driven regime ($\Upsilon_{\mathrm{gas}} = 0.75$) and pure gas ($\Upsilon_{\mathrm{gas}} = 1$).

These mixtures behave similarly to niacin-acetone mixtures, the predominant interactions are thermal and no chemical synergy seems to manifest in any regime. Looking in detail to the experimental results in **Figure 1.17**, it can be seen that data for pure gas, gas-driven and dual-driven regions, behave similarly among them and drastically different from the data with $\Upsilon_{\mathrm{gas}} \leq 0.05$. The maximum $\left(\frac{\mathrm{d}P}{\mathrm{d}t}\right)_{\max}$ values for $0.4 \leq \Upsilon_{\mathrm{gas}} \leq 1$ are found between 1500 and $2000\,\frac{\mathrm{bar}}{\mathrm{s}}$, whereas maximum values for the dust-driven region do not even reach $500\,\frac{\mathrm{bar}}{\mathrm{s}}$. This is particularly remarkable, for mixtures with $\Upsilon_{\mathrm{gas}} = 0.4$. These mixtures are mainly composed of starch from the point of view of their oxygen demand, but they behave as though they where mostly composed of gas.

As a matter of fact, looking back to **Figure 1.16**, one can see that the line for $y_{\mathrm{gas}} = 8.5\%$ passes close to the most severe point for mixtures with $\Upsilon_{\mathrm{gas}} = 0.4$ and this line ($y_{\mathrm{gas}} = 8.5\%$) remains mainly in the same severity contour of $\left(\frac{\mathrm{d}P}{\mathrm{d}t}\right)_{\max}$ =1300-1400 $\frac{\mathrm{bar}}{\mathrm{s}}$ as one moves towards $\Upsilon_{\mathrm{gas}} = 1$. This seems as if methane consumed all the oxygen before starch could react. In fact, what **Figure 1.16** is telling us, is that the MEC line is not separating one regime from another, but that, *in the case of methane/starch mixtures*, a dual-driven regime does not exist, and that there are only three regimes: dust-driven, gas-driven and synergic regime. $y_{\mathrm{gas}} = 8.5\%$ seems rather as a breaking point for methane/starch hybrid mixtures, below this line, starch is not competing with methane for oxygen, so after methane

[5]In opposition to synergic regime

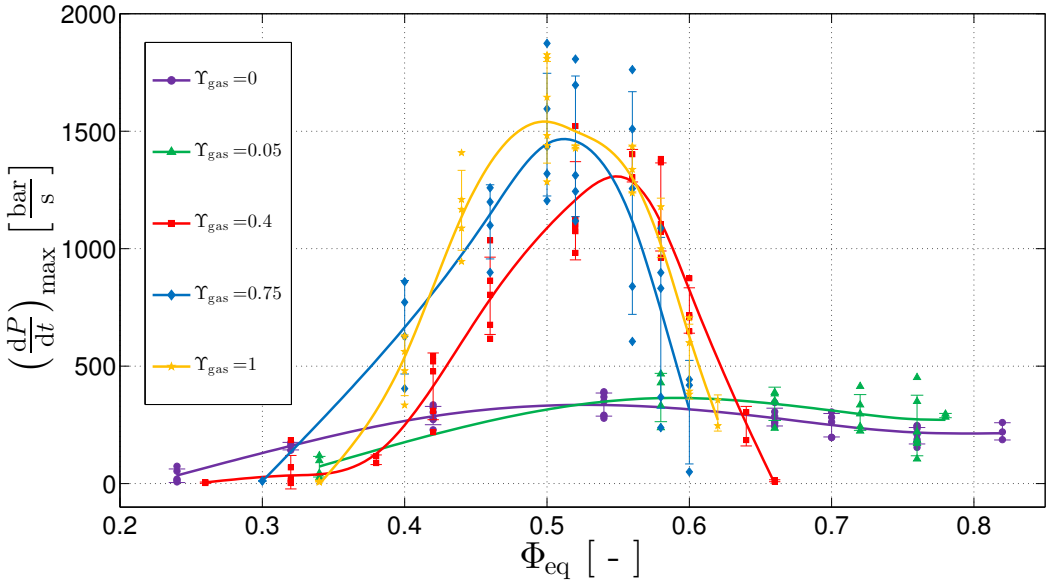

(a) Complete data

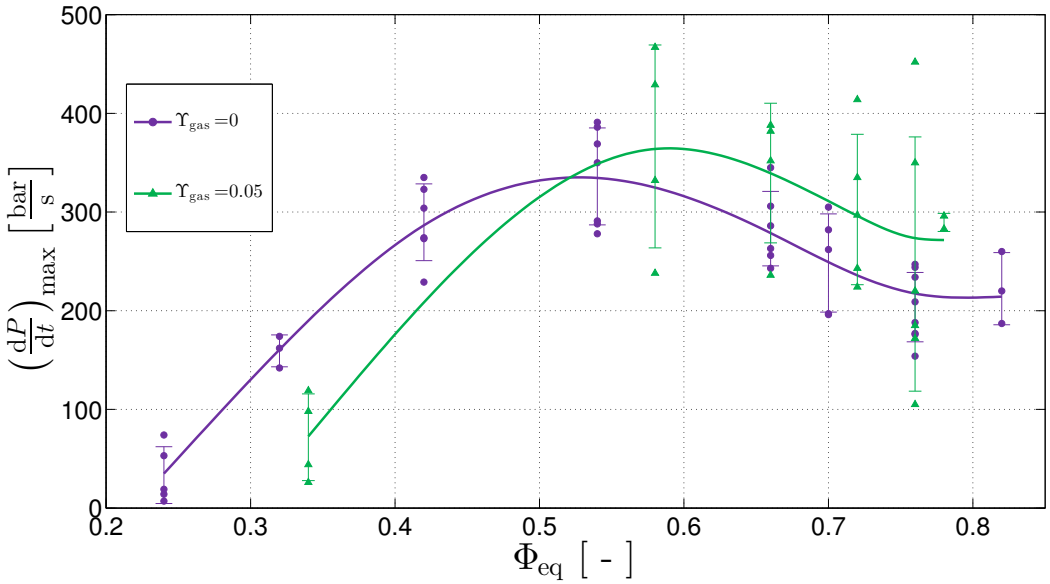

(b) Values in the dust driven domain

Figure 1.17. Experimental results of pressure rise rate, $\left(\frac{dP}{dt}\right)_{max}$ for starch-methane mixtures

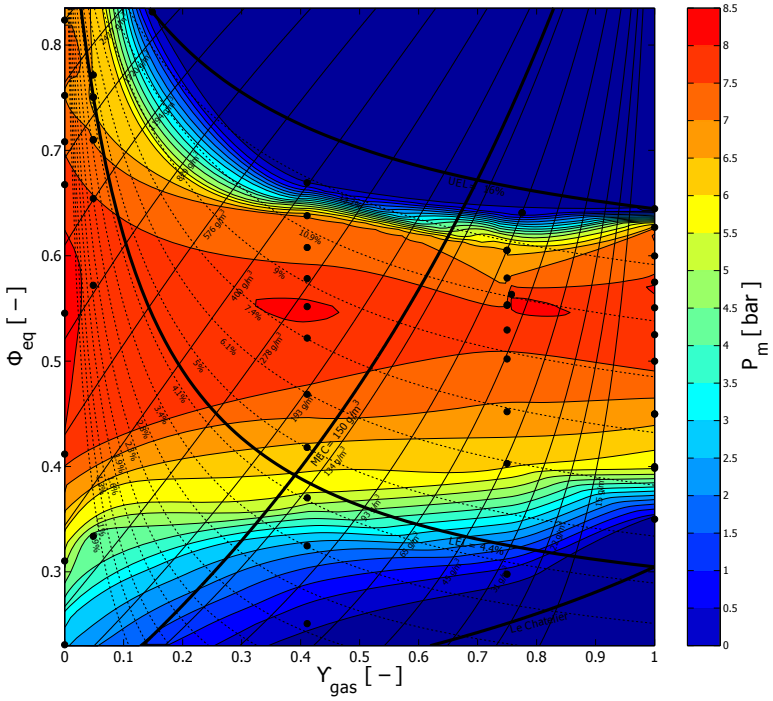

Figure 1.18. Overpressure map for the starch/methane mixtures. Υ_{gas} and Φ_{eq} are defined by **Equations 1.25** and **1.28** respectively. y_{gas} and C_{dust} are represented by the pointed and solid lines respectively

has been consumed starch can still react, which is off course not the case for mixtures $\Phi_{\text{eq}} \geq 0.5$.

Consequently, one would expect that at that, breaking point of 8.5% the consumption of oxygen and the temperature increased, because of the combustion of methane. This situation, should cause the non reacting starch to pyrolyse. This would mean the pyrolysis of starch would cause an increase of the overpressure that the gas would cause by its own, because of the introduction additional molecules into the gas phase. Notice that methane combustion does not generate additional molecules and therefore the overpressure it causes is just related to the temperature increase. This is in fact, what **Figure 1.18** shows, as pure 8.5% pure methane explosion would cause an overpressure of 6.7 bar, while the presence of equivalent 260 $\frac{\text{g}}{\text{m}^3}$ of starch that did not affect the rate of pressure rise, causes an overpressure of 8.1 bar. Of course this does not prove that overpressure is caused by the pyrolysis of starch, but together with the analysis of **Figure 1.16**, it becomes, at the very least, considerably plausible. The definitive proof would be given through the measurement of the concentration of the gases in the sphere after the explosion at these conditions (and maybe others along the 8.5% with higher concentrations of dust). If true, this situation may prove to be an additional risk for the combustion of mixtures similar to this one, as a sudden introduction of oxygen would generate a secondary combustion of the pyrolysis gases.

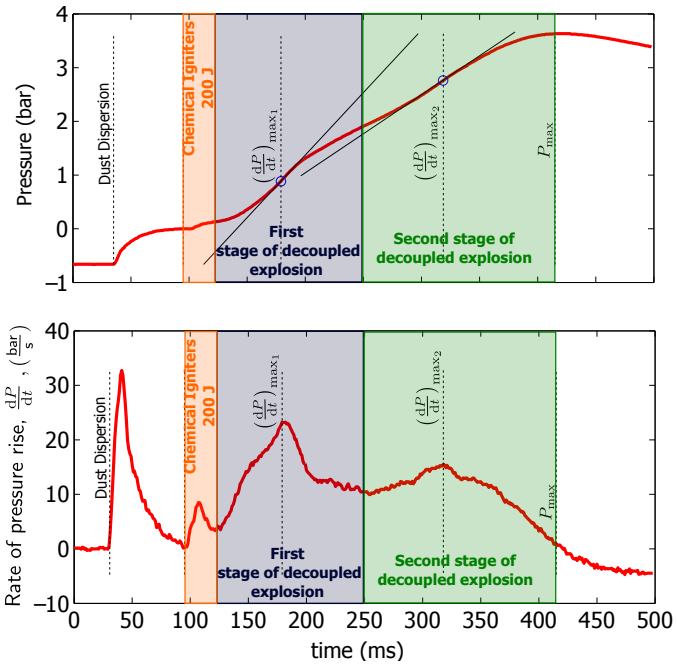

Figure 1.19. Decoupled explosion in sinergic regime. Explosion produced in the 20 L with a hybrid mixture of starch at 106.6 $\frac{g}{m^3}$ and methane at 3.41 %vol , $t_v = 60$ ms and chemical igniters of 200 J.

1.3.4.2. Evidence for Decoupled Explosion of Hybrid Mixture

Although explosions in this regime do not usually reach high pressures or rates of pressure rise, they may exhibit particular behaviours that evidence the synergistic interactions between the components as the ones that were previously described for the methane/starch mixtures. One such example is presented in **Figure 1.19**, that shows the evolution of pressure in the 20 l sphere of an explosion of starch-methane (106.6 $\frac{g}{m^3}$ and 3.41 %vol). The presence of four stages during the explosion can be observed in this figure, characterised by the four peaks in the $\frac{dP}{dt}$ curve. The first two, are usually encountered in this kind of test and are caused by the dispersion of dust and the posterior chemical ignition. On the contrary, after the ignition, only a single stage of explosion is usually observed, instead of the two stages of **decoupled explosion** observed in **Figure 1.19**.

Table 1.4 shows a summary of the 174 tests, used to build **Figures 1.16** to **1.17**. Concentrations of starch and methane as those from **Figure 1.19**, were tested 6 times, 4 of which were ignited with 200 J igniters (500 J for the other 2). And even though a broad range of different concentrations of dust and gas were tested, decoupled behaviour was observed only twice and both times the concentrations and ignition energy were the same (106.6 $\frac{g}{m^3}$, 3.41 %vol ans IE=200 J. The ignition was always triggered at t_v =60 ms with chemical igniters of 200 J, 500 J and 1 kJ.

These results imply that such behaviour is the result of the synergic interactions between dust and gas described for this mixture at $y_{gas} = 8.5\%$. Therefore, it is reasonable to suggest that between 120 and 250 ms, the combustion of methane

Table 1.4. Summary of experimental data of the explosivity values for starch-methane mixtures with t_v =60 ms, from **Table A.1**

Chemical Igniters:		IE=200 J			IE=500 J			IE=1000 J			Total		
C_{dust} $\frac{g}{m^3}$	y_{gas} %v/v	n	P_m bar	$\left(\frac{dP}{dt}\right)_{max}$ $\frac{bar}{s}$	n	P_m bar	$\left(\frac{dP}{dt}\right)_{max}$ $\frac{bar}{s}$	n	P_m bar	$\left(\frac{dP}{dt}\right)_{max}$ $\frac{bar}{s}$	n	P_m bar	$\left(\frac{dP}{dt}\right)_{max}$ $\frac{bar}{s}$
0	5.4	3	0.1 ± 0.0	7 ± 1	2	0.2 ± 0.0	9 ± 1				5	0.1 ± 0.0	8 ± 1
0	6.5	2	5.7 ± 0.1	595 ± 33	2	5.7 ± 0.3	407 ± 73				4	5.7 ± 0.2	501 ± 110
0	7.9	3	6.6 ± 0.0	1221 ± 136	2	6.8 ± 0.1	1077 ± 132				5	6.7 ± 0.1	1163 ± 152
0	9.5	3	7.4 ± 0.0	1516 ± 227	3	7.8 ± 0.1	1645 ± 134				6	7.6 ± 0.2	1580 ± 197
0	10.4	2	7.6 ± 0.1	1432 ± 5							2	7.6 ± 0.1	1432 ± 5
0	11.4	3	7.6 ± 0.0	1337 ± 81							3	7.6 ± 0.0	1337 ± 81
0	12.4				2	7.9 ± 0.0	1089 ± 90				2	7.9 ± 0.0	1089 ± 90
0	13.6	2	6.7 ± 0.1	387 ± 7	2	7.5 ± 0.1	652 ± 53				4	7.1 ± 0.4	519 ± 138
0	15.0				2	7.0 ± 0.1	301 ± 55				2	7.0 ± 0.1	301 ± 55
28	3.9	1	0.1 ± 0.0	12 ± 0				1	0.3 ± 0.0	10 ± 0	2	0.2 ± 0.1	11 ± 1
44	6.1	2	6.2 ± 0.1	816 ± 44				2	6.2 ± 0.1	516 ± 112	4	6.2 ± 0.1	666 ± 172
53	7.3	2	6.8 ± 0.1	1229 ± 30				2	7.0 ± 0.1	999 ± 100	4	6.9 ± 0.1	1114 ± 137
64	8.8	2	7.1 ± 0.2	1377 ± 58				3	7.7 ± 0.2	1558 ± 275	5	7.5 ± 0.4	1485 ± 233
71	9.7	2	6.9 ± 0.2	1181 ± 63				3	7.9 ± 0.1	1605 ± 212	5	7.5 ± 0.5	1435 ± 268
75	2.4	2	0.0 ± 0.0	4 ± 2							2	0.0 ± 0.0	4 ± 2
77	10.6	2	6.7 ± 0.2	722 ± 117				3	7.9 ± 0.0	1509 ± 207	5	7.4 ± 0.6	1194 ± 424
84	11.6	2	6.1 ± 0.1	303 ± 65				3	7.5 ± 0.0	939 ± 108	5	6.9 ± 0.7	684 ± 325
93	12.8							3	6.5 ± 0.7	304 ± 180	3	6.5 ± 0.7	304 ± 180
107	3.4	4	1.0 ± 1.5	10 ± 7	2	4.8 ± 0.4	127 ± 58				6	2.3 ± 2.2	49 ± 65
129	4.1	2	5.3 ± 0.1	102 ± 15							2	5.3 ± 0.1	102 ± 15
157	5.0	3	6.4 ± 0.2	357 ± 136	2	6.5 ± 0.0	499 ± 22				5	6.4 ± 0.2	414 ± 127
190	6.1	3	7.2 ± 0.1	719 ± 105	2	7.7 ± 0.0	920 ± 116				5	7.4 ± 0.2	799 ± 147
229	0.0				2	1.4 ± 1.3	13 ± 6	3	3.3 ± 1.0	47 ± 25	5	2.6 ± 1.5	33 ± 26
232	7.4	3	7.8 ± 0.1	1193 ± 236	2	7.9 ± 0.0	1114 ± 12				5	7.9 ± 0.1	1161 ± 187
259	8.3	2	8.1 ± 0.0	1353 ± 49							2	8.1 ± 0.0	1353 ± 49
286	9.2	3	7.8 ± 0.1	1284 ± 128	2	7.5 ± 0.0	1018 ± 56				5	7.7 ± 0.2	1178 ± 168
319	10.2	2	7.4 ± 0.2	678 ± 30	2	7.2 ± 0.0	796 ± 79				4	7.3 ± 0.2	737 ± 84
324	0.8	2	4.0 ± 0.7	62 ± 36	2	4.5 ± 0.8	82 ± 38				4	4.3 ± 0.7	72 ± 38

(Continues on next page)

Table 1.4 Summary of experimental data of the explosivity values for starch-methane mixtures from **Table A.1**

(continued from previous page)

		IE=200 J			IE=500 J			IE=1000 J			Total		
C_{dust} $\frac{\text{g}}{\text{m}^3}$	y_{gas} %v/v	n	P_{m} bar	$\left(\frac{\text{d}P}{\text{d}t}\right)_{\text{max}}$ $\frac{\text{bar}}{\text{s}}$	n	P_{m} bar	$\left(\frac{\text{d}P}{\text{d}t}\right)_{\text{max}}$ $\frac{\text{bar}}{\text{s}}$	n	P_{m} bar	$\left(\frac{\text{d}P}{\text{d}t}\right)_{\text{max}}$ $\frac{\text{bar}}{\text{s}}$	n	P_{m} bar	$\left(\frac{\text{d}P}{\text{d}t}\right)_{\text{max}}$ $\frac{\text{bar}}{\text{s}}$
344	0.0							3	5.2 ± 0.0	159 ± 13	3	5.2 ± 0.0	159 ± 13
358	11.5	2	6.8 ± 0.3	245 ± 60							2	6.8 ± 0.3	245 ± 60
405	12.9	2	0.0 ± 0.0	12 ± 3							2	0.0 ± 0.0	12 ± 3
534	0.0				3	7.7 ± 0.3	269 ± 31	3	7.7 ± 0.3	310 ± 27	6	7.7 ± 0.3	290 ± 36
854	2.0	2	8.1 ± 0.1	448 ± 19	2	7.5 ± 0.3	285 ± 47				4	7.8 ± 0.4	367 ± 89
916	0.0				4	8.4 ± 0.1	307 ± 36	3	8.5 ± 0.1	376 ± 18	7	8.5 ± 0.1	336 ± 46
1200	2.8	2	7.6 ± 0.2	312 ± 76	2	7.5 ± 0.0	367 ± 15				4	7.6 ± 0.1	340 ± 61
1533	0.0				3	7.7 ± 0.1	254 ± 8	3	7.6 ± 0.0	312 ± 24	6	7.7 ± 0.1	283 ± 34
1540	3.6	2	6.8 ± 0.2	234 ± 10	3	7.2 ± 0.1	349 ± 49				5	7.1 ± 0.3	303 ± 68
1853	0.0				2	7.4 ± 0.2	230 ± 33	3	7.4 ± 0.1	261 ± 47	5	7.4 ± 0.1	248 ± 45
1875	4.4	2	6.0 ± 0.2	145 ± 40	4	6.7 ± 0.3	299 ± 110				6	6.5 ± 0.4	247 ± 118
2095	4.9				2	6.5 ± 0.1	290 ± 7				2	6.5 ± 0.1	290 ± 7
2316	0.0				2	7.1 ± 0.2	216 ± 28	6	7.0 ± 0.3	200 ± 33	8	7.0 ± 0.3	204 ± 33
3567	0.0							3	7.4 ± 0.6	222 ± 30	3	7.4 ± 0.6	222 ± 30
Total		**69**			**58**			**47**			**174**		

takes place with little to no participation of starch. Nevertheless, because of the presence of starch (C_{dust} =106.6 $\frac{\text{g}}{\text{m}^3}$ *vs.* MEC =150 $\frac{\text{g}}{\text{m}^3}$) the initial kernel is able to propagate through the gas phase although methane is below its lower explosive limit ($y_{\text{gas}} = 3.4\%$ *vs.* LEL =4.8 %vol). This first stage increases the temperature enough for the starch to pyrolyse, conducing to a later stage where the combustion of the pyrolysis gases takes place between 250 and 400 ms.

This is representative of the synergic interactions of hybrid mixtures adding up to the set of particular behaviours that were previously described and that become more evident in the synergic regime because of the disadvantageous conditions the mixture faces to achieve combustion there.

1.4. Additional considerations

The approach to the analysis on the severity proposed here in terms of the Φ_{eq} and Υ_{gas}, has been shown to be very helpful in visualising different aspects of the behaviour of varied dust-gas hybrid mixtures. It was also shown to be useful in identifying particular combinations of concentrations that would be important to test in order to properly characterise the mixture and the risks that it may represent. Having a tool like this one implemented in the KSEP software for the 20 l sphere would be an important improvement over the hybrid mixture's module that accompanies the program and only requires the knowledge of the molecular formulae of the compounds.

The calculation of Φ_{eq} requires to estimate ε_{v}, which can be done with the experimental values of the pure components. And although it may seem a bit of a stretch to assert that it can be estimated through **Equation 1.27**, this kind of simplification may prove to be useful for analysing mixtures without performing additional tests or complicated calculations.

In fact, **Figures 1.12** to **1.18** exhibit a tendency to symmetry around $\Phi_{\text{eq}} = 0.5$, so this can be used to formulate empirical models, by reducing the required tests for the characterization to the obtention of the data for the pure compounds and the line for $\Phi_{\text{eq}} = 0.5$. At the very least, over this line is where the maximum severity values of the mixture are more likely to be found.

The pyrolysis of the organic compounds has been shown to be a likely explanation of the particular behaviours of hybrid mixtures, which is more than a good reason to dedicate the next chapter to this analysis.

RÉSUMÉ

Spécificités des mélanges hybrides gaz/solide

Ce chapitre met en évidence les comportements particuliers des mélanges hybrides poussière-gaz. Il est divisé en trois parties : la première présente les particularités de l'allumage de mélanges hybrides et principalement comment l'énergie minimale d'inflammation (EMI) d'une poussière peut-être grandement réduite par la présence de faibles quantités de gaz. Les concentrations minimales explosives (CME) et limites inférieures d'explosivités (LIE) sont également affectées, de manière importante et non proportionnelle aux quantités introduites, par rapport aux limites des composés purs.

En effet, considérer que le domaine d'inflammabilité est simplement encadré par la CME de la poussière et de la LIE du gaz est une erreur. En fait, les mélanges contenant des concentrations de poussières et de gaz respectivement en dessous de la CME et de la LIE sont parfois sensibles à une source externe d'inflammation. En outre, la règle de mélange dite de Le Chatelier est souvent inappropriée pour prédire les concentrations limites d'explosion de mélanges poussière-gaz. A contrario, l'expression quadratique proposée par Bartknecht (1989) semble être plus adéquate pour décrire ces limites, bien qu'elle tende à surestimer les limites d'inflammabilité. Le modèle de Le Chatelier est construit sur la base d'une loi de mélange proportionnelle aux quantités de combustibles, mais ne prend pas en considération la contribution thermodynamique des composants, caractérisé par leur enthalpie de combustion, en lien avec la température de flamme adiabatique. Cet aspect a été pris en compte par Khalili et al. (2012) dans un modèle qui tient compte des limites d'inflammabilité des composants et de leur enthalpie de combustion, en utilisant des bilans énergétiques pour la combustion de la poussière, du gaz et du mélange hybride. Cette amélioration des modèles a été notamment validée pour des mélanges hexane ou méthane/amidon et éthanol/stéarate de magnésium. Néanmoins, le modèle serait insuffisant pour prédire les limites d'inflammabilité proche de la ligne de Le Chatelier comme pour les mélanges tourteaux de tournesol/hexane. En raison des résultats préliminaires. La solution pour un modèle englobant les limites inférieure d'explosivité de mélanges hybrides peut être trouvée dans une description appropriée des températures adiabatiques de mélanges hybrides $T_{\mathrm{ad}_{\mathrm{hyb}}}$. Un tel modèle serait probablement sous la forme :

$$T_{\mathrm{ad}_{\mathrm{hyb}}}\left(y_{\mathrm{gas}}, C_{\mathrm{dust}}\right) = T_0 - \frac{C_{\mathrm{dust}}\Delta_{\mathrm{c}}\hat{H}_{\mathrm{dust}} + y_{\mathrm{gas}}\rho_{\mathrm{gas}}\Delta_{\mathrm{c}}\hat{H}_{\mathrm{gas}}}{\rho_{\mathrm{air}}\tilde{C}_{P\mathrm{air}} + y_{\mathrm{gas}}\rho_{\mathrm{gas}}\tilde{C}_{P\mathrm{gas}} + C_{\mathrm{dust}}\tilde{C}_{P\mathrm{dust}}}$$

La deuxième partie de ce chapitre, montre l'analyse de la sévérité de différents mélanges hybrides, ainsi que les interactions qui les rendent parfois dissemblables de leurs composants purs. Les limites d'inflammabilité du solide et du gaz ont été utilisées par Garcia-Agreda et al. (2011) pour définir les régimes d'explosion pour les mélanges hybrides en fonction de leur composition. Ainsi, en fonction de la concentration du gaz et de la poussière dans le mélange, la cinétique de l'explosion résultante dépend principalement de l'un de ses composants ou des deux dans des proportions équivalentes. L'explosion de mélanges dont les concentrations de gaz et de poussière sont respectivement supérieures à la LIE et à la CME est ainsi gouvernée par un régime dit « à double carburant » (dual fuel), tandis que les régimes dominés par la poussière (dust driven) ou le gaz (gas driven) sont ceux dans lesquels soit le gaz soit la poussière sont respectivement en dessous de la LIE ou de la CME. Enfin, les explosions de mélanges dont les concentrations de gaz et de poussières sont en-dessous de la LIE et de la CME sont dites en régime synergique (synergic regime).

Sanchirico et al. (2011) ont également proposé de tracer les valeurs expérimentales de sévérité du mélange (pression maximale et vitesse maximale d'explosion) en fonction de leurs compositions sur la position correspondante sur les axes. La sévérité serait alors représentée par le diamètre du point sur le graphique. L'auteur propose ici une autre alternative qui vise à utiliser les définitions de la fraction de la demande en oxygène du gaz et de la richesse en combustible normalisée à teneur en masse volatile équivalente. Un exemple de ce type de représentation est la **Figure 1.12** (page 27) pour un mélange niacine/acétone. Cette nouvelle approche peut se révéler très utile pour identifier les particularités des mélanges hybrides, en proposant des modèles prédictifs empiriques et surtout en réduisant la quantité de tests nécessaires pour caractériser ces mélanges.

Chapter 2

Study on the Pyrolysis of Organic Particles During an Explosion

Contents

2.1. Introduction

Consider a spherical particle of organic material, submerged in a burning environment as the one depicted in **Figure 2.1**. If heat transfer is so fast as to overcome the diffusion of oxygen to the surface of the particle, the solid will reach its decomposing temperature and pyrolysis gases will be produced and ejected to the surroundings. These gases will flow outside the particle, leaving behind a porous char shell that will probably fractionate into smaller pieces and/or burn. Consequently, if this phenomenon is occurring for a vast quantity of particles inside a dust cloud, a combustible solid-gas hybrid mixture will be formed. This chapter deals with the flash pyrolysis of biomass particles immersed in a high temperature environment such as the one provided by a flame. For particles having small diameters (generally $<30\,\mu m$), the heating as well as the pyrolysis steps are very fast, and the combustion kinetics can be reduced to the oxidation in homogeneous gas phase. However, this assertion is not always valid and the pyrolysis step should not be systematically neglected. In fact, the devolatilization of the solid particles becomes rate-controlling at high dust loadings and for large particle sizes (Hertzberg et al., 1988).

Although the competition among combustion and volatilization of solid reactions has not been thoroughly quantified here; the purpose is to address each one of these processes separately before addressing the competition between them. However, some of the results shown in **Chapter 1** already present a compelling argument for the ubiquity of the volatilization step among organic compounds. This is shown for example, with the decoupled reaction presented in **Figure 1.19** or the low values of the mass fraction of combustible volatiles (ε_v) of the solids presented in **Table 1.3**. Such values are rather indicative of what fraction of the solid actually undergoes combustion either in a direct or indirect reaction pathway, as it would be understood from **Equation 1.27**. In fact, Di Benedetto and Russo (2007) have defined ε_v as the fraction of the solid that is volatilized into combustible gases. Furthermore, these values imply that, at the end of the explosion, the solid residue will remain immersed inside the hot burnt gases which will unequivocally lead to the pyrolysis of any solid that was not burnt or pyrolyzed.

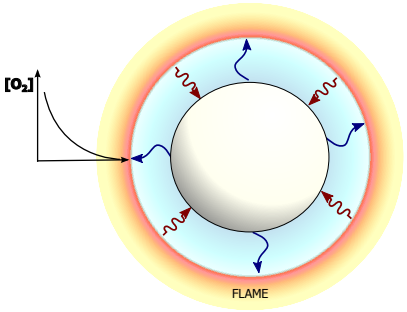

Figure 2.1. Representation of the pyrolysis of an organic particle inside a flame due to lack of oxygen

From the experimental point of view, our team has already published results that highlight the importance of the pyrolysis step on dust explosions (Dufaud et al., 2012a; Dufaud et al., 2012b). The analysis in this chapter continues this perspective, by neglecting the combustion of both the solid and the gas, to focus on the understanding of the conditions that lead to the production of pyrolysis gases. The experimental study was done using a modified Godbert-Greenwald oven to perform the flash pyrolysis of starch and the volatile material was collected for quantifying its composition. Alongside the severity of mixtures of starch and pyrolysis gases was

tested using a synthetic mixture similar to the gases released by pyrolyzed starch. Additionally, a model for the decomposition of one particle was developed, to better understand the conditions that improve the production of gases. The use of this model shows that the time scales involved in the pyrolysis of biomass particles are so short, it is possible to assert that pyrolysis is relevant a process during the combustion of organic dusts.

2.2. Composition of the Gases from the Flash Pyrolysis of Starch

2.2.1. Experimental Set-up

The Godbert-Greenwald furnace, which is conventionally used to determine the minimum ignition temperature of a dust cloud, has been modified in order to analyze the pyrolysis gases. In such oven, the dust is dispersed by an air blast into an open vertical tube, which can be electrically heated in the temperature range of 20-1000 °C (IEC standard 1241-2-1, 1994). In this study, two coaxial Inconel cylinders have been inserted within the oven tube to ensure the airtightness of the chamber (see **Figure 2.2**). The oxygen adsorbed onto the powders has been eliminated by argon flushing.

The pyrolysis gases were sampled in a collapsible Tedlar bag and analyzed thanks to a four-way micro gas chromatography (µGC) (Varian, CP 4900). The µGC process allows to quantify gases from H_2 to C_8 separated by four columns: two molecular sieves, one PoraPlot U, and one CP Wax. Argon was used in the reactor as an inert carrier gas, rather than nitrogen, to improve the peak resolution. The argon pulse allows fast introduction of the particles inside the preheated reactor. The pressure of the argon pulse can be modified to obtain residence times from 20 ms to 50 ms. Although, this method for modifying the residence times has the secondary effect of changing the momentum of the fluid and consequently the turbulence and the heat exchange. This last statement was nonetheless tested with the model

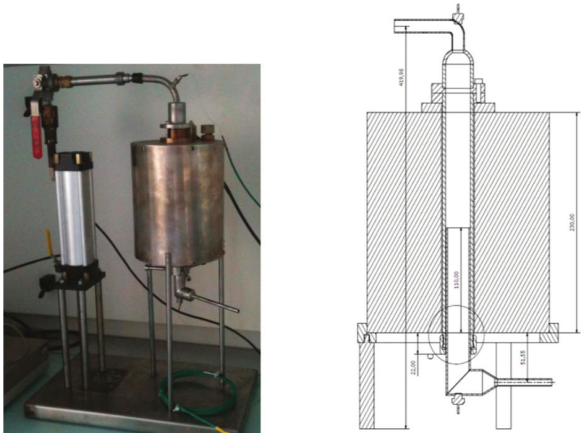

Figure 2.2. Flash pyrolysis reactor. based on the modified Godbert-Greenwald oven.

presented ahead, and it was found that the momentum of the fluid does not really affect the pyrolysis of the dust.

Pyrolysis experiments were performed at various reactor temperatures, but always greater than 823 K, to enhance the external heat transfer from the reactor to the particles. The pyrolysis onset temperature for the particles remains unknown and lower than the reactor temperature. However this temperature is still around of even below of the temperature of the flame that would eventually cause the pyrolysis of the particles. It should be noted that, by considering a one-component mechanism of pyrolysis, the organic compound is classically transformed to char, tar, and gases (Di Blasi, 2008). However, at high temperatures, which is the case during a dust explosion, there is a predominance of devolatilization (versus charring), leading to a significant increase of the gas formation rates. This point was numerically corroborated in this study. It has also been empirically proven that, for low equivalence ratios, the starch particles vanish upstream of the flame, which implies that the devolatilization can be considered to be complete for such compounds (Proust, 2006a). As a consequence, charring was not measured here. Using the modified Godbert-Greenwald reactor allows to sample the pyrolysis gases and provides similar heating rates to those encountered by the particles in the 20-L sphere. Therefore, the heating conditions of particles are rather similar to those obtained during the explosivity measurements in the 20-L sphere (high external heat transfer; see **Section 2.3** in page 48).

2.2.2. Results and Discussion

The set-up previously described was used to pyrolyse 0.2 and 1 g of wheat-starch at temperatures between 830 and 1120 K. The composition of the gaseous effluent was analysed and the results are presented in **Figures 2.3** and **2.4**. The major components found were hydrogen H_2, carbon monoxide (CO), carbon dioxide (CO_2), methane CH_4. Small concentrations of ethylene C_2H_2 and ethane C_2H_6 were also found, as well as negligible concentrations (below 0.4%) of benzene and acetylene. These results, are compared to those of Bozier (2004) (**Table 2.1**). It should be noted that, besides from carbon dioxide, the overall mass fractions are in rather good agreement. The main differences observed can be mainly explained by the facts that the biomasses are not exactly the same and also by the variation of the reactor temperatures between the two tests: 850-1124 K for this study and 1100-1200 K for the work of Bozier. The influences of the residence time (500 ms for Bozier) and the water activity should also be considered (Mazurkiewicz et al., 1993). The results from Bozier (2004) were used to synthesise a mixture of pyrolysis gases to be tested severity-wise in hybrid mixtures with starch.

Table 2.1. Composition of gases produced by thermal decomposition of starch according to Bozier (2004)

Compound	(%v/v)
Hydrogen	22.29%
Methane	8.41%
Carbon monoxide	56.16%
Carbon dioxide	3.57%
Ethylene	7.21%
Ethane	1.49%
Acetylene	0.86%

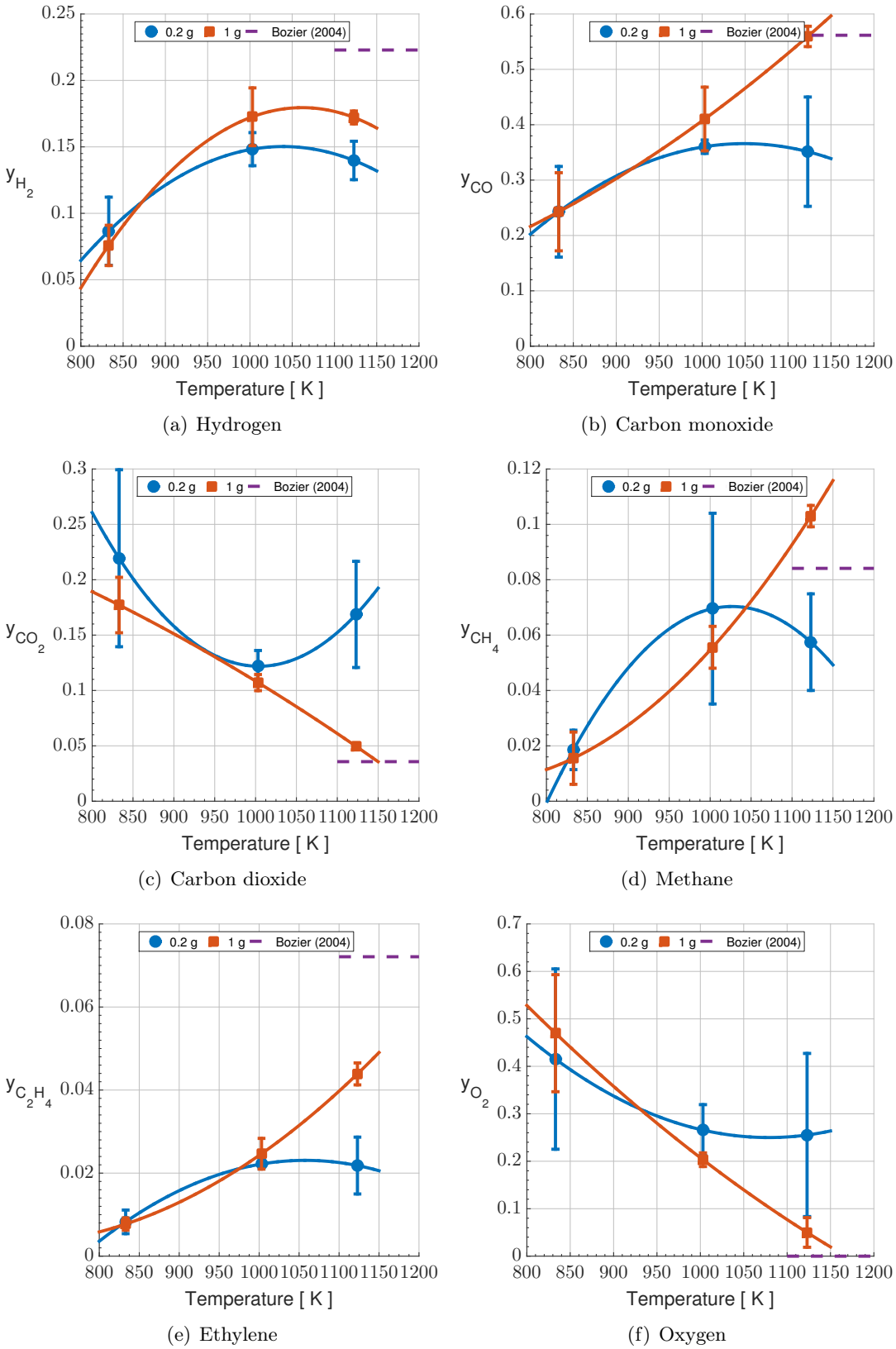

(a) Hydrogen

(b) Carbon monoxide

(c) Carbon dioxide

(d) Methane

(e) Ethylene

(f) Oxygen

Figure 2.3. Molar concentrations of the gas products from the flash pyrolysis of starch. The masses in the legends are those of starch introduced in the chamber prior dispersion. The error bars represent confidence intervals of 95%. Δ P= 0.03 bar.

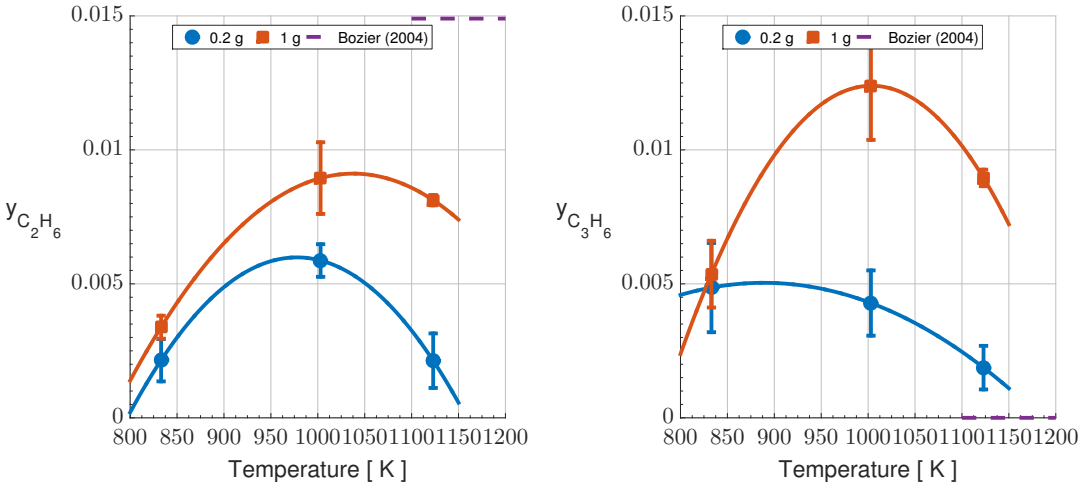

(a) Ethane (b) Propylene

Figure 2.4. Molar concentrations of the gas products from the flash pyrolysis of starch. The masses in the legends are those of starch introduced in the chamber prior dispersion. The error bars represent confidence intervals of 95%. $\Delta P = 0.03$ bar.

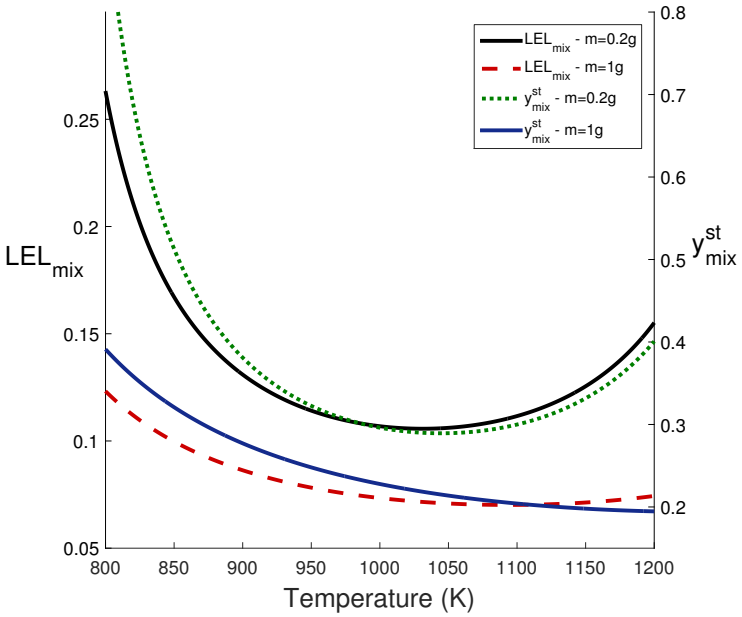

Figure 2.5. Lower explosive limit ($\mathrm{LEL_{mix}}$) and stoichiometric concentration ($y^{\mathrm{st}}_{\mathrm{mix}}$) of pyrolysis gases from flash volatilization of starch in air.

Figure 2.3 shows that, as temperature increases there is a general increment in the production of the main combustible gases, H_2, CO and CH_4, and a general decrease in CO_2 an O_2. Oxygen appears in the mixture, because it makes part of the structure of starch in the first place. The mass on its part does not seem to have an important effect on the results at lower temperature. On the contrary, when temperature and mass increase, there seems to be a lower release of oxygen from the starch which affects the production of CO_2 and so more CO is released.

The experimental values obtained in this work were used to fit first and second order polynomials that are represented by the continuous lines in **Figures 2.3** and **2.4**. These polynomials where used to estimate with Le Chaltelier's rule the LEL of the mixture as a function of the pyrolysis temperature, as well as the stoichiometric concentration in air. **Figure 2.5** shows such behaviour according to the polynomials for 0.2 g. Minimal values of 7% and 20% are respectively obtained for the LEL and the stoichiometric concentration at 1020 K. Such temperatures can be easily attained during the explosion of a starch cloud, which according to these data could rapidly achieve a double a regime of hybrid mixtures explosions. In the context of the present study organic dusts become the promoters of hybrid mixtures even if they start just as dust explosions.

2.3. Severity tests

Hybrid mixtures of starch and pyrolysis gases were tested for their severity parameters, $P_{\max}$ and $\left(\frac{\mathrm{d}P}{\mathrm{d}t}\right)_{\max}$, using a 20-L sphere (Kühner AG), according to the EN 14034-3 standard that is consistent with ISO 6184-1 (1985). The tests performed on starch and/or on pyrolysis gases have been carried out with 100 J chemical igniters, in order to avoid strong overdriving effects (Cashdollar, 2000). The fuel concentration and the ratio of gas:solid have been expressed in terms of the normalized fuel equivalence ratio at equivalent volatile mass content of dust, Φ_{eq} and the fraction of oxygen demand Υ_{gas}, respectively (see pages 25 to 26).

2.3.1. Results

In order to examine the influence of the pyrolysis step during a dust explosion, the explosive behavior of starch, its pyrolysis gases and hybrid mixtures of both has been determined and compared. In **Figure 2.6**, it is clearly visible that the maximum explosion pressures of both substances are not so different: the maximum overpressures vary, respectively, from 7.5 bar to 8.5 bar for the gas and the starch powder, which is consistent from a thermodynamical point of view. In contrast, the maximum rates of pressure rise are totally different. The maximum values of $\left(\frac{\mathrm{d}P}{\mathrm{d}t}\right)_{\max}$ are 2830 $\frac{\mathrm{bar}}{\mathrm{s}}$ for pyrolysis gases and < 400 $\frac{\mathrm{bar}}{\mathrm{s}}$ for starch.

From a kinetic point of view, the impact and the predominance of the pyrolysis step of the dust explosion is then evident (Hertzberg et al., 1988). Other experiments have been done on sieved starch to obtain various samples with different particle sizes distributions, with d_{50} values ranging from 10 µm to 70 µm (Dufaud, 2011). The evolution of the minimum ignition energy (MIE) values of these samples demonstrates that the classical cubic dependence of the MIE (Van der Wel, 1993),

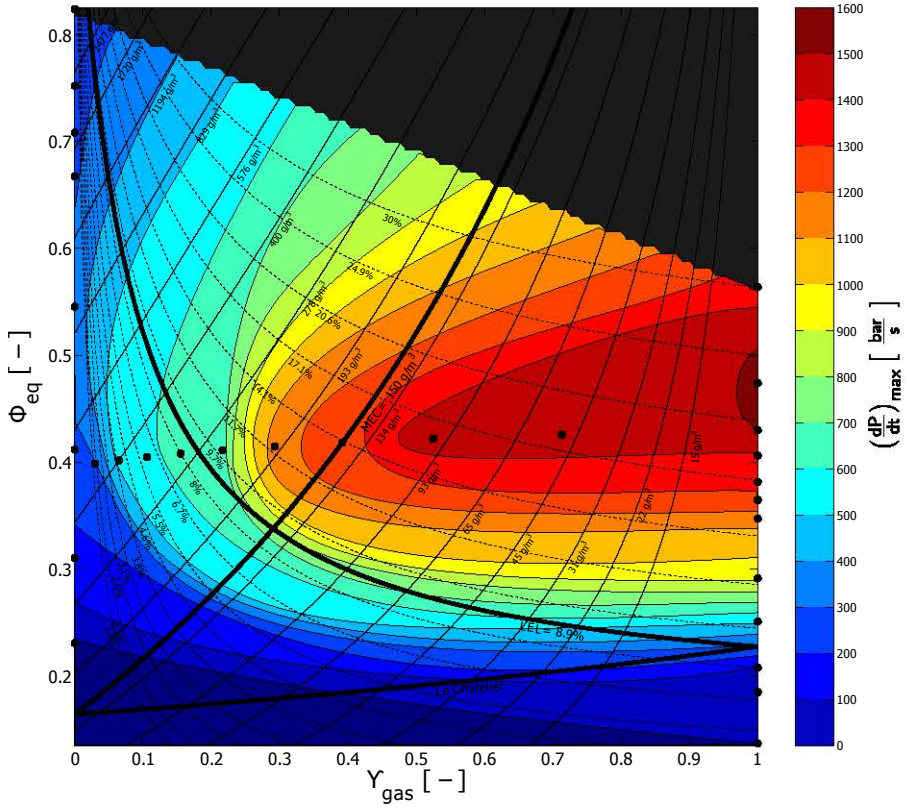

(a) Rate of pressure rise

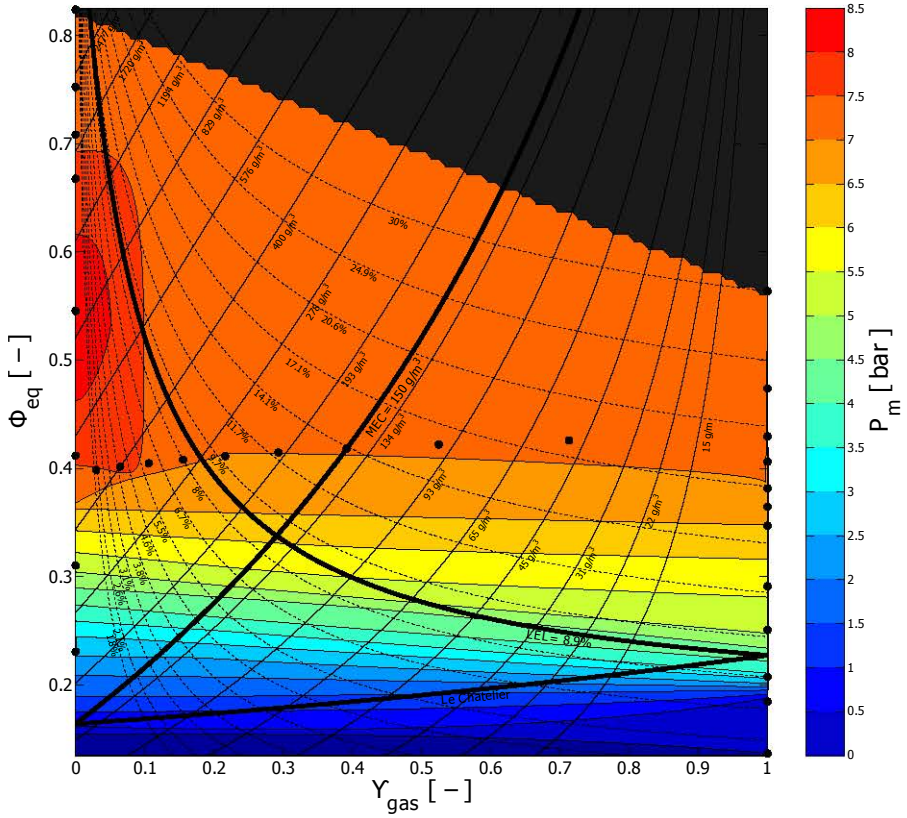

(b) Overpressure

Figure 2.6. Severity for mixtures of starch and pyrolysis gases

as a function of the initial particle diameter found for a boundary diffusion limitation, cannot be applied for starch particles having a mean diameter greater than $\sim 20\,\mu m$. The hypothesis of a boundary diffusion limitation for the starch sample studied here is thereby confirmed.

At this point of the discussion, it should be emphasized that, even if the starch powder and the pyrolysis gases have been tested and compared for the same fuel equivalence ratios, the observed variations are not systematically and totally due to the differences in the pyrolysis and combustion kinetics. In fact, by replacing a combustible solid with its pyrolysis gases, the initial turbulence level generated by the dispersion phase within the 20-L sphere may also be modified, depending on the size of the particles. Moreover, the presence of solid particles upstream of the flame can also interfere with heat transfer by inducing light diffraction and absorption (Proust, 2006a), thus, they could modify the propagation of the flame, with regard to a gas flame.

Concerning the hybrid mixtures of starch and its pyrolysis gases, it should be noted that the maximum rates of pressure rise, $\left(\frac{dP}{dt}\right)_{max}$, of such hybrid mixtures range between the value of the dust and that of the gas in the mixture. Moreover, the dust explosivity is strongly promoted by the addition of combustible gas. However, it should be pointed out that this difference is more significant for values of Φ_{eq} above 0.2. Consequently, it could be assumed that starch still plays a significant role in the combustion kinetics down to this limit; for greater amounts of fuel, the specific behavior of the combustible gases is clearly predominant.

As discussed in the previous chapter, a small quantity of combustible gases plays a significant role on the hybrid mixture ignition phase. Such addition, as low as 1%(v/v), induces changes in the rate-limiting step of the combustion reaction, from boundary diffusion to homogeneous gas phase reaction, and implies a drastic decrease of the MIE. Thus, the introduction of pyrolysis gases to starch particles enhances their ignitability and reduces the impact of the heterogeneous gas/solid reaction on the dust explosion kinetics.

2.4. Model for the Flash Pyrolysis of a Spherical Biomass Particle

Various efforts have previously been done to model the pyrolysis of biomass. Some examples include the models from Authier et al. (2009), Chan et al. (1985), and Haseli et al. (2011), the latter being the one with which the present model shares most commonalities. Additionally, an extensive and detailed description of various pyrolysis models has been compiled by Di Blasi (2008). The context of the formulation of most of such models is predominantly related to the energetic exploitation of the decomposition products of pyrolysis. Consequently, their application deals mainly with the conditions for increasing or reducing the yield of a given product, that are destined to industrial/energetic applications. For this reason, neither of those models consider dimensions of solid as small as the ones involved in dust explosions. If they do, they do it for samples of settled material with masses that amount to milligrams or grams. Furthermore, they use rather long time scales (ranging from various seconds to hours) and low temperatures (not as high as those

of a naked flame). Not only are these conditions incompatible with those necessary for the *flash pyrolysis* that is under consideration here, but the use these models are given to, does not relate to the possibility of the immediate combustion of the gases liberated.

A model for understanding the flash pyrolysis of biomass was developed for the interior of one spherical particle. The model was formulated in spherical coordinates supposing that changes occur exclusively in the radial direction and that the gradients in the angular and azimuthal directions are negligible. The particle was fractionated into smaller volumes (20 to 30 depending on the size of the particle) in a similar manner as it would be done when using the finite volume method. The evolution of the variables between components was not interpolated with fractionated second order polynomials as would usually be done when modelling finite volumes. In this case, a set of third order polynomials was used to interpolate the variables. This polynomials have the characteristic of sharing the same values of the first and second derivatives at the intersections which is called spline interpolation. Consequently the upwind differencing scheme is irrelevant in this case. Furthermore the use of such splines allows to convert the equations of the model into ordinary differential equations that can be easily solved using a Runge-Kutta-like method.

2.4.1. Kinetic Model

Although, the emphasis was put on modelling the pyrolysis of starch, the only study found to quantify this process is the one published by Desai et al. (1972). Nevertheless, their model's validity is limited to maximum 650 K (which is not a flame-high temperature) and there is no decoupling of the carbonization and gasification reactions, making it unsuitable for the purposes of this study. Consequently, the kinetic values used to describe this pyrolysis were approached from those of lignocellulosic materials. The reaction path used for the model is shown in **Figure 2.7** and consists of a simplified mechanism that produces, pyrolysis gases, char and tar. The former one can also follow a secondary reaction that further decomposes it into pyrolysis gases.

Four kinetic models were chosen because they decouple the pyrolysis process into different reactions as in **Figure 2.7**, allowing to quantify the amount of combustible gases produced and because they are suited for high temperatures. The details of these models are presented in **Table 2.2**.

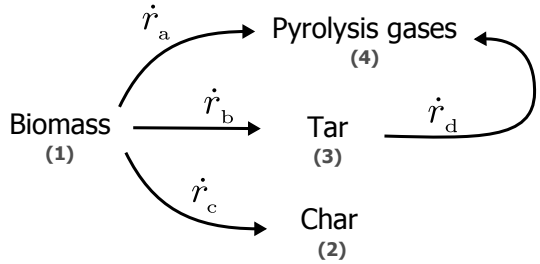

Figure 2.7. General reaction path of flash pyrolysis of Biomass

Reaction rates are modelled as first order reactions with rate constants k_j following

Table 2.2. Kinetic models for pyrolysis of biomass[†]

Reference	**Feedstock (variety, size mass)**	**Experimental system**	**Temperature (K)**	**Reaction**	A_j $(\frac{1}{s})$	E_j $(\frac{kJ}{mol})$
Chan et al. (1985)	Wood	–	–	a	1.30×10^8	140
				b	2.00×10^8	133
				c	1.08×10^7	121
				d [‡]	$0 - 1.48 \times 10^6$	144
Font et al. (1990)	Almond shells	Pyroprobe 100	733-878	a	1.52×10^7	139
	300-500 µm			b	5.85×10^6	119
	2 mg			c	2.98×10^3	73
				d	0	–
Wagenaar et al. (1993)	Pine	Thermogravimetric	553-873	a	1.11×10^{11}	177
	100-125µm	analysis		b	9.28×10^9	149
		Drop tube		c	3.05×10^7	125
				d	0	–
Di Blasi and Branca (2001)	Beech	Tube furnace	573-708	a	4.40×10^9	153
	<80 µm			b	1.10×10^{10}	148
	9 mg			c	3.30×10^6	112
				d	0	0

[†] This table was partially extracted from Di Blasi (2008)

[‡] For Chan et al., this reaction produces gas and secondary tars in a ratio that depends on *adaptable* stoichiometric coefficients. The two extremes were considered in the present work.

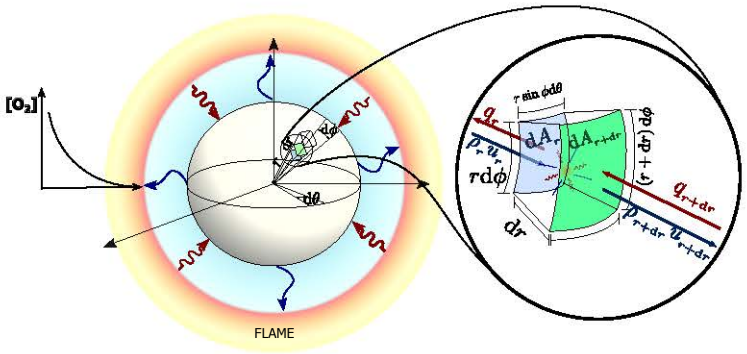

Figure 2.8. Representation of the discrete volume for solution of the pyrolysis of a sphere of biomass

the Arrhenius law:

$$\dot{r}_{\mathrm{a}} = k_{\mathrm{a}}\rho_1 \tag{2.1}$$
$$\dot{r}_{\mathrm{b}} = k_{\mathrm{b}}\rho_1 \tag{2.2}$$
$$\dot{r}_{\mathrm{c}} = k_{\mathrm{c}}\rho_1 \tag{2.3}$$
$$\dot{r}_{\mathrm{d}} = k_{\mathrm{d}}\rho_3 \tag{2.4}$$
$$k_j = A_j \exp\left(-\frac{E_j}{RT}\right) \tag{2.5}$$

where ρ_i are in $\frac{\mathrm{kg}}{\mathrm{m}^3}$.

2.4.2. Mass conservation

Consider the differential volume depicted in **Figure 2.8**. The equations for mass conservation can be stated for solids and gases as follows:

$$\frac{\partial \rho_i}{\partial t} = \begin{cases} \dot{R}_i & , \quad \forall i = \{1;2\} \\ -\nabla \cdot (\rho_i \vec{u}) + \dot{R}_i & , \quad \forall i = \{3;4\} \end{cases} \tag{2.6}$$

with i representing each of the components considered in the model, biomass (1), char (2), tar (3) and gas (4) and $\dot{R}_i$ representing the net generation of component i. Here the diffusion of oxygen is neglected as well ad the corresponding combustion reaction(s). The term on the right of **Equation 2.6** represents accumulation of component i, while the convection term is expressed in spherical coordinates after neglecting the gradients in the polar and azimuthal directions as:

$$\nabla \cdot (\rho_i \vec{u}) = \frac{1}{r^2}\frac{\partial}{\partial r}\left(r^2 \rho_i u_r\right) + \frac{1}{\cancel{\rho_i \sin\phi}}\frac{\partial\left(\cancel{\rho_i u_\theta}\right)}{\partial\theta} + \frac{1}{\cancel{\rho_i \sin\phi}}\frac{\partial}{\partial\phi}\cancel{\left(\sin\phi \rho_i u_\theta\right)} \tag{2.7}$$

This term equals zero for the case of solid components. Consequently, the resulting form of **Equation 2.6** for each of the components of the pyrolysis reaction path from **Figure 2.7**, can be expressed as follows:

$$\frac{\partial \rho_1}{\partial t} = \dot{R}_1 \tag{2.8}$$
$$\frac{\partial \rho_2}{\partial t} = \dot{R}_2 \tag{2.9}$$
$$\frac{\partial \rho_3}{\partial t} = \dot{R}_3 - \frac{1}{r^2}\frac{\partial}{\partial r}\left(r^2 u_r \rho_3\right) \tag{2.10}$$
$$\frac{\partial \rho_4}{\partial t} = \dot{R}_4 - \frac{1}{r^2}\frac{\partial}{\partial r}\left(r^2 u_r \rho_4\right) \tag{2.11}$$

Where $\dot{R}_i$ are defined as in terms of the rates of reactions $\dot{r}_i$:

$$\dot{R}_1 = -\left(\dot{r}_{\mathrm{a}} + \dot{r}_{\mathrm{b}} + \dot{r}_{\mathrm{c}}\right) = -\left(k_{\mathrm{a}} + k_{\mathrm{b}} + k_{\mathrm{c}}\right)\rho_1 \tag{2.12}$$
$$\dot{R}_2 = \dot{r}_{\mathrm{c}} = k_{\mathrm{c}}\rho_1 \tag{2.13}$$
$$\dot{R}_3 = \dot{r}_{\mathrm{b}} - \dot{r}_{\mathrm{d}} = k_{\mathrm{b}}\rho_1 - k_{\mathrm{d}}\rho_3 \tag{2.14}$$
$$\dot{R}_4 = \dot{r}_{\mathrm{a}} + \dot{r}_{\mathrm{d}} = k_{\mathrm{a}}\rho_1 + k_{\mathrm{d}}\rho_3 \tag{2.15}$$

The velocity of the gases ($\vec{u}$) for the convection term is calculated with Darcy's equation:

$$\vec{u} = -\frac{\kappa}{\mu}\nabla P \tag{2.16}$$

where μ and κ are respectively the viscosity of the gaseous phase and the permeability of the solid phase, estimated as a linear relation of the permeability of biomass and char:

$$\kappa = \left(\kappa_1 - \kappa_2\right)\frac{\rho_1}{\rho_{1_0}} + \kappa_2 \tag{2.17}$$

Pressure is calculated in terms of the components in the gas phase, which is considered ideal:

$$P = \sum_{i=3}^{4} \frac{\widehat{\rho}_i}{\tilde{M}_i} RT \tag{2.18}$$

$\tilde{M}_i$ represents the molar mass of the component i and the symbol « $\widehat{\ }$ » over $\widehat{\rho}_i$ indicates that these are the mass concentrations of the gases calculated in void volume basis through the porosity of the solid at each point in the solid (ε): $\rho_i = \varepsilon\widehat{\rho}_i$. With ε defined in terms of densities of the solid components as:

$$\varepsilon = 1 - \frac{(1-\varepsilon_0)}{\rho_{1_0}}\sum_{i=1}^{2}\rho_i \tag{2.19}$$

The time derivative of pressure in a differential volume is then calculated in terms of the time derivatives of the components and temperature as:

$$\frac{\partial P}{\partial t} = \sum_{i=3}^{4} \left[\frac{RT}{\tilde{M}_i} \frac{\partial \widehat{\rho}_i}{\partial t} + \frac{\widehat{\rho}_i}{\tilde{M}_i} R \frac{\partial T}{\partial t} \right] \tag{2.20}$$

$$\frac{\partial P}{\partial t} = \sum_{i=3}^{4} \left[\frac{RT}{\varepsilon \tilde{M}_i} \frac{\partial \rho_i}{\partial t} + \frac{\rho_i R}{\varepsilon \tilde{M}_i} \frac{\partial T}{\partial t} \right] + \sum_{i=3}^{4} \left[\frac{\rho_i RT\left(1-\varepsilon_0\right)}{\rho_{1_0} \tilde{M}_i \varepsilon^2} \right] \sum_{i=1}^{2} \frac{\partial \rho_i}{\partial t} \tag{2.21}$$

$$\frac{\partial P}{\partial t} = \frac{RT}{\varepsilon} \left[\sum_{i=3}^{4} \frac{1}{\tilde{M}_i} \frac{\partial \rho_i}{\partial t} \right] + \frac{R}{\varepsilon} \frac{\partial T}{\partial t} \left[\sum_{i=3}^{4} \frac{\rho_i}{\tilde{M}_i} \right] + \frac{RT\left(1-\varepsilon_0\right)}{\rho_{1_0} \varepsilon^2} \left[\sum_{i=3}^{4} \frac{\rho_i}{\tilde{M}_i} \right] \left[\sum_{i=1}^{2} \frac{\partial \rho_i}{\partial t} \right] \tag{2.22}$$

The last term of **Equation 2.22** accounts for augmentation of the porosity that changes in three orders of magnitude. The time derivatives of the components have already been determined with **Equations 2.8** to **2.11** whereas $\frac{\partial T}{\partial t}$ is obtained from the energy balance and is described by **Equation 2.31**. This equation is helpful because of the important role that pressure plays in the convective transfer of matter and energy. For this reason $\frac{\partial P}{\partial t}$ actually helps to give stability and speed to the numerical integration algorithm. Nevertheless, this means that **Equation 2.22** would be redundant if the mass conservation equations for gases (**Equations 2.10** and **2.11**) were not replaced by **Equations 2.22** and **2.23**

$$\frac{\partial w_4}{\partial t} = \frac{1}{\rho_3 + \rho_4} \frac{\partial \rho_4}{\partial t} - \frac{\rho_4}{\left(\rho_3 + \rho_4\right)^2} \left(\frac{\partial \rho_3}{\partial t} + \frac{\partial \rho_4}{\partial t} \right) \tag{2.23}$$

That is obtained from the differentiation of the mass fraction of the pyrolysis gases in the gas phase:

$$w_4 = \frac{\rho_4}{\rho_3 + \rho_4} \tag{2.24}$$

2.4.3. Conservation of Energy

The general equation for the conservation of energy when viscous dissipation is neglected has the following form:

$$\frac{\partial \left(\rho \hat{U}\right)}{\partial t} + \nabla \cdot \left(\rho \hat{U} \vec{u}\right) = \nabla \cdot (\lambda \nabla T) - P \nabla \cdot (\vec{u}) \tag{2.25}$$

Which can be expressed in words as:

Rate of energy increase in the differential volume	+	Net energy flow leaving the volume	=	Rate energy of increase due to conduction	+	reversible rate of energy increase per unit volume by compression

Considering that there is no convection term for biomass and char, **Equation**

2.25 can be expressed in terms of the individual components as:

$$\frac{\partial}{\partial t}\left(\sum_{i=1}^{4}\rho_i\hat{U}_i\right)+\nabla\cdot\left(\sum_{i=3}^{4}\varepsilon\widehat{\rho}_i\hat{U}_i\vec{u}\right)=\nabla\cdot(\lambda\nabla T)-P\nabla\cdot(\vec{u}) \tag{2.26}$$

$$\sum_{i=1}^{4}\left[\rho_i\frac{\partial\hat{U}_i}{\partial t}+\hat{U}_i\frac{\partial\rho_i}{\partial t}\right]+\sum_{i=3}^{4}\left[\nabla\cdot\left(\varepsilon\rho_i\hat{U}_i\vec{u}\right)\right]=\nabla\cdot(\lambda\nabla T)-P\nabla\cdot(\vec{u}) \tag{2.27}$$

Replacing the equations for mass conservation (**Equation 2.6**):

$$\begin{aligned}\sum_{i=1}^{4}\left[\rho_i\frac{\partial\hat{U}_i}{\partial t}+\dot{R}_i\hat{U}_i\right]+\sum_{i=3}^{4}\left[\nabla\cdot\left(\rho_i\hat{U}_i\vec{u}\right)-\hat{U}_i\nabla\cdot(\rho_i\vec{u})\right]\\=\nabla\cdot(\lambda\nabla T)-P\nabla\cdot(\vec{u})\end{aligned} \tag{2.28}$$

Thought the definition of the gradient of a product, the second term at the left can be simplified:

$$\sum_{i=1}^{4}\left[\rho_i\frac{\partial\hat{U}_i}{\partial t}+\dot{R}_i\hat{U}_i\right]+\sum_{i=3}^{4}\left[\rho_i\vec{u}\cdot\nabla\hat{U}_i\right]=\nabla\cdot(\lambda\nabla T)-P\nabla\cdot(\vec{u}) \tag{2.29}$$

If one considers that the components are either solid or ideal gases whose heat capacity changes are negligible then:

$$\sum_{i=1}^{4}\rho_i\hat{C}_{V_i}\frac{\partial T}{\partial t}=-\sum_{i=3}^{4}\left[\rho_i\vec{u}\hat{C}_{V_i}\cdot\nabla T\right]+\nabla\cdot(\lambda\nabla T)-P\nabla\cdot(\vec{u})-\sum_{i=1}^{4}\dot{R}_i\hat{U}_i \tag{2.30}$$

Replacing Darcy's definition for velocity (**Equation 2.16**):

$$\sum_{i=1}^{4}\rho_i\hat{C}_{V_i}\frac{\partial T}{\partial t}=\sum_{i=3}^{4}\left[\rho_i\hat{C}_{V_i}\right]\frac{\kappa}{\mu}\nabla P\cdot\nabla T+\nabla\cdot(\lambda\nabla T)+P\nabla\cdot\left(\frac{\kappa}{\mu}\nabla P\right)-\sum_{i=1}^{4}\dot{R}_i\hat{U}_i \tag{2.31}$$

Notice that up to this point, all the equations of the model can be applied to any coordinate system with as much dimensions as needed. Fortunately, our case only requires one dimension in spheric coordinates which transforms the energy balance into:

$$\sum_{i=1}^{4} \rho_i \hat{C}_{V_i} \frac{\partial T}{\partial t} = \sum_{i=3}^{4} \left[\rho_i \hat{C}_{V_i}\right] \frac{\kappa}{\mu} \frac{\partial P}{\partial r} \frac{\partial T}{\partial r} + \frac{1}{r^2} \frac{\partial}{\partial r} \left(r^2 \lambda \frac{\partial T}{\partial r}\right) + \frac{P}{r^2} \frac{\partial}{\partial r} \left(r^2 \frac{\kappa}{\mu} \frac{\partial P}{\partial r}\right) - \sum_{i=1}^{4} \dot{R}_i \hat{U}_i \tag{2.32}$$

Finally the last term for energy generation can be expressed in terms of the reaction energies as:

$$\sum_{i=1}^{4} \rho_i \hat{C}_{V_i} \frac{\partial T}{\partial t} = \sum_{i=3}^{4} \left[\rho_i \hat{C}_{V_i}\right] \frac{\kappa}{\mu} \frac{\partial P}{\partial r} \frac{\partial T}{\partial r} + \frac{1}{r^2} \frac{\partial}{\partial r} \left(r^2 \lambda \frac{\partial T}{\partial r}\right) + \frac{P}{r^2} \frac{\partial}{\partial r} \left(r^2 \frac{\kappa}{\mu} \frac{\partial P}{\partial r}\right) - \sum_{j=1}^{4} \dot{r}_j \Delta \hat{U}_{\mathrm{rxn}_j} \tag{2.33}$$

with:

$$\text{bio} \rightarrow \text{gas}: \quad \Delta \hat{U}_{\mathrm{rxn}_a} = \int_{T^\circ}^{T} \left[\hat{C}_{V_4} - \hat{C}_{P_1}\right] \mathrm{d}T + \Delta \hat{H}^\circ_{\mathrm{rxn}_a} \tag{2.34}$$

$$\text{bio} \rightarrow \text{tar}: \quad \Delta \hat{U}_{\mathrm{rxn}_b} = \int_{T^\circ}^{T} \left[\hat{C}_{V_3} - \hat{C}_{P_1}\right] \mathrm{d}T + \Delta \hat{H}^\circ_{\mathrm{rxn}_b} \tag{2.35}$$

$$\text{bio} \rightarrow \text{char}: \quad \Delta \hat{U}_{\mathrm{rxn}_c} = \int_{T^\circ}^{T} \left[\hat{C}_{P_2} - \hat{C}_{P_1}\right] \mathrm{d}T + \Delta \hat{H}^\circ_{\mathrm{rxn}_c} \tag{2.36}$$

$$\text{tar} \rightarrow \text{gas}: \quad \Delta \hat{U}_{\mathrm{rxn}_d} = \int_{T^\circ}^{T} \left[\hat{C}_{V_4} - \hat{C}_{V_3}\right] \mathrm{d}T + \Delta \hat{H}^\circ_{\mathrm{rxn}_d} \tag{2.37}$$

2.4.4. Enthalpy of reaction

Some of the literature on the enthalpy of reaction of pyrolysis, acknowledges a lack of agreement on whether the pyrolysis of biomass is an endothermic or an exothermic process (Milosavljevic et al., 1996; Haseli et al., 2011). The values used in this model are those reported by Milosavljevic et al., who decouple the energies for each reaction(gasification, carbonization and tar formation). According to Milosavljevic et al., while the enthalpy of reaction for the formation of char is exothermic ($-2000\,\frac{\mathrm{kJ}}{\mathrm{kg}}$) at standard temperature, the formation of pyrolysis gases is endothermic ($538\,\frac{\mathrm{kJ}}{\mathrm{kg}}$). So at first glance, this could explain, in part, the lack of agreement on this subject: on the one hand, for all of the kinetic models considered here, the pre-exponential factor of the kinetic constant for the reaction biomass→ char, is lower than the other ones, but the activation energy is also lower. This suggests

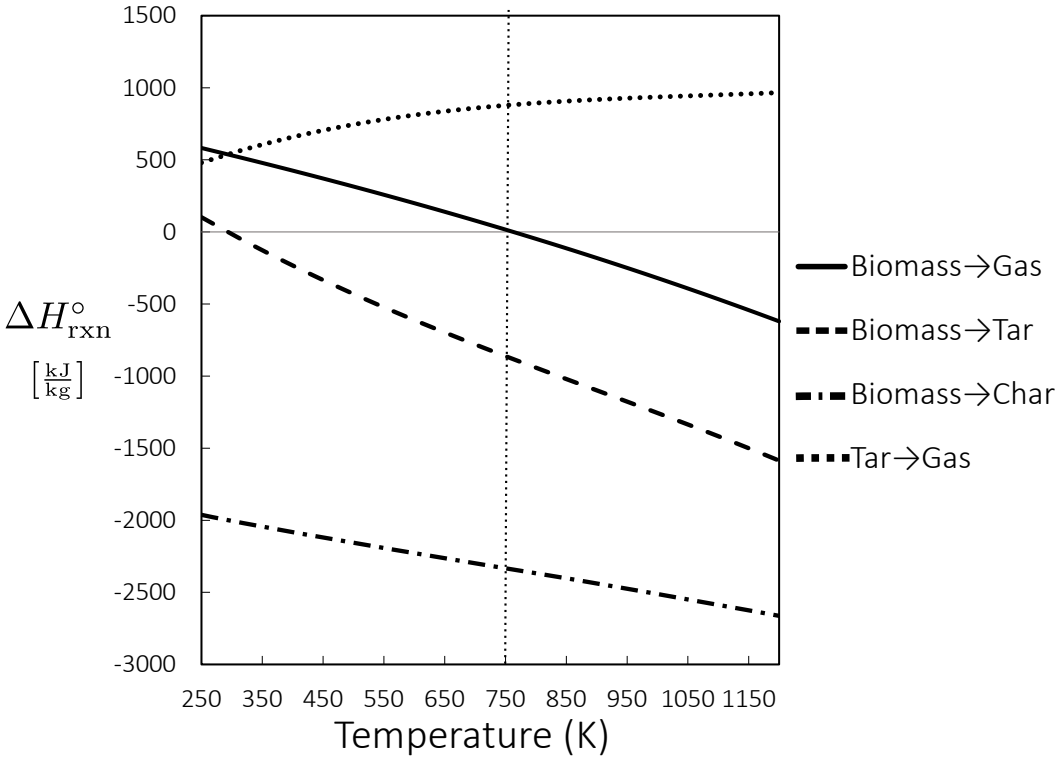

Figure 2.9. Enthalpies of reaction of biomass pyrolysis. Calculated with the values in **Table 2.3**

that at low temperatures, the formation of char may be privileged, thus making the net pyrolysis process exothermic. On the other hand, and more importantly, heat capacity is considerably higher for biomass than for the pyrolysis gases. Consequently, although the production of gas is endothermic at standard temperature, there is a temperature at which, the heat stored in the reacting biomass is higher than both, the standard heat of reaction and the heat necessary to heat up the gas produced. In simpler words, there is a temperature after which the gasification of biomass (biomass → gas) is an exothermic reaction. This temperature, for the present case is 750 K as shown in **Figure 2.9**.

This means that depending on the organic material pyrolyzed, it is conceivable that a combination of kinetic parameters could exist, that makes the process exothermic at low temperatures (higher char production), endothermic if gas production largely overcomes char production, and exothermic again after reaching the temperature that makes the heat capacity of biomass large enough.

This discussion, is presented here because the author finds it speculatively interesting, but, it is not applicable for the practical purposes of this model: an analysis on the behaviour of $\sum_i^4 k_i \Delta H_{\mathrm{rxn}_i}$ shows that the pyrolysis process is exothermic for any temperature above 298.15 K for the four kinetic models presented in **Table 2.2**. Furthermore, as mentioned before, the temperature after which even the gasification reaction is exothermic is 750 K, which is the minimum temperature used in this analysis. Consequently, in this model the pyrolysis process is always exothermic. Moreover, the temperatures produced during an explosion are considerably higher,

so the exothermicity of the pyrolysis reaction will be also increase the exothermicity of the combustion reaction in general.

2.4.5. Boundary conditions

If $y(r)$ represents either T, P or ρ_i, then at the centre of the particle ($r = 0$), the gradient of any of these variables equals zero:

$$\frac{\partial y}{\partial r}(r = 0) = 0 \tag{2.38}$$

For the external surface of the particle ($r = \frac{d_\mathrm{p}}{2}$) **Equations 2.8** to **2.11** for mass conservation and **Equation 2.33** for energy conservation remain the same. Whereas pressure is kept constant at atmospheric conditions, $P\left(r = \frac{d_\mathrm{p}}{2}\right) = P_\mathrm{atm}$.

On the other hand, heat flow from the exterior of the particle is transferred through radiation and convection to the surface and through conduction thereafter:

$$\lambda \frac{\partial T}{\partial t}\left(r = \tfrac{d_\mathrm{p}}{2}\right) = h_\mathrm{conv}\left(T_\infty - T\right) + \sigma e\left(T_\infty^4 - T^4\right) \tag{2.39}$$

The convection coefficient (h_conv) is estimated from the Nusselt number, whose value is obtained from the following relation (Padet, 2015) for $\mathrm{Re} > 0$:

$$\mathrm{Nu} = 2 + 0.03\mathrm{Pr}^{0.33}\mathrm{Re}^{0.54} + 0.35\mathrm{Pr}^{0.36}\mathrm{Re}^{0.58} \tag{2.40}$$

The properties of the external fluid involved in this calculation (viscosity, conductivity and heat capacity) were equated to those of air. Concerning the estimation of the Reynolds number, the velocity of the particle was taken to be a factor between 0.01 to 10 of the terminal velocity (σ_p) of the free falling particle, defined by **Equation 2.41**, as explained in **Chapter 3** (page 98):

$$\sigma_\mathrm{p} = \sqrt{\frac{g{d_\mathrm{p}}^2\left(\rho_\mathrm{p} - \rho_\mathrm{air}\right)}{18\mu_\mathrm{air}}} \tag{2.41}$$

Indeed σ_p is the most sensible value for estimating Re if the observer is the particle immersed in a moving fluid. In that case, the velocity of the external fluid would either be:

- rapidly descending towards σ_p, if the particle was previously subjected to a force that shot it at a faster velocity than that of the surrounding fluid.
- stagnant, if the particle is moving at the same speed of the fluid.
- or slowly ascending towards σ_p, after the particle achieved the velocity of the fluid.

All these variations are certainly found during the dispersion of a dust and when given enough time they will converge towards σ_p.

2.4.6. Summary of the model for the pyrolysis of one biomass

To summarize, the set of ordinary differential equations that must be solved, is composed of the time derivatives of the densities of biomass (ρ_1), and char (ρ_2); the change in the mass fraction of the pyrolysis gases in the gas phase (w_4); the pressure (P), and the temperature (T):

$$\frac{\partial \rho_1}{\partial t} = \dot{R}_1 \tag{2.42}$$

$$\frac{\partial \rho_2}{\partial t} = \dot{R}_2 \tag{2.43}$$

$$\begin{aligned}\sum_{i=1}^{4} \rho_i \hat{C}_{V_i} \frac{\partial T}{\partial t} = &\sum_{i=3}^{4} \left[\rho_i \hat{C}_{V_i}\right] \frac{\kappa}{\mu} \frac{\partial P}{\partial r} \frac{\partial T}{\partial r} + \frac{1}{r^2} \frac{\partial}{\partial r}\left(r^2 \lambda \frac{\partial T}{\partial r}\right) \\ &+ \frac{P}{r^2} \frac{\partial}{\partial r}\left(r^2 \frac{\kappa}{\mu} \frac{\partial P}{\partial r}\right) - \sum_{j=1}^{4} \dot{r}_j \Delta \hat{U}_{\mathrm{rxn}_j}\end{aligned} \tag{2.44}$$

$$\frac{\partial w_4}{\partial t} = \frac{1}{\rho_3 + \rho_4} \frac{\partial \rho_4}{\partial t} - \frac{\rho_4}{(\rho_3 + \rho_4)^2}\left(\frac{\partial \rho_3}{\partial t} + \frac{\partial \rho_4}{\partial t}\right) \tag{2.45}$$

$$\begin{aligned}\frac{\partial P}{\partial t} = &\frac{RT}{\varepsilon}\left[\sum_{i=3}^{4} \frac{1}{\tilde{M}_i} \frac{\partial \rho_i}{\partial t}\right] + \frac{R}{\varepsilon} \frac{\partial T}{\partial t}\left[\sum_{i=3}^{4} \frac{\rho_i}{\tilde{M}_i}\right] \\ &+ \frac{RT\left(1 - \varepsilon_0\right)}{\rho_{1_0} \varepsilon^2}\left[\sum_{i=3}^{4} \frac{\rho_i}{\tilde{M}_i}\right]\left[\sum_{i=1}^{2} \frac{\partial \rho_i}{\partial t}\right]\end{aligned} \tag{2.46}$$

for which the mass balances of tar (ρ_3) and pyrolysis gases (ρ_4) are auxiliary equations:

$$\frac{\partial \rho_3}{\partial t} = \dot{R}_3 - \frac{1}{r^2} \frac{\partial}{\partial r}\left(r^2 u_r \rho_3\right) = \dot{R}_3 + \frac{1}{r^2} \frac{\partial}{\partial r}\left(r^2 \tfrac{\kappa}{\mu} \tfrac{\partial P}{\partial r} \rho_3\right) \tag{2.47}$$

$$\frac{\partial \rho_4}{\partial t} = \dot{R}_2 - \frac{1}{r^2} \frac{\partial}{\partial r}\left(r^2 u_r \rho_4\right) = \dot{R}_4 + \frac{1}{r^2} \frac{\partial}{\partial r}\left(r^2 \tfrac{\kappa}{\mu} \tfrac{\partial P}{\partial r} \rho_4\right) \tag{2.48}$$

The boundary conditions at $r = \frac{d_\mathrm{p}}{2}$ involve, constant pressure and the energy balance:

$$\lambda \frac{\partial T}{\partial r}\left(r = \tfrac{d_\mathrm{p}}{2}\right) = h_{\mathrm{conv}}\left(T_\infty - T\right) + \sigma e\left(T_\infty^4 - T^4\right) \tag{2.49}$$

at $r = 0$ the radial derivatives of every variable are equal to zero.

The values related to the estimation of the rates of reaction $\dot{r}_j$ are presented in **Table 2.2** (page 53). As for the remaining parameters and properties used in this model they are all compiled **Table 2.3** (page 62). Finally, the detail of the algorithm implemented for solving this set of equations can be found in **Appendix B**.

Table 2.3. Parameters of particle pyrolysis model

Molar masses
$\tilde{M}_3 = 128 \cdot 10^{-3} \frac{\text{kg}}{\text{mol}}$
$\tilde{M}_4 = 44 \cdot 10^{-3} \frac{\text{kg}}{\text{mol}}$

Heat Capacities(*)
$\hat{C}_{P_i}\left(\frac{\text{kJ}}{\text{kg K}}\right) = \sum_{j=0}^{2} a_{ij} T^j$
$\hat{C}_{V_i} = \hat{C}_{P_i} - \frac{R}{\tilde{M}_i} \qquad \forall i = \{3;4\}$

i	a_{i0}	$a_{i1} \cdot 10^3$	$a_{i2} \cdot 10^7$
Bio (1)	1.5	1	0
Char (2)	0.44	2	-6.7
Tar (3)	-0.162	4.6	-20
Gas (4)	0.761	0.7	-2

Thermal conductivity
$\lambda = (1-\varepsilon)\frac{\rho_1\lambda_1+\rho_2\lambda_2}{\rho_1+\rho_2} + \varepsilon\lambda_{\text{gases}}$
$\lambda_1 = 0.35 \frac{\text{W}}{\text{m K}}$ (‡)
$\lambda_2 = 0.1 \frac{\text{W}}{\text{m K}}$ (*)
$\lambda_{\text{gases}} = 0.026 \frac{\text{W}}{\text{m K}}$ (*)

Enthalpies of reaction‡‡
$\Delta\hat{H}^\circ_{\text{rxn}_a} = 538 \frac{\text{kJ}}{\text{kg}}$
$\Delta\hat{H}^\circ_{\text{rxn}_b} = 0 \frac{\text{kJ}}{\text{kg}}$
$\Delta\hat{H}^\circ_{\text{rxn}_c} = -2000 \frac{\text{kJ}}{\text{kg}}$
$\Delta\hat{H}^\circ_{\text{rxn}_d} = 538 \frac{\text{kJ}}{\text{kg}}$

Viscosity of gas phase(*)
$\mu = 3 \cdot 10^{-5} \frac{\text{kg}}{\text{m s}}$

Permeability(*)
$\kappa = (\kappa_1 - \kappa_2)\frac{\rho_1}{\rho_{1_0}} + \kappa_2$
$\kappa_1 = 5 \cdot 10^{-8}\,\text{m}^2$
$\kappa_2 = 1 \cdot 10^{-5}\,\text{m}^2$

Initial Conditions
$P_0 = 1\,\text{bar}$
$\rho_{1_0} = 1440 \frac{\text{kg}}{\text{m}^3}$ (‡)
$\varepsilon_0 = V_\text{p}\rho_{1_0}$
$V_\text{p} = 1.1 \cdot 10^{-6} \frac{\text{m}^3}{\text{kg}}$ (††)
$T_0 = 293.15\,\text{K}$

Reference temperature
$T^\circ = 293.15\,\text{K}$

Boundary Conditions
$P_\infty = 1\,\text{bar}$
$h_\text{conv} = \frac{\text{Nu}\lambda_\text{air}}{d_\text{p}}$
$\text{Nu} = 2 + 0.03\text{Pr}^{0.33}\text{Re}^{0.54}$
$+0.35\text{Pr}^{0.36}\text{Re}^{0.58}$ (§)

Emisivity of particle
$e = 0.95$ §§

External air properties
$\hat{C}_{P_\text{air}}\left(\frac{\text{J}}{\text{kg K}}\right) = \sum_{i=0}^{3} b_i T^i$
$b_0 = 991.75$
$b_1 = -4.7034 \cdot 10^{-2}$
$b_2 = 3.2310 \cdot 10^{-4}$
$b_3 = -1.2914 \cdot 10^{-7}$

$\mu_\text{air}\,(\text{Pa s}) = 8.4419 \cdot 10^{-25}\sqrt{\frac{\tilde{M}T}{\sigma^2\Omega}}$ (‖)
$\Omega = A\,(T^*)^{-B} + \sum_{i=1}^{2} C_i \exp\left(-D_i T^*\right)$
$A = 1.16145$
$B = 0.14874$
$C_1 = 0.52487$
$D_1 = 0.77320$
$C_2 = 2.16178$
$D_2 = 2.43787$
$T^* = \frac{k}{\epsilon}T$
$\sigma_\text{air} = 3.617 \cdot 10^{-10}\,\text{m}$
$\left(\frac{\epsilon}{k}\right)_\text{air} = 97\,\text{K}$
$\tilde{M}_\text{air} = 28.97 \cdot 10^{-3} \frac{\text{kg}}{\text{mol}}$

$\lambda_\text{air}\left(\frac{\text{W}}{\text{m K}}\right) = \sum_{i=0}^{7} c_i T^i$ (**)
$c_0 = -9.474 \cdot 10^{-4}$
$c_1 = 1.1961 \cdot 10^{-4}$
$c_2 = -2.3632 \cdot 10^{-7}$
$c_3 = 8.406 \cdot 10^{-10}$
$c_4 = -1.747 \cdot 10^{-12}$
$c_5 = 1.904 \cdot 10^{-15}$
$c_6 = -1.035 \cdot 10^{-18}$
$c_7 = 2.228 \cdot 10^{-22}$

(*) Haseli et al., 2011
(†) Authier et al., 2009
(§) Padet, 2015
(‡) Karathanos and Saravacos, 1993
(‖) Welty, 2008
(**) Vargaftik, 1993
(††) Juszczak et al., 2002
§§ Buitrago Acevedo, 2014
‡‡ Milosavljevic et al., 1996

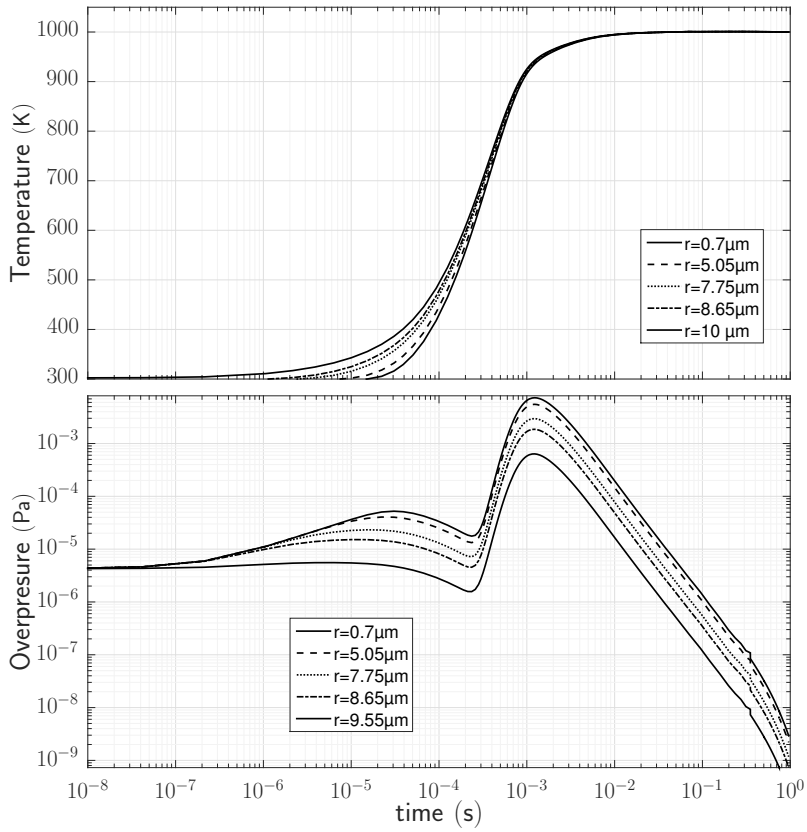

(a) Pressure and Temperature

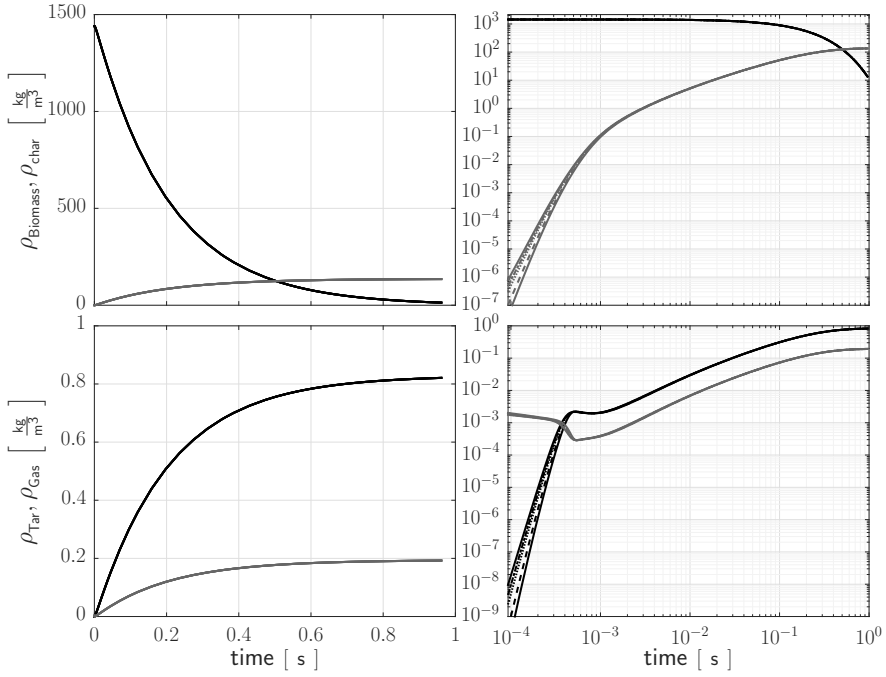

(b) Densities

Figure 2.10. Pressure, temperature and densities profiles for a particle with $r = 10\,\mu m$ using Font kinetics and 1000 K, external fluid velocity equal to $1\sigma_p$. Black lines represent biomass and tar densities whereas gray lines stand for char and gas

2.5. Results of the Pyrolysis Model

Multiple simulations of this model were performed using the technique described in **Appendix B**. Besides the four sets of kinetic constants presented in **Table 2.2**, three more parameters were adjusted: the particle diameter (d_p) was varied between 5 and 100 µm ; the thermal effects of the surrounding environment were changed through the external temperature of T_∞ (750-1200 K) and the speed of the gas moving around the particle, thus affecting the coefficient for heat transfer through convection h_{conv} as explained in page 60.

Figures 2.10 and **2.11** show the behaviour of temperature, pressure and densities for particles with 20 µm and 100 µm in diameter pyrolyzed at 1000 K[1]. Results for a large particle were chosen to be shown here because size increases temperature and pressure gradients and enhances some behaviours that are common to other sizes but cannot be seen as clearly. An interesting feature that is put forward in **Figure 2.11** is the effect of the exothermicity of the reaction. Indeed, although the external temperature is 1000 K, the internal temperature reaches a maximum of 1021 K because of the limitations of the particle to evacuate the heat released either by convection or conduction. It is true that the kinetic constants used in this system should be limited to temperatures a couple hundred degrees below 1000 K and that this extrapolation may have an impact that could explain to some degree that behaviour. Nevertheless, because the reaction is always exothermic (as explained in page 59) the same effect is still present in a lesser degree for temperatures in the range of validity.

In fact **Figure 2.12** shows how the exothermicity of the reaction affects the structure of the solid phase when the temperature inside the particle rises above the external temperature. Although for all practical purposes, the temperature inside the particle is homogeneous, as the reaction progresses, the porosity towards the centre is higher than it is on its surface. Consequently when pyrolysis is happening in complete absence of combustion, the particle will have a stronger structural integrity on the outside and the process will not behave as a reducing core. In fact, once the outer shell gets weak enough for it to be torn out by external forces, the same forces will also disintegrate the weaker rest of the particle. In contrast, the opposite behaviour may probably result if combustion was accounted, because then combustion would happen mainly on the outer shells and the structure would be debilitated from the outside towards the inside.

It should be noted that most of the interesting behaviours that both, temperature and overpressure exhibit, happen during a heating stage, before the reaction actually begins. **Figures 2.10** and **2.11** show that as temperature increases, its gradient also does. A point is reached at which the temperature difference between the surface and the centre can be as high as 20 K for 5 µm-particles and 100 K for 100 µm-particles. Later as temperature raises towards its maximum, its gradient becomes minimum, before establishing around the external temperature. This temperature increase causes a gas expansion that drives an augmentation of the internal pressure.

In the meantime, pyrolysis is happening at a very slow rate but the minuscule

[1]Because of space limitations similar figures for different temperatures and particle sizes are presented in **Appendix C**

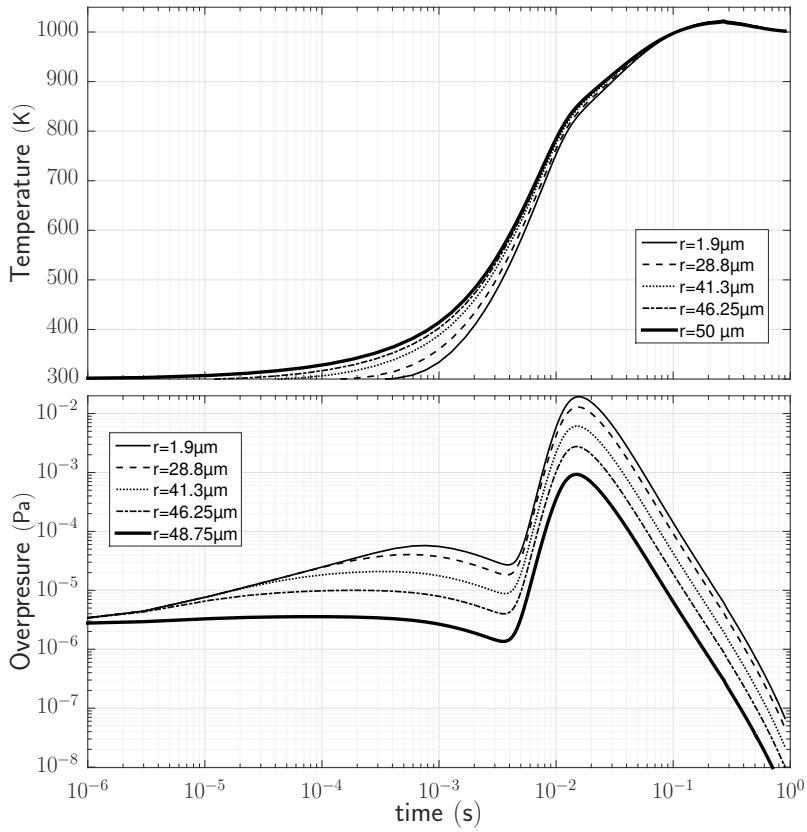

(a) Pressure and Temperature

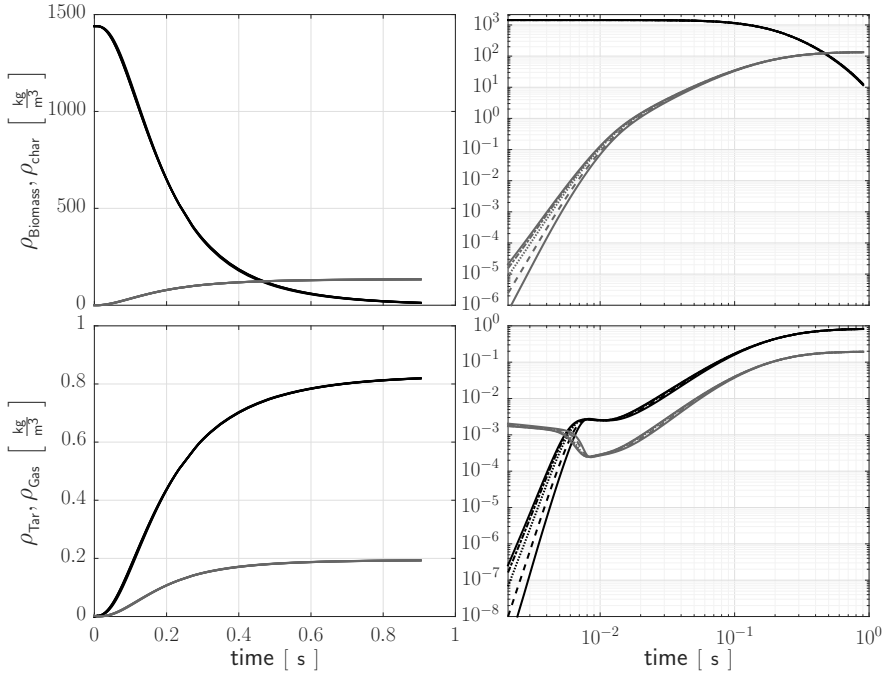

(b) Densities

Figure 2.11. Pressure, temperature and densities profiles for a particle with $r = 50\,\mu\text{m}$ using Font kinetics and 1000 K, external fluid velocity equal to $1\sigma_p$. Black lines represent biomass and tar densities whereas gray lines stand for char and gas

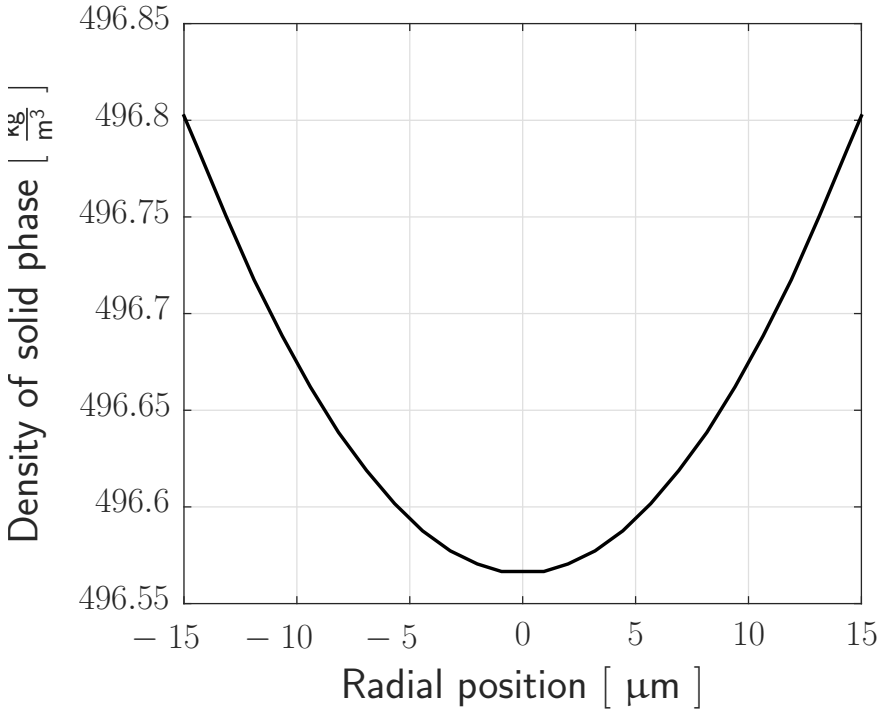

Figure 2.12. Density of solid phase of a 30 µm particle after 150 ms. Pyrolysis at 850 K using Wagenaar et al., 1993 constants and external velocity equal to σ_{p}.

initial porosity (0.0016) allows for a rapid change of the composition ratio of the gas phase, and tar suddenly becomes a major component of that phase. Because tar has a larger molar weight, a molecular expansion causes a second pressure increase that reaches a peak and then descends monotonically towards zero. At that point temperature reaches its maximum value and only then biomass seems to react at an a appreciable rate. This behaviour is coherent with the analysis on the thermal regimes described by Di Blasi (1999) and Di Benedetto et al. (2010) that is presented next.

2.5.1. Thermal Regimes for the Pyrolysis Reaction

Di Blasi (1999) and Di Benedetto et al. (2010) have described the regimes that dominate the thermal decomposition of organic dusts according to the characteristic times of the phenomena that limit the process. These regimes can be described according to three sequential processes that are involved in pyrolysis: external heat transfer, internal heat transfer and the pyrolysis reaction; the slowest one among these three will consequently limit the whole process. The order of magnitude of the times involved in each of theses processes can be estimated through their characteristic times: τ_{ext}, τ_{int} and τ_{pyro} defined by **Equations 2.50** to **2.52**.

$$\tau_{\text{ext}} = \frac{\rho_{1_0} \hat{C}_{P_1} \Delta T d_{\text{p}}}{6\left[h_{\text{conv}} \Delta T + \sigma e \left(T_\infty^4 - T_0^4\right)\right]} \tag{2.50}$$

$$\tau_{\text{int}} = \frac{\rho_{1_0} {d_{\text{p}}}^2 \hat{C}_{P_1}}{12\lambda_1} \tag{2.51}$$

$$\tau_{\text{pyro}} = \frac{1}{\sum_{j=1}^{3} A_j \exp\left(-\frac{E_j}{RT_\infty}\right)} \tag{2.52}$$

From this perspective, the slowest process can be predicted by comparing three adimensional numbers that compare the times between each stage. The Biot number (Bi) relates the characteristic times of external heat transfer (τ_{ext}) and internal heat transfer (τ_{int}) driven by the temperature difference between the particle and the environment, $\Delta T = T_\infty - T_0$:

$$\text{Bi} = \frac{\tau_{\text{int}}}{\tau_{\text{ext}}} = \frac{d_{\text{p}}\left[h_{\text{conv}} \Delta T + \sigma e \left(T_\infty^4 - T_0^4\right)\right]}{2\lambda_1 \Delta T} \tag{2.53}$$

Thus, if the Biot number is much higher than 1, then the limiting thermal process is heat transfer inside the particle. In which case the Thiele number (Th):

$$\text{Th} = \frac{\tau_{\text{int}}}{\tau_{\text{pyro}}} = \frac{{d_{\text{p}}}^2 \hat{C}_{P_1} \sum_{i=1}^{3} \dot{r}_j}{12\lambda_1} \tag{2.54}$$

indicates whether the overall process is indeed limited by internal heat transfer or if the characteristic time of the pyrolysis reaction τ_{pyro}, has a greater influence. Therefore, when $\text{Bi} \gg 1$ and $\text{Th} \gg 1$, then $\tau_{\text{ext}} \ll \tau_{\text{int}} \gg \tau_{\text{pyro}}$ and so, the whole process is limited by the heat transfer inside the particle. Contrarily, when $\text{Bi} \gg 1$ and $\text{Th} \ll 1$, the process is limited by the speed of the pyrolysis reaction because $\tau_{\text{pyro}} \gg \tau_{\text{int}} \gg \tau_{\text{ext}}$.

The last one can also be the case even if $\text{Bi} \ll 1$, as long as the characteristic time of pyrolysis reaction τ_{pyro} is greater than the characteristic time of external heat transfer τ_{ext}. These two characteristic times are compared by the Damköhler number Da:

$$\text{Da} = \frac{\tau_{\text{ext}}}{\tau_{\text{pyro}}} = \frac{d_{\text{p}} \hat{C}_{P_1} \Delta T \sum_{j=1}^{3} \dot{r}_j}{6\left[h_{\text{conv}} \Delta T + \sigma e \left(T_\infty^4 - T_0^4\right)\right]} \tag{2.55}$$

Consequently if $\text{Bi} \ll 1$ and $\text{Da} \ll 1$ then $\tau_{\text{pyro}} \gg \tau_{\text{ext}} \gg \tau_{\text{int}}$, and the limiting phenomenon will still be the pyrolysis reaction. Whereas, if $\text{Bi} \ll 1$ and $\text{Da} \gg 1$, then $\tau_{\text{int}} \ll \tau_{\text{ext}} \gg \tau_{\text{pyro}}$, making the external heat transfer the limiting phenomenon.

In this analysis the only extrinsic variables are the particle diameter and the external and initial internal temperatures, d_{p}, T_0 and T_∞ respectively (h_{conv} being a function of intrinsic variables and the mentioned extrinsic variables). Concurrently, the analysis performed in this chapter has also been focused on the effect of the diameter, the external temperature and the pyrolysis constants. Hence, the regimes described in terms of the Biot, Damköhler and Thiele numbers are mapped in **Figure 2.13**, for biomass particles with the properties presented in **Table 2.3**.

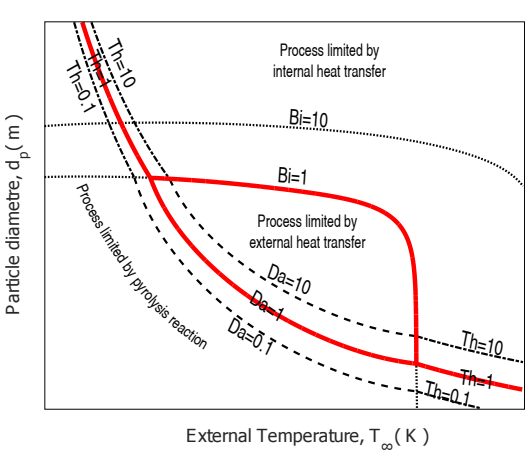

(a) Description of the construction of the limits for each regime

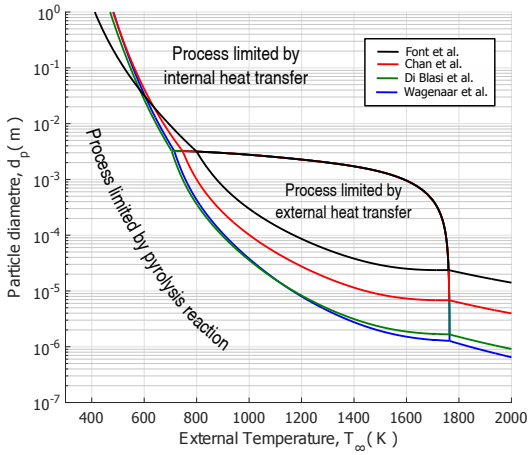

(b) Consolidated regime limits for each kinetic model

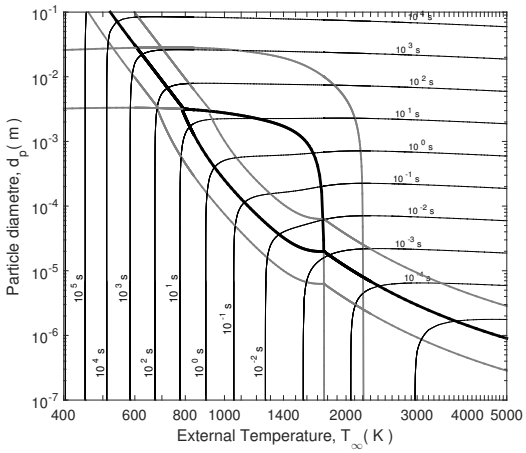

(c) Process times with Font et al. (1990) kinetics

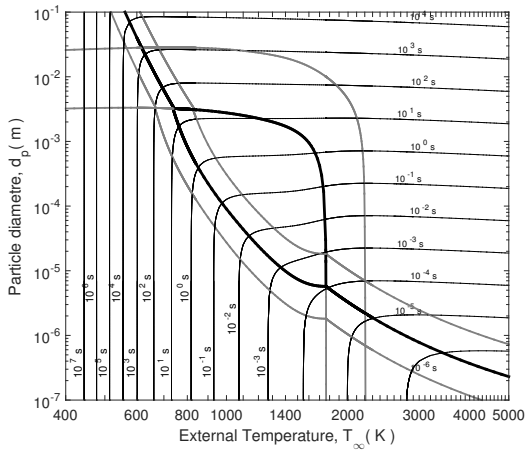

(d) Process times with Chan et al. (1985) kinetics

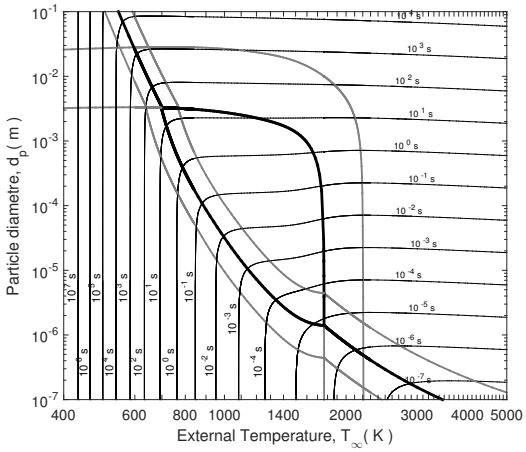

(e) Process times with Di Blasi and Branca (2001) kinetics

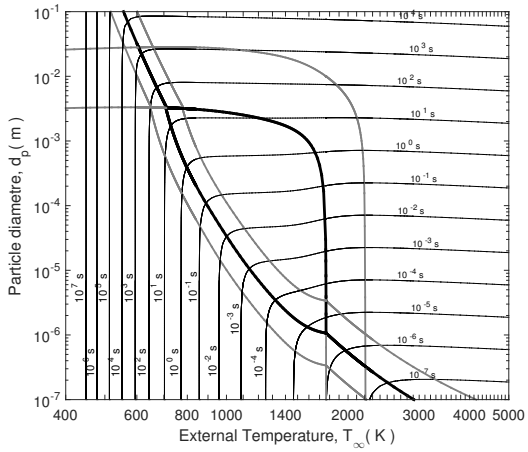

(f) Process times with Wagenaar et al. (1993) kinetics

Figure 2.13. Pyrolysis limiting regimes according to the particle size, the external temperature and the kinetic model. Time contours in subfigures (c) to (f) represent the addition of the characteristic times; τ_{ext}, τ_{int} and τ_{pyro}

This figure shows how the regimes can be determined by the particle diameter and the external temperature. While the pyrolysis constants influence both the Thiele and Damköhler number, the Biot number is obviously independent on the pyrolysis model. Consequently, the frontier between internal and external heat transfer regimes is the same regardless of the kinetic model, while the lines defined by the Damköhler and Thiele numbers are variable.

This approach helps to explain the behaviours demonstrated by the variables portrayed in **Figures 2.10** and **2.11**, that indicate that the reaction has barely started when the internal temperature has already attained the external temperature. Indeed, the temperatures and particle diameters considered (5-100 µm and 750-1200 K) can be mostly found on the region where the pyrolysis reaction is the limiting phenomenon. Nevertheless, the maximum diameters and temperatures are close to, or even after, the limit where the external heat transfer starts to dominate the advancement of the process (Da<1 and Bi<1). Furthermore, since this approach could not account for the reduction of ΔT, that decreases towards zero as the process advances, it is to expect that a limited external heat transfer would play a more important role than predicted.

Counter-intuitively, the role that a limited external heat exchange plays, is not to slow down the process, on the contrary it stimulates it. This is because the reaction is exothermic; thus, as the reaction releases heat it is not able to evacuate it to its environment. Indeed, even if the exothermicity of the reaction is also unaccounted in this adimensional analysis, it is easy to infer the behaviour exhibited by a self-heating system that fails to efficiently exchange energy with its environment. Naturally, the simulations of the model show, that as diameter and external temperature increase, the incapacity to release heat causes a thermal runaway and the simulation is interrupted when temperature diverges towards infinity.

This kind of behaviour is rare for Font et al. kinetic model while in simulations using Chan et al., Wagenaar et al. and Di Blasi and Branca kinetic models exhibit it in a greater degree. This is in accordance with the predictions drawn from **Figure 2.13**. This figure also shows that all characteristic times for the process are almost the same in Wagenaar et al. and Di Blasi and Branca kinetics. Although, this analysis fails to discriminate the ratios in the yields of each product. Doing so requires a deeper look into the differences between the kinetic constants of each reaction.

2.5.2. The effect of kinetic constants on biomass conversion

The raw data of ρ_i, P and T produced by the numerical integration of the model was exploited to have further insights into the phenomenon of flash pyrolysis. For instance, the mass $m_i(t)$ of any of the components, biomass (1), char (2), tar (3) or gas (3) at a given time t, estimated by:

$$m_i(t) = 4\pi \int_0^{\frac{d_p}{2}} \rho_{1_{t,r}} r^2 \mathrm{d}r \qquad \forall i = 1, 2, 3, 4 \tag{2.56}$$

and the initial mass m_0:

$$m_0 = \frac{\pi \rho_{1_0} (d_\mathrm{p})^3}{6} \tag{2.57}$$

are used to calculate the comsumption of biomass (X_1) and the char yield (x_2):

$$X_1(t) = 1 - \frac{24}{\rho_{1_0} {d_\mathrm{p}}^3} \int_0^{\frac{d_\mathrm{p}}{2}} \rho_{1_{t,r}} r^2 \mathrm{d}r \tag{2.58}$$

$$x_2(t) = \frac{24}{\rho_{1_0} {d_\mathrm{p}}^3} \int_0^{\frac{d_\mathrm{p}}{2}} \rho_{2_{t,r}} r^2 \mathrm{d}r \tag{2.59}$$

Additionally, the mass flow leaving the particle at any time $\dot{m}_{i_\mathrm{out}}(t)$ for tar ($i = 3$) or gas ($i = 4$) is estimated as the product between the mass flux of the component i at the external boundary $(\rho_i u_r)_{t,\frac{d_\mathrm{p}}{2}}$, and the surface of the sphere, $\pi {d_\mathrm{p}}^2$:

$$\dot{m}_{i_\mathrm{out}}(t) = \pi {d_\mathrm{p}}^2 (\rho_i u_r)_{t\frac{d_\mathrm{p}}{2}} \qquad \forall i = 3, 4 \tag{2.60}$$

Therefore, the yields for tar and pyrolysis gases (x_3 and x_4 respectively) are calculated as the ratios between the time integral of $\dot{m}_{i_\mathrm{out}}(t)$ and the initial mass m_0:

$$x_i(t) = \frac{6}{\rho_{1_0} d_\mathrm{p}} \int_0^t (\rho_i u_r)_{t,\frac{d_\mathrm{p}}{2}} \, \mathrm{d}t \qquad \forall i = 3, 4 \tag{2.61}$$

The evolution of biomass consumption (X_1) and the yields of each product (x_2, x_3 and x_4) can be visualized for each of the kinetic models in **Figures 2.14** to **2.17**. These figures represent the evolution of a particle with a 20 µm diameter, other diameters are not presented because the effect of the diameter on the final yield is negligible. Indeed, the change in diameter only influences the time required for the particle to volatilize, but it does not really have an impact on the final yields; whose values are depend more on temperature than on any other parameter.

According to **Figures 2.14** to **2.17**, tar is consistently the major product of biomass pyrolysis with a minimum of 50% at 750 K with Font's kinetic model, and a maximum of 80% at almost any temperature through Di Blasi's kinetics. In fact it would seem as if temperature affected mostly char and gas yields with little to no impact on tar. This is specially true when using Di Blasi and Branca and Chan et al. kinetic constants, whose values in the frequency factor A_j for tar are the the largest ones. Furthermore, independently from the kinetic model tested, as temperature increases, yields for char are reduced with an increase on the production of pyrolysis gases, which is to be expected because of the relation between the activation energies of each reaction.

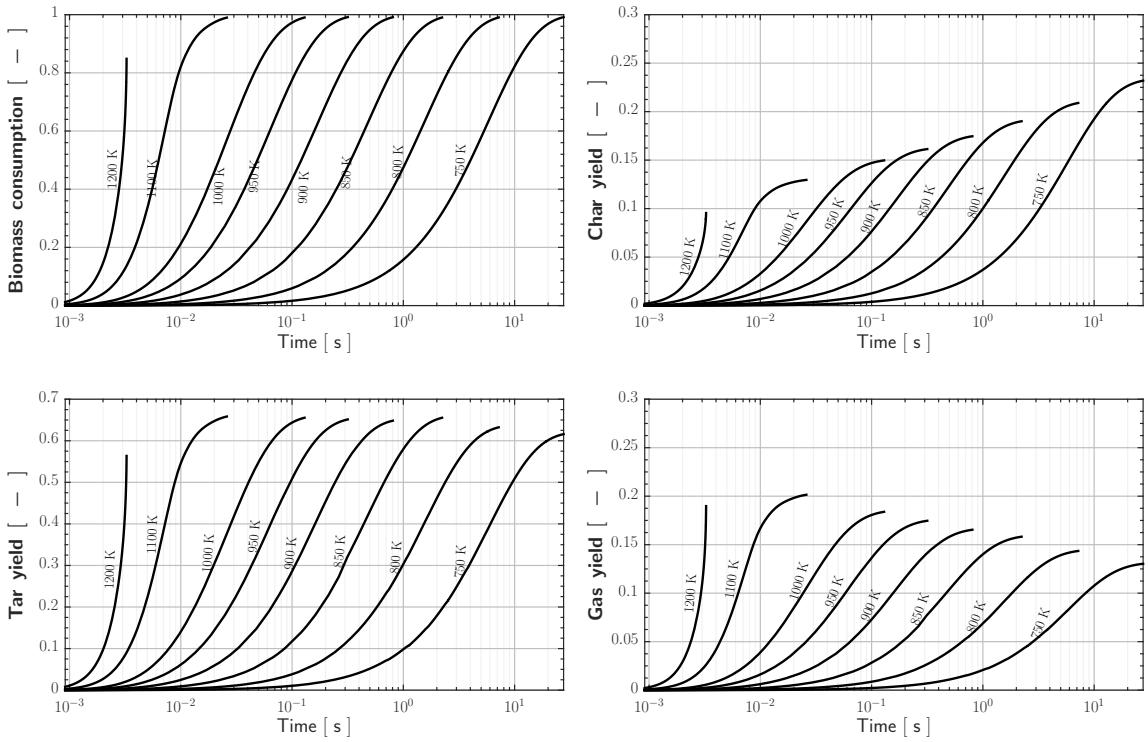

Figure 2.14. Component yields using Chan et al. kinetics. $d_\mathrm{p} = 20\,\mu\mathrm{m}$

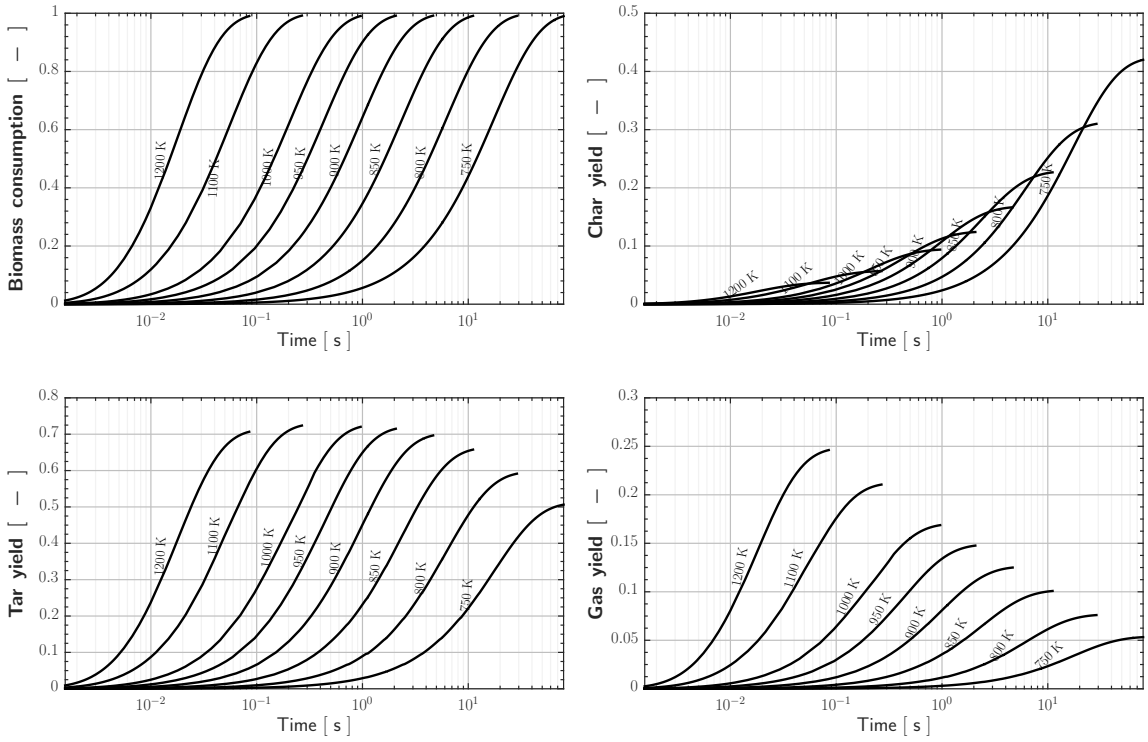

Figure 2.15. Component yields using Font et al. kinetics. $d_\mathrm{p} = 20\,\mu\mathrm{m}$

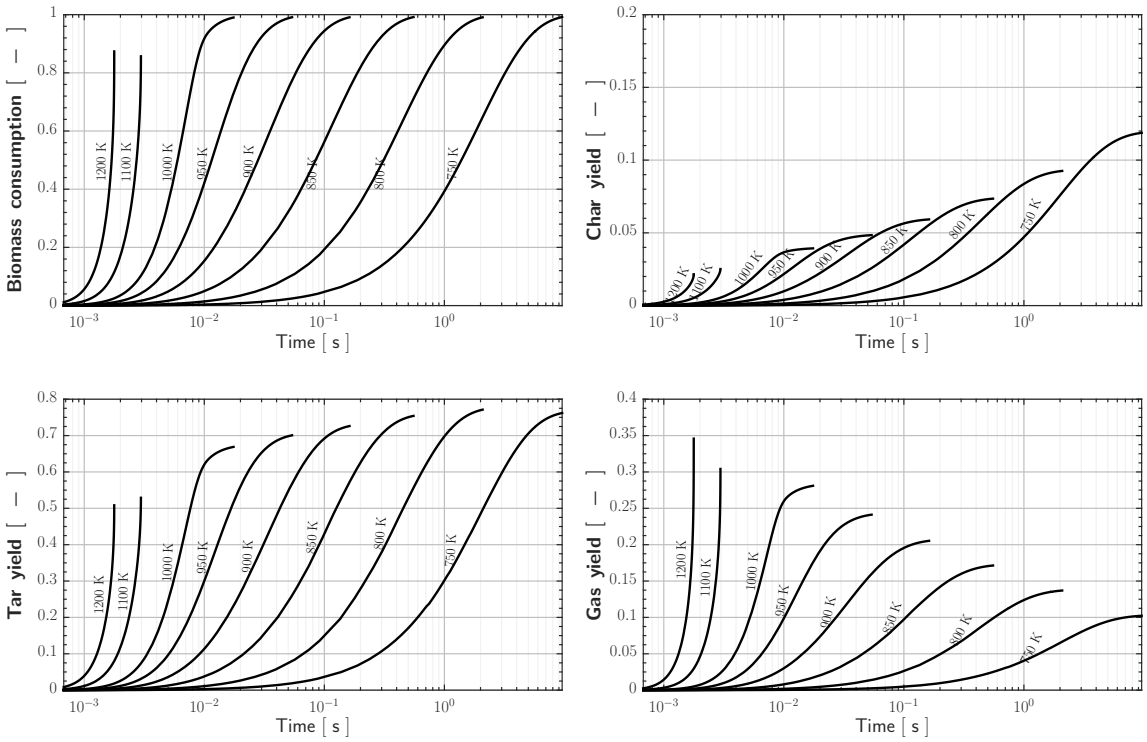

Figure 2.16. Component yields using Wagenaar et al. kinetics. $d_\mathrm{p} = 20\,\mu\mathrm{m}$

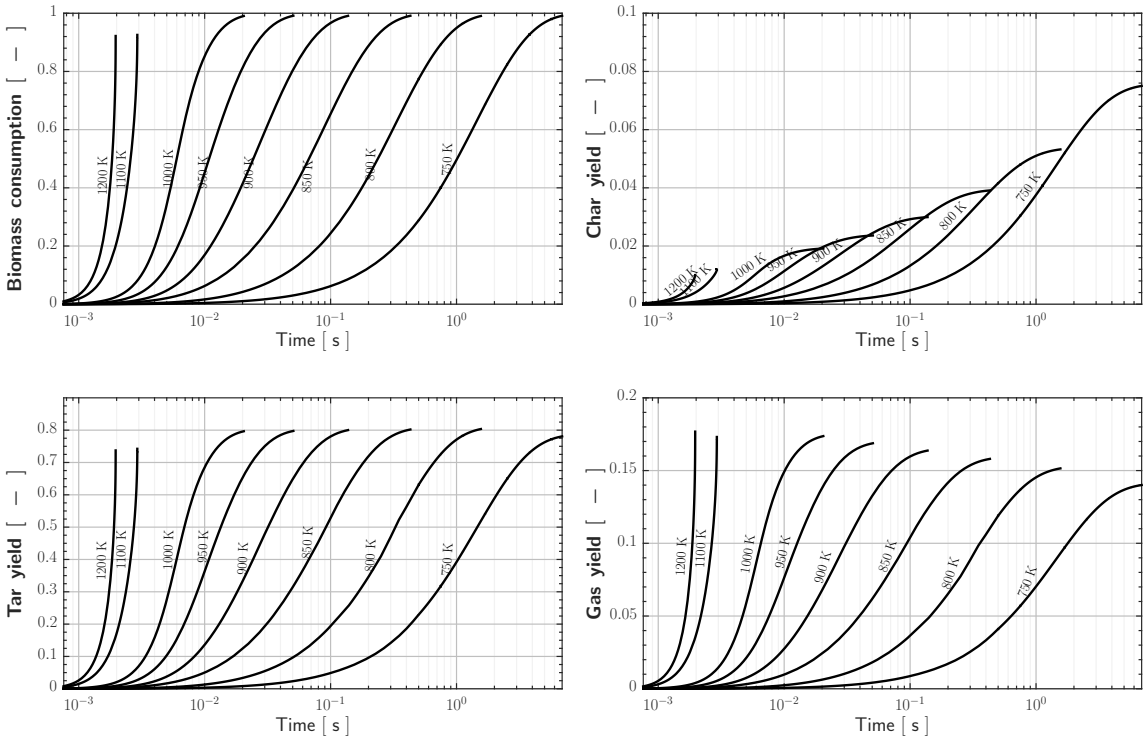

Figure 2.17. Component yields using Di Blasi and Branca kinetics. $d_\mathrm{p} = 20\,\mu\mathrm{m}$

2.5.3. Reaching the LEL of pyrolysis gases

Consider that a volume V contains a concentration C_{dust} of biomass particles with size d_{p}, then the number of particles N_{p}, inside V can be estimated as:

$$N_{\text{p}} = \frac{6C_{\text{dust}}V}{\pi {d_{\text{p}}}^3 \rho_{1_0}} \tag{2.62}$$

If these particles are pyrolysed at a temperature T_∞, and pressure P_∞, the number of moles of pyrolysis gas n_4 liberated by a particle , at a given time t, depends on the yield of gas $x_4(t)$ and is calculated as:

$$n_4(t) = \frac{\pi {d_{\text{p}}}^3 \rho_{1_0}}{6\tilde{M}_4} x_4(t) \tag{2.63}$$

consequently the concentration of the pyrolysis gases liberated in molar basis y_4, assuming that there is no water vapour that may eventually react, is:

$$y_4 = N_{\text{p}} \frac{n_4 R T_\infty}{P_\infty V} = \frac{R T_\infty C_{\text{dust}}}{\tilde{M}_4 P_\infty} x_4(t) \tag{2.64}$$

Thus, **Equation 2.64** can be rearranged as:

$$\frac{C_{\text{dust}}}{y_4} = \frac{\tilde{M}_4 P_\infty}{R T_\infty x_4(t)} \tag{2.65}$$

to provide a function that can be used to evaluate the initial dust concentration necessary to reach any concentration of pyrolysis gases y_4 at a given time t.

Figure 2.18, shows on the left vertical axes the behaviour of this function for different temperatures and particle diameters with the kinetic model that provides higher yields of pyrolysis gas (Wagenaar et al.). The vertical axes on the right could, at first glance, be considered an overload of information that confuses the reading of the graph, but they do have a simplifying purpose. For instance, the experimental analysis on the composition of pyrolysis gases of starch allows to estimate that the minimum LEL for starch pyrolysis gases is 7.8% which is reached at 1020 K (**Figure 2.5**); multiplying both sides of **Equation 2.65** by 0.078, allows to estimate $C_{\text{dust}}^{\text{LEL}}$, the initial dust concentration necessary to reach the LEL of pyrolysis gases after a time t. Graphically this would only displace the lines downwards but the shape (and the units) of the graph would remain the same. Thus, the right axes allow to use the same graph to consider particular situations of interest. The latter also includes any situation in which an interest exist to know the initial dust concentration necessary to reach the stoichiometric concentration of pyrolysis gases ($C_{\text{dust}}^{y_{\text{st}}}$).

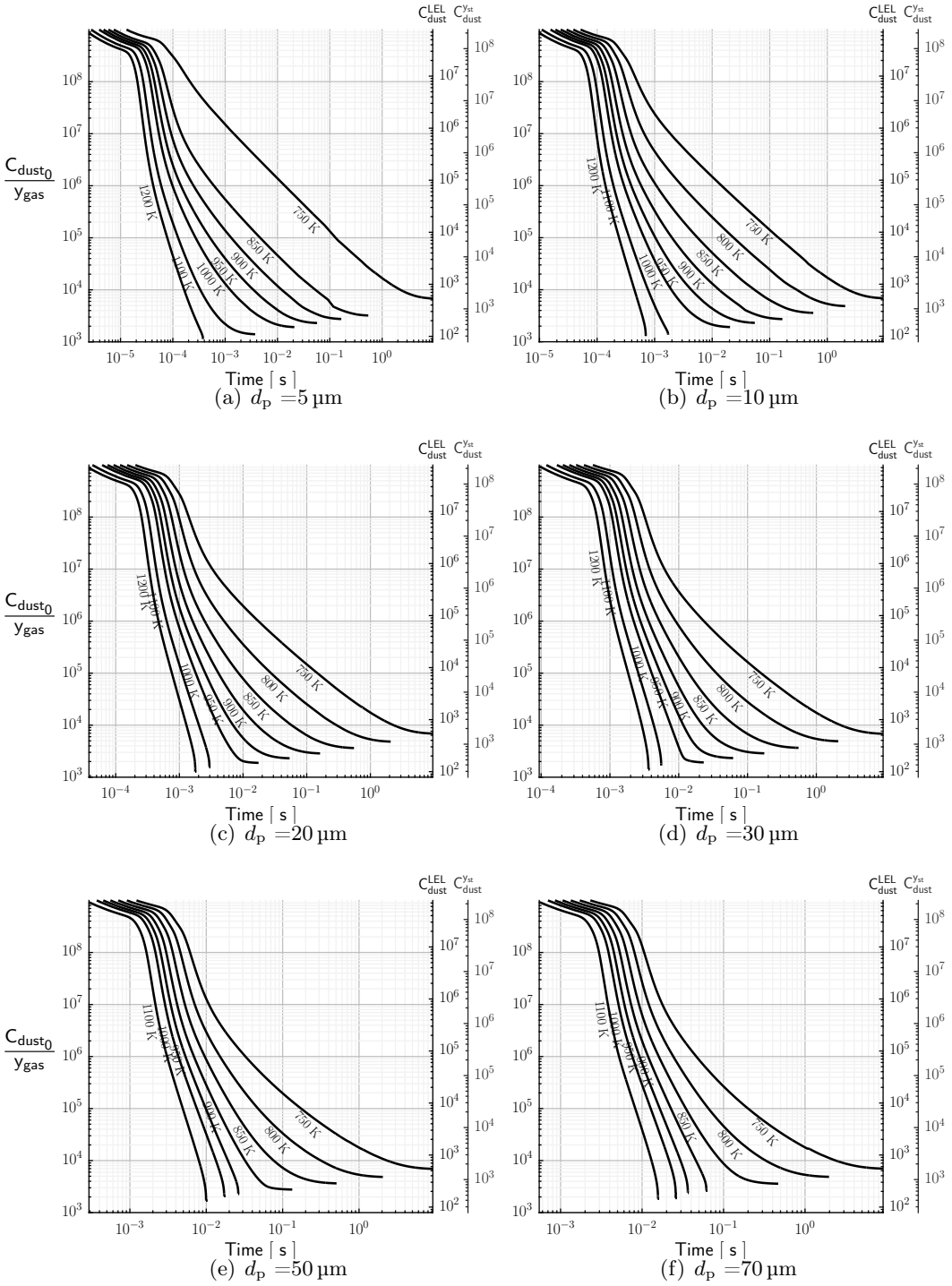

(a) d_p =5 µm (b) d_p =10 µm

(c) d_p =20 µm (d) d_p =30 µm

(e) d_p =50 µm (f) d_p =70 µm

Figure 2.18. Initial C_dust necessary to reach a concentration of y_4 in pyrolysis gases at time t using to **Wagenaar** kinetics, auxiliary axes on the left show the initial concentration necessary to reach the LEL =7.8% and the stoichiometric concentration (23%) of pyrolysis gases. Units for C_dust are in $\frac{\mathrm{g}}{\mathrm{m}^3}$

Example 2.1. *Consider a system containing a dust cloud consisting of* 10 µm *biomass particles with a concentration of* $1000\,\frac{\mathrm{g}}{\mathrm{m}}$. *Suppose that this cloud is pyrolyzed at* 1000 K *and* 1 bar. *Assuming that the* LEL *and stoichiometric concentration in air of the pyrolysis gases are 7.8% and 23% respectively,* ***Figure 2.18*** *can be used to estimate the time it would take for the system to reach the* LEL *or the stoichiometric concentration.*

One can either,

a) *use the left axis by calculating the left side of* ***Equation 2.65*** *for each of those concentrations:*

$$\frac{C_{\mathrm{dust}}}{\mathrm{LEL}} = \frac{1000\,\frac{\mathrm{g}}{\mathrm{m}^3}}{0.078} = 1.3\cdot 10^4\,\frac{\mathrm{g}}{\mathrm{m}^3} \qquad \frac{C_{\mathrm{dust}}}{y^{\mathrm{st}}_{\mathrm{mix}}} = \frac{1000\,\frac{\mathrm{g}}{\mathrm{m}^3}}{0.23} = 4.3\cdot 10^3\,\frac{\mathrm{g}}{\mathrm{m}^3}$$

b) *use the right axes to go directly from* $C^{\mathrm{LEL}}_{\mathrm{dust}} = C^{y_{\mathrm{st}}}_{\mathrm{dust}} = 1000\,\frac{\mathrm{g}}{\mathrm{m}^3}$ *to the line for* 1000 K

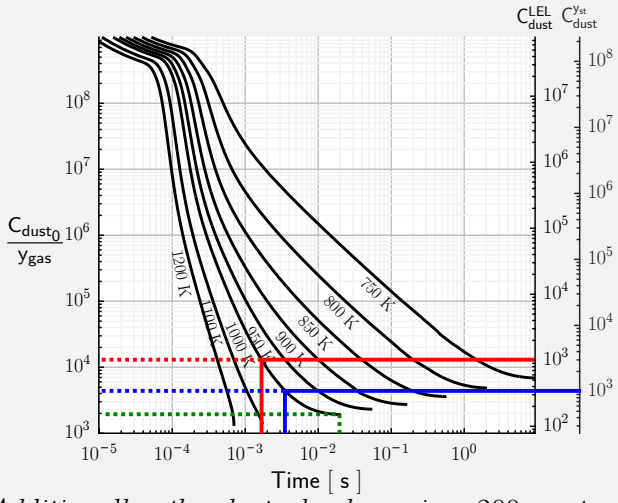

as represented at left in red for the LEL *and blue for the stoichiometric concentration. Both approaches allow to estimate that this dust cloud would reach the* LEL *after* 1.6 ms *and the stoichiometric concentration in* 3.5 ms *(assuming the mixture does not combust up to that point).*

Additionally, the dust cloud requires 200 ms *to completely pyrolyse (green line), at which point* $\frac{C_{\mathrm{dust}_0}}{y_{\mathrm{gas}}} = 1900$. *So the final concentration of pyrolysis gases after* 20 ms *under this conditions will be 52%.*

2.6. Future developments and perspectives

2.6.1. Pressure and Competition Between Pyrolysis and Combustion

In this study pressure outside the particle was considered to be always constant, and as such, the overpressure inside it does not even reach a 1 Pa. This means that the gases are evacuated at a faster rate than they are produced. Furthermore, as the reaction advances, the porosity goes from 0.0016 to 0.8 thus improving the permeability and forcing the gas to expand which explains the monotonicity of the pressure decrease after it reaches its maximum (**Figures 2.10** and **2.11**). If both combustion were considered the competition between combustion and pyrolysis

could be very different in a open and closed systems, since pressure can be considered constant in the first one, whereas is raises more that 5 times the initial value in latter. In the open systems, the only phenomenon driving the diffusion of oxygen towards the particle is the concentration differential, but the particle is at the same time ejecting gases which is opposes to that process. On the contrary, in closed systems the diffusion oxygen into the particle is driven also by the concentration differential but, mostly because of the hydraulic forces generated by the pressure differential. In fact this pressure could cause an implosion of the solid structure when it has been weaken enough.

2.6.2. Ignition and pyrolysis

It has been corroborated with this model, that the production of pyrolysis gases is estimulated by temperature (**Figures 2.14** to **2.16**). A logical consequence, is that an increase in temperature reduces both, the initial dust concentration necessary to achieve the LEL of pyrolysis gases ($C_{\text{dust}}^{\text{LEL}}$) and the time it takes to reach it (**Figure 2.18**). It can also be observed that the change in particle size does not have a major effect on $C_{\text{dust}}^{\text{LEL}}$ but it does affect the time necessary to achieve it. This happens because for any dust concentration C_{dust}, the particle size does not change the total mass in the system but it may change the homogeneity of the mixture when the solid is volatilized. Homogenization is assumed to be instantaneous in the development of **Equation 2.65** but turbulence could pay a more important role at this point.

Nevertheless, this perspective presents an opportunity to further explore the link between ignition and pyrolysis of organic dusts. **Figure 2.18** and its equivalents for other kinetic models (See **Appendix C**) present final values of $C_{\text{dust}}^{\text{LEL}}$ that vary between 100 and 1000 $\frac{\text{g}}{\text{m}^3}$ depending on the kinetic model and the external temperature. This situation could suggest a testable link between ignition and pyrolysis: on the one hand, the minimal value for $C_{\text{dust}}^{\text{LEL}}$ is reached at the maximal temperature evaluated (1200 K) and its order of magnitude is consistent with the MEC of some organic dusts; on the other hand, higher temperatures are expected to increase the production of pyrolysis gases in even shorter times. Furthermore it is expected that, at higher temperatures the diffusion of oxygen towards the particle would no be able to compete with the volatilization of the solid. This is important because the ignition period is characterized by high temperatures during very short periods of time.

For instance Han et al. (2010) and Han et al. (2011) have performed numerical simulations of the ignition of hydrogen and methane with detailed chemical models. Their results regarding the behaviour of temperature (**Figure 2.19**), show how spark ignitions lasting 40 and 80 µs, rise the temperature higher than 8000 K. After the ignition temperatures stablish between 1700 and 2000 K where it is sustained during up to 2 ms. This behaviour is closely similar for both gases and the slight differences in the curves seem to be independent of the chemical nature of the mixture and mostly related to the differences in ignition energy (IE) and time (t_i). This consideration can be justified on the fact that the simulation for hydrogen exhibits higher temperatures than methane despite the fact that the adiabatic temperature of methane is more than twice that of hydrogen.

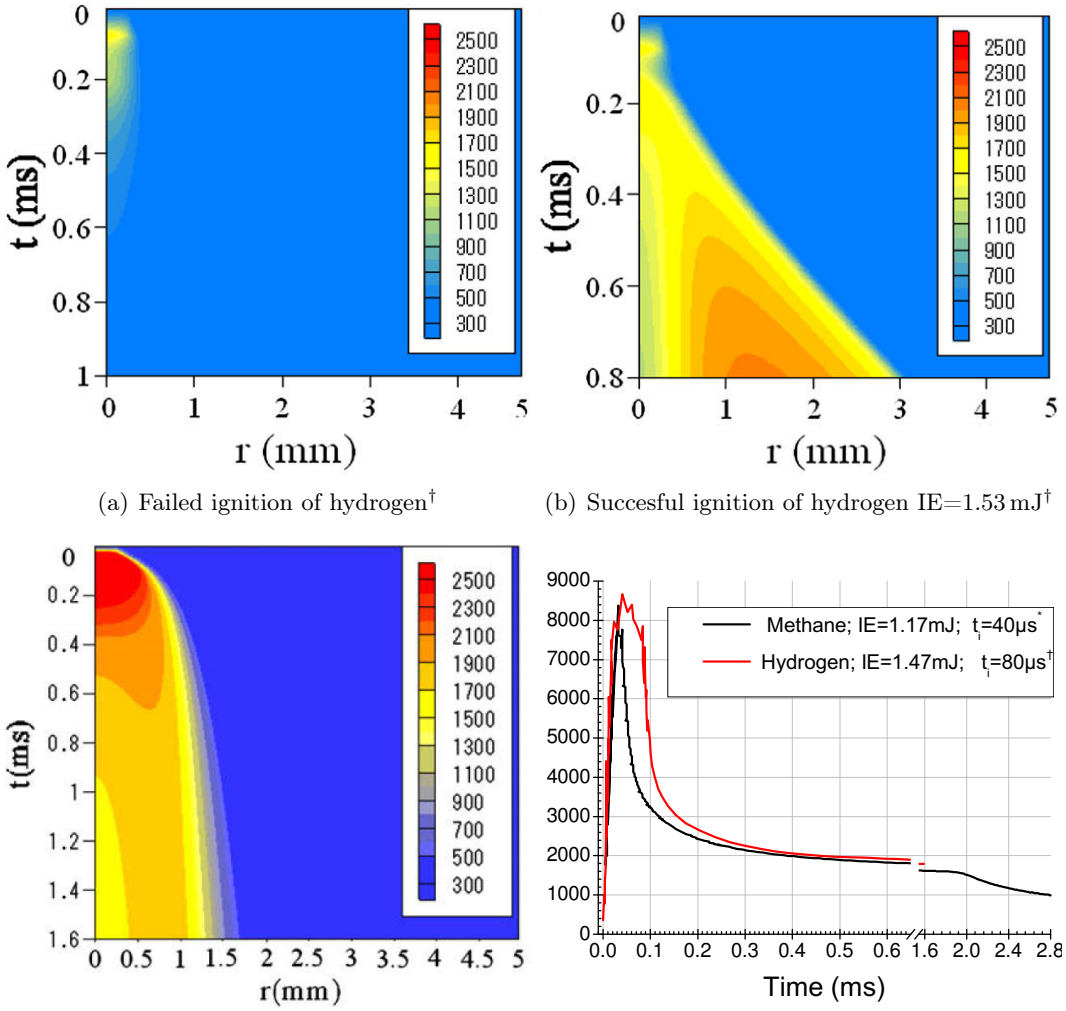

(a) Failed ignition of hydrogen†

(b) Succesful ignition of hydrogen IE=1.53 mJ†

(c) Succesful ignition of methane, IE=1.36 mJ*

(d) Maximum temperature history

Figure 2.19. Behaviour of temperature during and after spark ignition of methane* and hydrogen† according to simulations involving detailed chemistry.
*Han et al. (2010)
†Han et al. (2011)

This reasoning provides an additional explanation to the independence of the MIE from d_p, below a given particle size (**Figure 1.3**). For temperatures above 1750 K the time required for the volatilization becomes independent of temperature and the particle size seems to be the only relevant extrinsic variable (**Figure 2.13**). The MIE can then be understood in the context of organic solids, as «the minimal energy capable of creating an ignition core that sustains for a sufficient period of time, a temperature high enough for the solid particles to completely pyrolyse in the regime limited by external heat transfer». Furthermore, the MEC of organic solids can then be understood as «the minimal concentration of dust, capable of liberating through pyrolysis, enough combustible gases for them to achieve the LEL ($C_{\text{dust}}^{\text{LEL}}$) under the conditions of temperature and time provided by the ignition core». In

fact the reason why the nature of the ignition source changes the observed MEC, besides the morphology of the kernel, could be nothing but time, meaning: how long each ignition source lasts, rather than what kind of chemical processes happen during that period. **Equation 2.65** can be modified as follows:

$$\frac{\mathrm{MEC}}{\mathrm{LEL}} = \frac{\tilde{M}_4 P_{\mathrm{atm}}}{R T_{\mathrm{ad}} \varepsilon_{\mathrm{v}}} \tag{2.66}$$

to predict that the MEC of starch is 64 $\frac{\mathrm{g}}{\mathrm{m}^3}$ which is twice the one obtained measured by Khalili (2012) for the raw starch used in the severity and pyrolysis tests that provided ε_{v} (volatile content of dusts, see **Section 1.3.2.3** in page 25) and LEL. This means that although **Equation 2.66** provides a good order of magnitude the equation require further development, for either two of the following things to happen. On the one hand, it could eventually provide a better agreement. On the other hand, it could to be completely disproven as a useful tool that could eventually relate the MEC, the LEL and the ε_{v} in the context of pyrolysis of organic solid compounds. It has to be considered that the LEL used in this calculation was 7.8% which is the one predicted for a temperature of 1020 K in the experimental analysis of flash pyrolysis. The composition of the gas has not yet been measured for the temperatures that are expected during ignition. Furthermore the inclusion of T_{ad} is completely arbitrary and implies that combustion is taking place.

RÉSUMÉ

Étude de la pyrolyse de particules organiques lors d'une explosion de poussières

Considérons une particule sphérique de matière organique, immergée dans un environnement à haute température (flamme). Si le transfert de chaleur est suffisamment rapide pour surmonter la diffusion de l'oxygène à la surface de la particule, le solide atteindra sa température de décomposition et des gaz de pyrolyse seront produits et éjectés à l'entourage. Ces gaz migreront à l'extérieur de la particule, laissant derrière eux une enveloppe de charbon poreuse qui sera probablement fractionnée en petits fragments et/ou brûlera.

Du point de vue expérimental, l'équipe SAFE a déjà publié des résultats qui mettent en évidence l'importance de l'étape de pyrolyse sur les explosions de poussière. L'analyse présentée dans ce chapitre poursuit cette perspective, en négligeant la combustion du solide et du gaz pour se concentrer sur la compréhension des conditions qui conduisent à la production de gaz de pyrolyse. L'étude expérimentale a été réalisée en utilisant un four Godbert-Greenwald modifié pour effectuer la pyrolyse flash de l'amidon entre 830 et 1120K. Les gaz de pyrolyse ont été recueillis puis analysés par micro-chromatographie en phase gazeuse afin de quantifier leur composition. Les principaux constituants sont l'hydrogène, le monoxyde de carbone, le dioxyde de carbone et le méthane. De faibles concentrations d'éthylène et d'éthane ont également été trouvées ainsi que des concentrations négligeables (inférieures à 0,4%) de benzène et d'acétylène. Ces résultats ont été comparés à ceux de Bozier (2004), avec un accord globalement satisfaisant, mis à part pour le dioxyde de carbone.

Parallèlement des mélanges hybrides de gaz de pyrolyse et d'amidon ont été testés en utilisant une sphère de 20 L selon la norme EN 14034-3. Les pressions maximales de ces deux substances ne sont pas si différentes : les surpressions maximales varient respectivement de 7,5 bar à 8,5 bars pour les gaz de pyrolyse et l'amidon, ce qui est cohérent d'un point de vue thermodynamique. En revanche, les vitesses maximales de montée en pression sont totalement différentes et varient de 2830 $\frac{\text{bar}}{\text{s}}$ pour les gaz de pyrolyse à 400 $\frac{\text{bar}}{\text{s}}$ pour l'amidon. En ce qui concerne les mélanges hybrides de l'amidon et de ses gaz de pyrolyse, il convient de noter que les vitesses maximales de montée en pression se situent entre la valeur de la poussière et celle du gaz dans le mélange. En outre, l'explosivité de la poussière est fortement favorisée par l'addition de gaz combustible. Toutefois, il convient de signaler que cette différence est plus importante pour des valeurs de richesse supérieures à 0,2. Par conséquent,

on peut supposer que l'amidon joue encore un rôle important dans la cinétique de combustion en-dessous de cette limite ; pour de plus grandes quantités de carburant, le comportement spécifique des gaz combustibles est clairement prédominant (gas driven). L'introduction de gaz de pyrolyse à des particules d'amidon augmente leur inflammabilité et réduit l'influence de la limitation diffusionnelle à la surface des particules.

Un modèle de pyrolyse flash de la biomasse a aussi été développé pour l'intérieur d'une particule sphérique organique, afin de mieux comprendre les conditions qui permettent de promouvoir la production de gaz de pyrolyse. Le modèle a été formulé en coordonnées sphériques, en supposant que des changements se produisent exclusivement dans le sens radial et que les gradients dans les directions angulaires et azimutales sont négligeables. La particule a été fractionnée en petits volumes (de 20 à 30 en fonction de la taille de la particule) de la même manière que cela se ferait en utilisant la méthode des volumes finis. Des ensembles de polynômes de troisième ordre ont été utilisés pour interpoler les variables. Ces polynômes ont la particularité de partager les mêmes valeurs de la première et seconde dérivées au niveau des intersections, ce qui est appelé interpolation spline.

Le système d'équations différentielles ordinaires qui a été résolu est composé des dérivées temporelles de la densité de la biomasse, du charbon, de la variation de la fraction massique des gaz de pyrolyse en phase gazeuse, des variations de la pression et de la température. Les conditions limites externes prennent en compte le rayonnement et la convection. Quatre modèles cinétiques adaptés aux hautes températures ont été choisis parce qu'ils découplent le processus de pyrolyse en 3 à 4 différentes réactions.

Les simulations suggèrent que le goudron est toujours le principal produit de la pyrolyse de la biomasse avec un rendement minimum de 50% à 750 K avec le modèle cinétique de Font et al. (1990) et avec un rendement maximum de 80% sur une large gamme de température avec la cinétique de Di Blasi et Branca (2001). En fait, il semblerait que la température affecte principalement les rendements de charbon et gaz avec peu ou pas d'impact sur le goudron. Cela est particulièrement vrai dans le cas des modèles cinétique de Chan et al. (1985) et Di Blasi et Branca (2001). En outre, indépendamment du modèle cinétique testé, lorsque la température augmente, le rendement de carbonisation est réduit avec une augmentation de la production de gaz de pyrolyse.

Les résultats du modèle permettent d'évaluer la concentration de poussière initiale nécessaire pour atteindre une concentration du gaz de pyrolyse à un moment donné, qui peut être utilisée pour estimer $C_{\text{dust}}^{\text{LEL}}$, la concentration de poussière initial nécessaire pour atteindre le LIE du gaz de pyrolyse après un certain temps (voir **Example 2.1**, page 76).

Il peut également être observé que le changement de la taille des particules n'a pas un effet majeur sur $C_{\text{dust}}^{\text{LEL}}$, mais elle influence le temps nécessaire pour l'atteindre. Cela se produit car, pour toutes les concentrations de poussière, la taille de particule ne change pas la masse totale dans le système, mais elle peut changer l'homogénéité du mélange lorsque le solide est volatilisé. L'homogénéité du milieu est considérée comme acquise dans le modèle, mais la turbulence peut jouer un rôle plus important à ce stade. Cette perspective présente une occasion pour explorer le lien entre l'allumage et la pyrolyse des poussières organiques : d'une part, la valeur

minimale de $C_{\text{dust}}^{\text{LEL}}$ est atteinte à la température maximale évaluée (1200 $_{\text{k}}$elvin) et son ordre de grandeur est conforme à la CME de quelques poussières organiques. En outre, la CME de solides organiques peut alors être interprétée comme étant la concentration minimale de poussière, capable de libérer par pyrolyse, suffisamment de gaz combustibles pour leur permettre d'atteindre le LIE ($C_{\text{dust}}^{\text{LEL}}$) dans les conditions de température et de temps fournies par le noyau d'allumage. D'autre part, des températures plus élevées devraient augmenter la production de gaz de pyrolyse dans les temps encore plus courts. En outre, il est prévu que, à des températures plus élevées, la diffusion de l'oxygène vers la particule ne sera pas en mesure de rivaliser avec la volatilisation de la matière solide. Ceci est un point important car la période d'allumage est caractérisée par des températures élevées pendant de très courtes périodes de temps.

Chapter 3

Quantification of Turbulence Due to the Dispersion of Dusts Prior Explosion

Contents

3.1. Introduction

One of the main objectives of the work presented in this document, is to better understand the influence of turbulence on the propagation of dust flames. This influence is performed through different mechanisms. Turbulence randomly modifies the flame profile increasing its surface, while enhancing its contact with the unburned material. It also accelerates mass transfer, more specifically it improves the contact of oxygen with the combustible. Paradoxically, high levels of turbulence can also dampen or quench the propagation of the flame, stretching it so much that they may cause the rupture of the flame front. While this kind of phenomena are more relevant after ignition, there is a special interest in analysing the way in which the turbulence of the media prior the explosion affects the later development of the flame. This initial turbulence is important as it influences the way the particles aggregate and the interaction of the flame kernel with the reactants through mass and heat transfer. It also plays a role in the concentration gradients of dust as a minimum level of turbulence is mandatory to produce a dust cloud. For this reason understanding the role of the initial turbulence could help in the understanding of the behaviour of the later deflagration.

An approach often used to *indirectly* evaluate the influence of turbulence on dust explosions is to relate the ignition time delay (t_v) to the level of turbulence (Dahoe, 2000, chap. 2.5.2). Moreover this approach has also been extended to the study of hybrid mixtures (Sanchirico et al., 2011; Dufaud et al., 2012a). The concept consists on varying the time between the moment at which dust is dispersed by an air current to create a dust cloud, and the moment when it is ignited by an energy source; thus varying the level of turbulence due to the reduction of the velocity of air after the current is ended. This is in fact the way that turbulence is accounted for in standardised tests for sensitivity and severity of dust explosions (IEC standard 1241-2-1 (1994) and ISO 6184-1 (1985) respectively).

This approach is very practical because of the ease to qualitatively relate t_v to the turbulence level. It allows to evaluate a parameter of interest at different levels of turbulence in a simple intuitive way, just as long as the other conditions remain the same. This imposes a constraint when one wants to extrapolate the results obtained in one geometry to a different one. For example: results obtained in the Siwek sphere and the Hartmann tube cannot be related at similar values of t_v and not just because of the evident geometrical differences. More important than geometry in this case, is the pressure difference at which both tests are performed that considerably affects the speed of the dispersion flow and so the turbulence level.

Such a limitation seems to be better explained because of the difficulty in defining what Wang et al. (2006b) calls a *dust cloud state*[1]. Having an appropriate definition of a dust cloud state might allow to relate the conditions found, not only in the various experimental apparatuses, but most importantly, to *confidently* extend the results found in controlled conditions to the industrial scale. While this definition

[1]"It appears that the basic question is perhaps not merely how to produce an experimental dust cloud, but rather whether a definition of the cloud states can be given. Provided the quantitative information on the state of a dust cloud (dust concentration, dynamic state, etc.) is obtained, one can correlate the observed flame propagation behaviours with this state, and correlate experimental data from different workers who have used different apparatus." (Wang et al., 2006b)

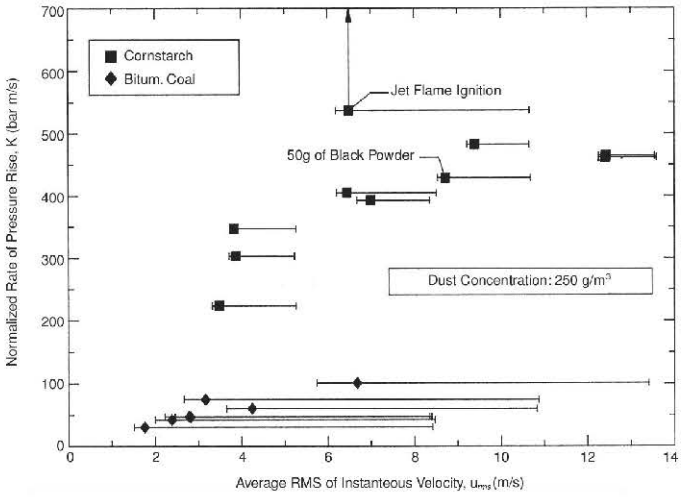

Figure 3.1. Rate of pressure rise in room-like structure as a function of RMS turbulent velocity. Data from (Tamanini, 1990), interpreted using the vent sizing correlation from (Tamanini and Valiulis, 1996)., extracted from (Tamanini, 1998)

has not been yet standardised, it might be self-explanatory that a comprehensive one shall consider *at least*, the concentration of the dust, its gradient and the degree of turbulence in the cloud, as it may locally influence the fuel equivalent ratio. Therefore one step forward for achieving the goal of relating the behaviour of a given mixture to different scenarios, is to quantitatively characterize the intensity of turbulence for the studied mixture. This is done through the estimation of quantities like u'_{rms} and u' as explained in **Section 3.4** in page 98. Some of the efforts that have already been done in this direction are mentioned below:

- Tamanini (1998) tested the maximum rate of pressure rise $\left(\frac{\mathrm{d}P}{\mathrm{d}t}\right)_{\max}$ at different turbulent states in a room-like structure (4.6m×4.6m×3.0 m) with cornstarch and bituminous coal. He measured turbulence using a a bi-directional impact probe at 46 different points (see **Figure 3.1**).
- Dahoe (2000) quantified turbulence inside an apparatus with the same dimensions as the Siwek sphere using Laser Doppler Anemometry (see **Figure 3.2**) and compared the results for different dispersion nozzles.
- Wang et al. (2006b) used Particle Image velocimetry inside a square vertical tube with 78cm height and 16cm on the sides to quantify turbulence and relate it to flame burning velocity as can be seen in **Figure 3.3**. In a similar fashion to the work presented here.

The study by Wang et al. (2006b) is of particular interest because the work presented here is developed as well in a vertical square tube, the method used for visualising turbulence is also Particle Image Velocimetry (PIV) and starch dust is also used. In contrast, their method for creating the dust cloud is with a continuous airflow that stops once the tube is filled with particles, whereas this study used and

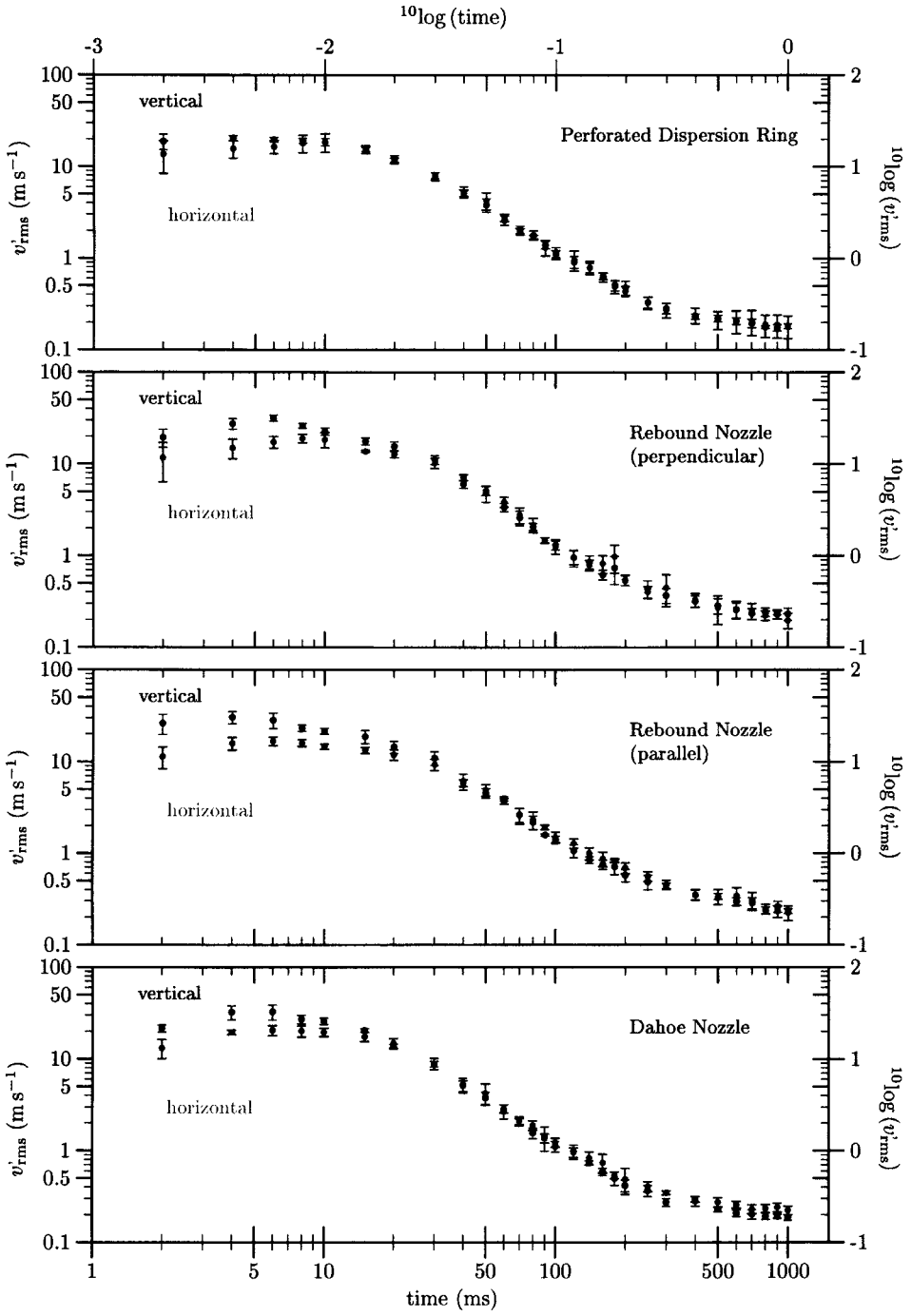

Figure 3.2. Root-mean-square values of the velocity fluctuations in the 20-liter sphere. Extracted from (Dahoe et al., 2001)

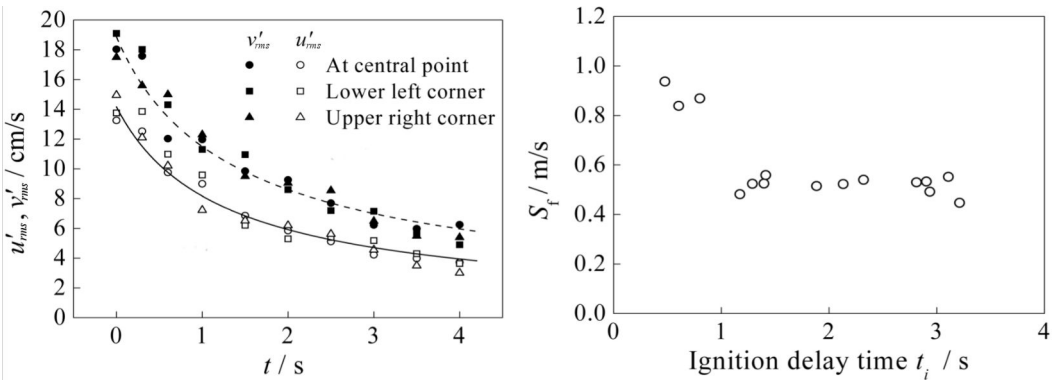

Figure 3.3. Flame propagation speed in a vertical squared tube at various turbulent states. Extracted from (Wang et al., 2006b)

air pulse as the one of the Mike apparatus that is intended to create a dust cloud at bottom of the tube. Another particularity that differences both studies is that here, turbulence is also studied during the dispersion stage which might be extrapolated to the Mike Apparatus.

3.1.1. A Glimpse Into Particle Image Velocimetry

Particle Image Velocimetry (PIV) is a technique allowing to trace 2D velocity vector fields for fluid flows that is considered to be non-intrusive. At least for the present case, intrusion is completely avoided; considering that, for liquid and gas flows, there must be a *negligible* intrusion with small quantities of seeding micro-particles. This is not necessary here since the velocity tracers are already present in the fluid. The velocity fields are built by measuring the displacement of particles in a given space of time whose duration is defined by two laser pulses. The laser pulses are sheet-shaped and cross a section of the fluid flow. As a laser pulse occurs, a picture of the flow is simultaneously taken from a perpendicular position to the laser sheet. The light scattered towards the camera by the particles in the flow, enables to identify the positions of the particles from the pictures taken. After the two images are recorded, they are analysed by dividing them in small control volumes called *interrogation areas*. Interrogation areas are compared from one picture to the other for evaluating the displacement of the particles in the elapsed time. Velocities are now *easily* calculated from the position and time data. Further detail into the specifics of the algorithms that translate the information in the pictures to quantifiable data, goes beyond the focus of this work but has been thoroughly explained by Adrian and Westerweel (2011). This study relies on a black box algorithm that returns the instantaneous velocity fields decomposed in horizontal and vertical components of the velocities as a function of the x and y coordinates. With this data available, it is possible to perform a further analysis on the behaviour of turbulence.

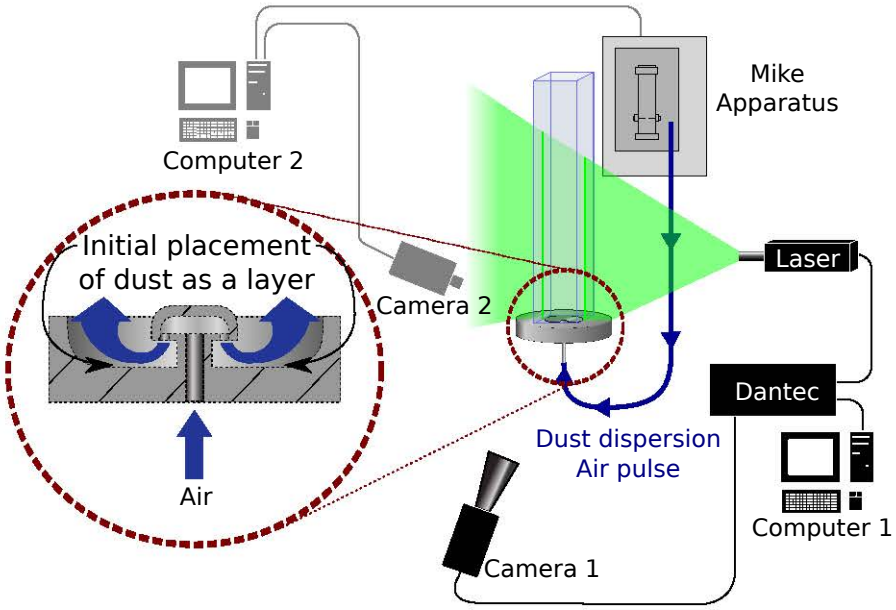

Figure 3.4. Diagram showing experimental setup for Particle Image Velocimetry (PIV) analysis in a square-section vertical tube.

3.2. Description of the Experimental Setup

As previously mentioned, the focus of this chapter is to quantify the turbulence caused by the dispersion of a dust cloud by an air current inside a vertical square tube. The dimensions of the tube were chosen to resemble those of the modified Hartmann tube used for the determination of the Minimal Ignition Energy of dust clouds. Moreover, the dimensions of the tube also allow to recreate the conditions inside the propagation tube used for the experimental setup described in **Chapter 4**. The experimental arrangement depicted in **Figure 3.4** is composed of 2 independent systems, each one controlled by `Computers 1` and 2. The first one is dedicated to the control of the equipments related to Particle Image Velocimetry. Whereas the second one controls the dispersion of dust inside the tube, as well as a high-speed camera (`Camera 2`), used to verify the moment of dust dispersion. Both systems are described in detail below.

3.2.1. Particle Image Velocimetry acquisition system

The system controlled by `Computer 1` in **Figure 3.4** is the one in charge of doing the PIV analysis at the interior of the tube and it is manufactured by Dantec Dynamics' [2]. It is composed of:

[2]The use of this equipment was possible thanks to Salaheddine Skali-Lami from LEMTA who kindly lent it to us and gave his assistance in the installation of the setup described here and on the interpretation of the data. Hereby I express once again my gratitude to him for the selfless cooperation he provided to this work.

LEMTA - Laboratoire d'Énergétique et de Mécanique Théorique et Appliquée - UMR 7563 - Université de Lorraine.

- The `Laser`, A light source including a crystal harmonic generator to produce a green light. By means of a cylindrical lens the light ray is transformed into a 0.25 mm thick plane. As it is inherent to the nature of the technique (see **Section 3.1.1** in page 87), it has actually 2 laser systems incorporated within it, each one independent from the other. Both lasers flash at a maximum frequency of 15Hz, thus, limiting the PIV analysis to be done in time intervals of 66.67 ms. The `Laser` was placed so the laser sheet would cross the tube through the middle at an angle of 90° to the glass surface.

- The `Camera 1`, a CCD camera (Kodak Mega plus ES.1.0), it takes pictures with a resolution 1008×1016 px^2 every time the `Laser` is shot. From a perpendicular position to the laser sheet, it was accommodated to grab images of the tube at a height ranges of 5 cm-12.5 cm and 6.5 cm-14 cm, while comprising the whole width of the tube (7 cm). **Figure 3.5** exemplifies the way laser and camera's *pairs of* shots are synchronized to light up the tube and recording the pictures needed for the analysis described in **Section 3.1.1** in page 87.

- `Dantec`, a flowmap type synchroniser from Dantec Dynamics (thus the name). It is the equipment responsible of synchronising the `Camera 1` and the `Laser` with the instructions imparted from `Computer 1`.

- `Computer 1`, allows to define the operating parameters for the `Dantec` to control of the PIV equipment. This is possible through the user interface provided by the Flow Manager Software® from Dantec Dynamics. Once the experimentation is finished, the software translates the information from the images to the numerical information of the velocity field. This is done by dividing the images in 40×41 *interrogation areas*.

3.2.2. Equipment for dust dispersion and dispersion time estimation

The second subsystem on **Figure 3.4** is commanded by `Computer 2` and is composed of three equipments whose function is related to dust dispersion:

- `Mike Apparatus` is the equipment used for testing the ignition sensitivity of dust. Its functionality to create an air current to disperse the dust cloud was exploited for this work. It has a 50 mL chamber that is pressurized to 8 bar, to be decompressed afterwards at the bottom of the `Translucent Square Tube`.

- `Translucent Square Tube`, at the center of this study, it is composed of a tube with 40 cm in length, 7 cm on the sides and a stainless-steel dust dispersion cup at the bottom. Dust is placed in the cup so the dust layer can be blown inside the tube by the air flow originated in the `Mike Apparatus` as described in the detailed zoom of **Figure 3.4**.

- `Camera 2`, It is a Phantom high speed camera with the capacity to capture 16000 fps. For this work it was set at 1000 fps with exposure time of 997 ms. It was used for filming the bottom of tube and thus permitting to establish the dispersion time through the comparison of the pictures taken by `Camera 1` with the apparition of flashes in the videos of `Camera 2`, and of course, the moment dust starts to be dispersed by the air flow.

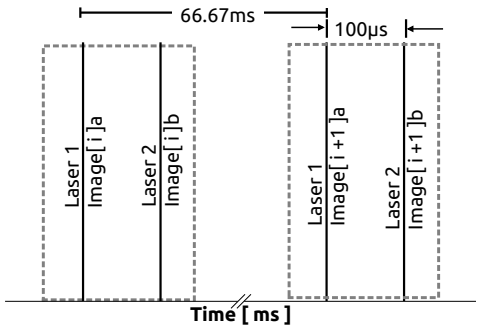

Figure 3.5. PIV laser and image shot setup for the set of experiments of glass beads described in Table 3.1 Dark lines represent the first and second pulse of the laser as well as the respective pictures a and b. The pointed gray lines enclose the elements of analysis necesary to produce estimate one velocity field

3.2.3. Some Considerations about the Experimental Framework

So far the reader may have already noticed some of the limitations imposed by the equipment used here for performing PIV. Perhaps the one that influences the analysis the most, is the maximum frequency of the laser pulses[3]. With a maximum value of 15 Hz, it is considerably small when the phenomenon to be analysed happens in a lapse of 250-500 ms. Hence, only 3-7 *pairs of* laser pulses can be produced within the duration of each dust dispersion. On the other hand, as it will be better explained in the next section, the analysis of turbulence intensity requires extensive statistical data particularly for estimating v'_{rms}. Coupling this facts with the unsteady nature of the phenomenon, it becomes clearer that the independence of the dust dispersion and the PIV systems is also a limitation. Regardless of the justification for using this configuration (ownership and availability of the PIV equipment), these limitations are reflected in the way experiments were performed and analysed. Consequently, it becomes evident that extensive sets of experiments had to be executed to obtain statistically relevant data as is reflected on **Table 3.1**.

Glass beads where used in a first stage to test the technique, as the beads with such a size do not attach so easily to the walls and do not agglomerate, avoiding the necessity of cleaning the tube after each dispersion. The total time lapse considered for the glass beads was 250 ms. In contrast, for the cases of dust starch, that sediments more slowly 500 ms where considered.

A question remains, what is the reason for considering just two values for the mass and not to cover the whole spectrum of the masses studied in page more or even just one? Before addressing this question let's remember that PIV is a technique developed for estimating velocity fields in gas and liquid fluids. In principle the presence of particles in the flow was not inherent for the fluid but rather an inclusion that had to be done in order to visualise the current lines. This inclusion may, in some way, be an intrusion that modifies the natural flow of the current. However, what was done here was to use the dust as a tracer. So if it is true that the

[3]Not to to be mistaken for light frequency spectrum.

Table 3.1. Summary of experiments performed with Particle Image Velocimetry

Dust Specifics			**PIV Parameters**		
Name	d_{50} (µm)	m (mg)	Tube section (cm)	Laser pulse delay[a] (µs)	Number of replicates
Wheat starch	25	78	6.5 - 14.0	150	70
Wheat starch	25	319	6.5 - 14.0	150	70
Glass	86	5000	5.0 - 12.5	100	20

[a] Time space between laser 1 and laser 2, defining a differential time lapse for estimating speed from a position differential.

presence of particles affects the flow, for the present study, it would be actually better to quantify this effect. Indeed, it has already been shown (Khalili, 2012) that dust modifies the natural flow of the heterogeneous mixtures with air increasing turbulence and consequently affecting the propagation of flames during an explosion.

Hence, to get back to the question about the number of values for the mass of starch in **Table 3.1**, Dantec Dynamics suggest in their website[4] that, as a rule of thumb, there might be 10-25 particles for each *interrogation area*. The ranges of mass values for starch that would be necessary to fulfil this rule according to the height of the dust cloud can be seen in **Table 3.2**. This table is a reflection of the following considerations: **First.** This study aims to analyse the velocity fields from the beginning to the end of dispersion. At the same time, the lowest point analysed is 6.5 cm and before the cloud reaches that point it is highly concentrated. On the other hand, according to the videos analysed in **Chapter 4**, the dust cloud can reach a maximum height of 30 cm, achieving then its minimum concentration after dispersion. **Second.** The area analysed measures 7×7.5 cm^2, the light sheet is 0.25 mm thick and the algorithm from the Flow Manager Software® divides it in 40×41 *interpolation areas*. **Third.** Particles are supposed to be perfectly spherical with d_{50} =25 µm, and ρ_p =0.49 g·cm^{-3}. In regard of this analysis, it is literally impossible to strictly accord to the rule of thumb for the whole interval: On the one hand, it would be necessary a minimum of 74 mg to reach the minimum of particles per interrogation area, when the dust cloud is less concentrated at 30 cm high. On the other hand, a maximum of 40 mg would be necessary to avoid exceeding 25 particles per interrogation area, when the dust cloud is most concentrated at 6.5 cm high. Therefore, the literal interpretation of the 10-25 particles-per-interrogation-area restriction leads to an empty interval of for the mass of dust. However, it is a *rule of thumb* not an imperative restriction. Furthermore, the rule of thumb was formulated for a technique (PIV) that is used mainly for analysing fluid currents that shall not be perturbed with large quantities of dust, whereas this study actually aims to quantify that effect. That does not mean anyway, that one could use this technique with as much dust as possible. In fact, what can be seen from the analyses performed is that 319 mg start to present complications for the PIV algorithm in differentiating the dust: there is too much dust so it is complicated to differentiate

[4] Accessed on May 6th, 2014. URL:
`http://www.dantecdynamics.com/measurement-principles-of-piv`

Table 3.2. Mass of starch (mg) for fitting PIV's rule of thumb

Height of dust cloud in the tube (cm)	**Number of Particles per interrogation area**	
	10	**25**
6.5	16	40
30	74	184

one particle from the other. Therefore, 319 mg where used to push the limits of the PIV analysis and this intention was not taken further because it seemed counterproductive.

3.3. Physical Description of the Phenomena Involved in Dust Cloud Formation

It may be a restatement to affirm that, one of the main reasons for dust explosions to even be possible is because of the small size of the combustible solid particles. Nevertheless, if the combustible solid material was not in a particulate form, not only it would not be called dust any more but there would also not be any explosion in most of the cases: because the small size allows for the dust to be dispersed in a cloud and oxygen can access the material in an easier way during an eventual combustion of the cloud. Dust clouds are formed because drag forces are able to compete in magnitude with the gravitational force due to the low weight particles have. This is why many of the devices used to study the explosive behaviour of dusts and its interaction with turbulence use an air pulse to disperse the dust (*eg.* the 20 L sphere or the modified Hartmann tube). This is also the case of the equipment used for this study. Furthermore, after the dispersion stage, a settling stage takes place during which, the drag forces are still preponderant. The way these forces interact with dust particles is tightly related to the velocity of air leaving the pressurised chamber that generates the air pulse. This section describes from a theoretic point of view, the behaviour of the velocity of air leaving the pressurized chamber through an orifice during the dispersion stage and its interaction with the dust during and after the expansion of gas.

3.3.1. Expansion of Air Through a Hole From a Pressurized Chamber

The way dust is dispersed with the Mike apparatus is in fact the typical case of a leak from a pressurized gas chamber through a hole. The models used for this kind of situation assume that this expansion is isentropic (Crowl and Louvar, 2001). **Equation 3.1** relates the behaviour of temperature and pressure inside the chamber at any moment to the initial values P_0 and T_0, where γ represents the ratio of heat capacities $\tilde{C}_P/\tilde{C}_V$.

At the same time, the velocity of air leaving the chamber depends on the pressure

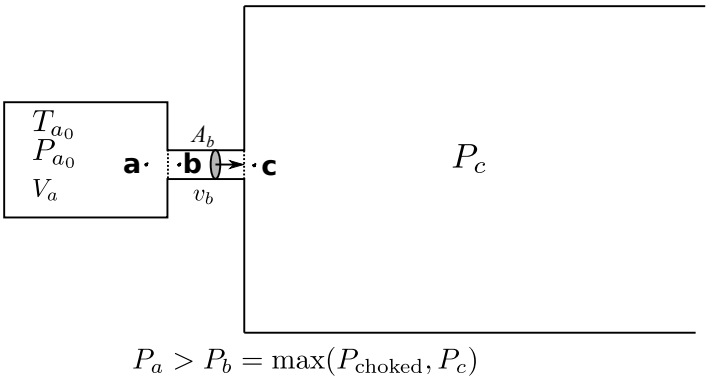

Figure 3.6. Representation for the free isentropic expansion of a presurized chamber through a leak

difference (more precisely pressure ratio) driving the expansion.

$$\left(\frac{P}{P_0}\right)^{\frac{\gamma-1}{\gamma}} = \frac{T}{T_0} \tag{3.1}$$

Considering the pressurized chamber with constant volume V_a and initial conditions P_{a_0} and T_{a_0} on the left of **Figure 3.6**, if the chamber is suddenly exposed the environment through point **b** the air will flow through that point until it reaches the external pressure P_c. The escaping velocity depends therefore on the pressure difference between points **a** and **c**. If the choked pressure P_{choked}, defined by **Equation 3.2** is greater than P_c, then the pressure at **b** would be equal to P_{choked} and the flow is maximum and independent from the pressure at **c**.

$$\frac{P_{\text{choked}}}{P_a} = \left(\frac{2}{\gamma+1}\right)^{\frac{\gamma}{\gamma-1}} \tag{3.2}$$

This thermodynamic restriction is due to the speed at which a pressure wave can travel in a fluid medium. It is defined by the Mach number Ma, when it equals 1. Consequently this kind of flow is called *sonic* or *choked* and the velocity of sound limiting it, will be called v_{choked} here to emphasize the context. This velocity is independent of the downstream pressure P_c but it is affected by the changing conditions at **a** during the expansion that also influence the conditions at **b** according to **Equation 3.2**. Therefore as the thermodynamic state at **b** changes v_{choked} changes according to **Equation 3.3**.

$$v_{\text{choked}} = \sqrt{\gamma \frac{R}{\tilde{M}} T} \tag{3.3}$$

On the other hand when $P_{\text{choked}} < P_c$ the pressure in **b** would be equal to P_c and the system would be in a *subsonic* regime. The velocity can then be estimated with the energy balance below for a surface perpendicular to the flow between points **a** and **b**.

$$\tilde{H}_a = \tilde{H}_b + \tilde{M}\frac{v_b^2}{2} \Rightarrow \tilde{C}_P T_a = \tilde{C}_P T_b + \tilde{M}\frac{{v_b}^2}{2}$$

Thus:

$$v_b = \sqrt{2\frac{\tilde{C}_P}{\tilde{M}}(T_a - T_b)} = \sqrt{2\frac{\gamma}{(\gamma-1)}\frac{R}{\tilde{M}}\left(T_a - T_{a_0}\left(\frac{P_c}{P_{a_0}}\right)^{\frac{\gamma}{\gamma-1}}\right)} \tag{3.4}$$

In both cases, *choked* or *subsonic*, **Equations 3.1** to **3.4** allow to estimate pressure and temperature inside the chamber at any moment and to relate them to the velocity in point **b**. However, time is not considered in any of them. So if there is any interest in estimating the dispersion time or the behaviour of any of these variables in time, it is necessary to consider the matter and energy balances for the pressurized chamber in **Figure 3.6** . **Equations 3.5** and **3.6** are the respective balances, for the adiabatic and isentropic expansion of and ideal gas in the the chamber **a**, this two equations together result in **Equation 3.7**.

$$\frac{\partial n_a}{\partial t} = -\frac{P_b A_b v_b}{R T_b} \tag{3.5}$$

$$\frac{\partial\left(n_a \tilde{U}_a\right)}{\partial t} = \frac{\partial n_a}{\partial t}\tilde{H}_a \tag{3.6}$$

$$n_a\frac{\partial \tilde{U}_a}{\partial t} = \frac{\partial n_a}{\partial t}\tilde{H}_a - \tilde{U}_a\frac{\partial n_a}{\partial t}$$

$$n_a\frac{\partial \tilde{U}_a}{\partial t} = \frac{P_b A_b v_b}{R T_b}\left(\tilde{H}_a - \tilde{U}_a\right)$$

$$\frac{\partial T_a}{\partial t} = -\frac{A_b R}{\tilde{C}_V V_a} v_b \left(\frac{P_b}{P_a}\right)\left(\frac{T_a^2}{T_b}\right)$$

This result is valid for a system were no pressure losses or restriction to the flow exist. For considering this phenomena, a friction coefficient $0 \leq C_\circ \leq 1$ can be included to get:

$$\frac{\partial T_a}{\partial t} = -\frac{C_\circ A_b R}{\tilde{C}_V V_a} v_b \left(\frac{P_b}{P_a}\right)\left(\frac{T_a^2}{T_b}\right) \tag{3.7}$$

Equation 3.7 can be used together with **Equations 3.1** to **3.4** to study the behaviour of the velocity as a function of time, of the initial state of the system and P_c for choked and *subsonic* flows.

3.3.1.1. Velocity as a Function of Time for a Choked Flow

Considering that the flow at **b** equals the choked pressure for the pressure in the chamber **Equations 3.1** to **3.3** give:

$$v_b = \sqrt{2\frac{\gamma R T_a}{(\gamma+1)\tilde{M}}} \;\Leftrightarrow\; T_a = \frac{\tilde{M}(\gamma+1){v_b}^2}{2\gamma} \;\Rightarrow\; \frac{\partial T_a}{\partial v_b} = \frac{\tilde{M}(\gamma+1)v_b}{\gamma R} \tag{3.8}$$

On the other hand, by doing some work on **Equations 3.1** and **3.2** the following relation is obtained:

$$\left(\frac{2}{\gamma+1}\right)^{\frac{1}{\gamma-1}} = \left(\frac{P_b}{P_a}\right)\left(\frac{T_a}{T_b}\right) \tag{3.9}$$

Equations 3.8 and **3.9** can then be replaced in **Equation 3.7** to obtain an expression independent from any other variable that can be easily integrated. the result is an expression for the velocity in the orifice as a function of time and the initial state of the system for a choked regime represented in **Equation 3.11**.

$$\int_{v_{\text{choked}_0}}^{v_{\text{choked}}(t)} {v_b}^{-2}\mathrm{d}v_b = -\int_0^t \frac{C_\circ A_b R}{2\tilde{C}_V V_a}\mathrm{d}t \tag{3.10}$$

$$v_{\text{choked}}(t) = v_{\text{choked}_0}\left(1+\frac{t}{\tau_{\text{choked}}}\right)^{-1} \quad \forall t | 0 \leq t \leq t_{\text{choked}} \tag{3.11}$$

where:

$$\tau_{\text{choked}} = \frac{2V_a}{(\gamma-1)C_\circ A_b v_{\text{choked}_0}}\left(\frac{\gamma+1}{2}\right)^{\frac{1}{\gamma-1}} \tag{3.12}$$

and

$$v_{\text{choked}_0} = \sqrt{\frac{2\gamma R T_{a_0}}{(\gamma+1)\tilde{M}}} \tag{3.13}$$

The velocity at the end of the choked regime v^*_{choked} is obtained from **Equations 3.1** to **3.3** for $P_{\text{choked}} = P_b = P_c$ resulting in **Equation 3.14**.Therefore, from **Equation 3.11** it is possible to estimate the time of the gas expansion in choked regime as shown in **Equation 3.15**.

$$v^*_{\text{choked}} = \sqrt{\frac{\gamma R T_{a_0}}{\tilde{M}}\left(\frac{P_c}{P_{a_0}}\right)^{\frac{\gamma-1}{\gamma}}} \tag{3.14}$$

$$t_{\text{choked}} = \tau_{\text{choked}}\left(\sqrt{\frac{2}{\gamma+1}}\left(\frac{P_{a_0}}{P_c}\right)^{\frac{\gamma-1}{2\gamma}} - 1\right) \tag{3.15}$$

Finally, the combination **Equations 3.1** to **3.3** with **Equation 3.11**, allows to relate the time behaviour of temperature and pressure in the chamber and in the orifice, as shown in **Equations 3.16** to **3.19**:

$$T_a(t) = T_{a_0}\left(1 + \frac{t}{\tau_{\text{choked}}}\right)^{-2} \tag{3.16}$$

$$P_a(t) = P_{a_0}\left(1 + \frac{t}{\tau_{\text{choked}}}\right)^{-\frac{2\gamma}{\gamma-1}} \tag{3.17}$$

$$T_b(t) = T_{a_0}\left(\frac{2}{\gamma+1}\right)\left(1 + \frac{t}{\tau_{\text{choked}}}\right)^{-2} \tag{3.18}$$

$$P_b(t) = P_{a_0}\left(\frac{2}{\gamma+1}\right)^{\frac{\gamma}{\gamma-1}}\left(1 + \frac{t}{\tau_{\text{choked}}}\right)^{-\frac{2\gamma}{\gamma-1}} \tag{3.19}$$

3.3.1.2. Velocity as a Function of Time for a Subsonic Regime

Once the pressure in the chamber arrives to a point where the corresponding choked pressure equals the pressure outside the chamber, the pressure in the throttling equals equals the pressure downstream and remains constant. Therefore temperature downstream also stays constant. This means that although the decompression continues to be isentropic, the air exiting the chamber no longer achieves the speed of sound. The way speed changes, starts then to depend on the pressure on both sides, which is indirectly expressed in **Equation 3.4**. Consequently, performing an analysis similar to the previous one for the subsonic regime using **Equation 3.4** instead of **Equation 3.3** reduces **Equation 3.7** to:

$$\frac{\partial v_b}{\partial t} = -\frac{C_\circ A_b \gamma R}{V_a \tilde{M}} T_{a_0}\left(\frac{P_c}{P_{a_0}}\right)^{\frac{1}{\gamma}}\left[\frac{\tilde{M}}{2RT_{a_0}}\left(\frac{\gamma-1}{\gamma}\right)v_b^2 + \left(\frac{P_c}{P_{a_0}}\right)^{\frac{\gamma-1}{\gamma}}\right]^{\frac{\gamma-2}{\gamma-1}} \tag{3.20}$$

where the initial temperature and pressure values, $T^*_{a_0}$ and $P^*_{a_0}$, could be either The values at the end of the sonic expansion (if the expansion starts choked) or the initial state of a completely subsonic expansion. In the analysis that follows the superscript *, will still be used for stressing that the initial property in question refers exclusively to the beginning of a subsonic expansion and not the initial state of the system in case the dispersion starts in sonic regime.

The complexity of **Equation 3.20** or any of its equivalents for pressure or temperature, make it difficult to obtain an analytic answer for either of them. For this reason a numeric integration was preferred for the analysis of the subsonic behaviour of the flow.

Figure 3.7 shows the behaviour of pressure, temperature and velocity for the expansion of air in the 50 mL chamber of the `Mike Apparatus` with $C_\circ$ =1. The figure shows the behaviour of those variables for both the chamber and the throttling point. It is interesting to notice that temperature and pressure maintain their rate of change after the throttling point, whereas velocity changes drastically between regimes.

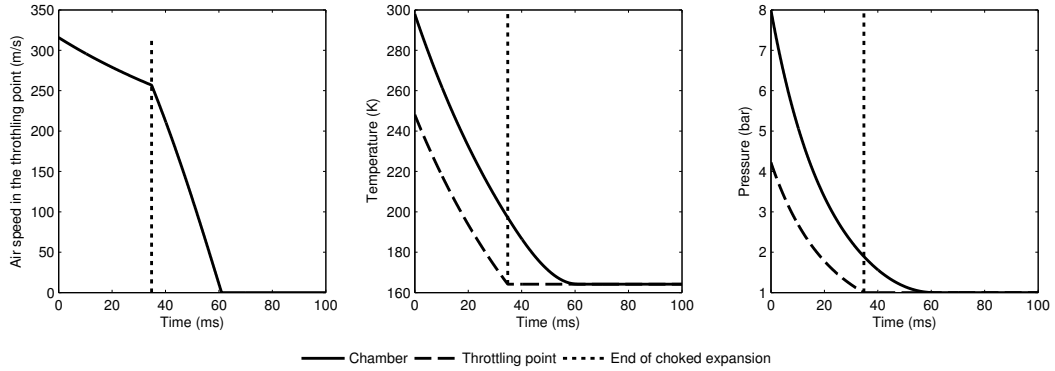

Figure 3.7. Behaviour of speed, pressure and temperature for the isentropic decompression of air in a 50 mL chamber throught an orifice with a 3.23 mm diameter, with intial pressure of 8 bar. The end of the choked expansion happens at 35 whereas the whole expansion finishes after 61 ms

3.3.2. Drag and Gravitational Forces Acting on a Particle

During the whole air expansion, the air leaving the chamber drags the powder deposited at the bottom of the `Translucent Square Tube`. At the same time gravity, as well as buoyancy forces, act on the particles in opposite directions. Therefore, studying the interaction of gravitational, drag and buoyancy forces on the particles allows to estimate the behaviour of particles during the dispersion. In particular, a spherical particle with diameter D and density ρ_p immersed in a fluid with density ρ_g is subjected to the three previously mentioned forces that can be expressed as follows:

- Gravitational force $m_\mathrm{p} g$
- Buoyancy force exerted by the fluid $m_\mathrm{p} g \left(\frac{\rho_\mathrm{g}}{\rho_\mathrm{p}}\right)$
- Drag force that is caused by the velocity difference v_p between the fluid (g) and the particle (p) $C_D {v_\mathrm{p}}^2 A_\mathrm{p} \rho_\mathrm{g}/2$, where A_p is the area of the particle projected on a surface perpendicular to its displacement and C_D is the drag coefficient.

Due to the small size of the particles, it can be considered that the drag forces are so strong with regard to gravity that the particles travel at speeds close to that of the fluid transporting them. This means that the Reynolds number of the fluid around the particle is actually quite small (not greater than 10^2) when the particle is the point of reference. Consequently by assuming that the particles are smooth and spherical, C_D can be estimated with $24Re^{-1}$ (Munson, 2009). Therefore an expression for the acceleration of the particle relative to the movement of the surrounding fluid can be defined as:

$$\frac{\partial v_\mathrm{p}}{\partial t} = -\frac{18\mu_\mathrm{g}}{\rho_\mathrm{p} {d_\mathrm{p}}^2} v_\mathrm{p} - g\frac{\rho_\mathrm{p} - \rho_\mathrm{g}}{\rho_\mathrm{p}}$$

That can be integrated through:

$$\int_{v_0}^{v_\mathrm{p}(t)} \left(\frac{1}{v_\mathrm{p}+\sigma_\mathrm{p}}\right) \mathrm{d}v_\mathrm{p} = -\frac{t}{\tau_\mathrm{p}} \tag{3.21}$$

where σ_p is the terminal velocity of the particle in the fluid, defined by:

$$\sigma_\mathrm{p} = \sqrt{\frac{gD^2\left(\rho_\mathrm{p}-\rho_\mathrm{g}\right)}{18\mu_\mathrm{g}}} \tag{3.22}$$

with τ_p the characteristic time for particle settling:

$$\tau_\mathrm{p} = \frac{\rho_\mathrm{p} D^2}{18\mu_\mathrm{g}} \tag{3.23}$$

The result of this integration is described by **Equation 3.24**, that represents the time behaviour of the movement of a particle with a relative velocity v_p:

$$v_\mathrm{p}\left(t\right) = \left(\sigma_\mathrm{p}+v_0\right)\exp\left(-\frac{t}{\tau_\mathrm{p}}\right) - \sigma_\mathrm{p} \tag{3.24}$$

At this point a model for the behaviour in time of v_p can be developed by putting **Equations 3.11**, **3.20** and **3.24** together. The purpose of doing so, is to provide a compelling model for the vertical velocity of dust particles inside the `Translucent Square tube` at different times. This model is to be used in the estimation of turbulence intensity by PIV, since the values of the mean velocity are required as will be further explained in the following section.

3.4. On the Terminology of Turbulence

The characterization of turbulence is often done through the analysis of the fluctuations of velocity from its mean value. While this concept is the one used by all of the studies presented in the introduction of this chapter (among many others), there doesn't seem to be an agreement on the terminology used to describe turbulent flows. This means that different authors use the same terms and symbols to refer to variables that being conceptually similar, are not exactly the same. For this reason a brief description of the terminology used in this document, to refer to turbulence related concepts, is developed next.

Consider the fixed point **P** in **Figure 3.8(a)**. As a turbulent flow travels in the right direction, velocity changes both in magnitude and direction. If the flow is stationary, and the horizontal component of velocity was to be measured at point **P**, one would probably see the horizontal component of velocity behave as the dashed line in **Figure 3.8(b)**. Furthermore, if the mean horizontal velocity $\overline{u}$ is calculated over time (t):

$$\overline{u} = \frac{1}{t}\int_0^t u(t)\mathrm{d}t \tag{3.25}$$

then the horizontal velocity could be expressed in terms of the mean and the velocity

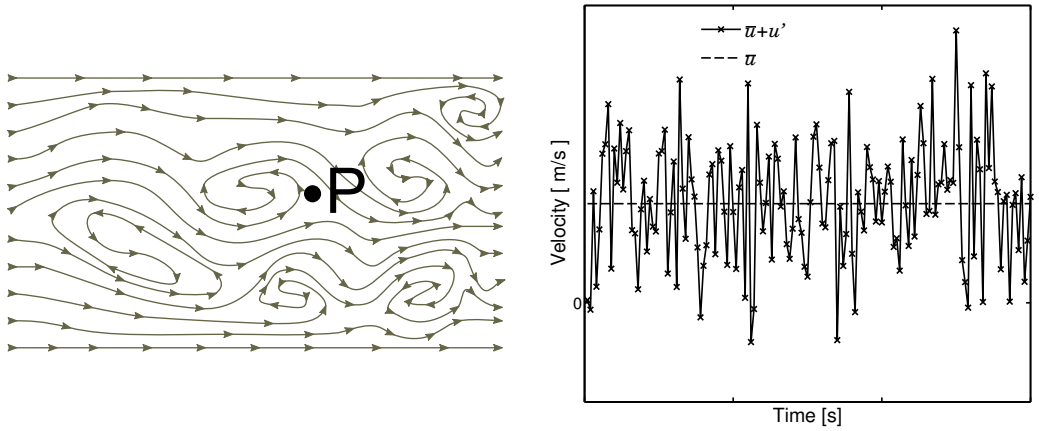

(a) Representation of a turbulent stream (b) Behaviour of velocity at point **P** in (a)

Figure 3.8. Representation of the behaviour of the velocity in a fixed point of a turbulent stream. Velocity is represented in (b) with the solid crossed line and is composed of its mean value $\overline{u}$ (pointed line) and the velocity fluctuations u'.

fluctuations u' as:

$$u(t) = \overline{u} + u'(t) \tag{3.26}$$

This implies that as long as the stream is laminar, values for u' remain zero because there are no deviations from $\overline{u}$. On the other hand, as the speed of the fluid increases and the flow transits to a turbulent regime, the magnitude of u' would vary more rapidly and strongly both in the positive and negative direction. Meaning that strong variations of u' respond to a more turbulent flow. Thus the *root-mean-square of the turbulent velocity fluctuation* (RMS) becomes an estimator of the turbulence of a current and for a stationary system is defined by:

$$u'_{\text{rms}} = \sqrt{\frac{1}{t}\int_0^t [u'(\tau)]^2 \mathrm{d}\tau} \tag{3.27}$$

Given that u'_{rms} is somehow one kind of mean of the absolute value of u', it is conceptually easy to understand and therefore widely used to describe turbulent flows. Nevertheless, it is sometimes also called *Turbulence intensity*, which in this text is a term used for a different quantity, although they are somehow related. Turbulence intensity (I_t) is a dimensionless quantity that considers that turbulence is a three-dimensional phenomenon as can be seen in **Equation 3.28** where v and w are orthogonal homologous of u.

$$I_t = \frac{\sqrt{[u'_{\text{rms}}]^2 + [v'_{\text{rms}}]^2 + [w'_{\text{rms}}]^2}}{\sqrt{\overline{u}^2 + \overline{v}^2 + \overline{w}^2}} \tag{3.28}$$

So far, the definition of turbulence related variables has been based on the as-

sumption of a system in steady state. This is specially evident in the definitions presented for mean terms of turbulence in **Equations 3.25** and **3.27**. Since, a steady state situation is clearly not consistent with the case considered in this chapter; different definitions, for non-steady systems, have to be provided. To do so, it is necessary to consider the time behaviour of velocity at the same point(s). This requires to perform n repetitions to quantify the mean value of velocity at the same spatial and temporal coordinates, thus replacing **Equations 3.25** and **3.27** with:

$$\overline{u}(t) = \frac{1}{n}\sum_{i=1}^{n} u_i(t) \tag{3.29}$$

and

$$u'_{\text{rms}}(t) = \sqrt{\frac{1}{n}\sum_{i=1}^{n}[u'_i(t)]^2} \tag{3.30}$$

3.4.1. Estimation of Mean Vertical Velocity

As discussed on page 90, one of the limitations of the experimental setup used for the PIV analysis is that the dust dispersion and PIV systems are not coupled. **Equations 3.29** and **3.30** help to better explain why is it a limitation: since the setup does not allow to coordinate the times at which the dust dispersion and the laser are initialized, there is no way to assure that the PIV analysis is done at the same time lapses after dispersion. Thus i order to be able to use **Equations 3.29** and **3.30** one would have to perform extensive repetitions so that the laser pulses coincide with post-dispersion times very often. Unfortunately with the laser pulsing at a maximum of 15 Hz the probabilities of this happening repeatedly are not high. Moreover, the number of replicates mentioned in **Table 3.1** do not allow for more than 2 or 3 coincidences in a lapse of 1 ms. Instead, the need to have aleatory repetitions at precise time intervals for the estimation of $\overline{v}$, was avoided by including the analysis of **Section 3.3** in page 92. Hence $\overline{u}(t)$ is estimated through a regression of the modelled velocity of the particles with the experimental values.

Consequently, two phenomena are considered for the estimation of $\overline{v}$. First of all, the expansion of the pressurized chamber is accounted with either **Equation 3.11** or **3.20** (through numerical integration) depending on whether the expansion is in sonic or subsonic regime. The time lapse defining the limit between both regimes, can be identified with **Equation 3.15**. However, the equations for the expansion of the pressurized chamber cannot be used directly to calculate the speed of air in the `Translucent Tube`. The change of area of the transition between the orifice (**b**) and the tube (**c**), has to be accounted. This is done, by considering the conservation of mass as presented in **Equation 3.31**.

$$v_c = \left(\frac{P_b}{P_c}\right)^{\frac{1}{\gamma}} \frac{A_b}{A_c} v_b \tag{3.31}$$

On the one hand, the sedimentation of the particles, driven by gravity and restricted by drag and buoyancy forces is considered with **Equation 3.24**. The equations relating these two phenomena were put together in a Matlab function

to simplify the calculations that are described in the annexes (see Matlab function `chamberexpansion.m` in page **??**).

On the other hand, during the first moment of the expansion, the air leaving the chamber gives an initial push to the dust at the bottom of the tube. Depending on the mass of the particles the energy gain from that initial push could maintain some inertia. That push translates into the initial velocity v_0 of **Equation 3.24**. Nevertheless for *light* particles, this parameter may be irrelevant. This is because this particles cannot achieve enough momentum to considerably deviate from the initial values velocity of the gas flow. For the cases where the sedimentation velocity as well as the initial velocity v_0 are important, this value can be estimated through a regression of the experimental data of obtain from PIV analysis. In fact another parameter that is relevant for either case, that can also be obtained from a regression of data is the friction coefficient $C_\circ$. The equation accounting for $\overline{v}$ in vertical direction is expressed in **Equation 3.32** as a function of time and the unknown parameters v_0 and $C_\circ$.

$$\overline{v}(t, C_\circ, v_0) = v_c(C_\circ, t) + v_\mathrm{p}(v_0, t) \tag{3.32}$$

The Matlab implementation of this function, `VelocityParticule.m`, can be found in page **??** followed by the function for the regression of data `getFit4V.m`.

3.5. Particle Image Velocimetry Analysis

As mentioned in **Section 3.1.1** in page 87, PIV works by illuminating with a laser sheet a moving fluid containing small particles that move with the flow and reflect the light induced. Two pictures of the moving fluid are taken in a short period of time. These pictures are then analysed by an algorithm that returns a matrix containing the horizontal and vertical velocities u and v with their corresponding coordinates x and y for multiple points on the area analysed. This information allows to build velocity vector fields like the ones presented in **Figure 3.9**. In this figure, three different dispersions of 78 mg of wheat starch are presented and separated by column.

It can be seen, that the time interval separating the vector fields is 66.67 ms, which corresponds to the limits imposed by the equipment. Nevertheless, the evolution of the degree of movement seems to be comparable from one dispersion to the other. However, statistically relevant data can be obtained by doing multiple repetitions. For the case of dust starch, 70 repetitions were performed for each of the masses considered and only 20 were done for the case of glass beads (as described on **Table 3.1**). A total of 510 velocity vector fields were obtained for each of the masses of wheat starch considered and 80 for the glass beads, as the time studied was shorter in that case.

The information of the velocity vector fields was grouped for each mass of each component and mean values for vertical and horizontal velocities were calculated. These values are represented with + on **Figure 3.10** where the colours allow to visualise the frequency of the raw data and its dispersion from the mean. For the vertical velocity the mean values for each velocity field were used to make a regression of data to the model synthesised by **Equation 3.32**. The result of the

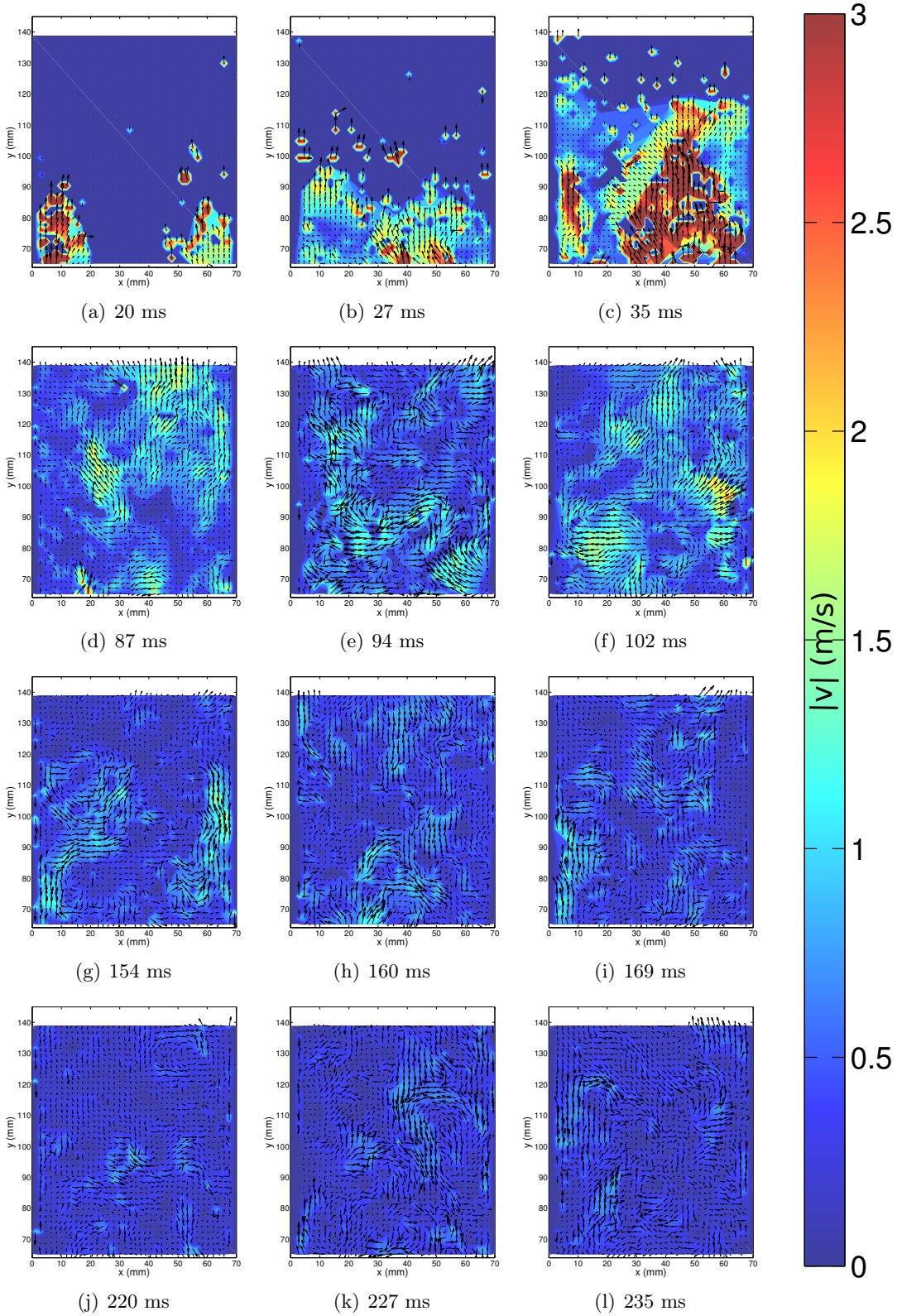

(a) 20 ms (b) 27 ms (c) 35 ms

(d) 87 ms (e) 94 ms (f) 102 ms

(g) 154 ms (h) 160 ms (i) 169 ms

(j) 220 ms (k) 227 ms (l) 235 ms

Figure 3.9. Velocity vector fields for the PIV analysis of 78 mg of wheat starch. Results from a same dust dispersion are grouped in columns.

Table 3.3. Summary parameters for data regression on the model of mean vertical velocity of particles dispersed by an air current (**Equation 3.32**)

	Glass beads 5 g	**Starch 78 mg**	**Starch 319 mg**
$C_\circ$	0.171	0.385	0.378
(Lower Bound)	0.157	0.374	0.367
(Upper Bound)	0.186	0.397	0.389
u_0 (m/s)	2.846	0	0
(Lower Bound)	2.661	-	-
(Upper Bound)	3.031	-	-
r^2	0.980	0.947	0.927
τ_{choked} (s)	0.885	0.393	0.401
τ_{p} (s)	5.406×10^{-2}	8.955×10^{-4}	8.955×10^{-4}
σ_{p} (m/s)	5.301×10^{-1}	8.764×10^{-3}	8.764×10^{-3}
v_{choked_0} (m/s)	315.8	315.8	315.8
v^*_{choked} (m/s)	256.9	256.9	256.9
t_{sonic} (s)	0.203	0.090	0.092
t_{subsonic} (s)	0.356	0.158	0.161

data regression is represented by a solid black line in **Figure 3.10** and its summary is presented in **Table 3.3**.

One of the first things that can be observed by comparing the results for glass and starch is that the part of the model accounting for sedimentation plays almost no role for the analysis on starch which is clearly not the case for glass beads. The main reason for this behaviour can be understood by considering difference of the terminal velocities σ_{p} between both dusts: $53\,\frac{\text{cm}}{\text{s}}$ vs $0.88\,\frac{\text{cm}}{\text{s}}$. In fact, the terminal velocity of the starch particles studied, is two orders of magnitude below the values of air speed. This explains why, for the case of starch the velocity of the particles apparently converges to zero.

For the glass beads on the contrary, not only σ_{p} is in the order of magnitude of the speed of air, but even the initial velocity is considerably high. It is in fact so high that it is almost 5 or 6 times, greater than the terminal velocity. Furthermore it doubles the initial velocity of air in the tube. This could mean that for the particles the air is moving downwards(towards them) at the same speed the air is moving upwards. This might be questionable since the air could not travel at such speed inside the tube. But that is the speed of air travelling in a tube with cross-area of $49\,\text{cm}^2$. Whereas the air gives the initial energy to the dust at a transition point for air from a very small area to one that is not yet the full area of the tube. Moreover, the friction between the steel of the dispersion cup and the glass beads is minimal, which may translate in the development of really high initial velocities for the glass. Furthermore, the drag coefficient C_D is inversely proportional to the diameter of the spheres and the difference of speed between the air and the particles. This means that the force resisting to the movement of the particles is not that strong, specially at the beginning of the dispersion because of the high velocity acquired initially and the big size of the particles that together with the high density of glass accounts for

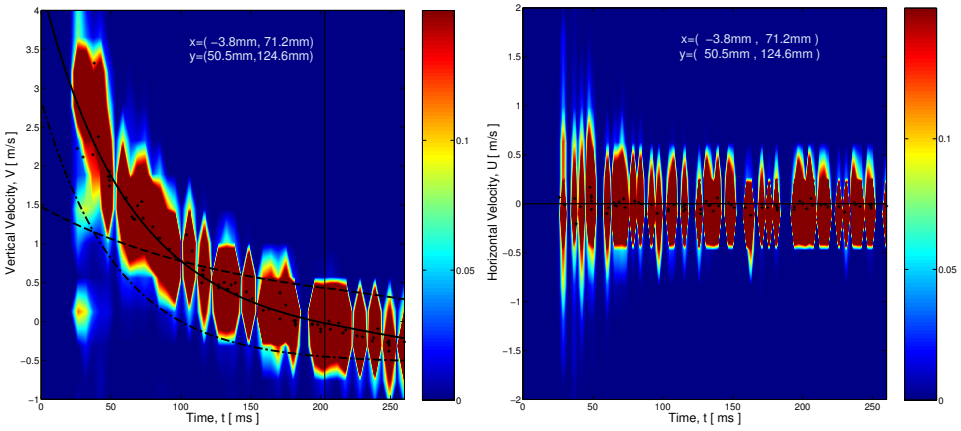

(a) 5 g of glass beads

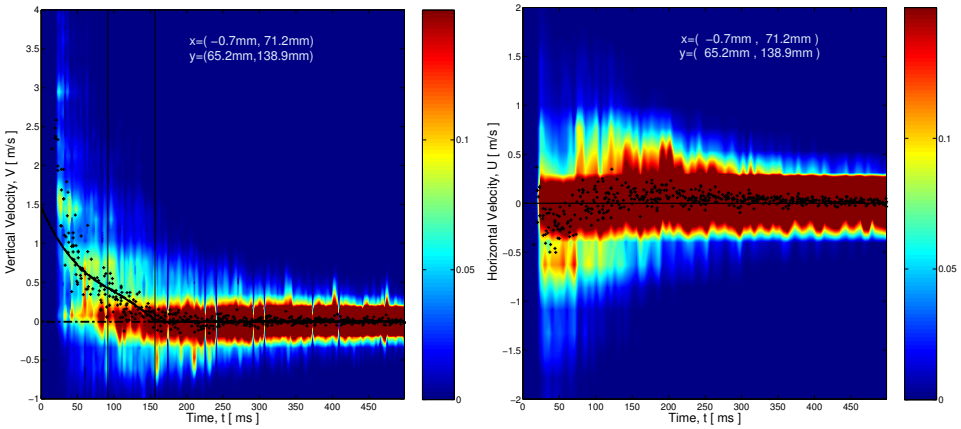

(b) 78mg of wheat starch

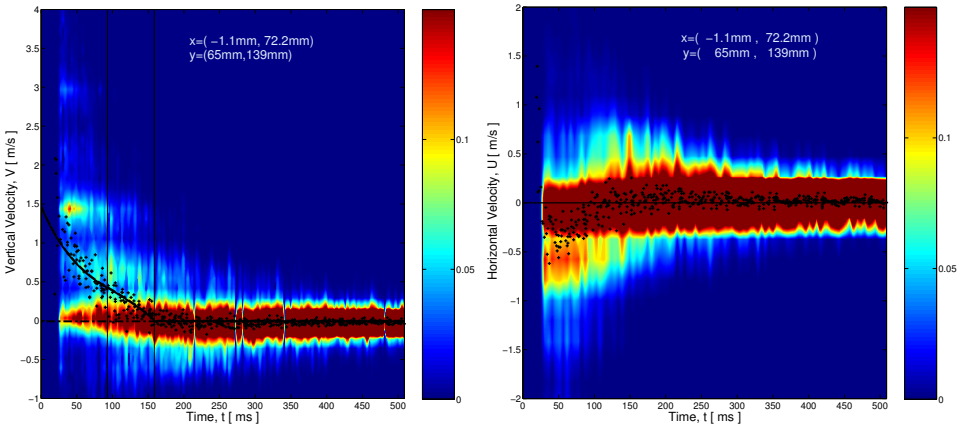

(c) 319mg of wheat starch

Figure 3.10. Behaviour of the vertical (left) and horizontal (right) velocity of particles according to the PIV analysis on 5mg of glass beads, 78 mg and 319 mg of wheat starch. The two vertical solid lines represent the end of the sonic and subsonic expansion. The mean values of the horizontal and vertical components of a single velocity field are represented with +. The solid thick line represents the model for aproximating the mean values that is the sum of the velocity of air (--) and the speed of sedimenting particles relative to the movement of air (-·-)

great inertia.

Paradoxically, it would be expected for the value of $C_\circ$ to be similar for all the cases, as this parameter is intrinsic to the equipment and not to the dust, but this is not what **Table 3.3** shows. While this is the case for both dispersions of starch, for the glass beads $C_\circ$ is less than a half (0.171) of the one estimated with starch (~ 0.38). Although there is a considerable difference in the number of repetitions performed for each dust, it does not seem plausible for this to be the reason. In fact the data for glass are not scattered as those of starch and they actually seem to converge. A better explanation seems be a difference variation of the length of the conduct used to connect the Mike apparatus to the vertical tube in between experiments.

Continuing the analysis of **Figure 3.10**, but now looking at the plots for horizontal velocity something appears once again to oppose the expectations. For starch dispersions, the initial values of the horizontal velocity seems to be mostly negative although they are expected to have an average value of 0. This could be explained because of the position of the light necessary to recognise the dispersion time with `camera 2`. This light may have influenced the results by saturating the pictures of the PIV analysis, thus complicating the recognition of the moving particles. Once that the mean values for velocity are estimated the analysis can then be focused on turbulence. **Figure 3.11** presents some results of turbulence intensity for various times with a spatial grid of 30×30 and time intervals of 5 ms. There are some intervals of time, particularly around 60, 121 and 180 ms where considerable differences in the turbulence intensity can be observed between the lower and the higher portions of the tube. These differences may be best appreciated in **Figure 3.12** where at initial times of dispersion, particularly between 50 and 100 ms the turbulence intensity at the bottom may sometimes double that at the top. This a particularity of this equipment that may be relevant in the analysis of flame propagation.

The results presented here show that for starch, the turbulence intensity starts the homogenize sometime after 150 ms, which is very close to the calculated time for the end of the dispersion. This is actually very logical since is the air expansion the one responsible for most if not all of the turbulence. In contrast, with the glass beads the little effect air can have on the falling glass, does not permit these big heavy particles to trace the turbulence in the flows as they are not very sensitive to it.

These results and the corresponding analysis show that particles with low terminal velocities σ_p, as is the case for starch, will usually follow the movement of the fluid. This means that the results presented here could be used for the analysis of different dusts who share the same property as long as they are used in similar equipment. The modified Hartmann tube for instance.

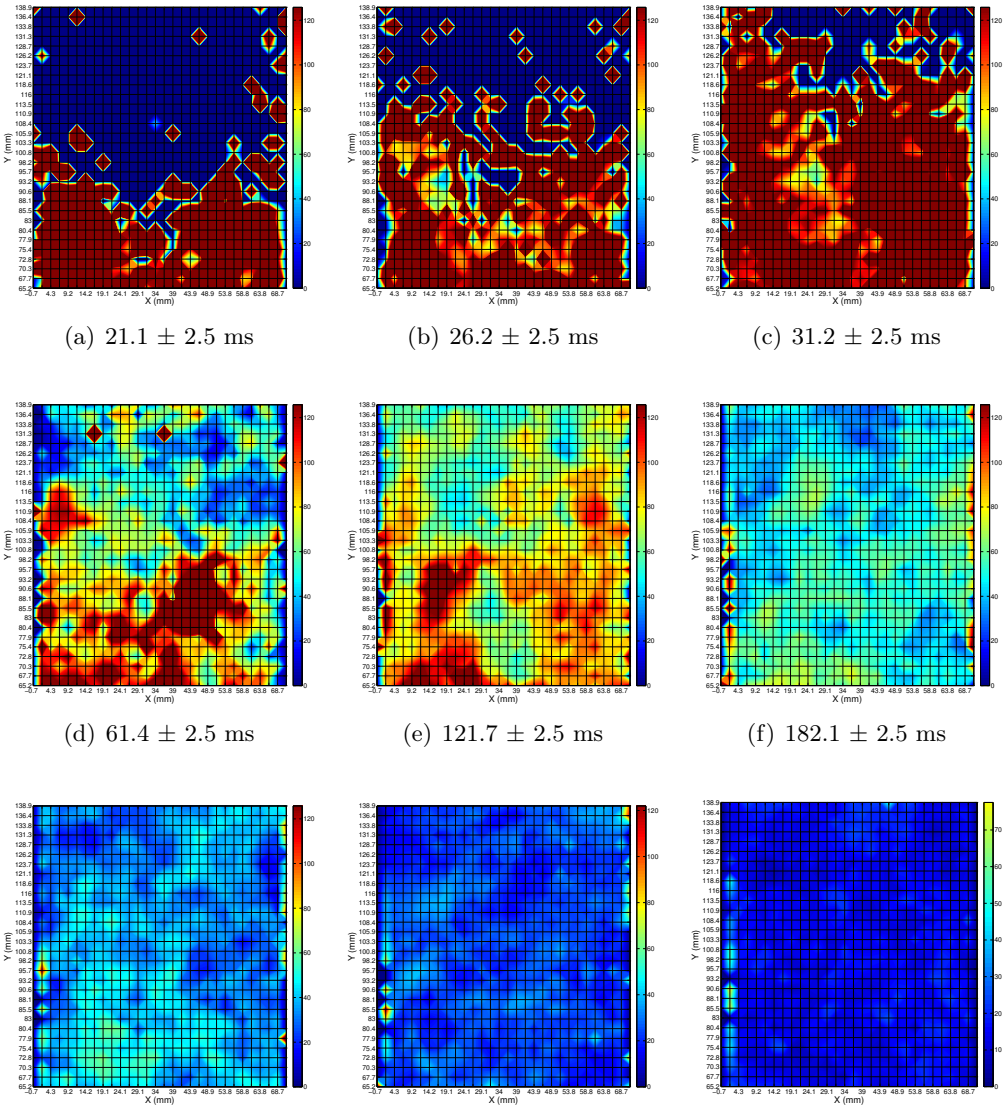

(a) 21.1 ± 2.5 ms (b) 26.2 ± 2.5 ms (c) 31.2 ± 2.5 ms

(d) 61.4 ± 2.5 ms (e) 121.7 ± 2.5 ms (f) 182.1 ± 2.5 ms

(g) 242.5 ± 2.5 ms (h) 302.8 ± 2.5 ms (i) 499 ± 2.5 ms

Figure 3.11. Turbulence intensity map for different times

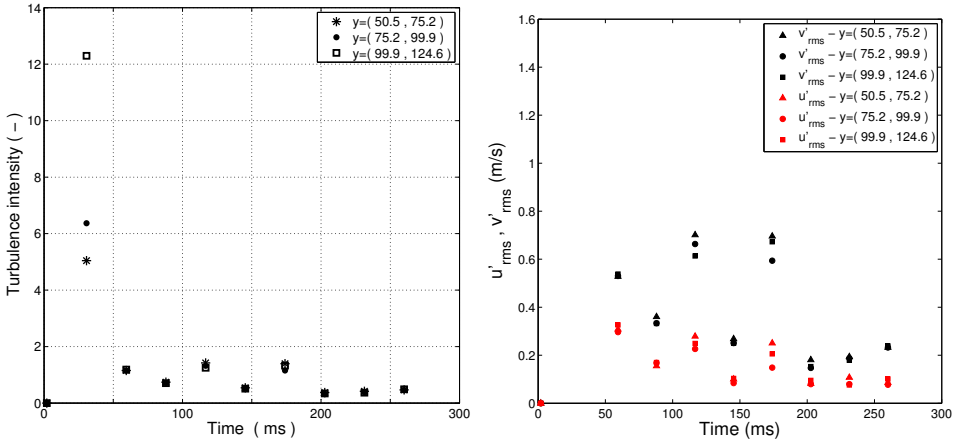

(a) Glass beads 5 g

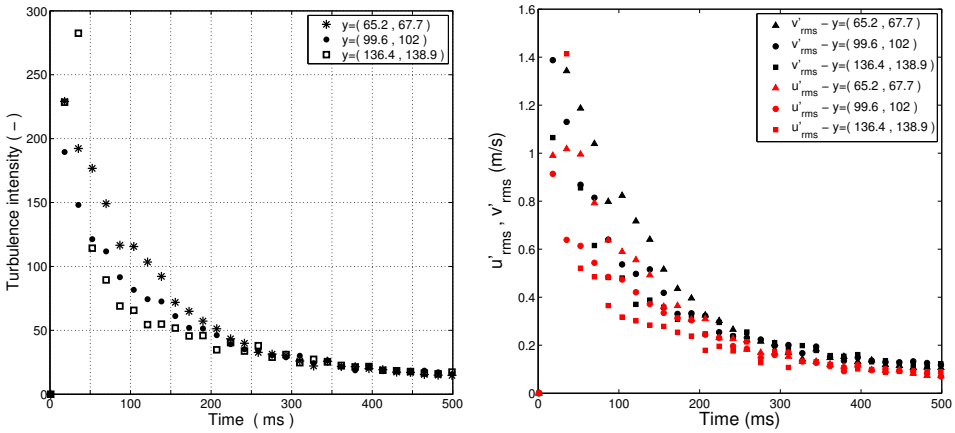

(b) Starch 78 mg

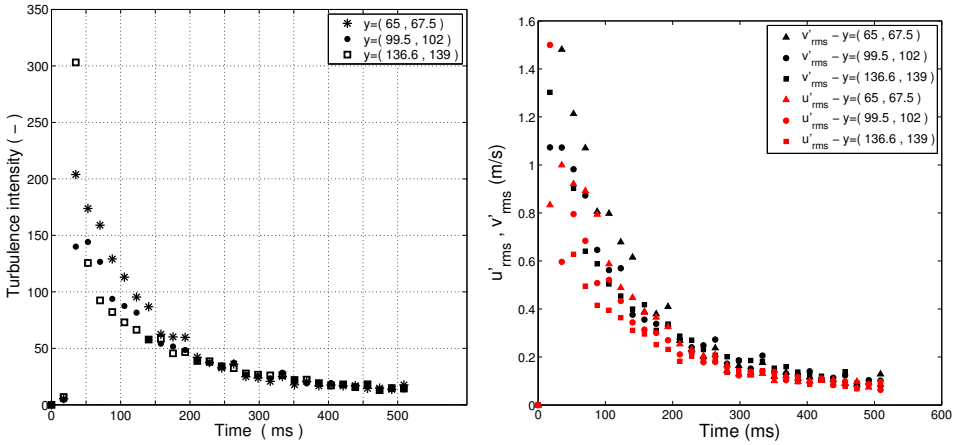

(c) Starch 319 mg

Figure 3.12. Behaviour of turbulence intensity (left) and root-mean-square velocities (right) in time for different heights.

RÉSUMÉ

Quantification de la turbulence générée lors de la dispersion de la poussière avant explosion

L'objectif dans de ce chapitre est de quantifier la turbulence causée par la dispersion d'un nuage de poussière par un pulse d'air comprimé à l'intérieur d'un tube carré vertical. Les dimensions du tube sont choisies de manière à ressembler à celles du tube de Hartmann modifié qui est utilisé pour la détermination de l'énergie minimale d'inflammation (EMI) de nuages de poudres. Par ailleurs, les dimensions du tube permettent également de recréer les conditions à l'intérieur du tube de propagation de flamme utilisé ultérieurement. Le dispositif expérimental est composé de 2 systèmes indépendants : le premier dédié à la commande des équipements liés à vélocimétrie par image de particules (PIV), le second dédié à la dispersion de la poussière à l'intérieur du tube, ainsi qu'une caméra à haut vitesse utilisée pour vérifier le moment de la dispersion de la poussière.

Ce chapitre décrit d'un point de vue théorique, le comportement de la vitesse de l'air sortant d'une chambre sous pression à travers un orifice lors de la phase de dispersion et son interaction avec la poussière pendant et après l'expansion du gaz. La façon dont la poussière est dispersée avec l'appareil de Hartmann modifié correspond assez bien au cas typique d'une fuite de gaz depuis une chambre sous pression à travers un orifice. Les modèles utilisés pour ce genre de situation supposent que cette expansion est isentropique. La vitesse de sortie dépend donc de la différence de pression entre l'intérieur et l'extérieur de la chambre (P_a et P_c respectivement) ainsi que de la pression à l'étranglement P_{choked}, définie en termes du ratio de capacités calorifiques. Si la pression à l'étranglement est supérieure à la pression extérieure ( ), le débit est maximal et indépendant de la pression extérieure (P_c). Cette restriction thermodynamique est due à la vitesse à laquelle une onde de pression peut se déplacer dans un milieu fluide. Elle est définie par un nombre de Mach égal à 1 (écoulement sonique). Par conséquent, ce type de flux est appelé sonique ou étranglée et la vitesse limitante du son, sera appelée ici v_{choked}. D'autre part, quand P_{choked} est inférieure à la pression extérieure, la pression au point d'étranglement sera proche de la pression externe et le système serait en régime subsonique. La vitesse peut alors être estimée avec un bilan énergétique pour une surface perpendiculaire à l'écoulement entre l'intérieur de la chambre et le point d'étranglement.

L'analyse développée dans ce chapitre, permet ainsi de prédire la pression, la température et la vitesse du gaz dans la chambre, le point d'étranglement et à

l'extérieur pendant les régimes sonique et subsonique de l'expansion. La vitesse extérieure est alors utilisée pour faire un bilan des forces de traînée, gravitationnelle et de flottabilité sur les particules dispersées, ce qui permet d'estimer leur vitesse verticale moyenne et de quantifier expérimentalement la turbulence à l'intérieur du tube lors de la dispersion de particules d'amidon et de verre.

En parallèle, l'étude expérimentale de l'hydrodynamique des particules dans un tube de propagation de flamme (de base et de système de dispersion similaires au tube de Hartmann modifié) a été conduite. Le montage expérimental est constitué d'un système de vélocimétrie à image de particules (PIV), d'une caméra ultra-rapide et d'un granulomètre laser in situ permettant de quantifier l'homogénéité du nuage et la distribution de taille de particules en fonction du temps. A l'aide de la PIV, la valeur efficace rms et l'intensité de la turbulence ont été déterminées lors d'une dispersion. En ce qui concerne la composante horizontale de la vitesse, sa valeur moyenne est constante et proche de zero (**Figure 3.10**, page 104). L'intensité de la turbulence varie grandement entre 50 ms et 250 ms (50 ms étant le temps moyen à partir duquel le nuage de poussière atteint la zone de mesure à hauteur de la source d'inflammation). Entre 50 et 120 ms, l'intensité des fluctuations de vitesse verticale restent très importante, ce qui traduit une turbulence intense mais conduit également à une faible reproductibilité des tests d'inflammation réalisés à ces temps. A partir de 130-150 ms, l'intensité de la turbulence qui a faiblit sensiblement se stabilise. La sédimentation des particules devient le phénomène prépondérant ce qui se traduit par une ségrégation progressive des fines et des grosses particules. Pour des nuages fortement concentrés (ce qui permet d'atteindre la CME malgré la sédimentation), cette zone peut être propice à l'inflammation de fines poussières et donc conduire à des valeurs d'EMI plus faibles et plus reproductibles.

Les résultats montrent que des particules avec de faibles vitesses terminales, comme c'est le cas pour l'amidon (de diamètre inférieur à 30 µm) suivront généralement le mouvement du fluide. Cela signifie également que les résultats présentés ici pourraient être utilisés pour l'analyse des différentes poussières qui partagent la même propriété tant qu'ils sont utilisés dans des équipements similaires : le tube de Hartmann modifié par exemple. Cette analyse permettra de choisir les meilleures conditions de tests : soient les plus reproductibles, soient les plus conservatives (ce qui ne correspond pas toujours aux mêmes paramètres de tests).

Chapter 4

Flame Propagation in a Vertical Tube

Contents

4.1. Introduction

Predicting the flame propagation during a dust explosion in complex geometries is still a challenge that mobilizes numerous technical, computational and human resources. A perfect knowledge of dust explosion mechanisms would be necessary to propose a fully predictive approach; but it should be carried out by taking into account the specific properties of each combustible powder, which is time consuming if not illusory. Another approach consists of determining experimentally the inherent characteristics of dust-air mixtures (such as the laminar flame speed) and using them as an input for Computational Fluid Dynamics simulation programs. But if the experimental characterization of the burning rates of gases from flame front speed is still delicate, it is considered as "one of the most complicated combustion process to be studied" when dealing with turbulent dust-air suspensions (Skjöld, 2003).

Such goal has been pursued for many years, starting with the characterization of the burning velocity of gas/air mixtures. The first estimation of a burning rate has been performed by Davy in 1815 on a methane flame. Soon experimental approaches such as the burner method and the tube method have been developed by scientists such as Bunsen or Mallard and Le Chatelier. The measurement principles of the flame speed were mainly based on the quantification of the volume flow rate of the gas-air mixture. The influence of the flame surface and, consequently, of flame stretching was first studied by Gouy in 1879 (taylor, 1991). It was only 50 years later that a new approach was proposed by Stevens: the contained explosion method. Nowadays, these three methods for measuring the laminar burning velocity of fuel-air mixtures are still used and have been also implemented for dust-air flames: burner method (Cassel, 1964; Dahoe et al., 2002; Goroshin et al., 1996), contained explosions method (Huéscar Medina et al., 2015; Skjöld, 2003; Van der Wel, 1993) or tube method (Proust and Veyssiere, 1988; Proust, 2006b; Schneider, 2006; Schneider and Proust, 2007; Wang et al., 2006a). Few works have been also devoted to the study of the flame propagation of hybrid mixtures. Bradley et al. (1989) and Bradley et al. (1994) studied the laminar burning velocities of methane-air-graphite mixtures and of fine coal dusts by using a burner. They notably underlined that the presence of the powder does not change the gas phase composition and kinetics during the combustion step. Liu et al. (2007) and Chen et al. (2008) studied the flame propagation of coal dust and methane in a vertical combustion vessel to measure the flame speed. They observed that the presence of methane, even at concentration lower than lower explosivity limit, increases the flame speed and the flame front temperature. They also showed some kind of decoupling between gas and dust combustion: in a first step, a feeble light due to methane combustion, was observed and only subsequently the coal dust starts participating.

However, if numerous studies have already been carried out, the large scatter in the experimental data collected by using the previous methods shows that determining the burning velocity of dust-air mixtures from the observation of flame front propagation is still delicate. Indeed, such issues are notably due to the variability of powders properties (particle size distribution, moisture...), the physical impossibility to generate a quiescent dust cloud, the impact of powder on the flame radiation. The latter consideration can probably be neglected when dealing with small or-

ganic particles for which the rate-limiting mechanism is generally the combustion of volatiles. Nevertheless, it is not the case for metal particle. Moreover, for Nusselt flames, i.e. when the combustion is limited by the oxygen diffusion at the surface of the particles (heterogeneous combustion such as for graphite or refractory metals), the residence time of powders head from the flame is not negligible and the flame deformation due to their presence should be taken into account.

As a consequence, the ultimate goal of this work was to develop an approach to assess fundamental flame propagation properties, not only from closed vessel experiments and pressure-time evolution curves, but from the analysis of the flame velocity as a function of its stretching and of the hydrodynamic instabilities. As previously shown, in a first step, the turbulence of the initial dust cloud and its potential effect on the powder ignition has been studied. The impact of the pyrolysis phase on organic dusts explosion has also been highlighted. In a logical way, the explosive behavior of gas-dusts hybrid mixtures composed of pyrolysis gases and organic dusts has been analyzed. Now, it is time to consider the turbulence/combustion interactions during the flame propagation in order to extract the "pseudo" laminar flame velocity of dust or hybrid mixtures.

4.2. Study on flame propagation

During Khalili (2012) and Garcia-Agreda (2010) doctoral works, they started the development of a technique that would allow to estimate the fundamental flame

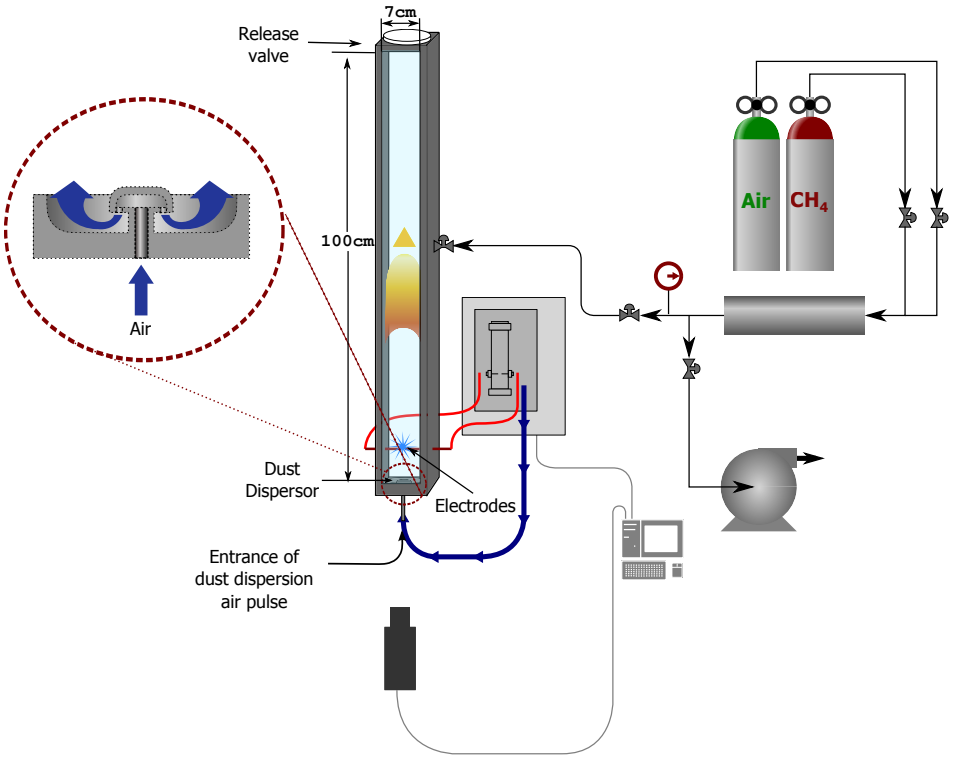

Figure 4.1. Equipment for flame propagation measurements

speed of gases, dusts and their hybrid mixtures. In the present work the technique was standarized to reduce the variations in the experimental conditions. The technique consists in analysing videos of flames propagating inside a vertical tube as the one depicted in **Figure 4.1**. The Mike apparatus used in **Chapter 3** for the analysis of turbulence inside a $7\,\text{cm} \times 7\,\text{cm} \times 40\,\text{cm}$ tube is connected in this case to a $7\,\text{cm} \times 7\,\text{cm} \times 100\,\text{cm}$ tube capable of enduring low pressure explosions. A steel cylinder allows to premix air with a combustible gas before introducing it inside the tube. The Mike apparatus is then used to disperse the dust and ignite an explosion. A high speed camera records the propagation of the flame and the resulting video is then analysed to deduce characteristic parameters of the of the mixture's combustion.

In this work a digital tool was developed to automatize the analysis of the videos. This would in principle facilitate the process while reducing human fallibility. The improvement of the technique helps to extend the availability of data by both the augmentation of the video frames that can be now analysed and also by allowing to analyse more videos in less time. Furthermore, this work also aims to reduce the inaccuracy inherent to the technique that previously approximated the surface of any flame to that of an ellipsoid using three extreme points of the flame front.

4.2.1. Estimation of unstretched burning velocity

For flat flames, the velocity of propagation equates with burning velocity, but the flames inside a tube do not propagate as such. Therefore it is necessary to consider the deformation of the flame. According to Andrews and Bradley (1972b) the ratio between the spatial velocity of the flame S_s and the burning velocity S_u, equals the ratio between the surface of the flame front A_f and the of the projection of the flame on a plane perpendicular to its displacement A_s as expressed by **Equation 4.1**:

$$S_u = S_s \frac{A_s}{Af} \tag{4.1}$$

This equation allows to estimate the burning velocity of a flame propagating inside a tube with one closed extreme and the ignition point a the located on the open side one. The conditions of validity are the following ones:

- S_u is constant over the whole surface of the flame.
- The spatial velocity S_s is uniform over the whole surface of the flame.
- The thickness of the flame is small in comparison to the curvature of the flame.

4.2.1.1. The effect of thermal expansion

The ignition point of the tube used in this study is placed on the closed side of the tube. Consequently the reactives are persecuted by the flame that is being pushed up by the hot burnt gases that act as a piston due to their thermal expansion as they leave the flame. Therefore a correction factor for the thermal expansion χ has to be included in **Equation 4.1**:

$$S_u = \frac{S_s}{\chi}\frac{A_s}{Af} \tag{4.2}$$

where the expansion coefficient can be approximated as:

$$\chi \approx \frac{\rho_\mathrm{u}}{\rho_\mathrm{b}} = \frac{T_\mathrm{b}}{T_\mathrm{u}} \tag{4.3}$$

with subindexes $_\mathrm{b}$ and $_\mathrm{u}$ meaning burned and unburned gases respectively. At this point another hypothesis is done to approximate the T_b with the adiabatic temperature for the mixture $T_\mathrm{ad}|_V$ that is calculated in this work with the CEA software[1].

4.2.1.2. The effect of stretching

The structure of a flame front propagating in a non uniform flow can be modified either by the influence of the on the reaction zone (stretching effect), or by the flame itself due to the effect of the dilatation of the gas (influence of the curvature). Landau (1944) showed that flames are always stretched to some degree at the scale of its thickness. Indeed, a flat flame is intrinsically unstable and tends to be deformed. The same insight was also formulated by Markstein (1964) while incorporating the effects of curvature of the reaction zones on the flame front. The reaction zone will consequently be deformed and modify the chemical reaction as well.

The rate of change of the surface determines its stretching K ($\frac{1}{\mathrm{s}}$) and was defined by Karlovitz et al. (1951) as:

$$K = \frac{1}{A_f}\frac{\mathrm{d}A_f}{\mathrm{d}t} \tag{4.4}$$

The stretching characterises the rate of change of the surface of the flame and its sign indicates the expansion or compression of the surface. This stretching can be decoupled in two different variables according to whether it is caused by the curvature K_c or the flow K_s. (Bradley et al., 1996; Bradley et al., 1998). Here it was considered that the stretching is mainly a hydrodynamic phenomenon, but it might be worthwhile to explore the significance of the disregarded one.

Clavin (1985) and Markstein (1964) stablished a relation between the flame's burning velocity S_u, the stretching K and the markstein length δ_M:

$$S_u = -\delta_\mathrm{M} K + S_u^0 \tag{4.5}$$

This equation allows to deduce the unstretched burning velocity S_u^0. Thus evaluating the slope of the variation of the velocity S_u as a function of the stretching factor K, provides Markstein length δ_M. If the modified Karlovitz number Ka_k and the Markstein number Ma, are now introduced the previous equation becomes:

$$\frac{S_u}{S_u^0} = 1 - \mathrm{Ma}\ \mathrm{Ka}_k \tag{4.6}$$

[1] (*NASA Chemical Equilibrium with Applications (CEA)*; Gordon and McBride, 1994; Gordon and McBride, 1996)

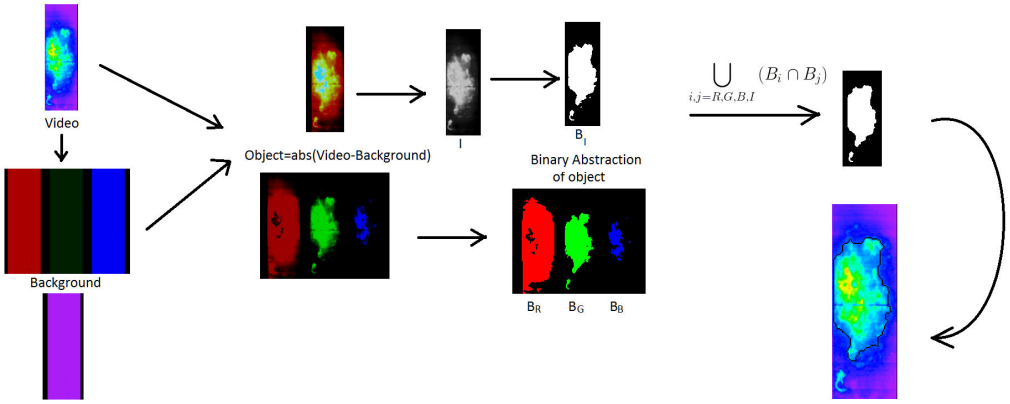

Figure 4.2. Example of the analysis of a propagating flame video

with $\mathrm{Ma} = \frac{\delta_M}{\delta_L}$ where δ_L is the flame thickness. The Markstein number represents the sensitivity of the flame to stretching (Clavin, 1985). The modified Karlovitz number Ka_k is therefore defined as an adimensional stretching.

4.2.2. Video analysis

With the purpose of obtaining those parameters, a model was developed in Matlab's Simulink using the Vision toolbox. This model analyses the videos of flames propagating in the vertical tube and extracts the profile of the flame for each frame in the video. In a previous stage, the user edits (if he finds it necessary) the video to enhance the flame with a faux colour filter. This can be done with the open source software VirtualDub, that among other filters, it has one to adjust the deformation of the videos caused by the perspective of the camera thus improving the accuracy.

The Simulink model can then separate each colour channel from the RGB image and analyse it separately. First, it estimates the background of the video by averaging the first 50 frames of the video that precede the igniting spark (the quantity of frames is optional). The moving object (the flame) can be now isolated as the absolute value of the difference between the background and the flame. This produces three different moving objects, one for each of the primary colours that compose a digital image (red, green and blue). An additional grey-scale object can be obtained as the addition of the three colours. These four images are then passed through a threshold filter that automatically deduces which pixels are the relevant ones because of their intensity (brightness). Four boolean images B_R, B_G, B_B and B_I are produced, each one portraying the zones of the frame that are remarkably different from the original background. A logical operation is now performed between these images as a means for deciding which region of the frame is indeed the flame F:

$$F = \bigcup_{i,j=R,G,B,I} (B_i \cap B_j) \tag{4.7}$$

$$\begin{aligned} F = &(B_R \cap B_G) \cup (B_B \cap B_G) \cup (B_R \cap B_G) \\ &\cup (B_I \cap B_R) \cup (B_I \cap B_G) \cup (B_I \cap B_B) \end{aligned} \tag{4.8}$$

This is as if each of the three colours R, G, B and the black and white image I "casted a vote" for each pixel to decide whether it has changed enough in comparison to the background. In this digital election the minimum number of votes necessary to be chosen is two. Then, from the boolean result of this virtual vote, the form of the profile can be detected. **Figure 4.2** exemplifies how is this process done.

The detected profile can be used in different ways to estimate the surface. The user can approximate the surface using three methods, depending on the direction of propagation of the flame as well as its structural characteristics. The first method is the automation of the manual process performed by Khalili (2012) and Garcia-Agreda (2010) for the approximation with parabolas of (laminar) flames propagating in one direction inside a tube. The second one is called "Method of Orthogonal Semi-Ellipses" (MOSES). It is an improvement of the first method so that turbulent flames can be also considered when analysing flames that migrate in one direction through a canal. The last one is called "Perimeter Revolution Interpolation for Surface Approximation" (PRISA) and can be applied for relatively unconfined flames that propagate in all directions. The MOSES and the PRISA methods are better explained in **Appendix ??**. The position of the flame is considered to be the highest one at each frame and the area of the section is that of the circle whose diameter equals the largest horizontal distance between two points on the flame front. Independently from the method use for estimating the surface of the flame, the process is always accompanied of an incertitude tied to the fact that a three dimensional object is being constructed from the projection of that object on a two dimensional surface.

With the position of the flame z, the estimated cross-section area A_s and the estimated flame surface A_f for different points in time t, the spatial velocity S_s and the stretching K can be calculated, using a *piece-wise* polynomial regression of the position and the surface of the flame. The derivation of such polynomials then provides the functions necessary to the analysis described in the previous section.

4.2.3. Results of the study

In this study 5 kinds of mixtures of starch and methane where chosen to compare the way their flames propagate. Each kind of mixture belongs to one of the regimes described in **Chapter 1**: gas-driven, dust-driven, dual driven or pure fuel (gas or dust). The mixture for each regime was chosen for being the one with the highest $\left(\frac{\mathrm{d}P}{\mathrm{d}t}\right)_{\max}$ found for in the severity tests presented in **Chapter 1** as shown in **Figure 4.3**. In **Table 4.1** the composition of those mixtures is listed as well as the adiabatic temperatures estimated with the CEA software.

The mixtures were ignited at t_{v} =120 ms and 180 ms with 1 J electric spark. Even methane flames were ignited 120 ms and 180 ms after the air flow generated by the Mike apparatus had disturbed from the bottom of the tube to induce turbulence. A control was also performed with laminar flames of methane to test the technique and the surface estimation methods. **Figure 4.4** shows examples of three frames of one video in each regime. Each of those flames actually propagates vertically upwards, but they are presented here in horizontal manner for convenience.

It can be seen at first glance, that one of the differences between gas and dust is that gas is not so sensitive to gravity when its flame propagate. Indeed, as methane

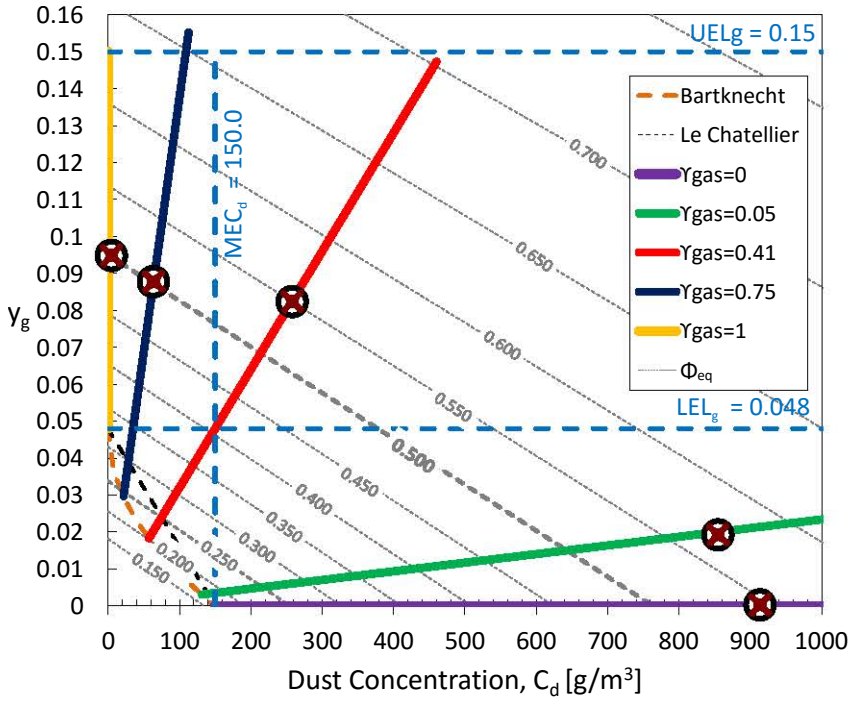

(a) Concentration map

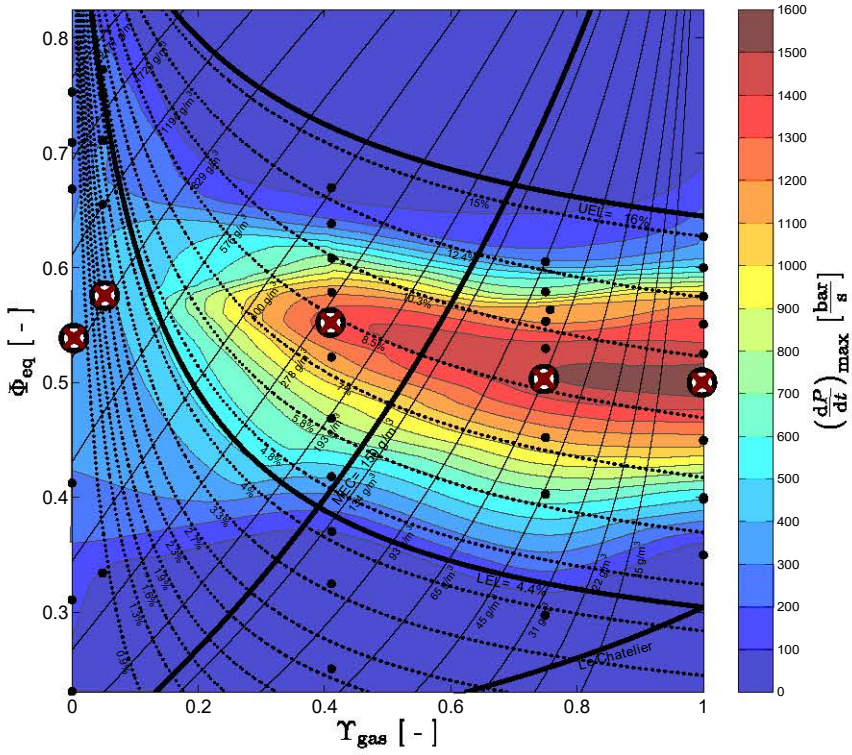

(b) Severity map

Mixture chosen for flame propagation tests

Figure 4.3. Selection of starch-methane mixtures in each regime for flame propagation tests. Selection criteria: maximum $\left(\frac{dP}{dt}\right)_{max}$ obtained in the 20 l sphere for experimental subsets with similar oxygen demand of gas fuel (Υ_{gas})

flames advance, they either completely consume the reactants, or the push them outside the tube, but there is no sign of delayed combustion once the flame has left the bottom of the tube. In contrast, even the explosion with low concentrations of starch, shows that starch takes a longer time to burn and that gravity acts on it preventing the unburnt starch to stay in front of the flame. Consequently, as the flame advances, a delayed reaction is prevalent in the region it leaves.

Still, each regime differs from the others in some degree and a progressive change in the structure of the flame happens as the ratio methane/starch decreases. Pure methane flames have the tendency to stabilize and the perturbations induced by the initial air flow dissipate while the flame surface smooths out as it seeks laminar-like behaviour. Because of the nature of the dust dispersion a gradient in dust concentration is inherent to this system. For this reason the flames in the gas-driven regime also seek this laminar-like behaviour in the later stages of the flame propagation. In this regime, the surface of the flame is more wrinkled than it is for methane flames, but its structure is still more similar to methane flames than it is to flames in the dual-driven regime. In fact the dual-fuel regime starts to exhibit a characteristic that is common to the dustier regimes. After advancing 20 cm a flame jet is sometimes projected over one wall, in front of the main flame, this jet usually curls back and rejoins the main flame that keeps advancing. Nevertheless, flames in the dual-fuel regime differ from those in the dustier ones in that, the flame continues to advance *as one* after the jet dissipates. Whereas, in the dustier regimes, the jet causes a rupture in the flame front. In these cases, the flame-jet does not dissipate but it creates a separate flame of its own. Hereby, two separate combustion zones are formed and the and the lower one stays burning long after the secondary flame has left the tube. Finally the sole morphologic difference between flames in the dust-driven regime and dust flames is that the first ones are less wrinkled as it would be expected because of the smoothing presence of gas. This transitional behaviour from the gas regime to the dust regime shows that flame stretching in dust flames

Table 4.1. Compositions of the mixtures used for flame propagation analysis.

		Regime				
		gas	gas-driven	dual fuel-driven	dust-driven	dust
y_{gas}	%(v/v)	9.50%	8.78%	8.47%	1.95%	0.00%
m_{dust}	mg	0	78	319	1048	1122
$C_{\text{dust}}{}^{*}$	$\frac{\text{g}}{\text{m}^3}$	0	63.84	260.41	855.51	915.92
$\Upsilon_{\text{gas}}{}^{\dagger}$	-	1	0.75	0.41	0.05	0
Φ_{eq}	-	0.5	0.5	0.55	0.56	0.53
$T_{\text{ad}}\|_V{}^{\ddagger}$	K	2224.51	2114.92	1512.43	951.18	951.53

* Calculated assuming that after dispersion the dust cloud always reaches 25 cm from the bottom.

† The fraction of oxygen demand by gaseous fuel.

‡ Adiabatic temperature at constant volume estimated with CEA software (*NASA Chemical Equilibrium with Applications (CEA)*; Gordon and McBride, 1994; Gordon and McBride, 1996).

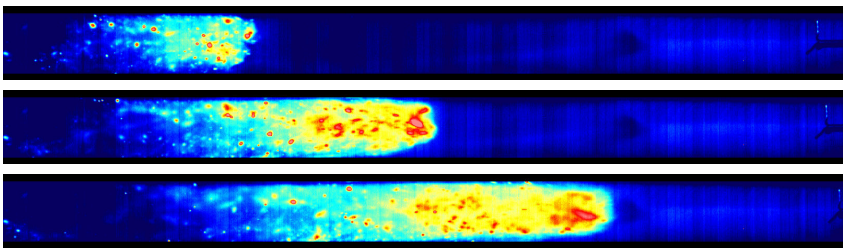

(a) Methane 9.5%, t=23.2 ms, 29.2 ms and 30.4 ms

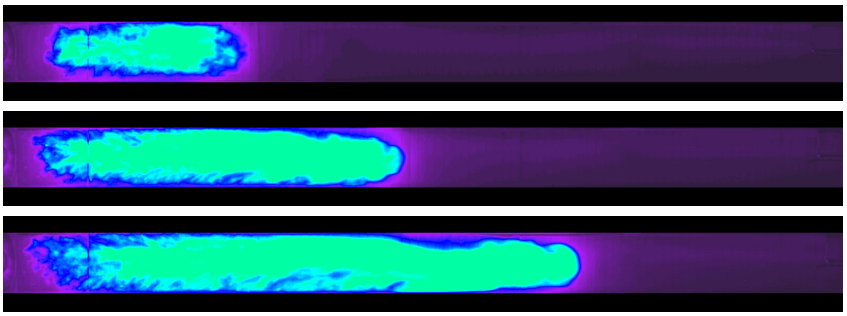

(b) Gas-driven, Methane 8.78%, Starch 78 mg, t=19.2 ms, 14.4 ms, and 28.8 ms

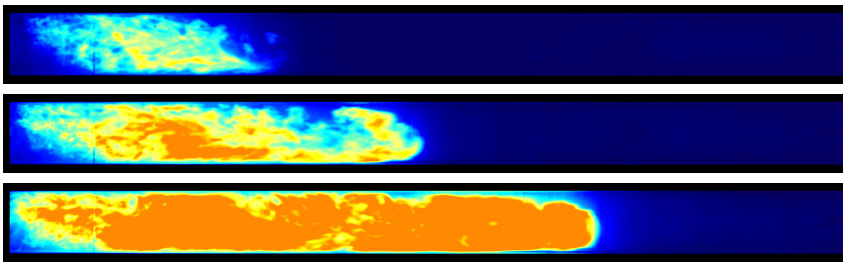

(c) Dual-driven, Methane 8.47%, Starch 319 mg, t=23.2 ms, 27 ms and 30.4 ms

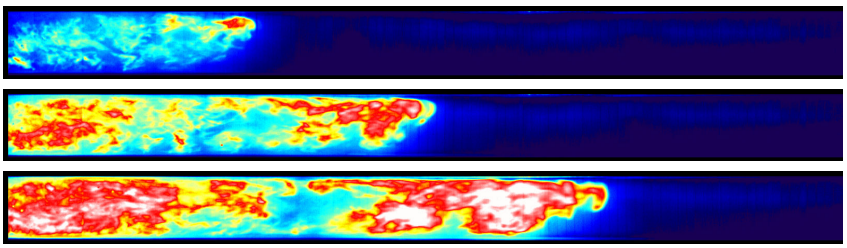

(d) Dust driven, Methane 1.95%, Starch 1048 mg, t=46.4 ms, 59.8 ms and 63.2 ms

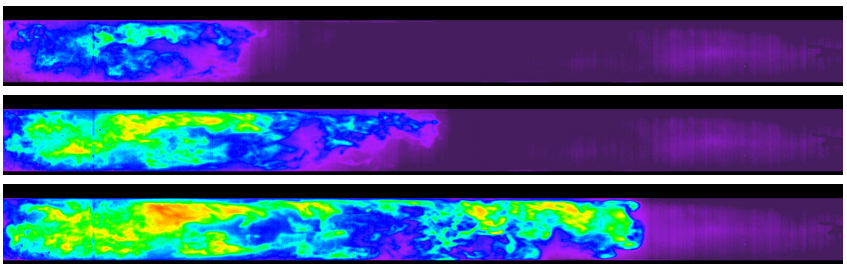

(e) Starch 1122 mg, t_v =120 ms, IE=1 J, t=73.8, 85.4 and 94 ms

Figure 4.4. Flame propagation of starch and methane mixtures, t_v =120 ms, IE=1 J. Frames were chosen for the flame front to appear at 20 cm, 40 cm and 60 cm from the electrodes. The images were modified to exhibit faux colour.

is intertwined with hydrodynamic deformations whereas gas flame deformation is tied to curvature. This is surely because of both the effect of gravity on settling the dust and the heterogeneous concentration of dust clouds. Indeed, the uneven combustion of those irregular concentration patterns induces momentum gradients that feed into the initial turbulence, whereas the uniformity of the gas combustion help to dissipate it.

4.2.3.1. Numerical analysis of experimental data

In this chapter three separate topics have been described. On the one hand, the theory that relates the burning velocity to the spatial velocity and the stretching of the flame has been presented. This theory has been validated for gases by its authors (Clavin, 1985; Markstein, 1964; Bradley et al., 1998). On the other hand, a will exists to validate this theory for the study of dust and gas/dust hybrid mixture flames. Therefore, the development of an experimental framework has been initiated in previous doctoral works (Garcia-Agreda, 2010; Khalili, 2012), as well as in the present one to achieve this goal. Nevertheless, although the experimental framework has the advantages of being simple, the exploitation of the experimental data is time consuming and complicated. Consequently, the third subject presented here, is the description of the numeric tool that has been developed to automatize the extraction and analysis of the experimental data in the form of explosion recordings, while increasing its accuracy.

The informatic tool has proved, as will be shown later, to be useful and efficient in the extraction and analysis of data from flame propagation videos. Vast amounts of information about the position and shape of a flame can be obtained from one video, in a relatively short time. Consequently, the way the data are exploited is what allows to determine whether the experimental technique has potential for importing a theory developed for gas combustion into the analysis of dust flames. Furthermore, the analysis of this data is what would allow to know if the theory is indeed adaptable or not.

The two methods for the estimation of the surface of a flame, propagating in one direction inside a tube (Paraboloid approximation and MOSES) were tested and they were both consistent with each other. The consistency they both share is that it is almost impossible to obtain any data that resembles each other under similar experimental conditions. The reason is that at each frame, a decision has to be made over the points were the flame front begins and ends. This requires to determine the zones were the flame is or not in contact with unburnt reactants. The judgement could be made arbitrarily, as was done before, or by relating somehow the distance of the naked flame to the wall with its thickness δ_L. Both possibilities conduct to inherent an unavoidable errors that render the technique untrustworthy. On the one hand, if the judgement is made arbitrarily at each frame by the experimenter, there might not be a way to make the technique consistent to an acceptable degree of error independently from the experimenter. On the other hand if the experimenter is removed, the shape the flame adopts in time, makes that different points of the flame to appear closer or further from the wall in an aleatory manner, and so the estimated surface raises and decreases very rapidly. This implies that both the automatized method of parabolas and the MOSES produce huge differences in the

calculated surface form one frame to the other although the morphology of flame has little variations. Take **Figure 4.5** as an example. Of course this is not the case for the first stages of the flame propagation before it approaches to the wall. But in that case neither the paraboloid method, nor the MOSES are suited for estimating the surface of the flame because the flame is naked from all sides during its early development.

This means that for the initial stages of the flame's development the PRISA method has to be used. Regarding this method, the reader is advised to consider that it has been developed for evaluating in a rapidly manner whether the explosion recordings could be analysed to characterize flames of combustible dusts and their mixtures with gases. As such, the objective of this method is to evaluate the plausibility of obtaining consistent and coherent results in a bigger equipment using a more accurate technique to estimate the surface of the flame. Indeed accuracy is not really the goal of the PRISA method, it was used here, in the analysis of explosions within a 7 cm space. Meanwhile, the 20 L Siwek sphere has received varied criticism, because it is considered that it does not provide sufficient space for the flame to develop to its full potential so that the severity of an explosion could be properly assessed. So the present results, are to be interpreted as an exploratory study that will lead to the development of a technique with stronger foundations. Nevertheless, the preliminary results that are presented next are, in the opinion of the author, beyond what was expected in terms of both accuracy and consistency. Thus paving the way for a future development that can be applied for the study of both, dust and hybrid mixture flames.

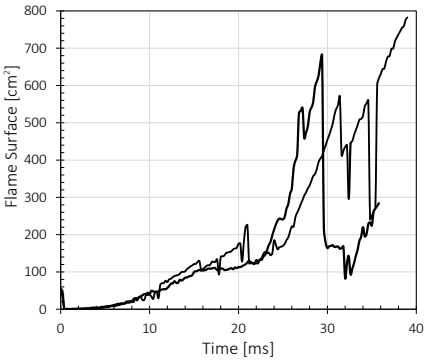

Figure 4.5. Estimation of the surface of the flame using the MOSES for two videos of flames in dual-fuel regime

Consider **Figures 4.6(a)** and **4.6(b)**, the way the regression lines are built over the experimental data has important repercussions on whether the exploitation of the data is successful or not. This is because the calculation of the burning velocity S_u is done with the time derivative of the position, and the calculation of the stretching depends on the time derivative of the surface area. So on both axes of the S_u vs K graph a the derivative a regression curve determines the quality of the regressed slope and y-intersect of an eventual straight line. Thus, besides the aleatory experimental errors, another source of error comes from this accumulation of approximations.

In this work the regressions were performed for the data produced in the totality of the tube without considering on the portion of the tube that was occupied by the flame. This was done so that any possible linear behaviour could be recognized independently from any personal bias. Once the linear behaviour was recognized, one would look at the region of the tube where it happened in order to identify if there was a common pattern between different videos. For this purpose, piece-wise polynomial regression was performed on the position, the surface and the section-

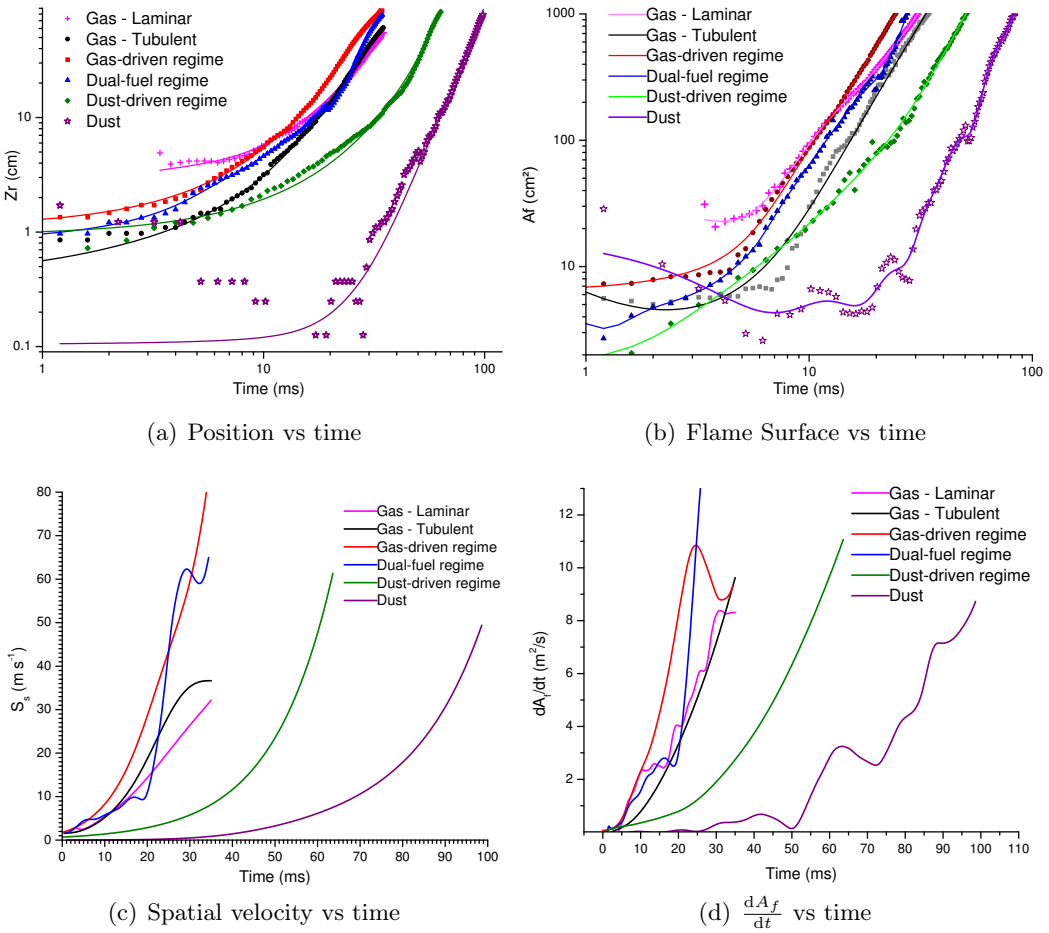

(a) Position vs time

(b) Flame Surface vs time

(c) Spatial velocity vs time

(d) $\frac{\mathrm{d}A_f}{\mathrm{d}t}$ vs time

Figure 4.6. Behaviour of flame position, surface, spatial velocity, and rate of flame surface change in time

area of the flame. The task was achieved using Matlab's function `fit` and its option `"smoothingspline"`. After derivation of the polynomials, S_u and K were calculated with both the experimental values and the polynomial fits.

Figure 4.7 shows the regression of the data for a laminar flame of methane at stoichiometric concentration. The black line represents S_u vs K according to the polynomial regressions while the points represent the equivalent calculation with the experimental data and the differentiated polynomials. Any deviation between both data permits to compare the goodness of the polynomial fittings and reflect on it to judge the S_u^0 and δ_M obtained. Red points represent the experimental data that was used to perform the linear regression. The times that bound those points are indicated and accompanied by the corresponding images of the flame.

It was confirmed with **Figure 4.7** that the development of the flame can be divided in three stages for this analysis:

1. An initial developing stage during which the flame is either stabilizing or too difficult to recognize by the detection algorithm.

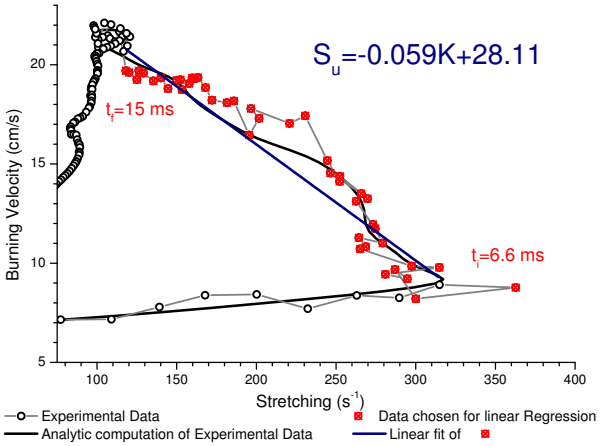

(a) Burning velocity vs stretching

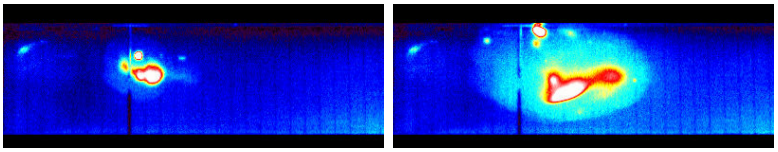

(b) 6.6 ms (c) 15 ms

Figure 4.7. Estimation of characteristic flame parameters of Methane at 9.5% (v/v) in laminar flow

2. A second stage of pseudo-spherical development that allows to implement Markstein's theory because it follows a linear behaviour.

3. And a later stage of propagation inside de tube where the flame is in contact or very close to the wall.

More importantly, the estimated burning velocity is well within the range of values reported for methane flames at 9.5% (Andrews and Bradley, 1972a).

The same analysis was then performed for flames in the regimes described by **Table 4.1** and the respective results were obtained through the analyses presented in **Figures 4.8** to **4.12**. A summary of the corresponding results is presented in **Table 4.2** (page 129) and **Figure 4.14** (page 130)

It is interesting from **Figure 4.8** that the polynomial regression was not accurate enough for according with the experimental data in the time lapse were the linear behaviour was perceived. This means that the accuracy of that measurement might be limited. Indeed, **Figure 4.6(b)** shows that the regression performed for the surface passes over the experimental values. Consequently the $\frac{\mathrm{d}A_f}{\mathrm{d}t}$ should have been higher during this period, and in turn, one should expect that the estimated values of δ_{M} and S_u^0 should be lower. Although, the author admits to not being certain on whether a better estimation would remain or not inside the 95% confidence interval presented.

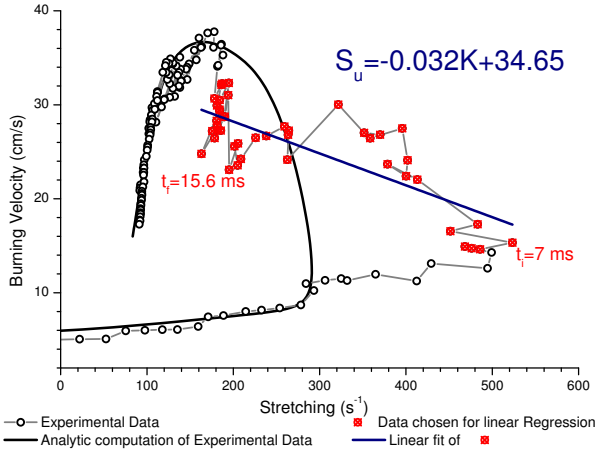

(a) Burning velocity vs stretching

(b) 7 ms (c) 15.6 ms

Figure 4.8. Estimation of characteristic flame parameters of methane at 9.5% (v/v), t_v =120 ms

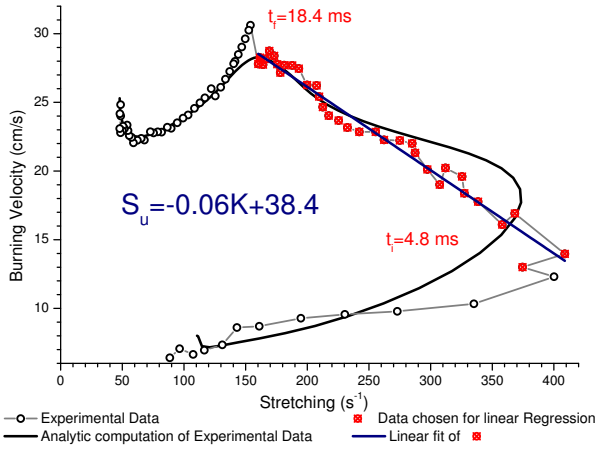

(a) Burning velocity vs stretching

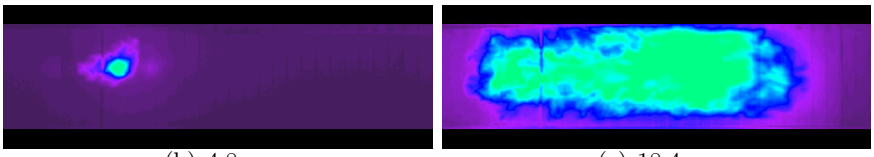

(b) 4.8 ms (c) 18.4 ms

Figure 4.9. Estimation of characteristic flame parameters of methane and starch, 8.78% (v/v) and 78 mg respectively, t_v =120 ms

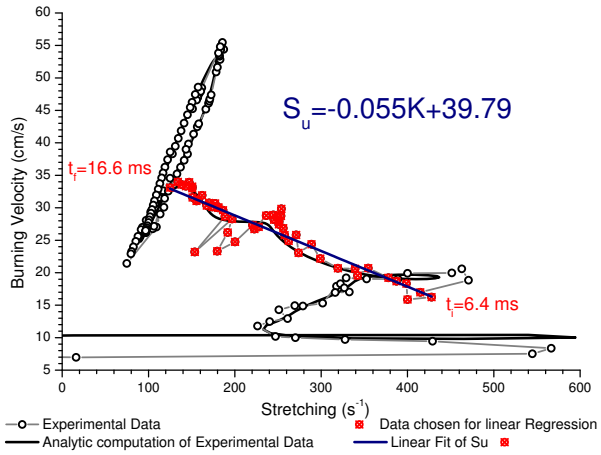

(a) Burning velocity vs stretching

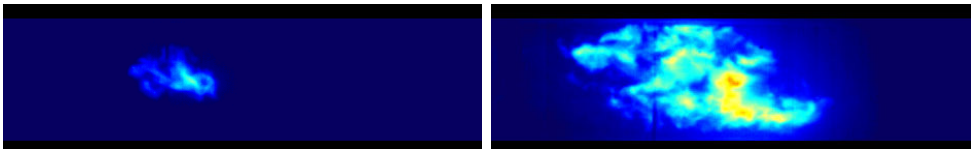

(b) 6.4 ms (c) 16.6 ms

Figure 4.10. Estimation of characteristic flame parameters of methane and starch, 8.47% (v/v) and 319 mg respectively, t_v =120 ms

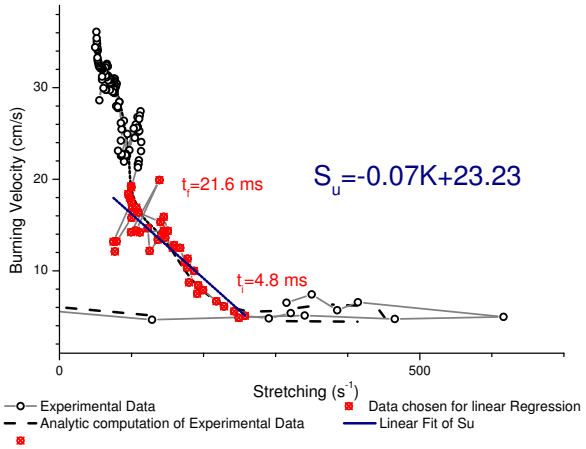

(a) Burning velocity vs stretching

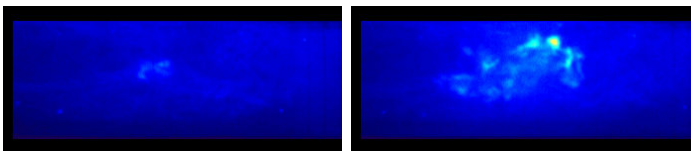

(b) 4.8 ms (c) 21.6 ms

Figure 4.11. Estimation of characteristic flame parameters of methane and starch, 1.92% (v/v) and 1048 mg respectively, t_v =120 ms

4.2.3.2. Identification of the conditions for the application of Markstein theory

It could be thought, because of most of the images of the flames that accompany **Figures 4.8** to **4.12** that Markstein's theory could be applied for dusts and their mixtures, as long as the flame is almost spherical and not deformed by the wall of the confinement. Nonetheless, **Figure 4.9**, for a flame in the gas-driven regime, seems to argue with this assertion. Indeed for the case of the flame in this figure, the linear relation between S_u and K ends beyond the conditions for which the method is expected to be valid.

The explanation for this behaviour resides in **Figure 4.13**. It can be seen that the end of the horizontal (related toA_s) growing stage of this flame is achieved in around 18.4 ms. Indeed, in the corresponding video, the flame starts growing to the left until it is very close to the wall, then it begins to grow to right. During this whole period, the flame has been constantly growing upwards,so when the flame has finally occupied the whole horizontal section of the tube, a great disproportion exists between its height and its width. This behaviour is consistent with the other flames. So it can be said that the end of the linear relation between S_u and K is determined by the end of the horizontal growth of the flame and not by its actual shape.

Regarding the beginning of this stage, it is consistent for every flame for the beginning of the continuous growth of the surface of flame as can be seen when compared with **Figure 4.6(b)**. Indeed, every flame takes some time after the ignition to start growing (this is particularly true for dusts), but once this period is concluded the flame surface starts to grow in a continuous way and this is the moment that marks the beginning of the linear relation between S_u and K.

4.2.3.3. Burning flame velocity and the the ration gas/dust

Finally, the results presented in **Figure 4.2Table 4.2** should not be analysed in terms of actual values of the burning velocity and the Markstein lengths but rather in terms of the tendencies that they evidence. On the one hand, these calculations have been done using a method for estimating the surface of the flame (PRISA) whose reliability can be debated. Albeit, the PRISA method still provides an estimation that is proportional to the perimeter of the projection of the flame in two dimensions. Nevertheless, the surface of the flame is nothing but the three-dimensional counterpart of the perimeter. Moreover, any method based on one video from just one perspective will still be based on a proportional relation between the perimeter and the surface, so the tendencies will be similar even if the exact values may vary. On the other hand, and probably most importantly, no repetitions were analysed here, so the added errors in every stage of the calculation shall encourage a careful perspective on the results.

Albeit all these disclaimers, the preliminary results suggest that hybrid mixtures count indeed with a synergistic effect that helps their flames to propagate faster. Although pure methane flames alone are faster than starch ones, the replacement of some methane by starch in a mixture seems to increase the propagation velocity of the flame. This effect is mostly true for the dual-fuel regime. This might be explained by two effects generated by the presence of the dust. First, the concentra-

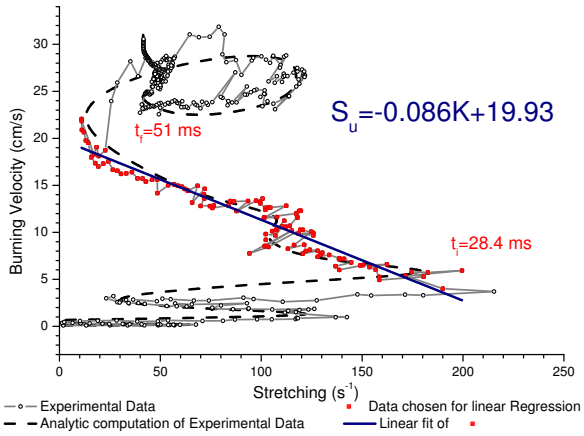

(a) Burning velocity vs stretching

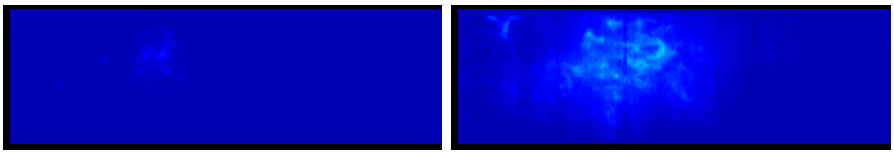

(b) 28.4 ms (c) 51 ms

Figure 4.12. Estimation of characteristic flame parameters of methane and starch, 1.92% (v/v) and 1048 mg respectively, t_v =120 ms

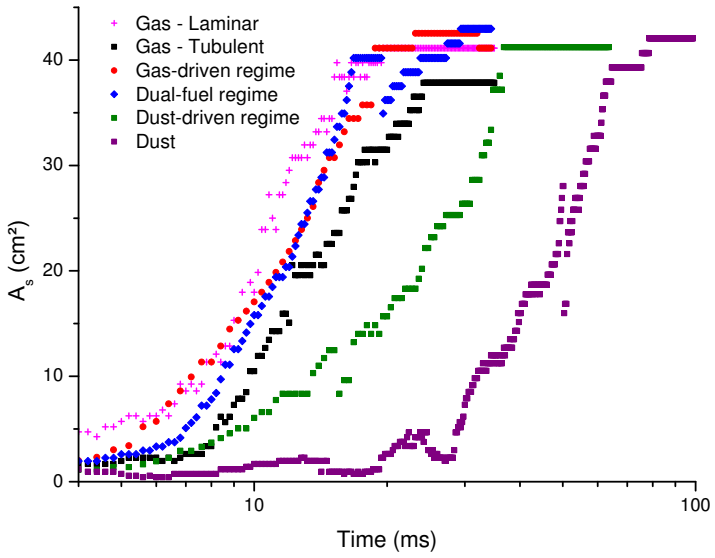

Figure 4.13. Cross section area of flame in terms of time

Table 4.2. Burning velocities and Markstein lengths of methane/starch mixtures deduced from video analysis of flame propagation

	Regime					
	gas (laminar)	gas	gas driven	dual fuel driven	dust driven	dust
y_{gas} [%(v/v)]	9.5%	9.50%	8.78%	8.47%	1.95%	-
m_{dust} [mg]	-	-	78	319	1048	1122
t_v [ms]	-	120	120	120	120	120
S_{u_0} [$\frac{cm}{s}$]	28.11	34.65	38.36	39.79	23.23	19.93
Lower Bound*	26.79	32.23	37.38	37.93	20.94	19.37
Upper Bound*	29.43	37.08	39.35	41.65	25.52	20.48
δ_M [mm]	0.59	0.32	0.61	0.55	0.70	0.86
Lower Bound*	0.53	0.24	0.57	0.47	0.55	0.81
Upper Bound*	0.65	0.41	0.65	0.62	0.86	0.91
r^2	0.96	0.60	0.97	0.81	0.68	0.90

* 95% Confidence on the linear regression.

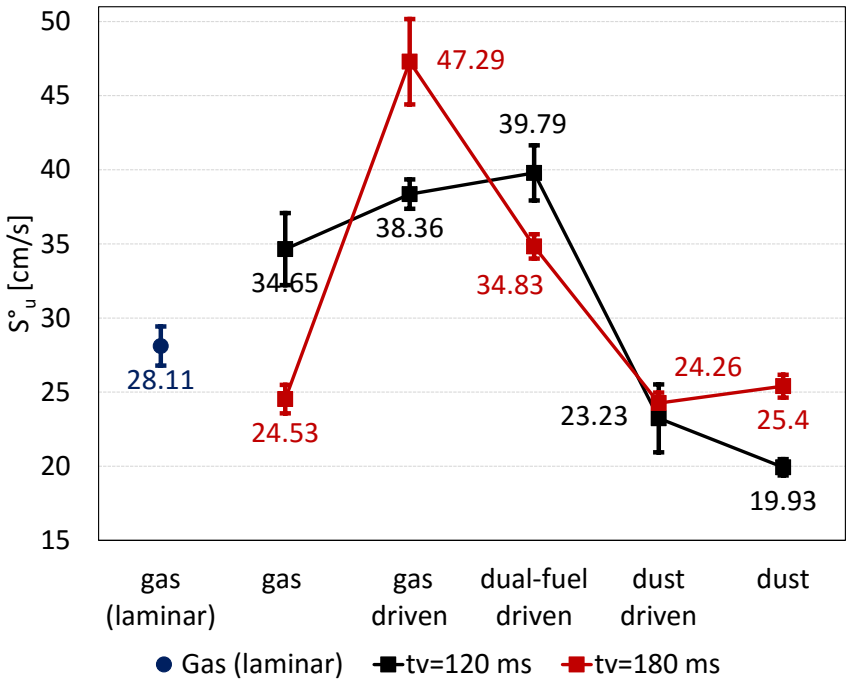

Figure 4.14. Burning velocities of methane/starch mixtures deduced from video analysis of flame propagation

tion gradient of the dust causes a dissimilar rate of combustion inside the flame, that induces a more curled flame and consequently a bigger surface thus, increasing the rate of consumption of the fuel. The second reason is also related to the uniformity of the presence of the dust whose combustion causes an additional perturbation. The burnt gases released, expand in an uncoordinated fashion that increases the momentum of the fluid and thus the turbulence in the mixture. Consequently the flame has a bigger surface and oxygen is more accessible.

RÉSUMÉ

Quantification de la turbulence générée lors de la dispersion de la poussière avant explosion

Prédire la propagation de la flamme pendant une explosion de poussière dans des géométries complexes est encore un défi qui mobilise de nombreuses ressources techniques, informatiques et humaines. Une connaissance parfaite des mécanismes d'explosion de poussières serait nécessaire pour proposer une approche totalement prédictive ; mais elle doit être effectuée en tenant compte des propriétés spécifiques de chaque poudre combustible, ce qui prendrait beaucoup de temps, voire serait illusoire. Une autre approche consiste à déterminer expérimentalement les caractéristiques intrinsèques des mélanges poussière-air (comme la vitesse de flamme laminaire) et de les utiliser comme une entrée des logiciels de simulation de type CFD. Néanmoins, si la caractérisation expérimentale de la vitesse de combustion des gaz à partir de la vitesse du front de flamme est encore délicate, lorsqu'il s'agit de suspensions de poussières dans l'air en milieu turbulent, cette caractérisation devient des plus ardues.

Le but ultime de ce travail était de développer une approche pour évaluer les propriétés fondamentales de propagation des flammes, non seulement à partir des expériences en milieu confiné et des courbes d'évolution de pression en fonction du temps, mais à aussi partir de l'analyse de la vitesse de flamme en fonction de son étirement et des instabilités hydrodynamiques. Considérer les interactions turbulence/ combustion pendant la propagation de la flamme permettra donc d'en extraire la vitesse de flamme "pseudo" laminaire des poussières ou des hybrides mélanges.

La méthode du tube semi-ouvert a été sélectionnée et adaptée afin de réduire l'impact des variations des conditions expérimentales. La technique consiste à analyser des vidéos de flammes se propageant à l'intérieur d'un tube vertical semi-ouvert de section droite carrée, de volume V= 4,9 L, de longueur L=100 cm et de côté D= 7cm, soit un rapport d'allongement L/D d'environ 14. Le tube est fermé à l'extrémité de l'allumage et équipé d'une soupape de sécurité à l'autre extrémité. Comme deux des faces opposées du tube sont en verre (les deux autres étant en acier inoxydable), il est possible de suivre visuellement le processus de propagation de la flamme à l'aide d'une caméra vidéo à haute vitesse à 10000 images par secondes. Le système d'allumage est constitué de deux électrodes de l'appareil Mike 3 pour des énergies inférieures à 1 J ou d'un système d'inflammation créé à cet effet pour des énergies comprises entre 1 et 100 J. La mise en suspension des poussières se fait par le système de génération de suspension du Mike 3. Le dispositif expérimental comprend

aussi un système d'injection de vapeurs et de gaz permanents. Un cylindre en acier permet de prémélanger l'air avec un gaz combustible avant de l'introduire dans le tube. Le tube de Hartmann modifié est ensuite utilisé pour disperser la poussière et pour déclencher une explosion.

Une caméra à haute vitesse enregistre la propagation de la flamme et la vidéo qui en résulte est ensuite analysé pour en déduire les paramètres caractéristiques de la combustion du mélange. La position du front de flamme est déterminée par traitement numérique des vidéos à l'aide d'un outil développé dans le cadre de cette thèse (Simulink - Matlab). La détection de la position et de la surface du front de flamme est automatisée, ce qui réduit les incertitudes dues à l'intervention humaine.

Une fois la vitesse spatiale de propagation du front de flamme déterminée, l'approche développée par Andrews et Bradley (1972b) pour les gaz peut être extrapolée, sous réserve de quelques hypothèses. La relation entre la vitesse spatiale de la flamme et la vitesse de flamme à étirement non nul S_u peut être exprimée en fonction du ratio entre la surface de la flamme et de la section du tube, mais également en prenant en compte le facteur d'expansion thermique χ entre les gaz chauds issus de la combustion et les gaz frais initiaux. Le facteur d'expansion est défini par le rapport entre la masse volumique des réactifs frais et celle des produits brûlés. Les températures adiabatiques de flamme sont calculées par le logiciel CEA. De plus, plusieurs facteurs influencent la vitesse de combustion comme entre autres la composition du mélange, la pression initiale, la température et l'intensité de la turbulence. L'effet de ce dernier facteur se traduit par la prise en compte d'un terme appelé « étirement ». Il s'agit de l'augmentation de la surface de flamme lorsque le front est soumis à une perturbation dans l'écoulement. Markstein (1964) puis Clavin (1985) ont établi une relation linéaire entre la vitesse fondamentale de flamme à étirement non nul S_u et le taux d'étirement K :

$$S_u = -\delta_{\mathrm{M}} K + S_u^0$$

où S_u^0 est la vitesse fondamentale à étirement nul. L'évaluation de la pente de la variation de la vitesse Su en fonction du taux d'étirement K donne une estimation de la longueur de Markstein δ_{M} et par la même, de la stabilité de la flamme.

Cinq types de mélanges d'amidon et de méthane ont été choisis pour comparer la façon dont leurs flammes se propagent. Chaque type de mélange appartient à l'un des régimes décrits au **Chapitre 1** : dominé par le gaz (gas driven), dominé par la poussière (dust driven), à double carburant (dual fuel driven) ou régime synergique (synergic effect). Le mélange pour chaque régime a été choisi pour être celui qui a la sévérité d'explosion la plus importante et en particulier la vitesse maximale de montée en pression la plus élevée (comme constaté dans les essais de sévérité présentés au **Chapitre 1**). Les mélanges ont été allumés avec un délai t_{v} de 120 ms et 180 ms avec étincelles électriques de 1 J. Des tests de validation ont été effectué sur du méthane pur dans des conditions similaires et pour des écoulements laminaires.

Les essais confirment que le développement de la flamme peut être divisé en trois étapes distinctes :

1. Une première étape de développement du noyau de flamme au cours de laquelle la flamme est soit trop instable à forte turbulence initiale, soit trop difficile à

reconnaître par l'algorithme de détection du fait de sa faible luminosité ou de son placement dans le nuage de poudres.

2. Une deuxième étape de développement pseudo-sphérique qui permet de mettre en œuvre la théorie de Markstein et Clavin.

3. Un stade ultérieur de la propagation à l'intérieur de tube où la flamme durant lequel la flamme est en contact indirect ou très près des parois (wall quenching).

Plus important encore, la vitesse de combustion estimée par la méthode développée dans cette thèse est bien en accord avec les valeurs rapportées pour flammes de méthane à 9,5% par divers auteurs, ce qui valide l'analyse pour les gaz purs.

Les résultats présentés sur la **Figure 4.14** ne doivent pas être analysées en termes de valeurs absolues de vitesse de combustion ou de longueurs de Markstein (non représentées ici), mais plutôt en termes des tendances mises en évidence. Cette prudence vient notamment de l'interrogation persistante quant à l'applicabilité des lois utilisées en milieux homogènes (présentées ci-dessus) aux explosions de poussières. D'autre part, du fait de l'hétérogénéité et de la turbulence inhérentes aux nuages de poudres, la surface de flamme devrait être déterminée en 3D, alors qu'elle ne peut être que visualisée en 2D avec cette méthode. Enfin, il faudrait extrapoler les vitesses non étirées déterminées à différents t_v (turbulence initiale du nuage – cold turbulence) pour obtenir une véritable vitesse laminaire de flamme à étirement nul.

Quoiqu'il en soit, les résultats préliminaires suggèrent que certains mélanges hybrides présentent effectivement un effet de synergie qui permet une propagation plus rapide de leurs flammes. Bien que des flammes de méthane pur soient plus rapides que celle d'amidon, le remplacement d'une partie du méthane par de l'amidon dans un mélange semble d'augmenter la vitesse de propagation de la flamme. Cet effet est surtout vérifié pour le régime à double carburant (dual fuel). Ceci peut être expliqué par deux effets engendrés par la présence de la poussière. En premier lieu, le gradient de concentration de poussière provoque une vitesse différente de la combustion à l'intérieur de la flamme, qui induit une flamme plus plissée et par conséquent une plus grande surface, ce qui augmente la vitesse de consommation du carburant. La deuxième raison est également liée à l'uniformité de la présence de la poussière en amont du front de flamme, ce qui provoque une perturbation supplémentaire lors de la propagation du front et son étirement potentiel par la pénétration de particules de plus grosses tailles (non encore volatilisées). Enfin, la présence de poudre modifie grandement les phénomènes radiatifs en amont du front de flamme.

Conclusions

In this document an effort has been done to propose diverse an hopefully original perspectives from which to study both, dust explosions and dust-gas hybrid mixture explosions. This was done with the conviction that, rather than a sudden almost discrete change in behaviours, hybrid mixtures exhibit a subtle progressive transition of behaviours. It goes from the explosion of a dust cloud, to the explosion of a gas, passing through the explosions of all the intermediate solid-gas mixtures that are classified with composition regimes. The classification of mixtures by composition regimes that was first described by Garcia-Agreda et al. (2011), would seem to consider that these intermediate mixtures can be classified according to seemingly strict lines defined by the lower explosivity limits of the pure components. They certainly can, but these limits shall be rather considered a diffused region where mixtures indistinguishably transit from one regime to the other.

Under this perspective, a way to quantify the ratio of gas to solid was proposed here: the fraction of oxygen demand. Although its use may appear to make the analysis more complicated than it should, it is actually not completely extraneous to the study of combustion, nor is it that complicated. This concept is already used on another discipline: environmental chemistry and its definition comes exactly from the chemical equation of combustion, although they may call it "respiration". Moreover, its definition is not that different from the fuel equivalent ratio that is already broadly used in the study of combustion. These concepts are probably the more sensible to use because in the field of combustion. Oxygen is the *coin* that enables or limits any chemical transaction, independently of the phase, density or molecular mass of the fuels involved. This is why they are useful for making comparisons between different kinds of fuels. Hopefully, the author has done a succesful job in demonstrating how useful it may be to generalise the use of the concept of fraction of oxygen demand into the study hybrid mixture combustion.

The pyrolysis of starch was also studied, as a way for dust clouds to transition into the dust-driven regime of hybrid mixtures. The experimental results suggest that under the high temperatures achieved during an explosion, the production of combustible gases increases, while the production of CO_2 is diminished. Furthermore the concentrations of the combustible gases released exceed lower explosive limits. This would be irrelevant if the times necessary to achieve such concentration were too long in comparison to combustion times. Nevertheless, the numerical analysis

performed here suggests that times vary, depending on the temperature and size of the particle, from less than 1 ms to 30 ms. In comparison, the flames of starch propagating inside a 100 cm × 7 cm × 7 cm tube last longer than 100 ms. These results, represent strong evidence that pyrolysis is present during the explosion of organic dusts like starch.

Furthermore this pyrolysis process, could be specially important during the ignition stage when the initial kernel may be causing a very fast pyrolysis of the dust that conduces later to the development of the flame.

The kinetic models for pyrolysis that are available to date were developed in the context of low temperature, slow pyrolysis of relatively big particles, that do not resemble the conditions of an explosion. Nonetheless, a model for the flash pyrolysis of small particles was developed. This model accompanied by the experimental framework for flash pyrolysis may represent the first step obtaining kinetic parameters for flash pyrolysis.

In the context of the study of initial turbulence of dust clouds, a model was developed for the sudden expansion of a pressurized gas through an orifice. This model may prove to be useful outside the field of combustion, for example in the analysis of atmospheric dispersions of hazardous gases.

The characterization of turbulence inside a vertical tube with crossed-section equal to 7 cm×7 cm was performed through PIV measurements. The results could be used for the analysis of turbulence of different dusts in similar equipments like the modified Hartmann tube as long as the particles have very low terminal velocities.

Furthermore, this results are destined to help in the estimation of the laminar burning velocities of dust and hybrid mixture flames.

In the same context a numerical tool was developed in Matlab's Simulink for the analysis of videos propagating flames. The results presented on this subject are preliminary but promising. The tool has proven to very useful in the extraction of morphological information of flames through time.

Furthermore, the theory used to apply the morphological information of the flame, was originally developed for gases, but the preliminary results presented here show that this theory could very easily be adapted for dust and hybrid mixtures.

Finally, most of the work presented here, posed problems that caused considerable struggle for the author, since he had to establish the experimental protocols for performing PIV and recording and analysing the videos of propagation flames. It is a source of big satisfaction knowing that three of his colleges and good friends are already benefiting from the work that was presented here. Indeed, in our research team three doctoral thesis are continuing the work on PIV measurement and flame propagation inside similar sphere to the 20L sphere. If these techniques prove to work as expected, it might not be surprising to find out that future versions of the 20 L sphere, incorporate also the analysis of flame propagation through video recordings.

Conclusions (Français)

Dans ce document, un effort a été fait pour proposer diverses perspectives pour étudier à la fois, les explosions de poussière et des mélanges hybrides poussière/gaz. Cela a été fait avec la conviction que, plutôt que d'un changement soudain presque 'discret' des comportements, les mélanges hybrides présentent une transition progressive subtile de comportements. Il va de l'explosion d'un nuage de poussière, à l'explosion d'un gaz, en passant par les explosions de tous les mélanges intermédiaires gaz-solide qui sont classés avec les régimes de composition. La classification des mélanges par des régimes de composition qui a été décrite par Garcia-Agreda semble considérer que ces mélanges intermédiaires peuvent être classés en fonction de lignes apparemment strictes définies par les limites d'explosivité inférieures des composants purs. Cette approche est utile, mais ces limites sont plutôt considérées comme une région diffuse où des mélanges 'transitent indistinctement' d'un régime à l'autre.

Dans cette perspective, un moyen de quantifier l'apport différentiel du gaz et du solide a été proposé ici : la richesse normée par la demande en oxygène. Bien que son utilisation puisse sembler rendre l'analyse plus compliquée qu'elle ne le devrait, elle permet de bien distinguer la contribution de chaque combustible. Ce concept est déjà utilisé sur une autre discipline : la chimie de l'environnement. En outre, sa définition n'est pas trop différente du rapport équivalent de carburant (richesse) qui est déjà largement utilisé dans l'étude de la combustion.

La pyrolyse de l'amidon a également été étudiée, comme un moyen pour les nuages de poussière de 'transiter' vers le régime de mélanges hybrides dominé par la poussière (dust driven). Les résultats expérimentaux suggèrent que dans le cadre des hautes températures atteintes lors d'une explosion, la production de gaz combustible augmente, alors que la production de dioxyde de carbone est diminuée. En outre, les concentrations des gaz combustibles libérés dépassent les limites inférieures d'explosivité. L'importance relative de la pyrolyse dans le processus d'explosion est définie par le ratio entre le temps de pyrolyse et le temps de combustion des gaz générés. L'analyse numérique effectuée ici suggère que les temps de pyrolyse varient en fonction de la température et de la taille de la particule, et courent une gamme allant de moins de 1ms à 30ms. À titre de comparaison, les flammes d'amidon se propageant à l'intérieur d'un tube de propagation de flamme d'un mètre de longueur (utilisé dans cette étude) durent plus de 100 ms. Ces résultats témoignent de l'importance de la

pyrolyse lors des explosions de poussières organiques comme l'amidon. En outre, la pyrolyse peut être particulièrement importante lors de la phase d'allumage lorsque le noyau initial se développe ou s'éteint en fonction notamment des régimes limitants de la combustion. Les modèles cinétiques de pyrolyse qui sont disponibles à ce jour ont été élaborés dans le contexte d'une pyrolyse relativement lente de grosses particules à basse température, ce qui ne ressemble pas les conditions d'une explosion. Ainsi, un modèle de pyrolyse flash de petites particules a été développé. Ce modèle, accompagné d'une étude expérimentale de pyrolyse flash peut être présenté comme une première étape d'obtention des paramètres cinétiques pour pyrolyse flash dans le cadre d'une explosion de poussières.

L'étude de la turbulence initiale des nuages de poussière a été conduite numériquement et expérimentalement. Un modèle a été mis au point pour la dispersion rapide d'un gaz sous pression à travers un orifice. Ce modèle peut se révéler utile en dehors du domaine de la combustion, par exemple dans l'analyse des dispersions atmosphériques de composés dangereux. La caractérisation de la turbulence dans un tube vertical de section transversale carrée de 7cm de côté a été réalisée par PIV. Les résultats peuvent être utilisés pour l'analyse de la turbulence des différentes poussières dans des équipements similaires, comme le tube de Hartmann modifié à condition que les particules aient des très faibles vitesses terminales (une faible inertie / particules-traceurs).

Ces travaux concurrent tous à l'estimation des vitesses de combustion laminaire de flammes de poussières et de mélanges hybrides. Dans ce contexte un outil numérique a été développé pour l'analyse des vidéos de propagation des flammes (Simulink – Matlab). Les résultats présentés sur ce sujet sont préliminaires mais prometteurs. L'outil s'est révélé très utile dans l'extraction de l'information morphologique des flammes dans le temps (vitesse, surface et étirement de flamme). En outre, la théorie permettant de déduire des vitesses laminaires de flamme de vitesses spatiales a été initialement développée pour les gaz, mais les résultats préliminaires présentés ici montrent qu'elle pourrait très facilement être adaptée pour les poussières et les mélanges hybrides moyennant quelques hypothèses et transformations. Enfin si les méthodes présentés et développés ici fonctionnent comme espéré, il ne serait pas surprenant de constater que les futures versions de la sphère de 20 L puissent intégrer également l'analyse de la propagation de la flamme par le biais d'enregistrements vidéos adéquats.

Bibliography

Adrian, Ronald J. and Jerry Westerweel (2011). *Particle Image Velocimetry*. Cambridge University Press. 585 pp. ISBN: 978-0-521-44008-0 (cit. on p. 88).

Amyotte, Paul R., Kenneth J. Mintz, Michael J. Pegg, and Yu Hong Sun (1993). "The ignitability of coal dust-air and methane-coal dust-air mixtures". In: *Fuel* 72.5, pp. 671–679. ISSN: 0016-2361. DOI: 16/0016-2361(93)90580-U (cit. on p. 3).

Andrews, G. E. and D. Bradley (1972a). "The burning velocity of methane-air mixtures". In: *Combustion and Flame* 19.2, pp. 275–288. ISSN: 0010-2180. DOI: 10.1016/S0010-2180(72)80218-9 (cit. on p. 124).

Andrews, G.E. and D. Bradley (1972b). "Determination of burning velocities: A critical review". In: *Combustion and Flame* 18.1, pp. 133–153. ISSN: 0010-2180. DOI: 10.1016/S0010-2180(72)80234-7 (cit. on pp. 114, 132).

Authier, Olivier, Monique Ferrer, Guillain Mauviel, Az-Eddine Khalfi, and Jacques Lédé (2009). "Wood Fast Pyrolysis: Comparison of Lagrangian and Eulerian Modeling Approaches with Experimental Measurements". In: *Industrial & Engineering Chemistry Research* 48.10, pp. 4796–4809. ISSN: 0888-5885, 1520-5045. DOI: 10.1021/ie801854c (cit. on pp. 50, 62).

Ballal, D. R. and A. H. Lefebvre (1979). "Ignition and flame quenching of flowing heterogeneous fuel-air mixtures". In: *Combustion and Flame* 35, pp. 155–168. ISSN: 0010-2180. DOI: 10.1016/0010-2180(79)90019-1 (cit. on p. 11).

Bartknecht, Wolfgang (1989). *Dust-explosions: course, prevention, protection*. Springer-Verlag. 288 pp. ISBN: 978-0-387-50100-0 (cit. on pp. 8, 15–17, 39).

Bjerketvedt, Dag, Jan Roar Bakke, and Kees van Wingerden (1997). "Gas explosion handbook". In: *Journal of Hazardous Materials*. Gas Explosions Handbook 52.1, pp. 1–150. ISSN: 0304-3894. DOI: 10.1016/S0304-3894(97)81620-2 (cit. on p. 15).

Bouillard, J., A. Vignes, O. Dufaud, L. Perrin, and D. Thomas (2010). "Ignition and explosion risks of nanopowders". In: *Journal of Hazardous Materials* 181.1,

pp. 873–880. ISSN: 0304-3894. DOI: 10.1016/j.jhazmat.2010.05.094 (cit. on pp. 10–13).

Bozier, Olivier (2004). "Contribution à l'étude des caractéristiques de combustion isochore d'une suspension de particules solides réactives. Génération de la suspension ; influence de l'état initial du mélange." PhD thesis. Université de Poitiers (cit. on pp. 44, 45, 80).

Bradley, D., Z. Chen, S. El-Sherif, S. El-Din Habik, G. John, and G. Dixon-Lewis (1994). "Structure of laminar premixed carbon-methane-air flames and ultrafine coal combustion". In: *Combustion and Flame* 96.1, pp. 80–96. ISSN: 0010-2180. DOI: 10.1016/0010-2180(94)90160-0 (cit. on p. 112).

Bradley, D., R.A. Hicks, M. Lawes, C.G.W. Sheppard, and R. Woolley (1998). "The Measurement of Laminar Burning Velocities and Markstein Numbers for Iso-octane–Air and Iso-octane–n-Heptane–Air Mixtures at Elevated Temperatures and Pressures in an Explosion Bomb". In: *Combustion and Flame* 115.1, pp. 126–144. ISSN: 0010-2180. DOI: 10.1016/S0010-2180(97)00349-0 (cit. on pp. 116, 120).

Bradley, Derek, G. Dixon-Lewis, and S. El-Din Habik (1989). "Lean flammability limits and laminar burning velocities of CH4-air-graphite mixtures and fine coal dusts". In: *Combustion and Flame* 77.1, pp. 41–50. ISSN: 0010-2180. DOI: 10.1016/0010-2180(89)90103-X (cit. on p. 112).

Bradley, Derek, P. H. Gaskell, and X. J. Gu (1996). "Burning velocities, markstein lengths, and flame quenching for spherical methane-air flames: A computational study". In: *Combustion and Flame* 104.1, pp. 176–198. ISSN: 0010-2180. DOI: 16/0010-2180(95)00115-8 (cit. on p. 116).

Britton, Laurence G. (1998). "Short communication: Estimating the minimum ignition energy of hybrid mixtures". In: *Process Safety Progress* 17.2, pp. 124–126. ISSN: 1547-5913. DOI: 10.1002/prs.680170208 (cit. on p. 9).

Buitrago Acevedo, Maria Fernanda (2014). "Detecting temperature and water stress in plants with Thermal Infrared Spectroscopy". Presentation. Netherlands Annual Ecology Meeting. Lunteren, Netherlands (cit. on p. 62).

Cashdollar, Kenneth L. (2000). "Overview of dust explosibility characteristics". In: *Journal of Loss Prevention in the Process Industries* 13.3, pp. 183–199. ISSN: 0950-4230. DOI: 10.1016/S0950-4230(99)00039-X (cit. on p. 48).

Cassel, Hans M. (1964). *Some fundamental aspects of dust flames*. Report of investigations / United States Department of the Interior, Bureau of Mines ;6551. Washington, D.C.: U.S. Dept. of the Interior, Bureau of Mines. ii, 51 p. (Cit. on p. 112).

Chan, Wai-Chun R., Marcia Kelbon, and Barbara B. Krieger (1985). "Modelling and experimental verification of physical and chemical processes during pyrolysis of a large biomass particle". In: *Fuel* 64.11, pp. 1505–1513. ISSN: 0016-2361. DOI: 10.1016/0016-2361(85)90364-3 (cit. on pp. 50, 53, 69–72, 81).

Chen, D. L., J. H. Sun, Q. S. Wang, and Y. Liu (2008). "Combustion Behaviors and Flame Structure of Methane/Coal Dust Hybrid in a Vertical Rectangle Chamber". In: *Combustion Science and Technology* 180.8, pp. 1518–1528. ISSN: 0010-2202. DOI: 10.1080/00102200802125651 (cit. on p. 112).

Clavin, Paul (1985). "Dynamic behavior of premixed flame fronts in laminar and turbulent flows". In: *Progress in Energy and Combustion Science* 11.1, pp. 1–59. ISSN: 0360-1285. DOI: 16/0360-1285(85)90012-7 (cit. on pp. 116, 120, 132).

Coward, H. F, G. W Jones, Etats-Unis, and Mines (Bureau) (1952). *Limits of flammability of gases and vapors, by H. F. Coward and G. W. Jones.* Washington: U.S. Government printing office (cit. on p. 18).

Crowl, Daniel A. and Joseph F. Louvar (2001). "Source Models". In: *Chemical Process Safety: Fundamentals with Applications*. Pearson Education. ISBN: 978-0-13-244055-4 (cit. on p. 93).

Dahoe, A. E., R.S. Cant, and B. Scarlett (2001). "On the Decay of Turbulence in the 20-Liter Explosion Sphere". In: *Flow, Turbulence and Combustion* 67.3, pp. 159–184. ISSN: 1386-6184. DOI: 10.1023/A:1015099110942 (cit. on p. 86).

Dahoe, A. E., K. Hanjalic, and B. Scarlett (2002). "Determination of the laminar burning velocity and the Markstein length of powder-air flames". In: *Powder Technology* 122.2, pp. 222–238. ISSN: 0032-5910. DOI: 16/S0032-5910(01)00419-3 (cit. on p. 112).

Dahoe, Arief Edsel (2000). *Dust explosions: a study of flame propagation*. ISBN: 90-90-13706-8 (cit. on pp. 84, 85).

Desai, D. H., C. K. Patel, K. C. Patel, and R. D. Patel (1972). "Kinetic Study on the Pyrolysis of Amylose and its Derivatives". In: *Starch - Stärke* 24.3, pp. 80–84. ISSN: 1521-379X. DOI: 10.1002/star.19720240304 (cit. on p. 51).

Di Benedetto, A. and P. Russo (2007). "Thermo-kinetic modelling of dust explosions". In: *Journal of Loss Prevention in the Process Industries* 20.4, pp. 303–309. ISSN: 0950-4230. DOI: 10.1016/j.jlp.2007.04.001 (cit. on pp. 3, 12, 25, 42).

Di Benedetto, A., P. Russo, P. Amyotte, and N. Marchand (2010). "Modelling the effect of particle size on dust explosions". In: *Chemical Engineering Science* 65.2, pp. 772–779. ISSN: 0009-2509. DOI: 16/j.ces.2009.09.029 (cit. on pp. 10, 67).

Di Blasi, Colomba (1999). "Transition between regimes in the degradation of thermoplastic polymers". In: *Polymer Degradation and Stability* 64.3, pp. 359–367. ISSN: 01413910. DOI: 10.1016/S0141-3910(98)00134-7 (cit. on p. 67).

– (2008). "Modeling chemical and physical processes of wood and biomass pyrolysis". In: *Progress in Energy and Combustion Science* 34.1, pp. 47–90. ISSN: 0360-1285. DOI: 10.1016/j.pecs.2006.12.001 (cit. on pp. 12, 44, 50, 53).

Di Blasi, Colomba and Carmen Branca (2001). "Kinetics of Primary Product Formation from Wood Pyrolysis". In: *Industrial & Engineering Chemistry Research* 40.23, pp. 5547–5556. ISSN: 0888-5885. DOI: 10.1021/ie000997e (cit. on pp. 53, 69–71, 73, 81).

Dufaud, O., L. Perrin, M. Traore, S. Chazelet, and D. Thomas (2009). "Explosions of vapour/dust hybrid mixtures: A particular class". In: *Powder Technology* 190.1, pp. 269–273. ISSN: 0032-5910. DOI: 10.1016/j.powtec.2008.04.046 (cit. on pp. 16, 22, 29–31, A-8, A-12, A-13).

Dufaud, Olivier (2011). *Application des principes de la sécurité intrinsèque aux explosions de poussières : de la modération en toutes choses* (cit. on p. 48).

Dufaud, Olivier and Laurent Perrin (2010). "State of the art: Promotion of early inherently safer design against dust explosions". In: *Chemical Engineering Transactions* 19, pp. 365–370 (cit. on p. 3).

Dufaud, Olivier, Laurent Perrin, and Mamadou Traoré (2008). "Dust/vapour explosions: Hybrid behaviours?" In: *Journal of Loss Prevention in the Process Industries* 21.4, pp. 481–484. ISSN: 0950-4230. DOI: 10.1016/j.jlp.2007.11.005 (cit. on pp. 3, 16, 18).

Dufaud, Olivier, Manon Poupeau, Imad Khalili, Nicolas Cuervo, Mélina Christodoulou, Roberto Olcese, Anthony Dufour, and Laurent Perrin (2012a). "Comparing Pyrolysis Gases and Dusts Explosivities: A Clue to Understanding Hybrid Mixtures Explosions?" In: *Industrial & Engineering Chemistry Research* 51.22, pp. 7656–7662. ISSN: 0888-5885. DOI: 10.1021/ie201646s (cit. on pp. 25, 42, 84).

Dufaud, Olivier, Imad Khalili, Nicolas Cuervo-Rodriguez, Roberto Olcese, Anthony Dufour, Laurent Perrin, and André Laurent (2012b). "Highlighting the Importance of the Pyrolysis Step on Dusts Explosions". In: *Chemical Engineering Transactions*. Vol. 26. Milano, pp. 369–374. ISBN: DOI: 10.3303/CET1226062 (cit. on pp. 25, 42).

Eckhoff, Rolf K. (2003). *Dust Explosions in the Process Industries*. Burlington: Gulf Professional Publishing. ISBN: 978-0-7506-7602-1 (cit. on p. 12).

Font, Rafael, Antonio Marcilla, Emilio Verdu, and Joaquin Devesa (1990). "Kinetics of the pyrolysis of almond shells and almond shells impregnated with cobalt dichloride in a fluidized bed reactor and in a pyroprobe 100". In: *Ind. Eng. Chem. Res.* 29.9, pp. 1846–1855. ISSN: 0888-5885. DOI: 10.1021/ie00105a016 (cit. on pp. 53, 69, 70, 81).

Franke, H. (1978). "Bestimmung der Minderstzudenergie von Kohlenstaub/Methan/Luft Gemisches (hybride. Gemische)". In: *VDI-Berichte* 304, pp. 69–72 (cit. on pp. 8, 9).

Garcia-Agreda, A., A. Di Benedetto, P. Russo, E. Salzano, and R. Sanchirico (2011). "Dust/gas mixtures explosion regimes". In: *Powder Technology* 205.1, pp. 81–86. ISSN: 0032-5910. DOI: 10.1016/j.powtec.2010.08.069 (cit. on pp. 17, 21, 22, 24, 25, 40, 135).

Garcia-Agreda, Anita (2010). "Study of hybrid mixture explosions". Tesi di dottorato, NonPeerReviewed (cit. on pp. 113, 117, 120).

Glor, Martin (2003). "Ignition hazard due to static electricity in particulate processes". In: *Powder Technology*. Electrostatic Phenomena in Particulate Processes

135–136, pp. 223–233. ISSN: 0032-5910. DOI: 10.1016/j.powtec.2003.08.017 (cit. on pp. 2, 10).

Gordon, Sanford and Bonnie J. McBride. *NASA Chemical Equilibrium with Applications (CEA)*. URL: http://www.grc.nasa.gov/WWW/CEAWeb/ (visited on 07/18/2014) (cit. on pp. 18, 19, 26, 115, 119).

– (1994). "Analysis". In: Computer Program for Calculation of Complex Chemical Equilibrium Compositions and Applications: NASA RP 1311 (cit. on pp. 18, 19, 26, 115, 119).

– (1996). "User's Manual and Program Description". In: *Computer Program for Calculation of Complex Chemical Equilibrium Compositions and Applications*. NASA RP 1311 (cit. on pp. 18, 19, 26, 115, 119).

Goroshin, S., I. Fomenko, and J.H.S. Lee (1996). "Burning velocities in fuel-rich aluminum dust clouds". In: *Symposium (International) on Combustion* 26.2, pp. 1961–1967. ISSN: 00820784. DOI: 10.1016/S0082-0784(96)80019-1 (cit. on p. 112).

Han, Jilin, Hiroshi Yamashita, and Naoki Hayashi (2010). "Numerical study on the spark ignition characteristics of a methane–air mixture using detailed chemical kinetics: Effect of equivalence ratio, electrode gap distance, and electrode radius on MIE, quenching distance, and ignition delay". In: *Combustion and Flame* 157.7, pp. 1414–1421. ISSN: 0010-2180. DOI: 10.1016/j.combustflame.2010.02.021 (cit. on pp. 77, 78).

– (2011). "Numerical study on the spark ignition characteristics of hydrogen–air mixture using detailed chemical kinetics". In: *International Journal of Hydrogen Energy* 36.15, pp. 9286–9297. ISSN: 0360-3199. DOI: 10.1016/j.ijhydene.2011.04.190 (cit. on pp. 77, 78).

Haseli, Y., J. A. van Oijen, and L. P. H. de Goey (2011). "Numerical study of the conversion time of single pyrolyzing biomass particles at high heating conditions". In: *Chemical Engineering Journal* 169.1, pp. 299–312. ISSN: 1385-8947. DOI: 10.1016/j.cej.2011.02.073 (cit. on pp. 50, 58, 62).

Hertzberg, M and Kl Cashdollar (1987). "Introduction to Dust Explosions". In: *Industrial Dust Explosions*. Ed. by Kl Cashdollar and M Hertzberg. 100 Barr Harbor Drive, PO Box C700, West Conshohocken, PA 19428-2959: ASTM International, pp. 5–5–28. ISBN: 978-0-8031-0957-5 (cit. on pp. 19, 20).

Hertzberg, M., A. Zlochower, R. S. Conti, and K. L. Cashdollar (1987). *Thermokinetic transport control and structural microscopic realities in coal and polymer pyrolysis and devolatilization. Their dominant role in dust explosions* (cit. on p. 3).

Hertzberg, Martin, Isaac A. Zlochower, and Kenneth L. Cashdollar (1988). "Volatility model for coal dust flame propagation and extinguishment". In: *Symposium (International) on Combustion* 21.1, pp. 325–333. ISSN: 00820784. DOI: 10.1016/S0082-0784(88)80260-1 (cit. on pp. 42, 48).

Huéscar Medina, Clara, Brian MacCoitir, Hamed Sattar, David J. F. Slatter, Herodotos N. Phylaktou, Gordon E. Andrews, and Bernard M. Gibbs (2015). "Comparison of the explosion characteristics and flame speeds of pulverised coals and biomass in the ISO standard 1 m3 dust explosion equipment". In: *Fuel*. The 10th European Conference on Coal Research and its Applications 151, pp. 91–101. ISSN: 0016-2361. DOI: 10.1016/j.fuel.2015.01.009 (cit. on p. 112).

IEC standard 1241-2-1 (1994). *Electrical apparatus for use in the presence of combustible dust. Part 2: Test method section 1: Methods for determining the minimum ignition temperature of dust* (cit. on pp. 8, 43, 84).

ISO 6184-1 (1985). *Explosion protection systems. Part 1 : Determination of explosion indices of combustible dusts in air*. International Standard Organization (cit. on pp. 48, 84).

Juszczak, Lesław, Teresa Fortuna, and Krystyna Wodnicka (2002). "Characteristics of cereal starch granules surface using nitrogen adsorption". In: *Journal of Food Engineering* 54.2, pp. 103–110. ISSN: 0260-8774. DOI: 10.1016/S0260-8774(01)00190-X (cit. on p. 62).

Karathanos, V. T. and G. D. Saravacos (1993). "Porosity and pore size distribution of starch materials". In: *Journal of Food Engineering* 18.3, pp. 259–280. ISSN: 0260-8774. DOI: 10.1016/0260-8774(93)90090-7 (cit. on p. 62).

Karlovitz, Béla, D. W. Denniston, and F. E. Wells (1951). "Investigation of Turbulent Flames". In: *The Journal of Chemical Physics* 19.5, p. 541. ISSN: 00219606. DOI: 10.1063/1.1748289 (cit. on p. 115).

Khalili, Imad (2012). "Sensibilité, sévérité et spécificités des explosions de mélanges hybrides gaz/vapeurs/poussières". PhD thesis. Université de Lorraine (cit. on pp. 79, 91, 113, 117, 120).

Khalili, Imad, Olivier Dufaud, Manon Poupeau, Nicolas Cuervo-Rodriguez, and Laurent Perrin (2012). "Ignition sensitivity of gas–vapor/dust hybrid mixtures". In: *Powder Technology* 217, pp. 199–206. ISSN: 0032-5910. DOI: 10.1016/j.powtec.2011.10.027 (cit. on pp. 9–11, 13–15, 18, 39, A-14).

Kondo, Shigeo, Akifumi Takahashi, and Kazuaki Tokuhashi (2003). "Calculation of minimum ignition energy of premixed gases". In: *Journal of Hazardous Materials* 103.1, pp. 11–23. ISSN: 0304-3894. DOI: 10.1016/S0304-3894(03)00226-7 (cit. on p. 15).

Landau, L.D (1944). "On the theory of slow combustion". In: *Acta Physicochimica URSS* 19, pp. 77–85 (cit. on p. 115).

Laurent, André (2011). *Sécurité des procédés chimiques. Connaissances et méthodes d'analyse des risques (2° Éd.)* Lavoisier. 634 pp. ISBN: 978-2-7430-6396-2 (cit. on p. 8).

Law, Chung K. (2006). *Combustion physics*. Cambridge University Press. 741 pp. ISBN: 978-0-521-87052-8 (cit. on pp. 23, 24).

Lees, Frank (2012). *Lees' Loss Prevention in the Process Industries: Hazard Identification, Assessment and Control*. Butterworth-Heinemann. 3685 pp. ISBN: 978-0-12-397782-3 (cit. on pp. 9, 15).

Levenspiel, Octave (1989). *The chemical reactor omnibook*. Distributed by OSU Book Stores. 720 pp. (cit. on p. 12).

Liu, Yi, Jinhua Sun, and Dongliang Chen (2007). "Flame propagation in hybrid mixture of coal dust and methane". In: *Journal of Loss Prevention in the Process Industries*. Selected Papers Presented at the Sixth International Symposium on Hazards, Prevention and Mitigation of Industrial ExplosionsSixth International Symposium on Hazards, Prevention, and Mitigation of Industrial Explosions 20.4, pp. 691–697. ISSN: 0950-4230. DOI: 10.1016/j.jlp.2007.04.029 (cit. on p. 112).

Markstein, G H (Ed.) (1964). *Nonsteady Flame Propagation*. Pergamon Press (cit. on pp. 115, 116, 120, 132).

Mazurkiewicz, J., J. Jarosinski, and P. Wolanski (1993). "Investigations of burning properties of cornstarch dust-air flame". In: *Archivum Combustionis* 13, pp. 189–189 (cit. on p. 45).

Milosavljevic, Ivan, Vahur Oja, and Eric M. Suuberg (1996). "Thermal Effects in Cellulose Pyrolysis: Relationship to Char Formation Processes". In: *Industrial & Engineering Chemistry Research* 35.3, pp. 653–662. ISSN: 0888-5885. DOI: 10.1021/ie9504381 (cit. on pp. 58, 62).

Munson, Bruce Roy (2009). *Fundamentals of fluid mechanics*. In collab. with T. H. Okiishi and Wade W. Huebsch. 6th ed. Hoboken, NJ: J. Wiley & Sons. 1 p. ISBN: 978-0-470-26284-9 (cit. on p. 97).

Padet, Jacques (2015). "Convection thermique et massique Nombre de Nusselt : partie 1". In: *Techniques de l'ingénieur Transferts thermiques* base documentaire : TIB214DUO. (ref. article : be8206). fre (cit. on pp. 60, 62).

Pellmont, Günther (1979). "Explosions und Zündverhalten von hybriden Gemischen aus brennbaren Stäuben und Brenngasen". PhD thesis (cit. on pp. 8, 9, 16).

– (1980). "Minimum Ignition Energy of Combustible Dusts and Explosion Behaviour of Hybrid Mixtures". In: 3rd International Symposium on Loss Prevention and Safety Promotion in the Process Industries. Vol. 3. Basel, Switzerland, pp. 851–862 (cit. on p. 8).

Proust, C. and B. Veyssiere (1988). "Fundamental Properties of Flames Propagating in Starch Dust-Air Mixtures". In: *Combustion Science and Technology* 62.4, pp. 149–172. ISSN: 0010-2202. DOI: 10.1080/00102208808924007 (cit. on p. 112).

Proust, Ch. (2006a). "A few fundamental aspects about ignition and flame propagation in dust clouds". In: *Journal of Loss Prevention in the Process Industries* 19.2, pp. 104–120. ISSN: 0950-4230. DOI: 10.1016/j.jlp.2005.06.035 (cit. on pp. 13, 15, 44, 48).

Proust, Christophe (2006b). "Flame propagation and combustion in some dust-air mixtures". In: *Journal of Loss Prevention in the Process Industries* 19.1, pp. 89–100. ISSN: 0950-4230. DOI: 10.1016/j.jlp.2005.06.026 (cit. on p. 112).

Sanchirico, R., A. Di Benedetto, A. Garcia-Agreda, and P. Russo (2011). "Study of the severity of hybrid mixture explosions and comparison to pure dust–air and vapour–air explosions". In: *Journal of Loss Prevention in the Process Industries* 24.5, pp. 648–655. ISSN: 0950-4230. DOI: 10.1016/j.jlp.2011.05.005 (cit. on pp. 21, 22, 24, 26–29, 40, 84, A-10).

Schneider, H. (2006). "Measurement of turbulent burning velocities by means of the open tube method". In: *Journal of Loss Prevention in the Process Industries* 19.2, pp. 130–134. ISSN: 0950-4230. DOI: 10.1016/j.jlp.2005.05.018 (cit. on p. 112).

Schneider, H. and Ch. Proust (2007). "Determination of turbulent burning velocities of dust air mixtures with the open tube method". In: *Journal of Loss Prevention in the Process Industries* 20.4, pp. 470–476. ISSN: 0950-4230. DOI: 16/j.jlp.2007.04.035 (cit. on p. 112).

Skjöld (2003). *selected aspects of turbulence and combustion in 20L explosion vessels* (cit. on p. 112).

Tamanini, Francesco (1990). "Turbulence effects on dust explosion venting". In: *Plant/Operations Progress* 9.1, pp. 52–60. ISSN: 1549-4632. DOI: 10.1002/prsb.720090111 (cit. on p. 85).

– (1998). "The role of turbulence in dust explosions". In: *Journal of Loss Prevention in the Process Industries* 11.1, pp. 1–10. ISSN: 0950-4230. DOI: 10.1016/S0950-4230(97)00026-0 (cit. on p. 85).

Tamanini, Francesco and John V. Valiulis (1996). "Improved guidelines for the sizing of vents in dust explosions". In: *Journal of Loss Prevention in the Process Industries* 9.1, pp. 105–118. ISSN: 0950-4230. DOI: 10.1016/0950-4230(95)00053-4 (cit. on p. 85).

taylor (1991). *Burning velocity and the influence of flame stretch* (cit. on p. 112).

Traore, Mamadou (2007). *Explosions de poussières et de mélanges hybrides: étude paramétrique et relation entre la cinétique de combustion et la violence de l'explosion.* 1 vols. France. 287 pp. (cit. on pp. 22, 29, 30, A-9).

Van der Wel, Peter G. J. (1993). "Ignition and propagation of dust explosions". info:eu-repo/semantics/doctoralthesis. Delft University Press (cit. on pp. 10, 11, 48, 112).

Vargaftik, Natan B. (1993). *Handbook of Thermal Conductivity of Liquids and Gases*. CRC Press. 362 pp. ISBN: 978-0-8493-9345-7 (cit. on p. 62).

Wagenaar, B. M., W. Prins, and W. P. M. van Swaaij (1993). "Flash pyrolysis kinetics of pine wood". In: *Fuel Processing Technology*. Third International Rolduc Symposium on Coal Science and Technology and Related Processes 36.1, pp. 291–298. ISSN: 0378-3820. DOI: 10.1016/0378-3820(93)90039-7 (cit. on pp. 53, 67, 69, 70, 73, 74).

Wang, Shuangfeng, Yikang Pu, Fu Jia, Artur Gutkowski, and Jozef Jarosinski (2006a). "An experimental study on the flame propagation in cornstarch dust clouds". In: *Combustion Science and Technology* 178.10, pp. 1957–1975. ISSN: 0010-2202, 1563-521X. DOI: 10.1080/00102200600790979 (cit. on p. 112).

Wang, Shuangfeng, Yikang Pu, Jia Fu, and Artur Gutkowski (2006b). "Effect of turbulence on flame propagation in cornstarch dust-air mixtures". In: *Journal of Thermal Science* 15.2, pp. 186–192. ISSN: 1003-2169. DOI: 10.1007/s11630-006-0186-4 (cit. on pp. 84, 85, 87).

Welty, James R., ed. (2008). *Fundamentals of momentum, heat, and mass transfer*. 5th ed. Danver, MA: Wiley. 711 pp. ISBN: 978-0-470-12868-8 (cit. on p. 62).

Appendixes

Appendix A
Experimental Data

Contents

A.1. Severity data

A.1.1. Starch/Methane

The following data of the explosions of hybrid mixtures where obtained in the 20 l sphere in the LRGP and in the University of Naples Federico II.

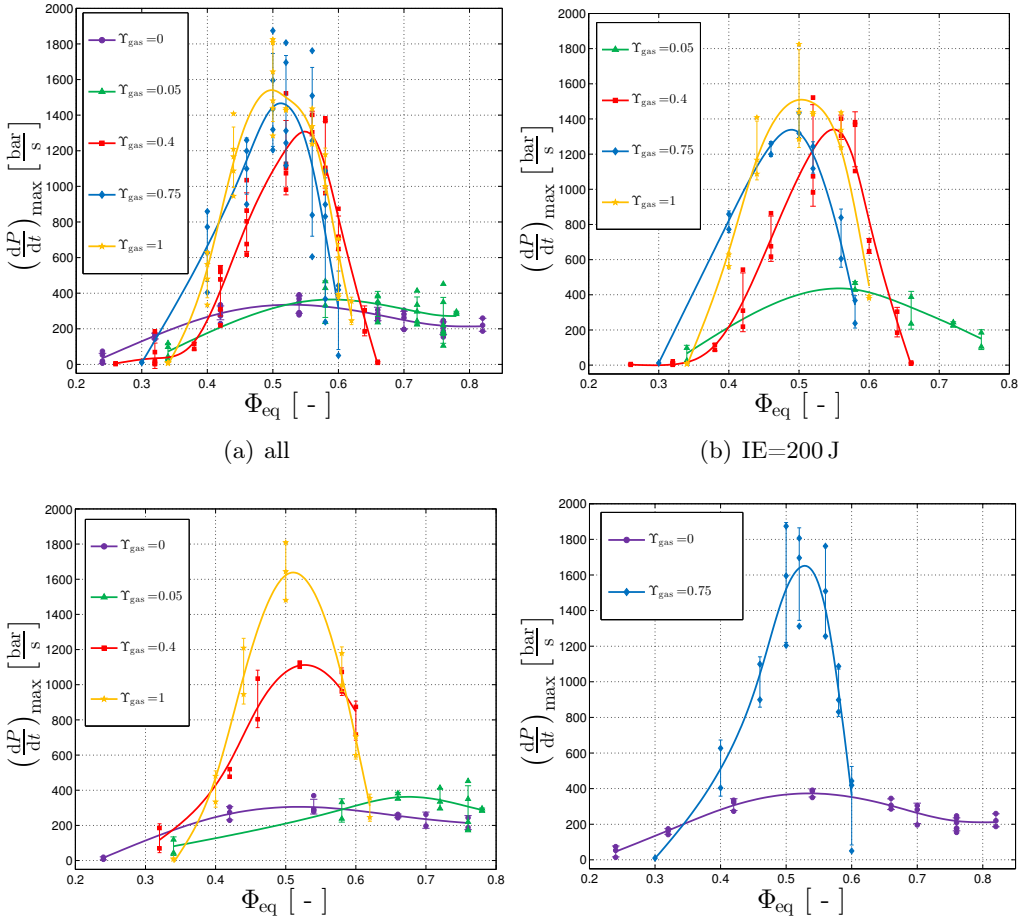

(a) all

(b) IE=200 J

(c) IE=500 J

(d) IE=1000 J

Figure A.1. Experimental results of pressure rise rate, $\left(\frac{dP}{dt}\right)_{max}$ for starch-methane mixtures, separated according to the ignition energy of the chemical igniters used

Table A.1. Explosivity values for starch-methane mixtures

C_{dust} $\frac{\text{g}}{\text{m}^3}$	y_{gas} %v/v	P_m bar	$\left(\frac{\text{d}P}{\text{d}t}\right)_{\text{max}}$ $\frac{\text{bar}}{\text{s}}$	t_{v} ms	IE J	P_{ip} bar	t_{ip} ms	comments
229.1	0.00	0.1	7	60	500	0.1	99.00	
229.1	0.00	2.7	19	60	500	0.6	157.00	
534.5	0.00	7.5	274	60	500	3.6	129.25	
534.5	0.00	0.1	1	60	500	0.1	402.37	
534.5	0.00	7.5	229	60	500	3.2	131.25	
534.5	0.00	7	161	60	500	3	138.50	
534.5	0.00	6	110	60	500	3.4	174.75	
534.5	0.00	8.1	304	60	500	3.9	130.75	just cleaned sphere
916.2	0.00	6.8	188	59	500	2.9	133.00	
916.2	0.00	8.3	278	59	500	3.4	144.50	
916.2	0.00	6.9	195	60	500	3	133.50	
916.2	0.00	7.3	179	60	500	3.7	138.25	
916.2	0.00	8.4	369	59	500	3.7	132.50	clean sphere
916.2	0.00	8.6	291	59	500	3.8	137.00	
916.2	0.00	8.3	288	59	500	4.1	141.75	
1532.9	0.00	7.6	243	60	500	3.9	142.00	
1532.9	0.00	7.7	256	59	500	3.8	133.25	
1532.9	0.00	7.8	263	60	500	4	126.75	
1853.3	0.00	7.3	197	60	500	4	149.75	
1853.3	0.00	7.6	262	60	500	4.3	136.25	
2315.9	0.00	6.9	188	60	500	3.5	127.25	
2315.9	0.00	7.3	244	60	500	4	139.00	
324.4	0.76	3.7	44	60	500	1.6	170.25	
324.4	0.76	5.2	119	60	500	2.6	148.75	
854.3	2.00	7.3	238	60	500	3.2	124.25	
854.3	2.00	7.8	332	60	500	3.8	127.00	bomba pulita
1200.2	2.81	7.5	382	60	500	3.5	122.75	
1200.2	2.81	7.6	352	60	500	4.1	119.75	
1540.5	3.60	7.3	414	60	500	3.9	117.00	
1540.5	3.60	7.3	335	60	500	4.1	130.75	
1540.5	3.60	7.1	297	60	500	3.7	120.00	
1875.2	4.40	6.4	172	60	500	2.6	150.50	
1875.2	4.40	6.8	452	59	500	3.6	126.00	
1875.2	4.40	7.2	350	60	500	4.2	144.75	bomba pulita
1875.2	4.40	6.4	220	60	500	3.6	133.50	bomba pulita con carta e un poco de acqua
2095.3	4.91	6.4	296	60	500	3.1	132.50	
2095.3	4.91	6.6	283	59	500	3.8	125.25	
106.6	3.41	4.5	69	60	500	2.6	194.75	
106.6	3.41	5.2	185	60	500	2.7	137.00	
156.6	5.01	6.5	520	60	500	3.8	102.60	
156.6	5.01	6.5	477	60	500	3.7	100.10	
190.1	6.08	7.7	1035	60	500	4.2	95.18	CH4 6.4
190.1	6.08	7.6	804	60	500	4	95.17	
231.9	7.42	7.9	1102	59	500	4.4	91.18	
231.9	7.42	7.9	1126	60	500	3.9	86.74	
285.9	9.20	7.6	1323	60	500	4	88.96	
285.9	9.20	7.6	962	60	500	4.2	103.51	
285.9	9.20	7.5	1073	60	500	4.4	91.91	*posible mistake of typing found int he ksep file as: 258,95

(Continues on next page)

Table A.1 Explosivity values for starch-methane mixtures

(continued from previous page)

C_{dust} $\frac{\text{g}}{\text{m}^3}$	y_{gas} %v/v	P_m bar	$\left(\frac{\text{d}P}{\text{d}t}\right)_{\text{max}}$ $\frac{\text{bar}}{\text{s}}$	t_{v} ms	IE J	P_{ip} bar	t_{ip} ms	comments
319.3	10.22	7.2	717	59	500	4.1	119.64	
319.3	10.22	7.1	874	60	500	3.7	93.10	
0.0	5.35	0.1	10	60	500	0.1	79.62	
0.0	5.35	0.2	8	60	500	0.1	81.86	
0.0	6.54	5.4	334	60	500	3.4	132.75	
0.0	6.54	5.9	480	60	500	3.9	121.91	
0.0	7.91	6.7	1209	59	500	4.1	87.93	
0.0	7.91	6.9	945	60	500	4	92.32	
0.0	9.50	6.3	1134	60	500	3.3	84.81	
0.0	9.50	7.7	1809	60	500	4.2	80.37	
0.0	9.50	7.9	1481	60	500	4.4	90.10	
0.0	9.50	7.9	1644	60	500	4.7	89.92	
0.0	12.44	7.9	1178	59	500	4.2	92.41	
0.0	12.44	7.9	999	60	500	4.5	108.14	
0.0	13.60	7.6	705	60	500	4.3	108.97	
0.0	13.60	7.4	599	60	500	4.2	126.00	
0.0	15.00	7.1	355	60	500	4.4	140.75	
0.0	15.00	6.9	246	60	500	3.9	183.75	
44.0	6.05	6.3	772	60	200	3.5	86.49	
70.5	9.70	7.1	1244	60	200	3.8	87.81	
44.0	6.05	6.1	859	60	200	3.3	91.43	
53.1	7.30	6.7	1259	60	200	3.6	83.06	
63.9	8.78	6.9	1319	60	200	4.1	85.33	
70.5	9.70	6.8	1118	60	200	3.8	89.11	
76.8	10.56	6.5	605	60	200	3.7	103.77	
84.3	11.60	5.9	238	60	200	3.7	157.00	
92.8	12.76	0.1	8	60	200	0.1	79.20	
63.9	8.78	7.2	1435	60	200	3.8	82.58	
76.8	10.56	6.9	839	60	200	3.9	100.46	
84.3	11.60	6.2	368	60	200	3.7	141.25	
92.8	12.76	0.1	6	60	200	0.1	81.20	
28.3	3.89	0.1	12	60	200	0.1	80.80	
53.1	7.30	6.9	1199	60	200	3.8	83.49	
0.0	5.35	4.2	46	60	200	2.3	372.14	Pas d'explosion 3 fois sur 5 : point enlevé
0.0	9.50	7.4	1825	60	200	4.4	81.41	
0.0	10.40	7.6	1889	60	200	4.5	80.71	
0.0	6.50	5.6	562	60	200	3.4	111.21	
0.0	11.40	7.6	1237	60	200	3.9	86.29	
0.0	7.90	6.6	1408	60	200	3.7	82.79	
0.0	13.60	6.8	380	60	200	3.7	125.28	
0.0	5.35	3.2	7	60	200	3	1627.00	Pas d'explosion 3 fois sur 5 : point enlevé
0.0	5.35	0.1	6	60	200	0.1	78.80	
0.0	5.35	0.1	9	60	200	0.1	76.95	
0.0	6.50	5.8	628	60	200	3.4	101.20	
0.0	7.90	6.7	1167	60	200	3.6	82.83	
0.0	9.50	7.5	1439	60	200	4.1	80.48	
0.0	10.40	7.7	1437	60	200	3.9	80.48	
0.0	11.40	7.5	1436	60	200	3.9	85.39	
0.0	13.60	6.5	393	60	200	3.9	110.17	

(Continues on next page)

Table A.1 Explosivity values for starch-methane mixtures

(continued from previous page)

C_{dust} $\frac{\text{g}}{\text{m}^3}$	y_{gas} %v/v	P_m bar	$\left(\frac{\text{d}P}{\text{d}t}\right)_{\text{max}}$ $\frac{\text{bar}}{\text{s}}$	t_{v} ms	IE J	P_{ip} bar	t_{ip} ms	comments
0.0	5.35	0.1	7	60	200	0.1	78.56	
0.0	7.90	6.6	1087	60	200	3.1	80.38	
0.0	9.50	7.4	1284	60	200	3.1	78.11	
0.0	10.40	7.5	1427	60	200	4.2	79.07	
0.0	11.40	7.6	1337	60	200	3.8	84.10	
231.9	7.42	8	1522	60	200	4.2	83.30	
319.3	10.22	7.2	708	60	200	4.1	100.47	
75.0	2.40	0	2	60	200	0.1	80.67	
106.6	3.41	3.6	21	60	200	0.8	140.00	
106.6	3.41	0.3	11	60	200	0.1	77.00	
129.3	4.14	5.2	87	60	200	3.2	134.75	
156.6	5.01	6.1	219	60	200	3.3	121.75	
75.0	2.40	0	6	60	200	0.1	76.87	
190.1	6.08	7.2	676	60	200	4.4	93.25	
231.9	7.42	7.7	1074	60	200	4.1	83.59	
285.9	9.15	7.9	1104	60	200	4.1	85.89	
319.3	10.22	7.6	648	60	200	4.4	97.35	
358.3	11.46	7.1	304	60	200	4.6	169.25	
106.6	3.41	0.2	2	60	200	0.1	644.00	
106.6	3.41	0.1	4	60	200	0.1	83.95	
156.6	5.01	6.4	310	60	200	3.6	107.51	
129.3	4.14	0.2	1	60	200	0.1	78.00	
129.3	4.14	5.4	116	60	200	2.1	116.00	
190.1	6.08	7.1	617	60	200	3.7	95.03	
285.9	9.15	7.9	1367	60	200	4.2	82.62	
231.9	7.42	7.8	982	60	200	4.3	84.49	
259.1	8.29	8	1304	60	200	4.5	87.32	
156.6	5.01	6.6	543	60	200	3.4	97.52	
259.1	8.29	8.1	1402	60	200	4.2	81.78	
404.5	12.94	0	9	60	200	0.1	74.89	
106.6	3.41	0.4	2	60	200	0.3	308.88	
190.1	6.08	7.3	864	60	200	3.8	88.30	
285.9	9.15	7.6	1382	60	200	4.4	87.05	
358.3	11.46	6.6	185	60	200	3.9	200.00	
404.5	12.94	0	15	60	200	0.1	80.78	
854.3	2.00	8.1	467	60	200	3.9	109.97	
1200.2	2.81	7.4	236	60	200	3.6	124.50	
1540.5	3.61	6.6	224	60	200	4.2	129.00	
1875.2	4.39	5.8	105	60	200	2.8	123.25	
324.4	0.76	3.4	26	60	200	0.8	128.75	
854.3	2.00	8.2	429	60	200	4	111.59	
1200.2	2.81	7.8	388	60	200	3.9	116.75	
1540.5	3.61	7	243	60	200	4.3	162.75	
1875.2	4.39	6.2	185	60	200	3.3	115.00	
324.4	0.76	4.7	98	60	200	1.5	114.00	
28.3	3.89	0.3	10	60	1000	0.1	75.00	
44.0	6.05	6.3	627	60	1000	3.3	88.69	
53.1	7.30	6.9	1099	60	1000	3.7	79.16	nettoyage de la sphère + papillon
63.9	8.78	7.5	1874	60	1000	4.6	76.43	
70.5	9.70	7.8	1696	60	1000	4.6	82.03	

(Continues on next page)

Table A.1 Explosivity values for starch-methane mixtures

(continued from previous page)

C_{dust} $\frac{\mathrm{g}}{\mathrm{m}^3}$	y_{gas} %v/v	P_m bar	$\left(\frac{\mathrm{d}P}{\mathrm{d}t}\right)_{\mathrm{max}}$ $\frac{\mathrm{bar}}{\mathrm{s}}$	t_{v} ms	IE J	P_{ip} bar	t_{ip} ms	comments
76.8	10.56	7.9	1509	60	1000	4.9	83.64	Nettoyage sphere + papillon
84.3	11.60	7.5	1087	60	1000	4.1	85.13	
28.3	3.89	0.1	11	60	1000	0.1	72.40	
63.9	8.78	7.9	1204	60	1000	4.8	77.43	nettoyage + démontage
70.5	9.70	8.1	1312	60	1000	4.2	81.98	montage de la sphère
76.8	10.56	7.9	1256	60	1000	4.7	80.61	
84.3	11.60	7.5	831	60	1000	4	83.96	
84.3	11.60	7.5	898	60	1000	4.1	83.58	nettoyage sphère + papillon
92.8	12.76	5.6	50	60	1000	4	232.25	
92.8	12.76	6.9	419	60	1000	3.8	92.57	
92.8	12.76	7.1	443	60	1000	4.1	98.20	
44.0	6.05	6	404	60	1000	3.3	91.60	nettoyage sphère + papillon
53.1	7.30	7	899	60	1000	3.9	84.09	
63.9	8.78	7.8	1595	60	1000	4.3	79.36	
70.5	9.70	7.9	1807	60	1000	4.3	75.18	
76.8	10.58	8	1762	60	1000	4.6	79.40	démontage sphère
229.1	0.00	1.9	14	60	1000	0.4	101.25	nettoyage complet
229.1	0.00	4.3	74	60	1000	2.5	129.50	nettoyage complet
343.6	0.00	5.2	142	60	1000	2.5	108.50	nettoyage complet
343.6	0.00	5.2	174	60	1000	3.4	115.75	nettoyage complet
343.6	0.00	5.2	162	60	1000	2.7	113.50	nettoyage complet
229.1	0.00	3.8	53	60	1000	1.9	120.75	nettoyage complet
534.5	0.00	7.4	273	60	1000	3.8	110.00	nettoyage complet
534.5	0.00	8.1	335	60	1000	4	101.15	nettoyage complet
534.5	0.00	7.7	323	60	1000	3.2	97.25	nettoyage complet
916.2	0.00	8.4	350	60	1000	3.9	99.81	nettoyage complet
916.2	0.00	8.6	391	60	1000	4.4	104.06	nettoyage complet
916.2	0.00	8.6	386	60	1000	4	115.75	nettoyage complet
1532.9	0.00	7.7	345	60	1000	4.1	117.00	nettoyage complet
1532.9	0.00	7.6	306	60	1000	3.6	105.38	nettoyage complet
1532.9	0.00	7.6	286	60	1000	3.9	111.81	nettoyage complet
1853.3	0.00	7.5	305	60	1000	3.7	124.00	nettoyage complet
1853.3	0.00	7.2	196	60	1000	3.2	112.25	nettoyage complet
1853.3	0.00	7.5	282	60	1000	4.1	122.25	nettoyage complet
2315.9	0.00	6.8	176	60	1000	3.4	125.25	nettoyage complet
2315.9	0.00	6.9	177	60	1000	4.1	126.50	nettoyage complet
2315.9	0.00	6.5	209	60	1000	3.4	127.50	nettoyage complet
2315.9	0.00	7.1	154	60	1000	3.5	124.25	nettoyage complet
2315.9	0.00	6.9	247	60	1000	3.5	117.75	nettoyage complet
2315.9	0.00	7.6	234	60	1000	4.3	124.50	nettoyage complet
3567.0	0.00	7	220	60	1000	4.1	138.00	nettoyage complet
3567.0	0.00	7	187	60	1000	4.5	165.25	nettoyage complet
3567.0	0.00	8.2	260	60	1000	4.6	130.75	nettoyage complet

A.1.2. Telithromycin/Toluene

Table A.2. Explosivity values for telithromycin-toluene mixtures.(Dufaud et al., 2009)

C_{dust} $\frac{\mathrm{g}}{\mathrm{m}^3}$	y_{gas} %v/v	P_{m} bar	$\left(\frac{\mathrm{d}P}{\mathrm{d}t}\right)_{\mathrm{max}}$ $\frac{\mathrm{bar}}{\mathrm{s}}$	t_{v} ms	C_{dust} $\frac{\mathrm{g}}{\mathrm{m}^3}$	y_{gas} %v/v	P_{m} bar	$\left(\frac{\mathrm{d}P}{\mathrm{d}t}\right)_{\mathrm{max}}$ $\frac{\mathrm{bar}}{\mathrm{s}}$	t_{v} ms
125	0.0	5.9	247	60	0	2.2	7.9	796	60
250	0.0	8.1	693	60	250	2.2	8.1	1624	60
500	0.0	8.1	727	60	500	2.2	7.3	1227	60
750	0.0	7.5	615	60	750	2.2	7.2	1183	60
1000	0.0	7.1	531	60	1000	2.2	6.6	949	60
0	0.6	1.7	70	60	0	5.5	8.4	1183	60
125	0.6	7.3	625	60	125	5.5	8.7	1841	60
250	0.6	8.2	996	60	250	5.5	7.7	1491	60
500	0.6	7.8	732	60	500	5.5	6.5	837	60
750	0.6	7.3	821	60	750	5.5	5.7	378	60
1000	0.6	7	757	60	1000	5.5	5.5	445	60
0	1.1	4.5	133	60	0	7.7	8.9	1620	60
125	1.1	8.5	1101	60	125	7.7	8.3	1276	60
250	1.1	8.5	1208	60	250	7.7	7.8	1353	60
500	1.1	7.9	1062	60	500	7.7	6.5	776	60
750	1.1	7.3	998	60	750	7.7	5.9	365	60
1000	1.1	6.9	880	60	1000	7.7	5.5	291	60
0	1.7	6.7	495	60	0	9.9	8.4	1280	60
125	1.7	8.1	1350	60	125	9.9	8.6	1379	60
250	1.7	7.8	1126	60	500	9.9	7.3	1134	60
500	1.7	7.3	1431	60	750	9.9	6.4	817	60
750	1.7	6.6	1058	60	1000	9.9	6.2	971	60
1000	1.7	6.3	888	60					

A.1.3. Telithromycin/Acetone

Table A.3. Explosivity values for telithromycin-acetone mixtures. (Traore, 2007)

C_{dust} $\frac{\text{g}}{\text{m}^3}$	y_{gas} %v/v	P_{m} bar	$\left(\frac{\text{d}P}{\text{d}t}\right)_{\text{max}}$ $\frac{\text{bar m}}{\text{s}}$	t_{v} ms
125	0	5.9	247	60
250	0	8.1	693	60
500	0	8.1	727	60
750	0	7.5	615	60
1000	0	7.1	531	60
0	0.016	3	46	60
125	0.016	7.8	762	60
250	0.016	8.1	879	60
500	0.016	8.1	857	60
750	0.016	7.2	717	60
1000	0.016	5.9	528	60
0	0.048	8.8	1306	60
125	0.048	8.8	1706	60
250	0.048	8.1	1588	60
500	0.048	6.9	1112	60
750	0.048	6.4	941	60
1000	0.048	5.9	714	60
0	0.096	6.7	229	60
125	0.096	6	122	60
250	0.096	5.8	52	60
500	0.096	5.9	44	60
750	0.096	5.7	61	60
1000	0.096	5	37	60
0	0.192	4.6	26	60
125	0.192	5.1	37	60
250	0.192	4.7	14	60
500	0.192	4.3	9	60
750	0.192	0.1	1	60
1000	0.192	0	0	60

A.1.4. Niacin/Acetone

Table A.4. Explosivity values for niacin-acetone mixtures. Data extracted from (Sanchirico et al., 2011)

C_{dust} $\frac{\text{g}}{\text{m}^3}$	y_{gas} %v/v	K_{st} $\frac{\text{bar m}}{\text{s}}$	t_{v} ms	C_{dust} $\frac{\text{g}}{\text{m}^3}$	y_{gas} %v/v	K_{st} $\frac{\text{bar m}}{\text{s}}$	t_{v} ms
312	0.00	98.5	60	125	2.50	362.5	30
312	0.00	22.5	120	62	2.50	222.5	30
125	0.00	8.5	30	62	2.55	169.5	60
125	0.00	9.5	60	30	2.55	23.5	30
125	0.00	8	30	30	2.55	18.5	120
125	0.00	9	60	62	2.55	70.5	120
125	0.00	0	120	0	2.55	7	120
250	0.00	94	30	125	2.55	134	120
250	0.00	83	60	100	2.55	118.5	120
250	0.00	20.5	120	0	2.85	19	60
312	0.00	98	60	0	3.30	61.5	60
500	0.00	156.5	30	30	3.50	347.5	30
500	0.00	130	60	0	3.50	115	30
500	0.00	52.5	120	0	3.55	84.5	120
750	0.00	56	120	62	3.80	314.5	60
750	0.00	127.5	60	100	3.80	347.5	60
750	0.00	144	30	62	3.80	503.5	30
1000	0.00	50.5	120	62	3.80	233.5	120
1000	0.00	133	30	30	3.80	165	120
1000	0.00	90.5	60	125	4.25	430.5	60
100	0.70	10.5	60	0	4.35	342.5	60
125	0.70	31.5	60	30	4.35	401.5	60
312	0.70	161	60	100	4.35	446	60
0	0.70	0	120	312	4.40	285.5	60
125	0.70	0.5	120	125	4.45	280	120
312	0.70	51	120	312	4.50	333	30
312	0.70	233	30	125	4.50	490	30
125	0.70	93.5	30	30	4.50	654.5	30
100	0.70	50	30	100	4.50	559.5	30
62	1.25	50	30	0	4.50	496.5	30
62	1.25	0	30	312	4.50	270.5	120
62	1.25	4	60	0	4.55	228	120
100	1.30	79	60	100	4.55	270.5	120
125	1.35	32.5	120	30	4.55	270.5	120
312	1.35	82.5	120	0	5.30	495.5	60
30	1.35	51	60	125	6.35	289.5	60
312	1.35	198	60	100	6.35	374	30
125	1.40	110	60	312	6.35	230	30

Continued on next page

Table A.4. Explosivity values for niacin-acetone mixtures
(continued from previous page)

C_{dust} $\frac{\text{g}}{\text{m}^3}$	y_{gas} %v/v	K_{st} $\frac{\text{bar m}}{\text{s}}$	t_{v} ms	C_{dust} $\frac{\text{g}}{\text{m}^3}$	y_{gas} %v/v	K_{st} $\frac{\text{bar m}}{\text{s}}$	t_{v} ms
0	1.45	0	120	0	6.35	628.5	30
100	1.50	122	30	125	6.40	388	30
312	1.50	306.5	30	0	6.40	493.5	60
125	1.50	207.5	30	100	6.40	308.5	120
100	1.90	22.5	120	30	6.45	349.5	60
62	1.95	55.5	60	312	6.45	213	60
62	2.00	34.5	30	125	6.45	235	120
62	2.05	107.5	30	100	6.45	272	60
100	2.45	208	60	30	6.50	296.5	120
312	2.45	253	60	312	6.50	189.5	120
30	2.45	41	60	30	6.50	600	30
312	2.50	141	120	0	6.50	307	120
30	2.50	16	30	0	7.15	282.5	120
100	2.50	306	30	0	7.45	422	60
0	2.50	10	30	30	7.50	441.5	30
312	2.50	354.5	30	0	7.50	512.5	30
125	2.50	243	60				

A.1.5. Niacin/Diisopropyl-ether

Table A.5. Explosivity values for niacin/diisopropyl-ether mixtures. (Dufaud et al., 2009)

C_{dust} $\frac{\mathrm{g}}{\mathrm{m}^3}$	y_{gas} %v/v	P_{m} bar	$\left(\frac{\mathrm{d}P}{\mathrm{d}t}\right)_{\mathrm{max}}$ $\frac{\mathrm{bar\,m}}{\mathrm{s}}$	t_{v} ms
60	0.0	2.5	64	60
125	0.0	5.2	252	60
250	0.0	6.7	422	60
500	0.0	8.4	673	60
750	0.0	7.7	670	60
1000	0.0	6.7	425	60
1250	0.0	6	361	60
1500	0.0	5.6	231	60
0	0.3	0	0	60
125	0.3	4.8	214	60
250	0.3	7.9	973	60
500	0.3	8.5	1145	60
750	0.3	7.6	849	60
1000	0.3	6.9	625	60
0	0.9	2.8	37	60
60	0.9	6.3	546	60
125	0.9	8	1059	60
250	0.9	8.8	1296	60
500	0.9	8.3	1123	60
750	0.9	7.4	1147	60
1000	0.9	5.9	591	60
0	1.7	7.5	616	60
60	1.7	7.5	696	60
125	1.7	8.9	1572	60
250	1.7	8.8	1725	60
500	1.7	7.5	1180	60
750	1.7	6.9	858	60
1000	1.7	5.9	389	60
0	2.6	8.8	1306	60
60	2.6	9	1553	60
125	2.6	8.6	1580	60
250	2.6	8	1083	60
500	2.6	6.5	302	60
750	2.6	5.9	116	60
1000	2.6	5	40	60
0	3.4	8.3	920	60
60	3.4	8.5	1067	60
125	3.4	8.2	1100	60

Table A.5. Explosivity values for niacin/diisopropyl-ether mixtures. (Dufaud et al., 2009)

C_{dust} $\frac{\mathrm{g}}{\mathrm{m}^3}$	y_{gas} %v/v	P_{m} bar	$\left(\frac{\mathrm{d}P}{\mathrm{d}t}\right)_{\mathrm{max}}$ $\frac{\mathrm{bar\,m}}{\mathrm{s}}$	t_{v} ms
250	3.4	7.2	486	60
500	3.4	6.1	85	60
750	3.4	5.7	67	60

A.1.6. Starch/Pyrolysis Gases

Table A.6. Explosivity values for starch/pyrolysis gases mixtures. Khalili et al., 2012

C_{dust} $\frac{\mathrm{g}}{\mathrm{m}^3}$	y_{gas} %v/v	P_{m} bar	$\left(\frac{\mathrm{d}P}{\mathrm{d}t}\right)_{\mathrm{max}}$ $\frac{\mathrm{bar}}{\mathrm{s}}$	t_{v} ms	C_{dust} $\frac{\mathrm{g}}{\mathrm{m}^3}$	y_{gas} %v/v	P_{m} bar	$\left(\frac{\mathrm{d}P}{\mathrm{d}t}\right)_{\mathrm{max}}$ $\frac{\mathrm{bar}}{\mathrm{s}}$	t_{v} ms
0	5%	0	4	60	534.45	0%	8.1	304	60
0	7%	0	5	60	534.45	0%	7.4	273	60
0	8%	3.4	86	60	534.45	0%	8.1	335	60
0	10%	5.2	514	60	534.45	0%	7.7	323	60
0	12%	5.6	928	60	916.20	0%	8.3	278	60
0	15%	6.5	1133	60	916.20	0%	8.4	369	60
0	16%	6.7	1306	60	916.20	0%	8.6	291	60
0	17%	6.8	1301	60	916.20	0%	8.3	288	60
0	19%	7.1	1384	60	916.20	0%	8.4	350	60
0	20%	7.4	1468	60	916.20	0%	8.6	391	60
0	20%	7.5	1570	60	916.20	0%	8.6	386	60
0	23%	7.5	1579	60	1532.90	0%	7.6	243	60
0	30%	7	1351	60	1532.90	0%	7.7	256	60
50	18%	7.5	1479	60	1532.90	0%	7.8	263	60
100	16%	7.4	1419	60	1532.90	0%	7.7	345	60
150	14%	7.1	1266	60	1532.90	0%	7.6	306	60
200	12%	7.3	1173	60	1532.90	0%	7.6	286	60
250	10%	6.8	406	60	1853.25	0%	7.3	197	60
250	10%	6.6	874	60	1853.25	0%	7.6	262	60
300	8%	7.1	673	60	1853.25	0%	7.5	305	60
350	6%	7.4	544	60	1853.25	0%	7.2	196	60
400	4%	7.8	531	60	1853.25	0%	7.5	282	60
450	2%	7.1	267	60	2315.95	0%	6.9	188	60
229.05	0%	0.1	7	60	2315.95	0%	7.3	244	60
229.05	0%	2.7	19	60	2315.95	0%	6.8	176	60
229.05	0%	1.9	14	60	2315.95	0%	6.9	177	60
229.05	0%	4.3	74	60	2315.95	0%	6.5	209	60
229.05	0%	3.8	53	60	2315.95	0%	7.1	154	60
343.60	0%	5.2	142	60	2315.95	0%	6.9	247	60
343.60	0%	5.2	174	60	2315.95	0%	7.6	234	60
343.60	0%	5.2	162	60	3567.00	0%	7	220	60
534.45	0%	7.5	274	60	3567.00	0%	7	187	60
534.45	0%	7.5	229	60	3567.00	0%	8.2	260	60

Appendix B
Integration of ordinary differential equations with spline interpolation

Contents

This appendix explains how the differential equations of the model for the pyrolysis of a particle of biomass (presented in **Chapter 2**) were integrated. A definition is first presented for functions of interpolating polynomials (splines) that are continuous up to their first and second derivatives over a domain (a, b). This concept is applied to the equations of the model that are then integrated with the aid of a typical Ordinary Differential Equation (ODE) solver; more specifically a solver for stiff ODEs is necessary. In this case the `ode23tb` from Matlab® was the choice, since it was empirically proven to be faster than `ode15s` and `ode23s` for this model.

B.1. Splines: continuous and derivable polynomial interpolation by segments

Some differential equations as the energy balance (**Equation B.1**) developed in **Section 2.4.3** in page 56, contain terms like the first one on the right side of **Equation B.1**, that could not be linearised (as one would do when using a finite volume r difference method) because of the multiplication of the pressure and temperature gradients.

$$\sum_{i=1}^{4} \rho_i \hat{C}_{V_i} \frac{\partial T}{\partial t} = \sum_{i=3}^{4} \left[\rho_i \hat{C}_{V_i}\right] \frac{\kappa}{\mu} \frac{\partial P}{\partial r} \frac{\partial T}{\partial r} + \frac{1}{r^2} \frac{\partial}{\partial r} \left(r^2 \lambda \frac{\partial T}{\partial r} \right) + \frac{P}{r^2} \frac{\partial}{\partial r} \left(r^2 \frac{\kappa}{\mu} \frac{\partial P}{\partial r} \right) - \sum_{j=1}^{4} \dot{r}_j \Delta \hat{U}_{\mathrm{rxn}_j} \tag{B.1}$$

If instead of attempting to linearise these gradients, continuous double-differentiable functions $\rho_i(r)$, $T(r)$ and $P(r)$ where available at a time t; then the set differential of equations:

$$\frac{\partial \vec{X}}{\partial t} = \vec{F}\left(r, \vec{X}, \tfrac{\partial \vec{X}}{\partial r}, \tfrac{\partial^2 \vec{X}}{\partial r^2}\right) \tag{B.2}$$

could be transformed to a set of ODEs:

$$\frac{\partial \vec{Y}}{\partial t} = \vec{G}\left(\vec{Y}\right) \tag{B.3}$$

where $\vec{Y}$ would be a vector containing the values of every variable in $\vec{X}$ at different positions along the domain of r. At that point a numerical algorithm for ODEs could resolve the system. Of course, if the functions $\rho_i(r, t)$, $P(r, t)$, $T(r, t)$ were available, then there would be no need to solve a set of differential equations in the first place. Nevertheless, the solvers for ODE provide the values of $\vec{Y}$ at a precedent time step and the next step is calculated from those values. Consequently, a *piecewise polynomial regression* can be performed with the values for ρ_i, T, P at different points in r, and then their values estimated for any point in r. The function that reunites the set of interpolating polynomials and their intervals of validity is called a *spline function*.

Definition B.1 (Spline function)**.** *Let* $\{P_1(r); P_2(r); \ldots; P_n(r)\}$ *be a set of* n *polynomials; and let* $\{[r_0, r_1); [r_1, r_2); \ldots; [r_{n-2}, r_{n-1}); [r_{n-1}, r_n]\}$ *be a set of* n *consecutive intervals between* a *and* b *such that* $a = r_0 < r_1 < r_2 < \ldots < r_n = b$*. If the polynomials* P_i *fulfil the condition* $P_i(r_i) = P_{i+1}(r_i)$ *for every* $i = 1, 2, \ldots n-1$*, then a* Spline function $\mathbb{P}(r)$ *can be defined over the interval* $a \leq r \leq b$ *such that:*

$$\mathbb{P}_{(r)} = \begin{cases} P_1(r) = \sum_{i=0}^{n_{P_1}} a_{P_{1i}} r^i \ , \ r_0 \leq r < r_1 \\ P_2(r) = \sum_{i=0}^{n_{P_2}} a_{P_{2i}} r^i \ , \ r_1 \leq r < r_2 \\ \qquad\qquad \vdots \\ P_n(r) = \sum_{i=0}^{n_{P_n}} a_{P_{ni}} r^i \ , \ r_{n-1} \leq r \leq r_n \end{cases} \tag{B.4}$$

and the polynomials P_i *are called* the picewice interpolanting polynomials *for the variable* P*.*

Because these functions are composed of polynomials and they all fit the condition $P_i(r_i) = P_{i+1}(r_i)$, they are guaranteed to be differentiable twice and the continuity is ensured for, and by, each polynomial. The challenge is for the first and second derivatives of $\mathbb{P}_{(r)}$ to be continuous. It requires them to also be spline functions and as such they will be represented with a double-stroked symbol $\partial_r(\mathbb{P}_{(r)})$ and $\partial_{rr}(\mathbb{P}_{(r)})$, and their definition will be a logical consequence of the definition of $\mathbb{P}_{(r)}$:

$$\partial_r(\mathbb{P}_{(r)}) = \begin{cases} \frac{\partial P_1}{\partial r}(r) \ , \ r_0 < r_1 \\ \frac{\partial P_2}{\partial r}(r) \ , \ r_1 \leq r < r_2 \\ \qquad \vdots \\ \frac{\partial P_n}{\partial r}(r) \ , \ r_{n-1} \leq r \leq r_n \end{cases} \tag{B.5}$$

$$\partial_{rr}(\mathbb{P}_{(r)}) = \begin{cases} \frac{\partial^2 P_1}{\partial r^2}(r) \ , \ r_0 \leq r < r_1 \\ \frac{\partial^2 P_2}{\partial r^2}(r) \ , \ r_1 \leq r < r_2 \\ \qquad \vdots \\ \frac{\partial^2 P_n}{\partial r^2}(r) \ , \ r_{n-1} \leq r \leq r_n \end{cases} \tag{B.6}$$

Since $\partial_r(\mathbb{P}_{(r)})$ and $\partial_{rr}(\mathbb{P}_{(r)})$ ought to be splines for the purposes of this work, then $\frac{\partial P_i}{\partial r}(r_i) = \frac{\partial P_{i+1}}{\partial r}(r_i)$ and $\frac{\partial^2 P_i}{\partial r^2}(r_i) = \frac{\partial^2 P_{i+1}}{\partial r^2}(r_i)$, for all $i = 1, 2, \ldots, n-1$.

Therefore, after producing splines that correctly model every variable in $\vec{X}$, then the right side of the system of **Equations B.2** can be transformed to products and additions between splines. Furthermore **Theorem B.1** guarantees the product of those functions to also be a spline with spline derivatives.

Theorem B.1 (Continuity of the product between interpolating polynomials and their derivatives)**.** *Given two couples of polynomials $P_1(r)$, $P_2(r)$ and $T_1(r)$, $T_2(r)$, if there is a point $r = a$ where the polynomials in each couple, as well as their derivatives meet each other, then the polynomials $R_i(r)$ (where $i = 1, 2$) obtained from the product between $P_i(r)$ and $T_i(r)$ will also meet each other at $r = a$, as well as their derivatives.*

PROOF: Consider four polynomials $P_1(r)$, $P_2(r)$, $T_1(r)$ and $T_2(r)$, of orders n_{P_1}, n_{P_2}, n_{T_1} and n_{T_2} respectively:

$$P_1(r) = \sum_{i=0}^{n_{P_1}} a_{P_{1i}} r^i \quad \text{(B.7)} \qquad P_2(r) = \sum_{i=0}^{n_{P_2}} a_{P_{2i}} r^i \quad \text{(B.8)}$$

$$T_1(r) = \sum_{i=0}^{n_{T_1}} a_{T_{1i}} r^i \quad \text{(B.9)} \qquad T_2(r) = \sum_{i=0}^{n_{T_2}} a_{T_{2i}} r^i \quad \text{(B.10)}$$

If there is a point $r = a$ at which $P_1(r)$, $P_2(r)$ together with their derivatives share the same values as well as for $T_1(r)$ and $T_2(r)$:

$$P_1(a) = P_2(a) \quad \text{(B.11)} \qquad T_1(a) = T_2(a) \quad \text{(B.12)}$$

$$\frac{\partial P_1}{\partial r}(a) = \frac{\partial P_2}{\partial r}(a) \quad \text{(B.13)} \qquad \frac{\partial T_1}{\partial r}(a) = \frac{\partial T_2}{\partial r}(a) \quad \text{(B.14)}$$

*then the polynomials $R_1(r) = P_1(r)T_1(r)$ and $R_2(r) = P_2(r)T_2(r)$ will meet at $r = a$ because of **Equations B.11** and **B.12**:*

$$R_1(a) = P_1(a)T_1(a) = P_2(a)T_2(a) = R_2(a) \quad \text{(B.15)}$$

*And their first derivatives will also meet at $r = a$ because of **Equations B.11** to **B.14**:*

$$\begin{aligned} \frac{\partial R_1}{\partial r}(a) &= P_1(a)\frac{\partial T_1}{\partial r}(a) + T_1(a)\frac{\partial P_1}{\partial r}(a) \\ &= P_2(a)\frac{\partial T_2}{\partial r}(a) + T_2(a)\frac{\partial P_2}{\partial r}(a) \\ &= \frac{\partial R_2}{\partial r}(a) \end{aligned} \quad \text{(B.16)}$$

In fact, given $\mathbb{P}_{(r)}$, $\partial_r(\mathbb{P}_{(r)})$ and $\partial_{rr}(\mathbb{P}_{(r)})$ and a second spline function with spline derivatives $\mathbb{T}_{(r)}$, $\partial_r(\mathbb{T}_{(r)})$ and $\partial_{rr}(\mathbb{T}_{(r)})$,

$$\mathbb{T}_{(r)} = \begin{cases} T_1(r) = \sum_{i=0}^{n_{T_1}} a_{T_{1i}} r^i \ , \ r_0 \leq r < r_1 \\ T_2(r) = \sum_{i=0}^{n_{T_2}} a_{T_{2i}} r^i \ , \ r_1 \leq r < r_2 \\ \qquad\qquad \vdots \\ T_n(r) = \sum_{i=0}^{n_{T_n}} a_{T_{ni}} r^i \ , \ r_{n-1} \leq r \leq r_n \end{cases} \quad \text{(B.17)}$$

$$\partial_r(\mathbb{T}_{(r)}) = \begin{cases} \frac{\partial T_1}{\partial r}(r) \ , \ r_0 \leq r < r_1 \\ \frac{\partial T_2}{\partial r}(r) \ , \ r_1 \leq r < r_2 \\ \qquad \vdots \\ \frac{\partial T_n}{\partial r}(r) \ , \ r_{n-1} \leq r \leq r_n \end{cases} \tag{B.18}$$

$$\partial_{rr}(\mathbb{T}_{(r)}) = \begin{cases} \frac{\partial^2 T_1}{\partial r^2}(r) \ , \ r_0 \leq r < r_1 \\ \frac{\partial^2 T_2}{\partial r^2}(r) \ , \ r_1 \leq r < r_2 \\ \qquad \vdots \\ \frac{\partial^2 T_n}{\partial r^2}(r) \ , \ r_{n-1} \leq r \leq r_n \end{cases} \tag{B.19}$$

then **Therorem B.1** guarantees, that if $\mathbb{R}_{(r)}$ is the product between $\mathbb{P}_{(r)}$ and $\mathbb{T}_{(r)}$ then it will be a spline function. Furthermore, because the first and second derivatives of $\mathbb{P}_{(r)}$ and $\mathbb{T}_{(r)}$ are splines, **Therorem B.1** guarantees that the first and second derivatives of $\mathbb{R}_{(r)}$ will also be splines. This all means, that the process of converting the system of **Equations B.2** into **Equation B.3** through the use of spline functions can be done without wondering about the continuity of the resulting functions.

B.1.1. Definition of the Interpolating Polynomials of This Model

Besides those already stipulated, some further considerations were necessary to define the characteristics of the polynomials used for the solution of the pyrolysis model. For correctly modelling each of the variables that define the state of the system (and consequently all of the other ones) ρ_i, T and P; their first derivative variables must be zero at the centre of the particle. This implies that the first polynomial of any spline $\mathbb{Y}_{(r)}$ must fulfil $\frac{\partial Y_1}{\partial t}(r_0) = 0$. Moreover, the way the polynomials are calculated, must be indifferent of the time, or the state of the system, and still be able to provide an appropriate approximation of the variable at any position. This means that the Runge phenomenon[1] should not happen or, if it does, it must be rapidly dissipated with the advancement of the integration instead of being magnified.

Suppose n values $\overline{y}_1, \overline{y}_2, \ldots, \overline{y}_n$ for a variable $y(r)$ are known at different points $\overline{r}_1, \overline{r}_2, \ldots, \overline{r}_n$ of the interval of r, $[r_0, r_n)$, besides one more value y_n at the external boundary ($r = r_n$). If a set of intervals $\{[r_0, r_1), [r_1, r_2), \ldots, [r_{n-2}, r_{n-1}), [r_{n-1}, r_n]\}$ is defined, so that $r_{i-1} < \overline{r}_i < r_i$, then a set of cubic polynomials for the spline function $\mathbb{Y}_{(r)}$ can be fabricated from the values $\overline{y}_i$ and y_n as exemplified in **Figure B.1**. In this model, the values of all the variables are homogeneous for every position and change smoothly from the outside towards the centre, driven by the high temperature at the external boundary. For this reason, the moment the value y_n at the external boundary is higher than all of the others, a spline function with spline derivatives would have zero derivatives at all points, except for the value at r_{n-1} where it would subtly descent before going up. This behaviour would not be

[1] By which a polynomial regression of a high enough order may oscillate between two points used to produce the polynomial

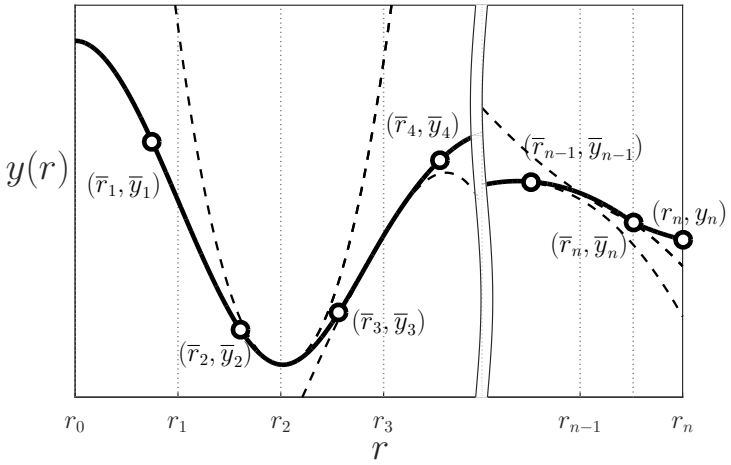

Figure B.1. Representation of a spline function. The thick continuous line represents the spline function $\mathbb{Y}_{(r)}$, while the dashed lines represent any of the polynomials $Y_i(r)$ that compose it. Vertical lines represent the points at which the polynomials are interrupted. $\overline{y}_i(r)$ are the values of $Y(r)$ at the centre of mass of the interval (r_{i-1}, r_i).

a concern if it was a dissipated in time, but it is not the case. As the value at r_n continues to raise the phenomenon increases in magnitude and eventually would cause the neighbouring value to decrease with it although the boundary should pull them all upwards.

To avoid this situation, a compromise was done between forcing all the variables to have a spline function with spline first and second derivatives; and instead they have the flexibility to have discontinuous first and second derivatives at one point. Nevertheless this discontinuity is spontaneously mitigated with the advancement of time in. As may be noticed in **Figure B.1**, that *flexible* point is $\overline{r}_{n-1}$, from where, a second order polynomial mediates the transition between the surface and the rest of the particle. The rest of the polynomials has order 3. Therefore any variable $y(r)$ in this model, whose spline function $\mathbb{Y}_{(r)}$ is obtained from a polynomial regression (instead of an operation between spline functions), is modelled as:

$$\mathbb{Y}_{(r)} = \begin{cases} Y_1(r) = a_{Y_{10}} r^3 + a_{Y_{11}} r^2 + a_{Y_{12}} r + a_{Y_{13}} & , \ r_0 \leq r < r_1 \\ Y_2(r) = a_{Y_{20}} r^3 + a_{Y_{21}} r^2 + a_{Y_{22}} r + a_{Y_{23}} & , \ r_1 \leq r < r_2 \\ \vdots & \\ Y_{n-1}(r) = a_{Y_{(n-1)0}} r^3 + a_{Y_{(n-1)1}} r^2 + a_{Y_{(n-1)2}} r + a_{Y_{(n-1)3}} & , \ r_{n-2} \leq r < r_{n-1} \\ Y_n(r) = a_{Y_{n0}} r^3 + a_{Y_{n1}} r^2 + a_{Y_{n2}} r + a_{Y_{n3}} & , \ r_{n-1} \leq r < \overline{r}_n \\ Y_{n+1}(r) = a_{Y_{(n+1)0}} r^2 + a_{Y_{(n+1)1}} r^1 + a_{Y_{(n+1)2}} & , \ \overline{r}_n \leq r \leq r_n \end{cases} \tag{B.20}$$

and the equations that have to be solved to obtain the constants of the polynomials

are the following ones:

$$\frac{\partial Y_1}{\partial r}(r_0) = 0 \tag{B.21}$$

$$Y_1(\overline{r}_2) = \overline{y}_2 \tag{B.22}$$

$$Y_k(\overline{r}_k) = \overline{y}_k \quad , \quad \forall k = 1, 2, \ldots, n-1 \tag{B.23}$$

$$Y_k(r_k) = Y_{j+1}(r_k) \quad , \quad \forall k = 1, 2, \ldots, n-1 \tag{B.24}$$

$$\frac{\partial Y_k}{\partial r}(r_k) = \frac{\partial Y_{j+1}}{\partial r}(r_k) \quad , \quad \forall k = 1, 2, \ldots, n-1 \tag{B.25}$$

$$\frac{\partial^2 Y_k}{\partial r^2}(r_k) = \frac{\partial^2 Y_{j+1}}{\partial r^2}(r_k) \quad , \quad \forall k = 1, 2, \ldots, n-1 \tag{B.26}$$

$$Y_n(\overline{r}_{n-1}) = \overline{y}_{n-1} \tag{B.27}$$

$$Y_n(\overline{r}_n) = \overline{y}_n \tag{B.28}$$

$$Y_n(r_{n-1}) = Y_{n+1}(r_{n-1}) \tag{B.29}$$

$$Y_{n+1}(\overline{r}_n) = \overline{y}_n \tag{B.30}$$

$$Y_{n+1}(r_n) = y_n \tag{B.31}$$

Equations B.21 to **B.31** constitute a system of $4n + 3$ linear equations, with only one solution that can be obtained with the inversion of the matrix. **Equation B.34** in page B-9 presents a representation of such system that may allow to better visualize its structure.

Notice that, for simplicity, the last polynomial can be considered a cubic one:

$$Y_{n+1}(r) = a^*_{Y_{(n+1)0}} r^3 + a_{Y_{(n+1)0}} r^2 + a_{Y_{(n+1)1}} r + a_{Y_{(n+1)2}} \tag{B.32}$$

whose first constant $= a^*_{Y_{(n+1)0}}$ equals zero. In which case the addition of the extra unknown is compensated with the equation:

$$a^*_{Y_{(n+1)0}} = 0 \tag{B.33}$$

B.2. Definitions of Matrix Operations for the Discretization of the Model

Since every spline function is still a function as any other, and specially a continuous one, the traditional definition of integrals and derivatives applies to them in the same manner, so there is no need to explain how are they calculated for spline functions. Nevertheless, a particular operator that will be called here the *spline integral* has to be defined, since it will be helpful for explaining the discretization of the model in the following section.

$$
\begin{pmatrix}
3\mathbf{r}_0^2 & 2\mathbf{r}_0 & 1 & \mathbf{0} & 0 & 0 & 0 & 0 & 0 & 0 & 0 & 0 & 0 & 0 & 0 & 0 & 0 & 0 \\
\bar{\mathbf{r}}_2^3 & \bar{\mathbf{r}}_2^2 & \bar{\mathbf{r}}_2 & 1 & 0 & 0 & 0 & 0 & 0 & 0 & 0 & 0 & 0 & 0 & 0 & 0 & 0 & 0 \\
\bar{\mathbf{r}}_1^3 & \bar{\mathbf{r}}_1^2 & \bar{\mathbf{r}}_1 & 1 & 0 & 0 & 0 & 0 & 0 & 0 & 0 & 0 & 0 & 0 & 0 & 0 & 0 & 0 \\
\mathbf{r}_1^3 & \mathbf{r}_1^2 & \mathbf{r}_1 & 1 & $-\mathbf{r}_1^3$ & $-\mathbf{r}_1^2$ & $-\mathbf{r}_1$ & -1 & 0 & 0 & 0 & 0 & 0 & 0 & 0 & 0 & 0 & 0 \\
$3\mathbf{r}_1^2$ & $2\mathbf{r}_1$ & 1 & 0 & $-3\mathbf{r}_1^2$ & $-2\mathbf{r}_1$ & -1 & 0 & 0 & 0 & 0 & 0 & 0 & 0 & 0 & 0 & 0 & 0 \\
$6\mathbf{r}_1$ & 2 & 0 & 0 & $-6\mathbf{r}_1$ & -2 & 0 & 0 & 0 & 0 & 0 & 0 & 0 & 0 & 0 & 0 & 0 & 0 \\
0 & 0 & 0 & 0 & $\bar{\mathbf{r}}_2^3$ & $\bar{\mathbf{r}}_2^2$ & $\bar{\mathbf{r}}_2$ & 1 & 0 & 0 & 0 & 0 & 0 & 0 & 0 & 0 & 0 & 0 \\
0 & 0 & 0 & 0 & $\mathbf{r}_2^3$ & $\mathbf{r}_2^2$ & $\mathbf{r}_2$ & 1 & $-\mathbf{r}_2^3$ & $-\mathbf{r}_2^2$ & $-\mathbf{r}_2$ & -1 & 0 & 0 & 0 & 0 & 0 & 0 \\
0 & 0 & 0 & 0 & $3\mathbf{r}_2^2$ & $2\mathbf{r}_2$ & 1 & 0 & $-3\mathbf{r}_2^2$ & $-2\mathbf{r}_2$ & -1 & 0 & 0 & 0 & 0 & 0 & 0 & 0 \\
0 & 0 & 0 & 0 & $6\mathbf{r}_2$ & 2 & 0 & 0 & $-6\mathbf{r}_2$ & -2 & 0 & 0 & 0 & 0 & 0 & 0 & 0 & 0 \\
 & & & & & & $\vdots$ & & & & & & $\ddots$ & & & & & \\
0 & 0 & 0 & 0 & 0 & 0 & 0 & 0 & 0 & 0 & 0 & 0 & $\bar{\mathbf{r}}_{n-1}^3$ & $\bar{\mathbf{r}}_{n-1}^2$ & $\bar{\mathbf{r}}_{n-1}$ & 1 & 0 & 0 \\
0 & 0 & 0 & 0 & 0 & 0 & 0 & 0 & 0 & 0 & 0 & 0 & $\bar{\mathbf{r}}_n^3$ & $\bar{\mathbf{r}}_n^2$ & $\bar{\mathbf{r}}_n$ & 1 & 0 & 0 \\
0 & 0 & 0 & 0 & 0 & 0 & 0 & 0 & 0 & 0 & 0 & 0 & $\mathbf{r}_n^3$ & $\mathbf{r}_n^2$ & $\mathbf{r}_n$ & 1 & $-\mathbf{r}_n^2$ & $-\mathbf{r}_n$ \\
0 & 0 & 0 & 0 & 0 & 0 & 0 & 0 & 0 & 0 & 0 & 0 & 0 & 0 & 0 & 0 & $\bar{\mathbf{r}}_n^2$ & $\bar{\mathbf{r}}_n$ \\
0 & 0 & 0 & 0 & 0 & 0 & 0 & 0 & 0 & 0 & 0 & 0 & 0 & 0 & 0 & 0 & $\mathbf{r}_n^2$ & $\mathbf{r}_n$
\end{pmatrix}
\begin{pmatrix}
a_{Y_{10}} \\ a_{Y_{11}} \\ a_{Y_{12}} \\ a_{Y_{13}} \\ a_{Y_{20}} \\ a_{Y_{21}} \\ a_{Y_{22}} \\ a_{Y_{23}} \\ a_{Y_{30}} \\ a_{Y_{31}} \\ a_{Y_{32}} \\ a_{Y_{33}} \\ \vdots \\ a_{Y_{n0}} \\ a_{Y_{n1}} \\ a_{Y_{n3}} \\ a_{Y_{n3}} \\ a_{Y_{(n+1)0}} \\ a_{Y_{(n+1)1}} \\ a_{Y_{(n+1)2}}
\end{pmatrix}
=
\begin{pmatrix}
0 \\ \bar{y}_2 \\ \\ \bar{y}_1 \\ 0 \\ 0 \\ 0 \\ \\ \bar{y}_2 \\ 0 \\ 0 \\ 0 \\ \vdots \\ \bar{y}_{n-1} \\ \bar{y}_n \\ 0 \\ \bar{y}_n \\ y_n
\end{pmatrix}
$$

Equation B.34. General system of linear equations for defining the interpolating polynomials.

Definition B.2 (The spline integral)**.** *Let* $\mathbb{P}_{(r)}$ *be a spline function and let* $\{[r_0, r_1); [r_1, r_2); \ldots; [r_{n-2}, r_{n-1}); [r_{n-1}, r_n]\}$ *be any set of intervals who may not necessarily be those that define* $\mathbb{P}_{(r)}$*. If* $\vec{r}$ *is the vector:*

$$\vec{r} = \begin{pmatrix} r_0 & r_1 & r_2 & \ldots & r_n \end{pmatrix}$$

Then the spline integral *of* $\mathbb{P}_{(r)}$*,* $\overrightarrow{\int\limits_{\vec{r}}} \mathbb{P}_{(r)} \mathrm{d}\vec{r}$*, is defined as the vector that contains the integrals of* $\mathbb{P}_{(r)}$ *for each one of the intervals in the set* $\{[r_0, r_1); [r_1, r_2); \ldots; [r_{n-2}, r_{n-1}); [r_{n-1}, r_n]\}$*:*

$$\overrightarrow{\int\limits_{\vec{r}}} \mathbb{P}_{(r)} \mathrm{d}\vec{r} = \begin{pmatrix} \int\limits_{r_0}^{r_1} \mathbb{P}_{(r)} \mathrm{d}r \\ \int\limits_{r_1}^{r_2} \mathbb{P}_{(r)} \mathrm{d}r \\ \vdots \\ \int\limits_{r_{n-1}}^{r_n} \mathbb{P}_{(r)} \mathrm{d}r \end{pmatrix} \tag{B.35}$$

Although it might be unnecessary two more operators are defined next, in order to establish an agreement on their use in this document.

Definition B.3 (Element-wise multiplication and division)**.** *The symbols* $\odot$ *and* $\oslash$ *represent binary operators between two matrices* $\mathbf{A}$ *and* $\mathbf{B}$ *with equal sizes* $n \times m$

$$\mathbf{A} = \begin{pmatrix} a_{11} & a_{12} & \ldots & a_{1m} \\ a_{21} & a_{22} & \ldots & a_{2m} \\ \vdots & \vdots & \ddots & \vdots \\ a_{n1} & a_{n2} & \ldots & a_{nm} \end{pmatrix} \text{ and } \mathbf{B} = \begin{pmatrix} b_{11} & b_{12} & \ldots & b_{1m} \\ b_{21} & b_{22} & \ldots & b_{2m} \\ \vdots & \vdots & \ddots & \vdots \\ b_{n1} & b_{n2} & \ldots & b_{nm} \end{pmatrix}$$

The operations $\mathbf{A} \odot \mathbf{B}$ *and* $\mathbf{A} \oslash \mathbf{B}$ *indicate the element-wise division and multiplication between the components of both matrices:*

$$\mathbf{A} \odot \mathbf{B} = \begin{pmatrix} a_{11}b_{11} & a_{12}b_{12} & \ldots & a_{1m}b_{1m} \\ a_{21}b_{21} & a_{22}b_{22} & \ldots & a_{2m}b_{2m} \\ \vdots & \vdots & \ddots & \vdots \\ a_{n1}b_{n1} & a_{n2}b_{n2} & \ldots & a_{nm}b_{nm} \end{pmatrix} \tag{B.36}$$

$$\mathbf{A} \oslash \mathbf{B} = \begin{pmatrix} a_{11}/b_{11} & a_{12}/b_{12} & \ldots & a_{1m}/b_{1m} \\ a_{21}/b_{21} & a_{22}/b_{22} & \ldots & a_{2m}/b_{2m} \\ \vdots & \vdots & \ddots & \vdots \\ a_{n1}/b_{n1} & a_{n2}/b_{n2} & \ldots & a_{nm}/b_{nm} \end{pmatrix} \tag{B.37}$$

B.3. Discretization of the model through splines

Consider the differential equations of the pyrolysis model:

$$\frac{\partial \rho_1}{\partial t} = \dot{R}_1 \tag{B.38}$$

$$\frac{\partial \rho_2}{\partial t} = \dot{R}_2 \tag{B.39}$$

$$\frac{\partial \rho_3}{\partial t} = \dot{R}_3 - \frac{1}{r^2}\frac{\partial}{\partial r}\left(r^2 u_r \rho_3\right) = \dot{R}_3 + \frac{1}{r^2}\frac{\partial}{\partial r}\left(r^2 \frac{\kappa}{\mu}\frac{\partial P}{\partial r}\rho_3\right) \tag{B.40}$$

$$\frac{\partial \rho_4}{\partial t} = \dot{R}_2 - \frac{1}{r^2}\frac{\partial}{\partial r}\left(r^2 u_r \rho_4\right) = \dot{R}_4 + \frac{1}{r^2}\frac{\partial}{\partial r}\left(r^2 \frac{\kappa}{\mu}\frac{\partial P}{\partial r}\rho_4\right) \tag{B.41}$$

$$\begin{aligned}\sum_{i=1}^{4} \rho_i \hat{C}_{V_i}\frac{\partial T}{\partial t} = &\sum_{i=3}^{4}\left[\rho_i \hat{C}_{V_i}\right]\frac{\kappa}{\mu}\frac{\partial P}{\partial r}\frac{\partial T}{\partial r} + \frac{1}{r^2}\frac{\partial}{\partial r}\left(r^2\lambda\frac{\partial T}{\partial r}\right) \\ &+ \frac{P}{r^2}\frac{\partial}{\partial r}\left(r^2\frac{\kappa}{\mu}\frac{\partial P}{\partial r}\right) - \sum_{j=1}^{4}\dot{r}_j \Delta\hat{U}_{\mathrm{rxn}_j}\end{aligned} \tag{B.42}$$

$$\frac{\partial w_4}{\partial t} = \frac{1}{\rho_3+\rho_4}\frac{\partial \rho_4}{\partial t} - \frac{\rho_4}{\left(\rho_3+\rho_4\right)^2}\left(\frac{\partial \rho_3}{\partial t} + \frac{\partial \rho_4}{\partial t}\right) \tag{B.43}$$

$$\begin{aligned}\frac{\partial P}{\partial t} = &\frac{RT}{\varepsilon}\left[\sum_{i=3}^{4}\frac{1}{\tilde{M}_i}\frac{\partial \rho_i}{\partial t}\right] + \frac{R}{\varepsilon}\frac{\partial T}{\partial t}\left[\sum_{i=3}^{4}\frac{\rho_i}{\tilde{M}_i}\right] \\ &+ \frac{RT\left(1-\varepsilon_0\right)}{\rho_{1_0}\varepsilon^2}\left[\sum_{i=3}^{4}\frac{\rho_i}{\tilde{M}_i}\right]\left[\sum_{i=1}^{2}\frac{\partial \rho_i}{\partial t}\right]\end{aligned} \tag{B.44}$$

if ρ_i, T, P, the heat capacities $\hat{C}_{Vi}$, the conductivity λ, the kinetic reaction constants k_j, and the energies of reaction $\Delta\hat{U}_{\mathrm{rxn}_j}$ are modelled as spline functions with spline first and second derivatives, $\mathbb{p}_i(r)$, $\mathbb{T}(r)$, $\mathbb{P}(r)$, $\hat{\mathbb{C}}_{\mathbb{V}_i}(r)$, $\mathbb{\lambda}(r)$, $\mathbb{k}_j(r)$ and $\Delta\hat{\mathbb{U}}_{\mathrm{rxn}_j}(r)$ respectively, for a set of intervals $\{[r_0, r_1); [r_1, r_2); \ldots; [r_{n-2}, r_{n-1}); [r_{n-1}, r_n]\}$, then **Equations B.38** to **B.49** can be transformed into splines as follows:

$$\partial_t(\mathbb{p}_1(r)) = \dot{\mathbb{R}}_1(r) \tag{B.45}$$

$$\partial_t(\mathbb{p}_2(r)) = \dot{\mathbb{R}}_2(r) \tag{B.46}$$

$$\partial_t(\mathbb{p}_3(r)) = \dot{\mathbb{R}}_3(r) + \tfrac{1}{r^2}\partial_r\left(r^2\tfrac{\mathbb{K}(r)}{\mu}\partial_r(\mathbb{P}(r))\mathbb{p}_3(r)\right) \tag{B.47}$$

$$\partial_t(\mathbb{p}_4(r)) = \dot{\mathbb{R}}_4(r) + \tfrac{1}{r^2}\partial_r\left(r^2\tfrac{\mathbb{K}(r)}{\mu}\partial_r(\mathbb{P}(r))\mathbb{p}_4(r)\right) \tag{B.48}$$

$$\sum_{i=1}^{4} \mathbb{p}_i(r)\hat{\mathbb{C}}_{\mathbb{V}_i}(r)\partial_t(\mathbb{T}(r)) = \sum_{i=3}^{4}\left[\mathbb{p}_i\hat{\mathbb{C}}_{\mathbb{V}_i}(r)\right]\frac{\mathbb{K}(r)}{\mu}\partial_r(\mathbb{P}(r))\partial_r(\mathbb{T}(r)) + \frac{1}{r^2}\partial_r\left(r^2\partial_r(\mathbb{T}(r))\mathbb{\lambda}\right) + \frac{\mathbb{P}(r)}{r^2}\partial_r\left(r^2\frac{\mathbb{K}(r)}{\mu}\partial_r(\mathbb{P}(r))\right) - \sum_{j=1}^{4}\dot{\mathbb{r}}_j(r)\Delta\hat{\mathbb{U}}_{\mathrm{rxn}_j}(r) \tag{B.49}$$

Doing so requires (as explained in the last section) $n+1$ values of each of the variables mentioned, one for each for the centres of mass of the n intervals and one at the external boundary:

$$\begin{array}{cc} \left(\overline{\rho_i}_1,\ \overline{\rho_i}_2,\ \ldots,\ \overline{\rho_i}_n,\ \rho_{i_n}\right) & \left(\overline{k_j}_1,\ \overline{k_j}_2,\ \ldots,\ \overline{k_j}_n,\ k_{j_n}\right) \\ \left(\overline{T}_1,\ \overline{T}_2,\ \ldots,\ \overline{T}_n,\ T_n\right) & \left(\overline{P}_1,\ \overline{P}_2,\ \ldots,\ \overline{P}_n,\ P_n\right) \\ \left(\overline{\lambda}_1,\ \overline{\lambda}_2,\ \ldots,\ \overline{\lambda}_n,\ \lambda_n\right) & \left(\overline{\hat{C}_{Vi_1}},\ \overline{\hat{C}_{Vi_2}},\ \ldots,\ \overline{\hat{C}_{Vi_n}},\ \hat{C}_{Vn}\right) \\ \multicolumn{2}{c}{\left(\overline{\Delta\hat{U}_{\mathrm{rxn}_j}}_1,\ \overline{\Delta\hat{U}_{\mathrm{rxn}_j}}_2,\ \ldots,\ \overline{\Delta\hat{U}_{\mathrm{rxn}_j}}_n,\ \Delta\hat{U}_{\mathrm{rxn}_j}\right)} \end{array}$$

Although $\hat{C}_V$, λ, k_j, and $\Delta\hat{U}_{\mathrm{rxn}_j}$, are all functions of ρ_i and T, their spline functions are not calculated as operations of $\mathbb{p}_i(r)$ and $\mathbb{T}(r)$; either because the definition of the variable does not consist of sums and multiplications (k_j and λ), or because the resulting spline would have an order three or four times higher than those of the original polynomials ($\hat{C}_V$, $\Delta\hat{U}_{\mathrm{rxn}_j}$). Instead, $\overline{\hat{C}_{Vi}}_k$, $\overline{\lambda}_k$, $\overline{k_j}_k$ and $\overline{\Delta\hat{U}_{\mathrm{rxn}_j}}_k$ (as well as those on the boundary r_n) are first calculated from the same values of $\overline{\rho_i}_k$ and $\overline{T}_k$ that are used to generate $\mathbb{p}_i(r)$ and $\mathbb{T}(r)$, and then the spline functions are produced.

In contrast, the splines for the rates of reaction are constructed through operations between other spline functions:

$$\dot{\mathbb{r}}_1(r) = \mathbb{k}_1(r)\mathbb{p}_1(r) \tag{B.50}$$

$$\dot{\mathbb{r}}_2(r) = \mathbb{k}_2(r)\mathbb{p}_1(r) \tag{B.51}$$

$$\dot{\mathbb{r}}_3(r) = \mathbb{k}_3(r)\mathbb{p}_1(r) \tag{B.52}$$

$$\dot{\mathbb{r}}_4(r) = \mathbb{k}_4(r)\mathbb{p}_3(r) \tag{B.53}$$

$$\dot{\mathbb{R}}_1(r) = -\sum_{j=1}^{3}\dot{\mathbb{r}}_j(r) \tag{B.54}$$

$$\dot{\mathbb{R}}_2(r) = \dot{\mathbb{r}}_3(r) \tag{B.55}$$

$$\dot{\mathbb{R}}_3(r) = \dot{\mathbb{r}}_2(r) - \dot{\mathbb{r}}_4(r) \tag{B.56}$$

$$\dot{\mathbb{R}}_4(r) = \dot{\mathbb{r}}_1(r) + \dot{\mathbb{r}}_4(r) \tag{B.57}$$

together with the permeability:

$$\mathbb{K}(r) = \frac{(\kappa_1-\kappa_2)}{\rho_{1_0}}\partial_r(\mathbb{p}_1(r)) \tag{B.58}$$

B.3.1. Volume Integration

Once the splines are calculated, it is possible to perform a volume integration. Consider an interval $[r_{k-1}, r_k]$, the one-dimensional volume (the model is considered to be symetrical in the radial and azimuthal directions) contained within this interval in spheric coordinates is:

$$V_k = \int_{r_{k-1}}^{r_k} r^2 \mathrm{d}r \tag{B.59}$$

A spheric solid whose density is a function of the radius $\rho(r)$, would contain within that same interval a mass of:

$$m_k = \int_{r_{k-1}}^{r_k} \rho(r) r^2 \mathrm{d}r \tag{B.60}$$

Therefore the average density of the volume V_k is defined as:

$$\overline{\rho}_k = \frac{\int_{r_{k-1}}^{r_k} \rho(r) r^2 \mathrm{d}r}{\int_{r_{k-1}}^{r_k} r^2 \mathrm{d}r} \tag{B.61}$$

In a similar manner, the mean change in the densities for each interval and each component in the pyrolysis model, can be estimated through the definition of the *spline integral* and the element-wise division $\oslash$ (provided in page B-10) as:

$$\frac{\overrightarrow{\partial \overline{\rho_i}}}{\partial t} = \begin{pmatrix} \frac{\partial \overline{\rho_i}_1}{\partial t} \\ \frac{\partial \overline{\rho_i}_2}{\partial t} \\ \vdots \\ \frac{\partial \overline{\rho_i}_n}{\partial t} \end{pmatrix} = \int_{\vec{r}}^{\rightarrow} \partial_t(\mathbb{p}_i(r)) r^2 \mathrm{d}\vec{r} \oslash \int_{\vec{r}}^{\rightarrow} r^2 \mathrm{d}\vec{r} \tag{B.62}$$

where $\partial_t(\mathbb{p}_i(r))$ is either of the spline functions defined by **Equations B.38** to **B.41**.

Contrastingly, because of the structure of **Equation B.49**, mean temperatures for each interval, are more conveniently calculated, as:

$$\frac{\overrightarrow{\partial \overline{T}}}{\partial t} = \int_{\vec{r}}^{\rightarrow} \sum_{i=1}^{4} \mathbb{p}_i(r) \hat{\mathbb{C}}_{\mathbb{V}_i}(r) \partial_t(\mathbb{T}(r)) r^2 \mathrm{d}\vec{r} \oslash \int_{\vec{r}}^{\rightarrow} \sum_{i=1}^{4} \mathbb{p}_i(r) \hat{\mathbb{C}}_{\mathbb{V}_i}(r) r^2 \mathrm{d}\vec{r} \tag{B.63}$$

Finally, the equations of change for the mean pressure and the mass fractions of the pyrolysis gases in the gas phase are calculated, not as an integration of spline functions, but as element-wise operations between the vectors $\overrightarrow{\overline{\rho_i}}$, $\frac{\overrightarrow{\partial \overline{\rho_i}}}{\partial t}$, $\overrightarrow{\overline{T}}$ and $\frac{\overrightarrow{\partial \overline{T}}}{\partial t}$:

$$\begin{aligned}\frac{\overrightarrow{\partial w_4}}{\partial t} = &\frac{\overrightarrow{\partial \rho_4}}{\partial t} \oslash \left(\overrightarrow{\rho_3} + \overrightarrow{\rho_4}\right) \\ &- \left[\overrightarrow{\rho_4} \odot \left(\frac{\overrightarrow{\partial \rho_3}}{\partial t} + \frac{\overrightarrow{\partial \rho_4}}{\partial t}\right)\right] \oslash \left[\left(\overrightarrow{\rho_3} + \overrightarrow{\rho_4}\right) \odot \left(\overrightarrow{\rho_3} + \overrightarrow{\rho_4}\right)\right]\end{aligned} \tag{B.64}$$

$$\begin{aligned}\frac{\overrightarrow{\partial P}}{\partial t} =& R\left[\overrightarrow{T} \odot \sum_{i=3}^{4} \frac{1}{\tilde{M}_i} \frac{\overrightarrow{\partial \rho_i}}{\partial t} + \frac{\overrightarrow{\partial T}}{\partial t} \odot \sum_{i=3}^{4} \frac{\overrightarrow{\rho_i}}{\tilde{M}_i}\right] \oslash \overrightarrow{\varepsilon} \\ &+ \frac{R\left(1-\varepsilon_0\right)}{\rho_{1_0}} \left[\overrightarrow{T} \odot \sum_{i=3}^{4} \frac{\overrightarrow{\rho_i}}{\tilde{M}_i} \odot \sum_{i=1}^{2} \frac{\overrightarrow{\partial \rho_i}}{\partial t}\right] \oslash \left[\overrightarrow{\varepsilon} \odot \overrightarrow{\varepsilon}\right]\end{aligned} \tag{B.65}$$

where the mean porosity vector $\overrightarrow{\varepsilon}$ is defined as:

$$\overrightarrow{\varepsilon} = 1 - \frac{(1-\varepsilon_0)}{\rho_{1_0}} \sum_{i=1}^{2} \overrightarrow{\rho_i} \tag{B.66}$$

Because of the way **Equations B.62** to **B.65** are defined, it is convenient for the values $\overline{\rho_i}$, $\overline{T}$, etc. provided for each interval to have radial coordinates at the centre of mass of each interval CM_i. This is not the centre of the interval, for the case of spheric volumes, even if the density is considered constant:

$$\overrightarrow{\overline{r}} = \overrightarrow{\mathrm{CM}} = \int_{\vec{r}}^{\rightarrow} \rho_{1_0} r^3 \mathrm{d}\vec{r} \oslash \int_{\vec{r}}^{\rightarrow} \rho_{1_0} r^2 \mathrm{d}\vec{r} = \int_{\vec{r}}^{\rightarrow} r^3 \mathrm{d}\vec{r} \oslash \int_{\vec{r}}^{\rightarrow} r^2 \mathrm{d}\vec{r} \tag{B.67}$$

so for any interval $[r_{i-1}, r_i)$:

$$\overline{r}_i = \mathrm{CM}_i = \frac{3\left(r_i^4 - r_{i-1}^4\right)}{4\left(r_i^3 - r_{i-1}^3\right)} \tag{B.68}$$

B.3.2. Boundary conditions

For the case of the centre of the particle, the set of equations used for calculating the polynomials imposes the condition for every variable Y to have a radial derivative equal to zero at that point $\frac{\partial Y}{\partial r}(r=0) = 0$.

Pressure, on the other hand, remains constant at the external boundary. The derivatives of the mass concentrations of the components $\frac{\partial \rho_{i_n}}{\partial t}$, can be calculated by evaluating **Equations B.38** to **B.41** at the radius of the particle $\frac{d_\mathrm{p}}{2}$. Allowing to estimate $\frac{\partial w_4}{\partial t}(r = \frac{d_\mathrm{p}}{2})$ through **Equation B.43**. The knowledge of the composition of the gas phase w_4 and the constant pressure at the boundary allow to estimate the values for ρ_{3_n} and ρ_{4_n} at the boundary $\frac{d_\mathrm{p}}{2}$.

Temperature, on the other hand, present the «difficulty» of being dependent of

the gradient and a forth order polynomial of the temperature T_n

$$\lambda \frac{\partial T_n}{\partial t} = h_{\text{conv}} \left(T_\infty - T_n \right) + \sigma e \left(T_\infty^4 - T_n^4 \right) \tag{B.69}$$

which is solved with a Newton-Raphson iteration for every time step. This requires, to suppose a value for T_n and then evaluate the spline functions for T and ρ_i, at each iteration.

B.3.3. Algorithm

An algorithm summarizing the calculations done to obtain the time derivatives of the mass concentrations, temperature and pressure is provided next.

Algorithm 1 Calculation of the time derivatives of the main variables at different points for the model of biomass pyrolysis

Precondition: $\vec{X}$ is a column vector containing the values $\overrightarrow{\overline{\rho_1}}$, ρ_{1n}, $\overrightarrow{\overline{\rho_2}}$, ρ_{2n}, $\overrightarrow{\overline{w_4}}$, w_{4n}, $\overrightarrow{\overline{P}}$ and $\overrightarrow{\overline{T}}$. $\vec{r}$ is the vector$\begin{pmatrix} r_0 & r_1 & \dots & r_n \end{pmatrix}$ that defines the intervals $[r_0, r_1), [r_1, r_2) \dots [r_{n-1}, r_n]$

1: **function** MassAndEnergyBalances($\vec{X}, \vec{r}$)
2: extract $\overrightarrow{\overline{\rho_1}}$, ρ_{1n}, $\overrightarrow{\overline{\rho_2}}$, ρ_{2n}, $\overrightarrow{\overline{w_4}}$, w_{4n}, $\overrightarrow{\overline{P}}$ and $\overrightarrow{\overline{T}}$. from $\vec{X}$
3: declare TOL: tolerance for the iteration of T_n
4: suppose $T_n = \frac{T_\infty + \overline{T}_1}{2}$
5: **repeat**
6: calculate $\overrightarrow{\overline{\rho_3}}$, ρ_{3n} and $\overrightarrow{\overline{\rho_4}}$, ρ_{4n}, using $\overrightarrow{\overline{w_4}}$, w_{4n}, $\overrightarrow{\overline{P}}$, $\overrightarrow{\overline{T}}$ and T_n.
7: Obtain the polynomials for $\mathbb{T}_{(r)}$ and $\mathbb{p}_{i(r)}, \forall i = 1, 2, 3, 4$
8: Obtain the polynomials for $\partial_r(\mathbb{T}_{(r)})$ from $\mathbb{T}_{(r)}$
9: evaluate FO $= \lambda \frac{\partial T_n}{\partial t} h_{\text{conv}} (T_\infty - T_n) + \sigma e \left(T_\infty^4 - T_n^4\right)$
10: **if** FO $> TOL$ **then**
11: adapt T_n using Newton-Raphson method
12: **end if**
13: **until** FO $\leq TOL$
14: evaluate the polynomials for $\mathbb{P}_{(r)}$, $\partial_r(\mathbb{P}_{(r)})$, $\Bbbk_{j(r)}$, $\dot{\mathbb{r}}_{j(r)}$, $\dot{\mathbb{R}}_{j(r)}$, $\hat{\mathbb{C}}_{\mathbb{V}_i(r)}$, $\Delta\hat{\mathbb{U}}_{\text{rxn}_j(r)}$, $\mathbb{K}_{(r)}$ and $\partial_r(\mathbb{K}_{(r)})$ for each reaction $j = 1, 2, 3, 4$ and component $i = 1, 2, 3, 4$
15: establish spline functions for $\partial_t(\mathbb{p}_{i(r)})$ and $\sum_{i=1}^{4} \mathbb{p}_{i(r)} \hat{\mathbb{C}}_{\mathbb{V}_i(r)} \partial_t(\mathbb{T}_{(r)})$
16: for each component $i = 1, 2, 3, 4$ evaluate volume integrals

$$\frac{\overrightarrow{\partial \overline{\rho_i}}}{\partial t} = \int_{\vec{r}}^{\rightarrow} \partial_t(\mathbb{p}_{i(r)}) r^2 \mathrm{d}\vec{r} \oplus \int_{\vec{r}}^{\rightarrow} r^2 \mathrm{d}\vec{r}$$

17: evaluate volume integral for energy balance:

$$\frac{\overrightarrow{\partial \overline{T}}}{\partial t} = \int_{\vec{r}}^{\rightarrow} \sum_{i=1}^{4} \mathbb{p}_{i(r)} \hat{\mathbb{C}}_{\mathbb{V}_i(r)} \partial_t(\mathbb{T}_{(r)}) r^2 \mathrm{d}\vec{r} \oplus \int_{\vec{r}}^{\rightarrow} \sum_{i=1}^{4} \mathbb{p}_{i(r)} \hat{\mathbb{C}}_{\mathbb{V}_i(r)} r^2 \mathrm{d}\vec{r}$$

18: evaluate $\frac{\partial \rho_{i_n}}{\partial t} = \partial_t \mathbb{p}_i \left(r = \frac{d_\text{p}}{2}\right)$ for each $i = 1, 2, 3, 4$
19: Use $\frac{\overrightarrow{\partial \overline{T}}}{\partial t}$, $\frac{\overrightarrow{\partial \overline{\rho_i}}}{\partial t}$, $\frac{\partial \rho_{i_n}}{\partial t}$ for evaluating $\frac{\overrightarrow{\partial \overline{w_4}}}{\partial t}$, $\frac{\partial w_{4_n}}{\partial t}$, and $\frac{\overrightarrow{\partial \overline{P}}}{\partial t}$
20: build a column vector $\frac{\overrightarrow{\partial \vec{X}}}{\partial t}$ with $\frac{\overrightarrow{\partial \overline{\rho_1}}}{\partial t}$, $\frac{\partial \rho_{1_n}}{\partial t}$, $\frac{\overrightarrow{\partial \overline{\rho_2}}}{\partial t}$, $\frac{\partial \rho_{2_n}}{\partial t}$, $\frac{\overrightarrow{\partial \overline{w_4}}}{\partial t}$, $\frac{\partial w_{4_n}}{\partial t}$, $\frac{\overrightarrow{\partial \overline{T}}}{\partial t}$, $\frac{\overrightarrow{\partial \overline{P}}}{\partial t}$
return $\frac{\overrightarrow{\partial \vec{X}}}{\partial t}$
21: **end function**

Appendix C
Results from pyrolysis simulations

Contents

C.1. Wagenaar

C.1.1. 750 K

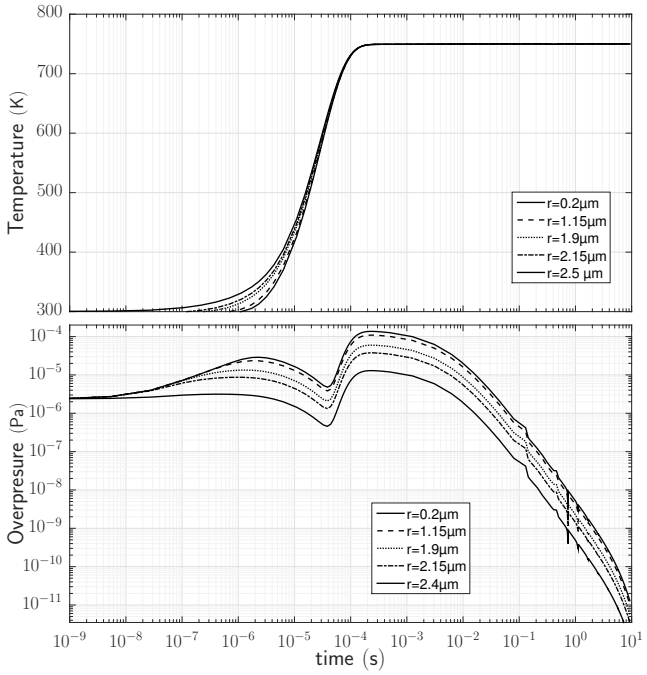

(a) Pressure and Temperature

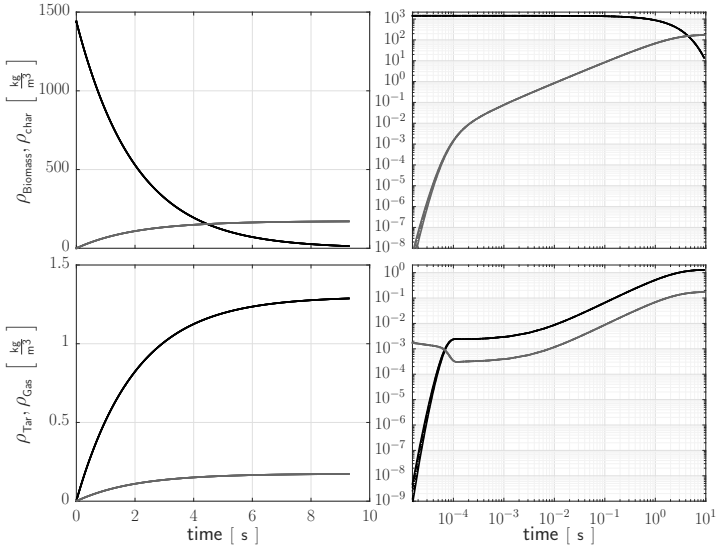

(b) Densities

Figure C.1. Pressure, temperature and densities profiles for a particle with $r = 2.5\,\mu\text{m}$ using Wagenaar kinetics and 750 K, external fluid velocity equal to $1\sigma_\text{p}$. Black lines represent biomass and tar densities whereas gray lines stand for char and gas

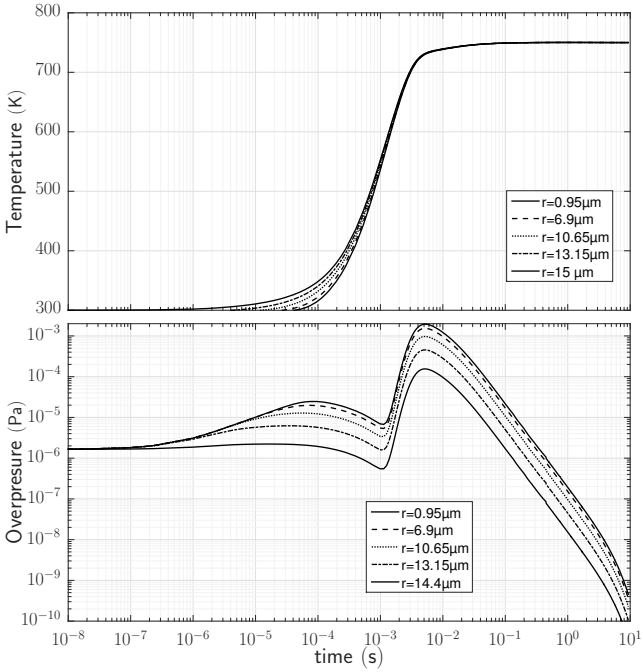

(a) Pressure and Temperature

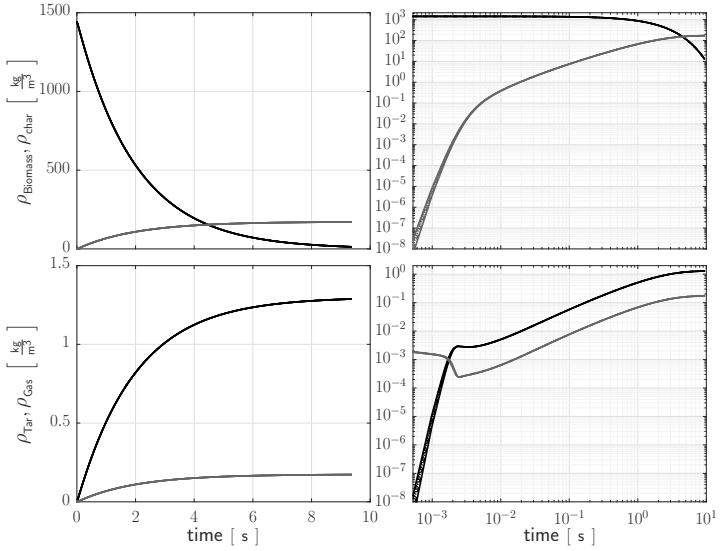

(b) Densities

Figure C.2. Pressure, temperature and densities profiles for a particle with $r = 15\,\mu m$ using Wagenaar kinetics and 750 K, external fluid velocity equal to $1\sigma_p$. Black lines represent biomass and tar densities whereas gray lines stand for char and gas

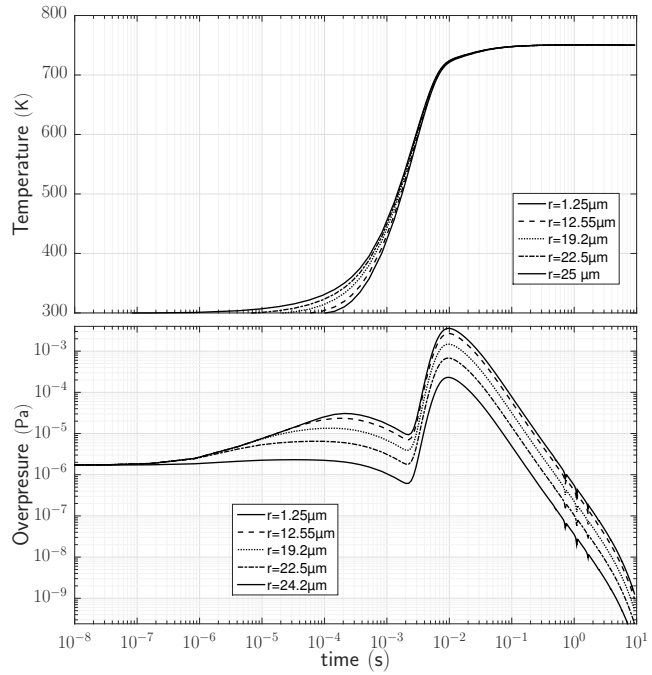

(a) Pressure and Temperature

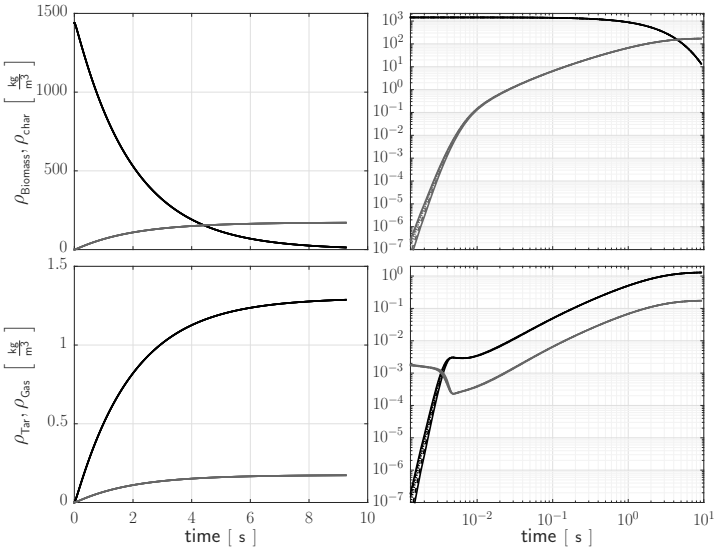

(b) Densities

Figure C.3. Pressure, temperature and densities profiles for a particle with $r = 25\,\mu\text{m}$ using Wagenaar kinetics and 750 K, external fluid velocity equal to $1\sigma_\text{p}$. Black lines represent biomass and tar densities whereas gray lines stand for char and gas

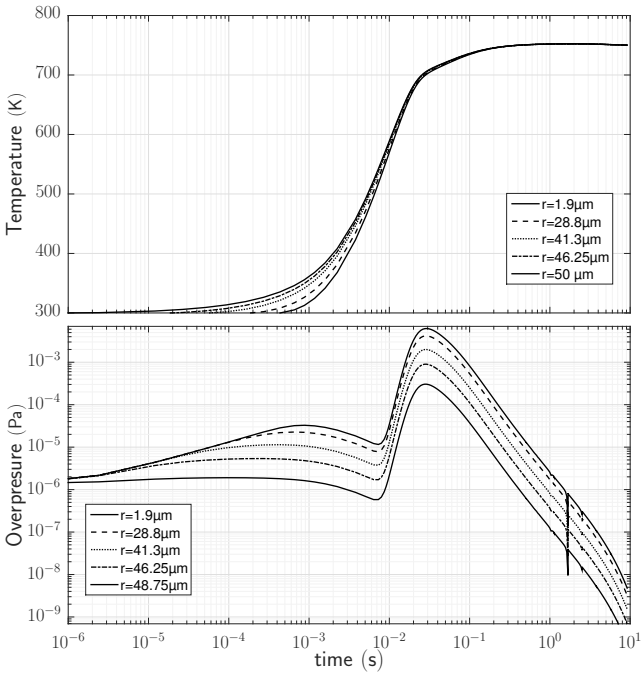

(a) Pressure and Temperature

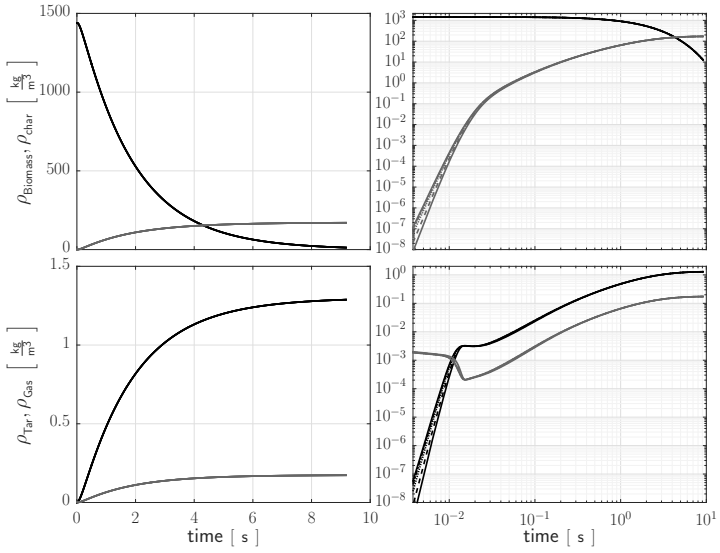

(b) Densities

Figure C.4. Pressure, temperature and densities profiles for a particle with $r = 50\,\mu\text{m}$ using Wagenaar kinetics and 750 K, external fluid velocity equal to $1\sigma_\text{p}$. Black lines represent biomass and tar densities whereas gray lines stand for char and gas

C.1.2. 1000 K

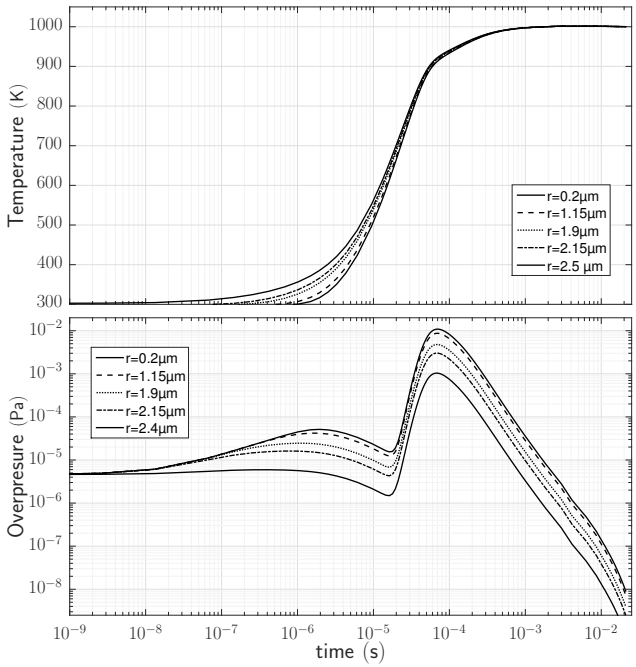

(a) Pressure and Temperature

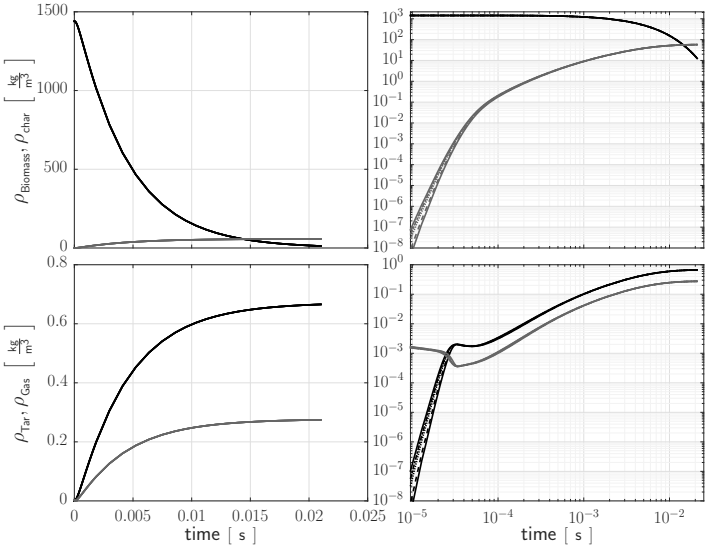

(b) Densities

Figure C.5. Pressure, temperature and densities profiles for a particle with $r = 2.5\,\mu\text{m}$ using Wagenaar kinetics and 1000 K, external fluid velocity equal to $1\sigma_\text{p}$. Black lines represent biomass and tar densities whereas gray lines stand for char and gas

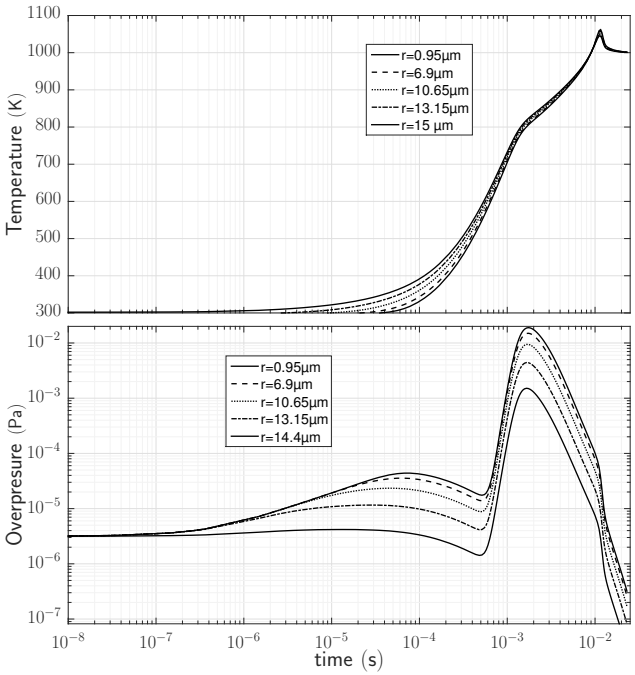

(a) Pressure and Temperature

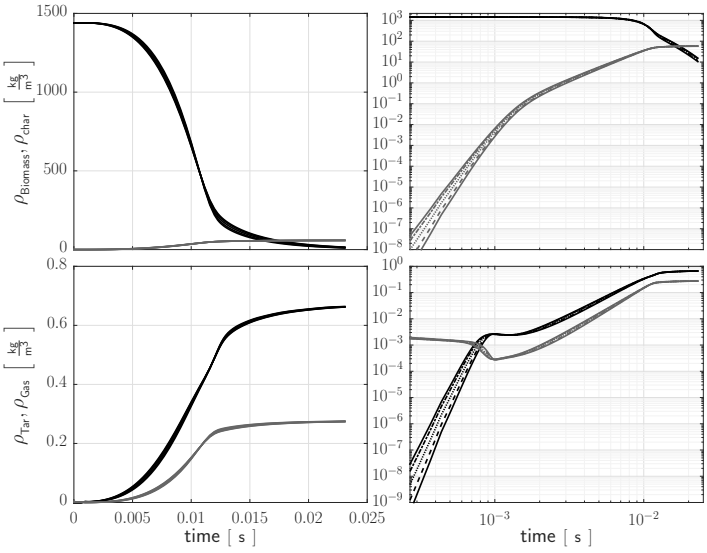

(b) Densities

Figure C.6. Pressure, temperature and densities profiles for a particle with $r = 15\,\mu\text{m}$ using Wagenaar kinetics and 1000 K, external fluid velocity equal to $1\sigma_\text{p}$. Black lines represent biomass and tar densities whereas gray lines stand for char and gas

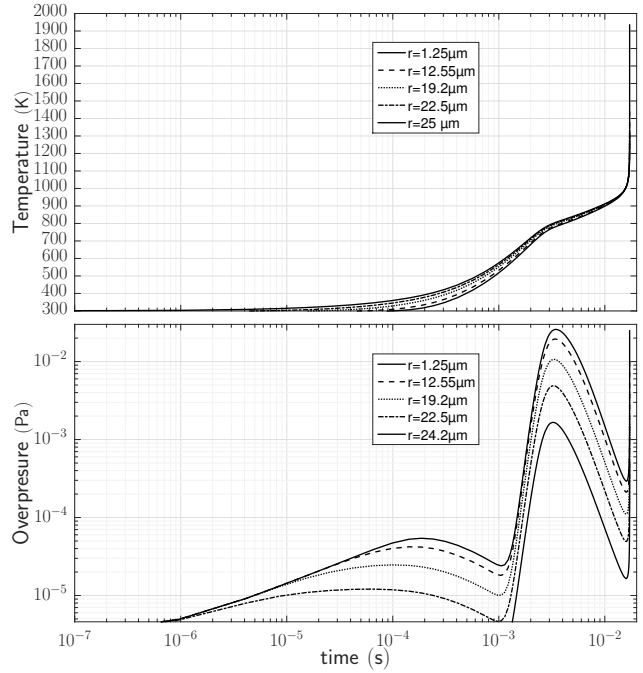

(a) Pressure and Temperature

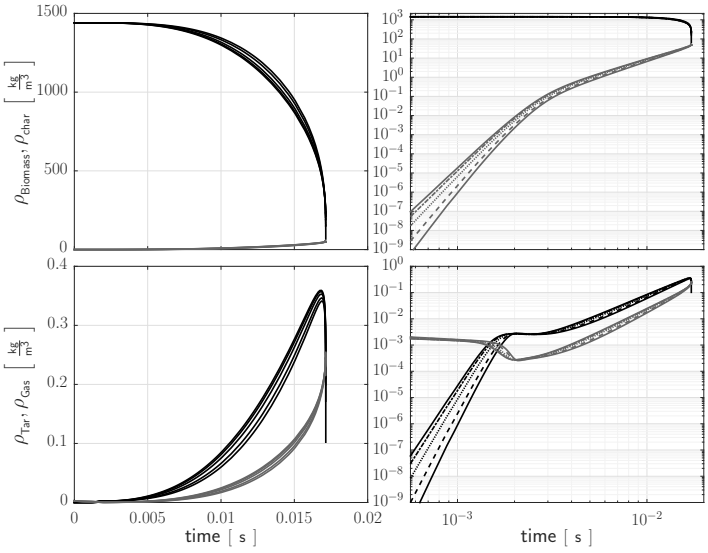

(b) Densities

Figure C.7. Pressure, temperature and densities profiles for a particle with $r = 25\,\mu\text{m}$ using Wagenaar kinetics and 1000 K, external fluid velocity equal to $1\sigma_\text{p}$. Black lines represent biomass and tar densities whereas gray lines stand for char and gas

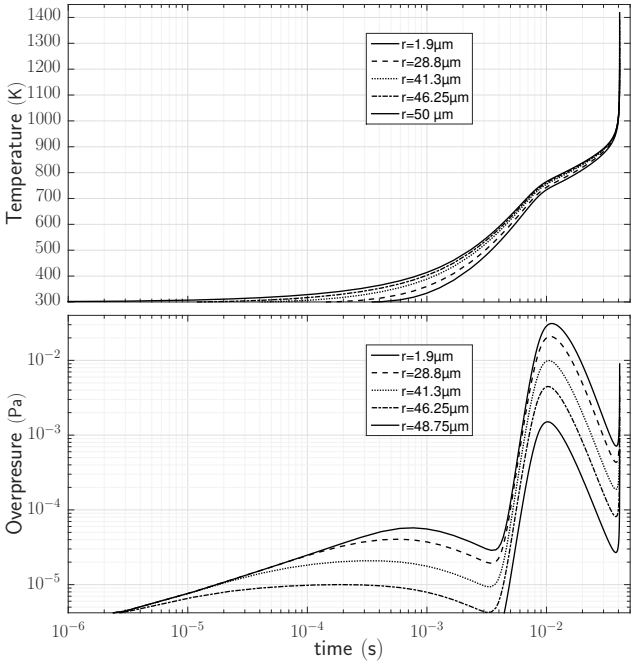

(a) Pressure and Temperature

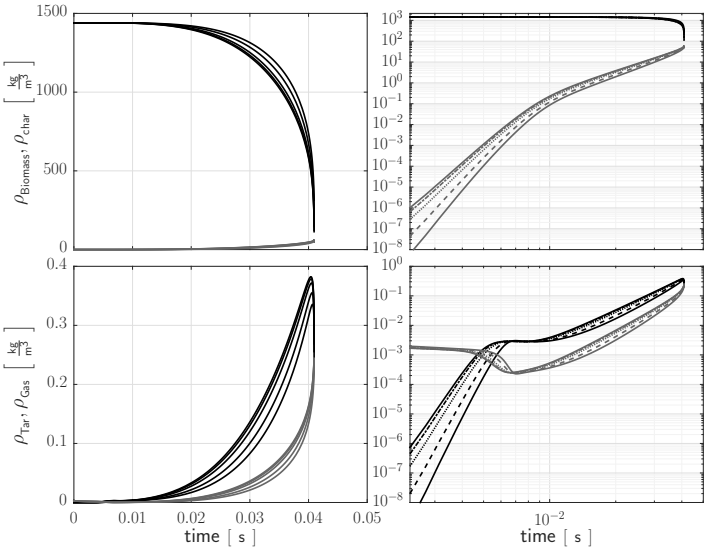

(b) Densities

Figure C.8. Pressure, temperature and densities profiles for a particle with $r = 50\,\mu\text{m}$ using Wagenaar kinetics and 1000 K, external fluid velocity equal to $1\sigma_\text{p}$. Black lines represent biomass and tar densities whereas gray lines stand for char and gas

C.1.3. Minimal C_{dust} to reach the LEL

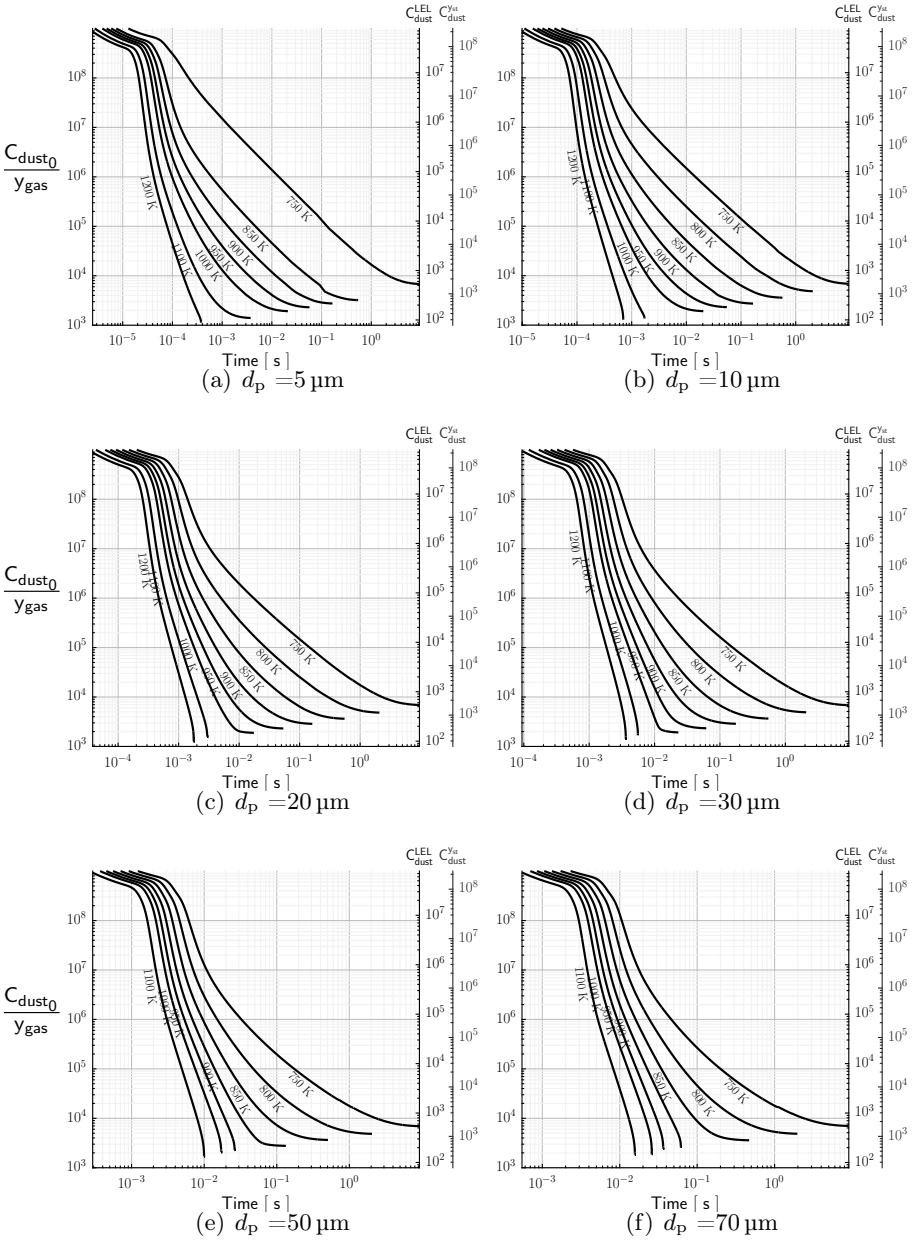

(a) d_{p} =5 µm (b) d_{p} =10 µm

(c) d_{p} =20 µm (d) d_{p} =30 µm

(e) d_{p} =50 µm (f) d_{p} =70 µm

Figure C.9. Initial C_{dust} necessary to reach a concentration of y_4 in pyrolysis gases at time t using to **Wagenaar** kinetics, auxiliary axes on the left show the initial concentration necessary to reach the LEL =7.8% and the stoichiometric concentration (23%) of pyrolysis gases. Units for C_{dust} are in $\frac{\mathrm{g}}{\mathrm{m}^3}$

C.2. DiBlasi

C.2.1. 750 K

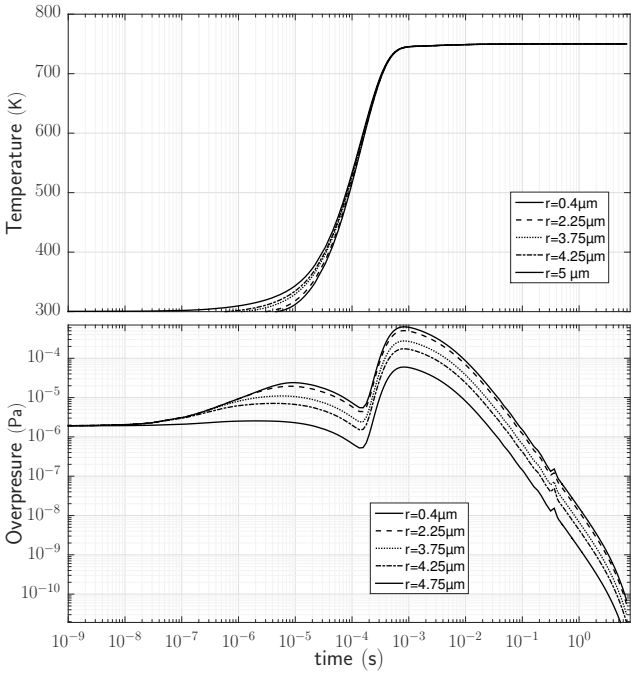

(a) Pressure and Temperature

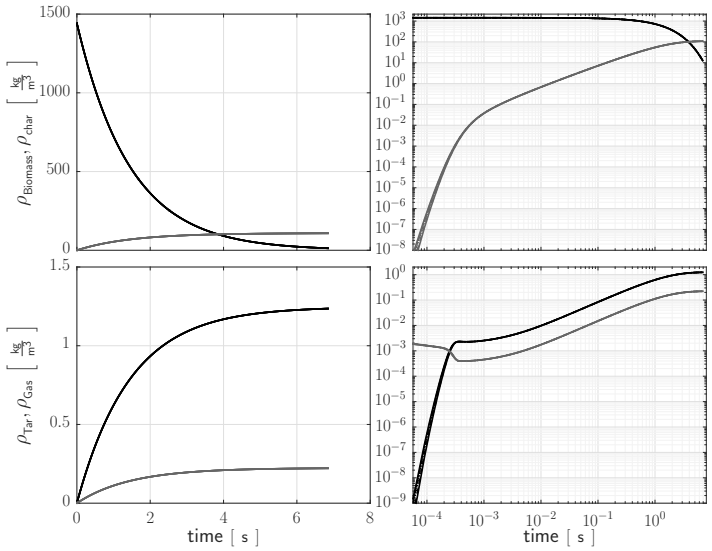

(b) Densities

Figure C.10. Pressure, temperature and densities profiles for a particle with $r = 5\,\mu\text{m}$ using DiBlasi kinetics and 750 K, external fluid velocity equal to $1\sigma_p$. Black lines represent biomass and tar densities whereas gray lines stand for char and gas

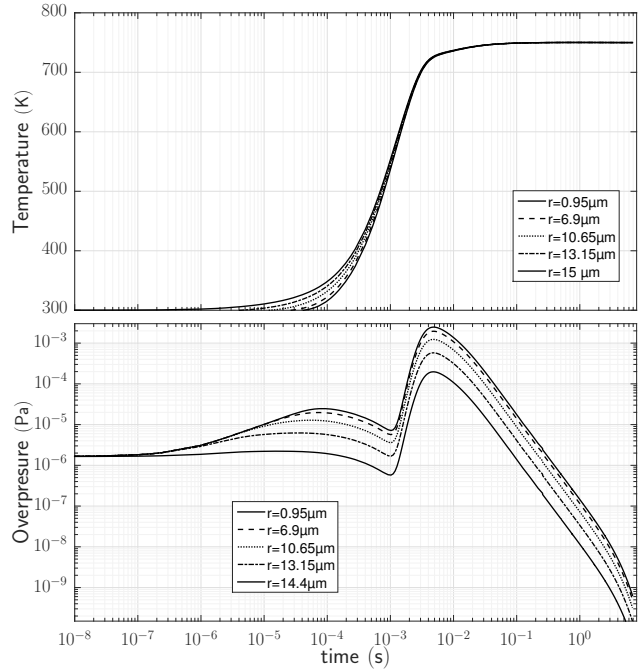

(a) Pressure and Temperature

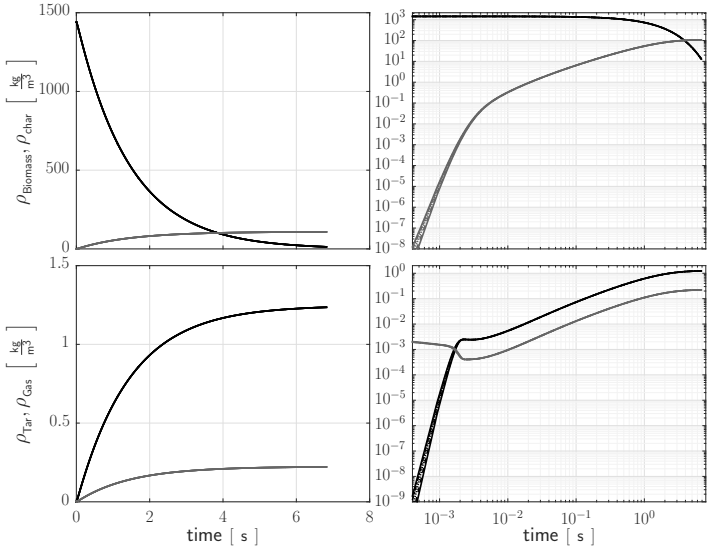

(b) Densities

Figure C.11. Pressure, temperature and densities profiles for a particle with $r = 15\,\mu\text{m}$ using DiBlasi kinetics and 750 K, external fluid velocity equal to $1\sigma_\text{p}$. Black lines represent biomass and tar densities whereas gray lines stand for char and gas

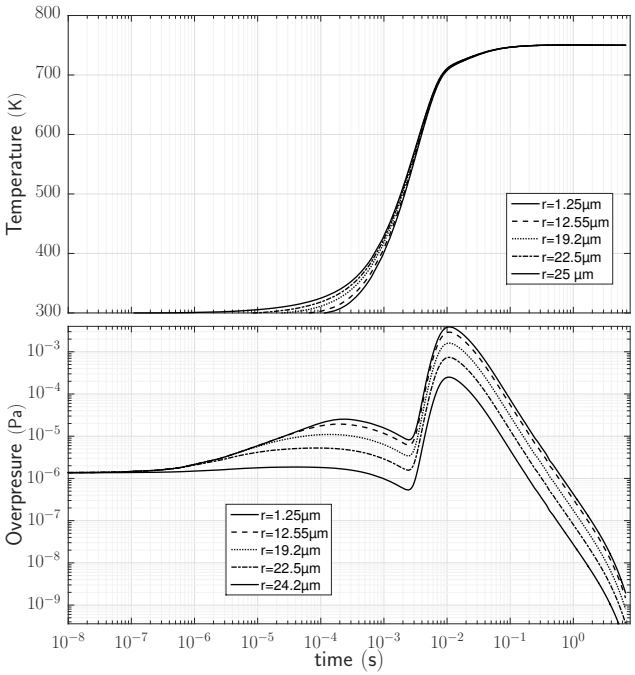

(a) Pressure and Temperature

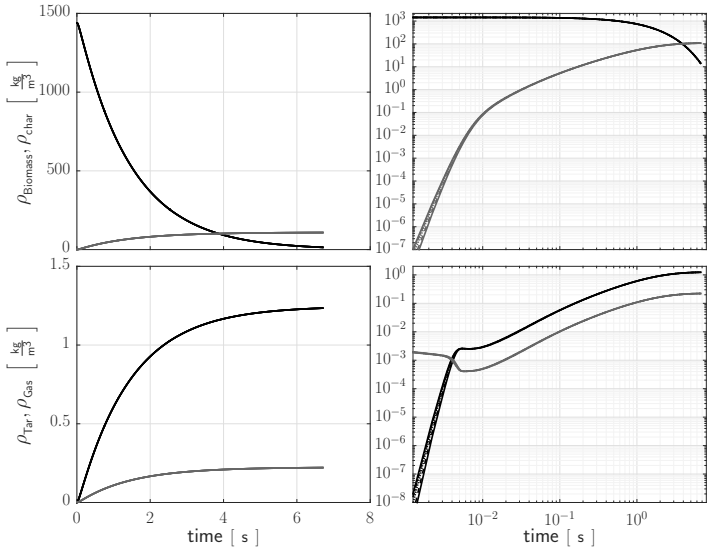

(b) Densities

Figure C.12. Pressure, temperature and densities profiles for a particle with $r = 25\,\mu\text{m}$ using DiBlasi kinetics and 750 K, external fluid velocity equal to $1\sigma_\text{p}$. Black lines represent biomass and tar densities whereas gray lines stand for char and gas

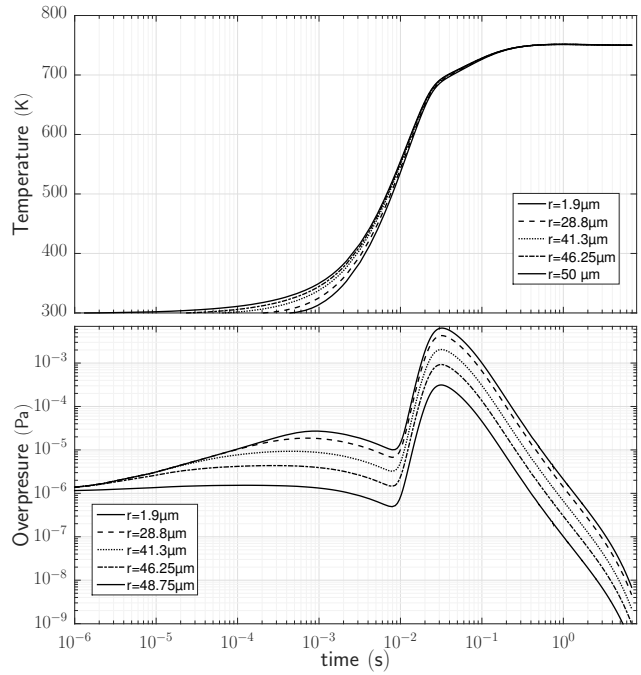

(a) Pressure and Temperature

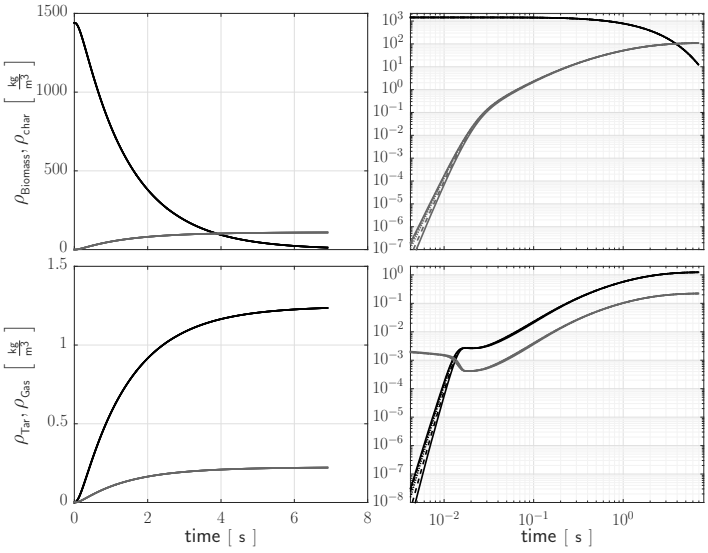

(b) Densities

Figure C.13. Pressure, temperature and densities profiles for a particle with $r = 50\,\mu\text{m}$ using DiBlasi kinetics and 750 K, external fluid velocity equal to $1\sigma_p$. Black lines represent biomass and tar densities whereas gray lines stand for char and gas

C.2.2. 1000 K

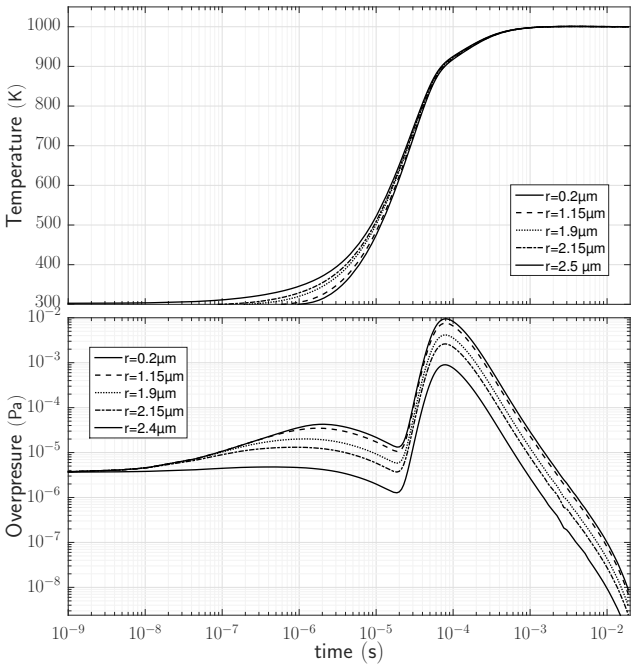

(a) Pressure and Temperature

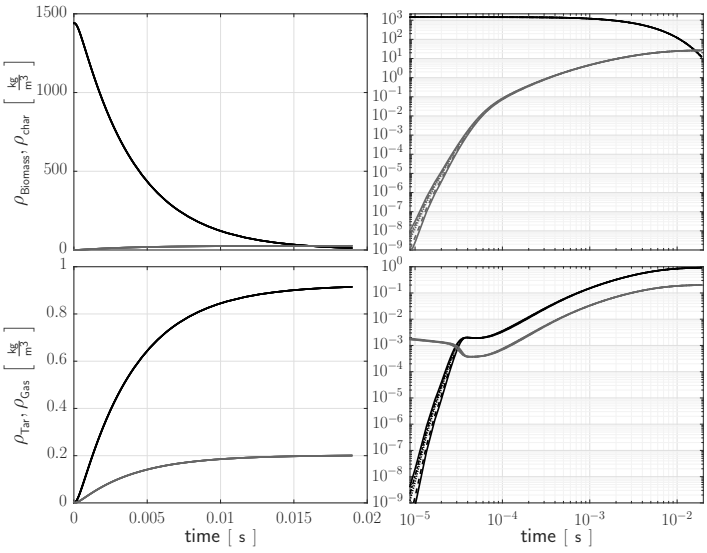

(b) Densities

Figure C.14. Pressure, temperature and densities profiles for a particle with $r = 2.5\,\mu\text{m}$ using DiBlasi kinetics and 1000 K, external fluid velocity equal to $1\sigma_\text{p}$. Black lines represent biomass and tar densities whereas gray lines stand for char and gas

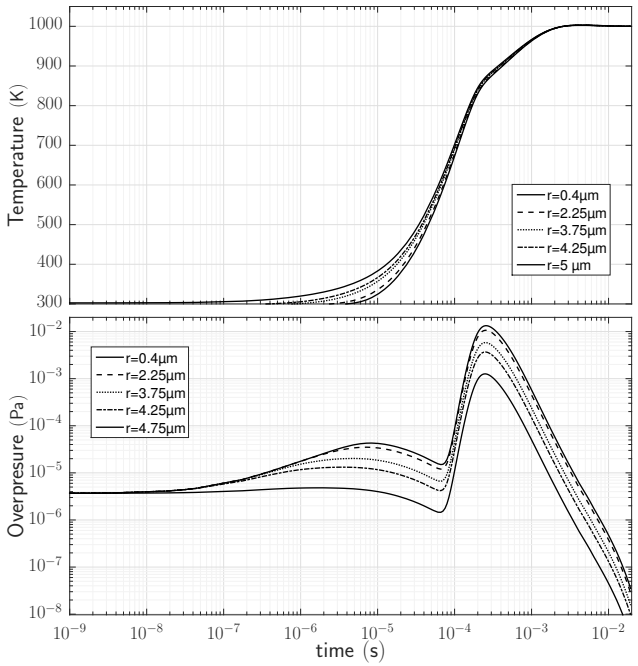

(a) Pressure and Temperature

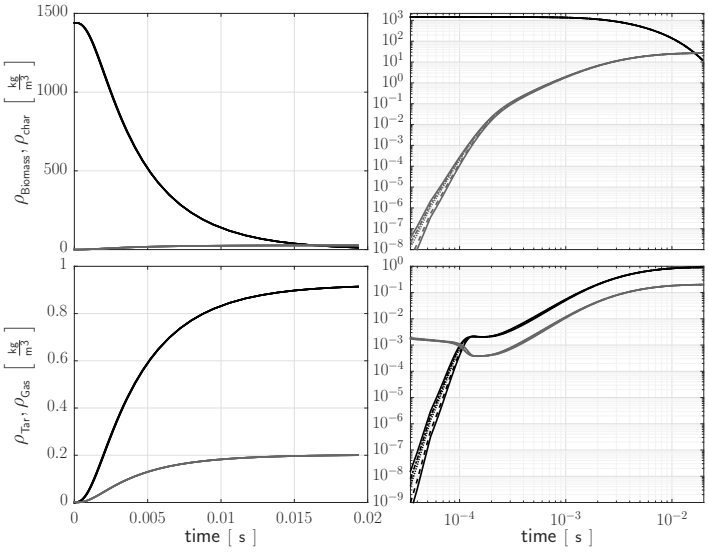

(b) Densities

Figure C.15. Pressure, temperature and densities profiles for a particle with $r = 5\,\mu\text{m}$ using DiBlasi kinetics and 1000 K, external fluid velocity equal to $1\sigma_\text{p}$. Black lines represent biomass and tar densities whereas gray lines stand for char and gas

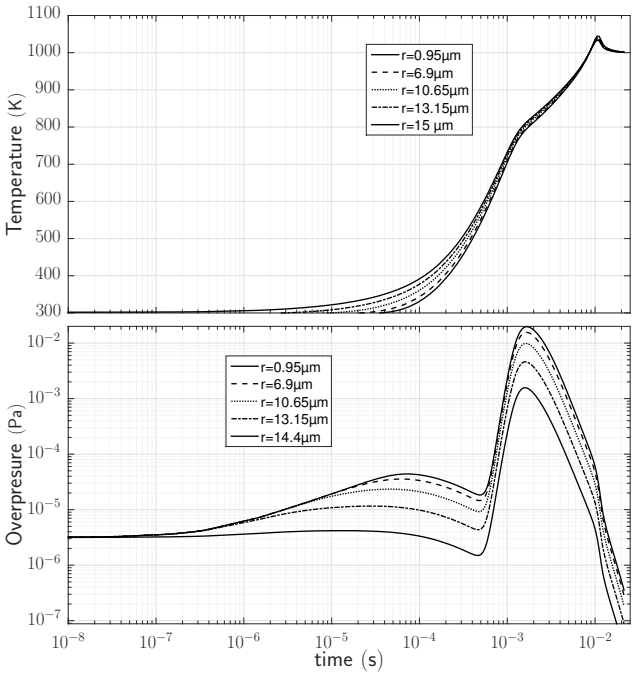

(a) Pressure and Temperature

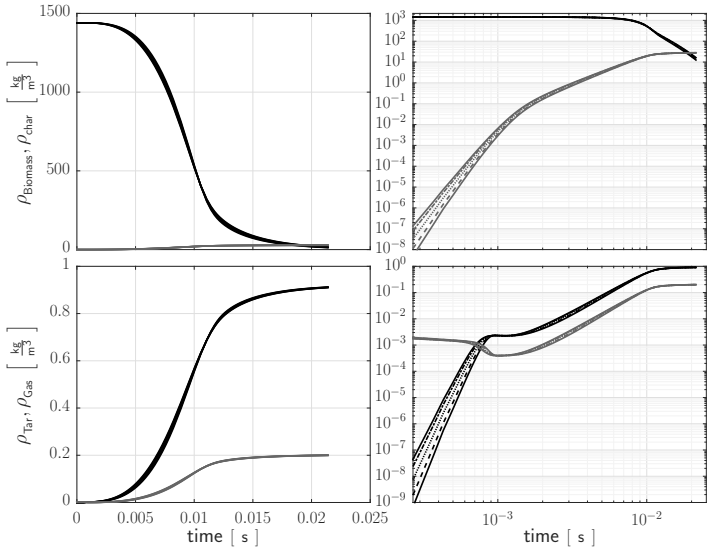

(b) Densities

Figure C.16. Pressure, temperature and densities profiles for a particle with $r = 15\,\mu\text{m}$ using DiBlasi kinetics and 1000 K, external fluid velocity equal to $1\sigma_\text{p}$. Black lines represent biomass and tar densities whereas gray lines stand for char and gas

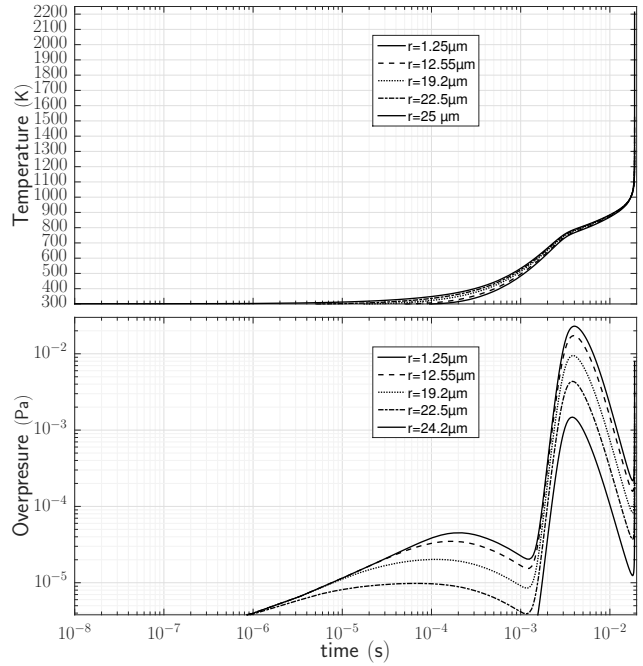

(a) Pressure and Temperature

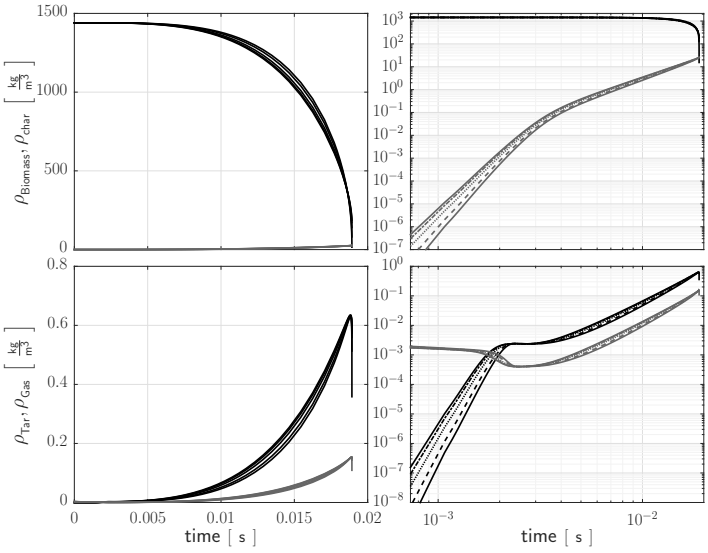

(b) Densities

Figure C.17. Pressure, temperature and densities profiles for a particle with $r = 25\,\mu\text{m}$ using DiBlasi kinetics and 1000 K, external fluid velocity equal to $1\sigma_\text{p}$. Black lines represent biomass and tar densities whereas gray lines stand for char and gas

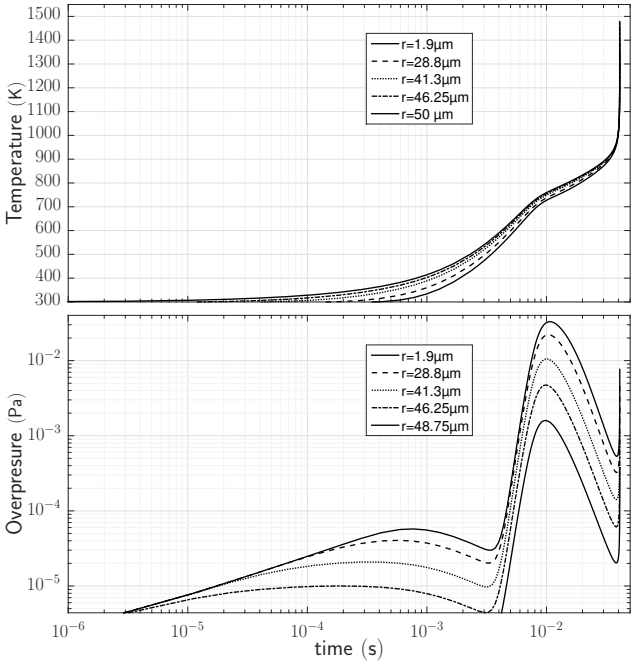

(a) Pressure and Temperature

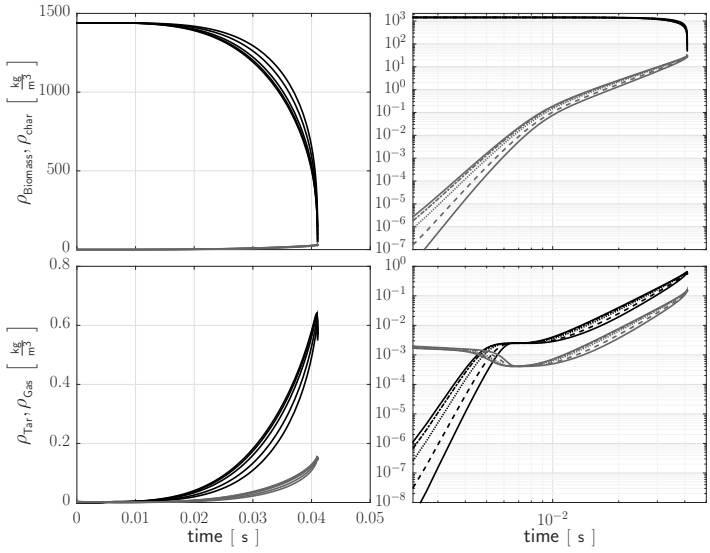

(b) Densities

Figure C.18. Pressure, temperature and densities profiles for a particle with $r = 50\,\mu\text{m}$ using DiBlasi kinetics and 1000 K, external fluid velocity equal to $1\sigma_\text{p}$. Black lines represent biomass and tar densities whereas gray lines stand for char and gas

C.2.3. Minimal C_{dust} to reach the LEL

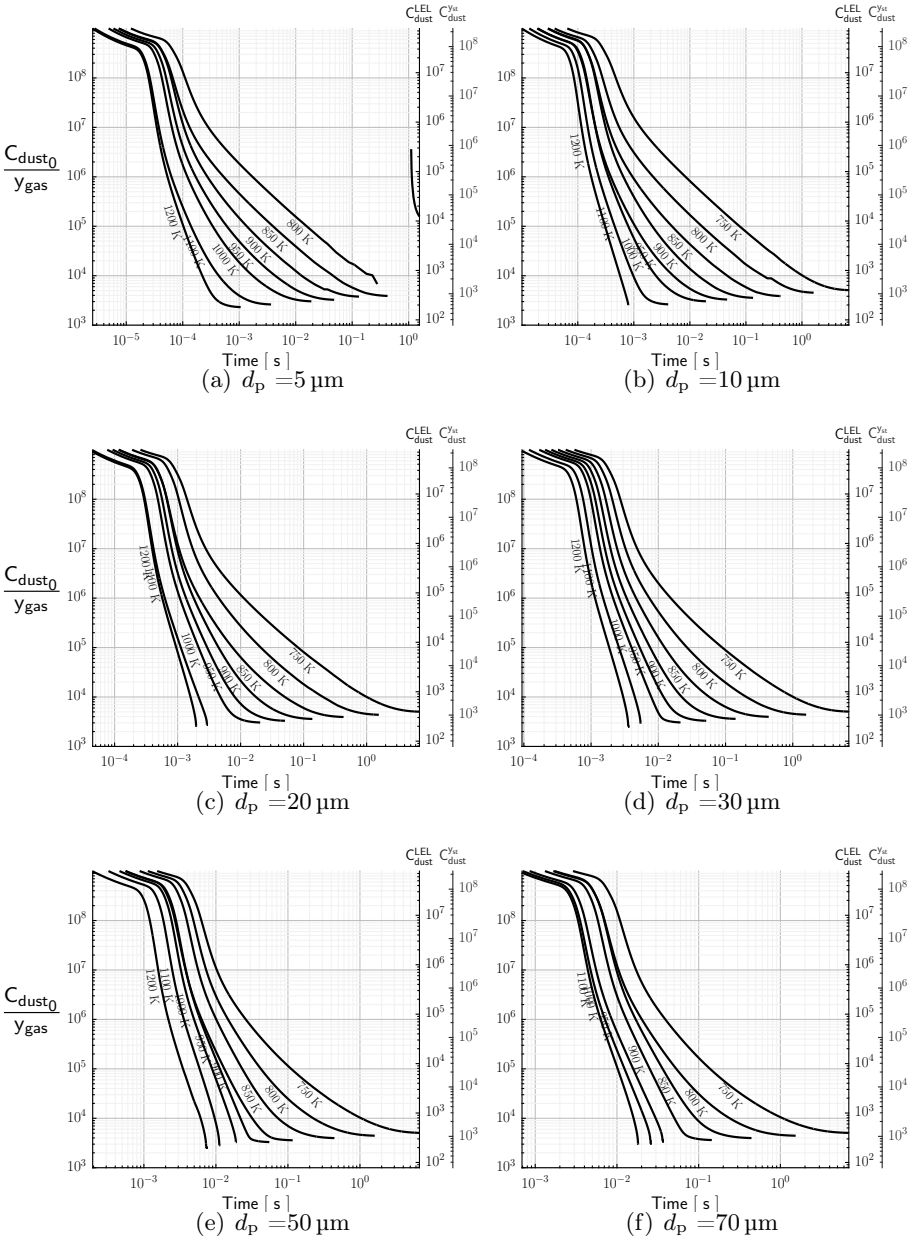

(a) d_{p} =5 µm (b) d_{p} =10 µm

(c) d_{p} =20 µm (d) d_{p} =30 µm

(e) d_{p} =50 µm (f) d_{p} =70 µm

Figure C.19. Initial C_{dust} necessary to reach a concentration of y_4 in pyrolysis gases at time t using to **DiBlasi** kinetics, auxiliary axes on the left show the initial concentration necessary to reach the LEL =7.8% and the stoichiometric concentration (23%) of pyrolysis gases. Units for C_{dust} are in $\frac{\text{g}}{\text{m}^3}$

C.3. Font

C.3.1. 750 K

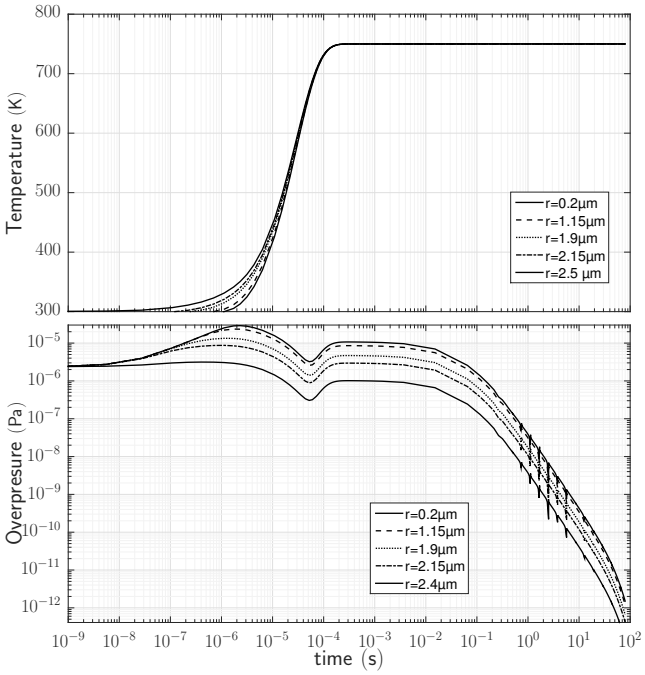

(a) Pressure and Temperature

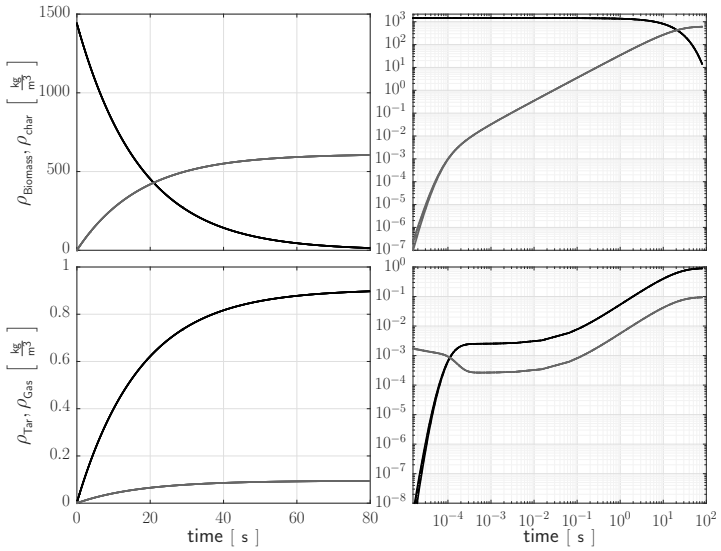

(b) Densities

Figure C.20. Pressure, temperature and densities profiles for a particle with $r = 2.5\,\mu\text{m}$ using Font kinetics and 750 K, external fluid velocity equal to $1\sigma_p$. Black lines represent biomass and tar densities whereas gray lines stand for char and gas

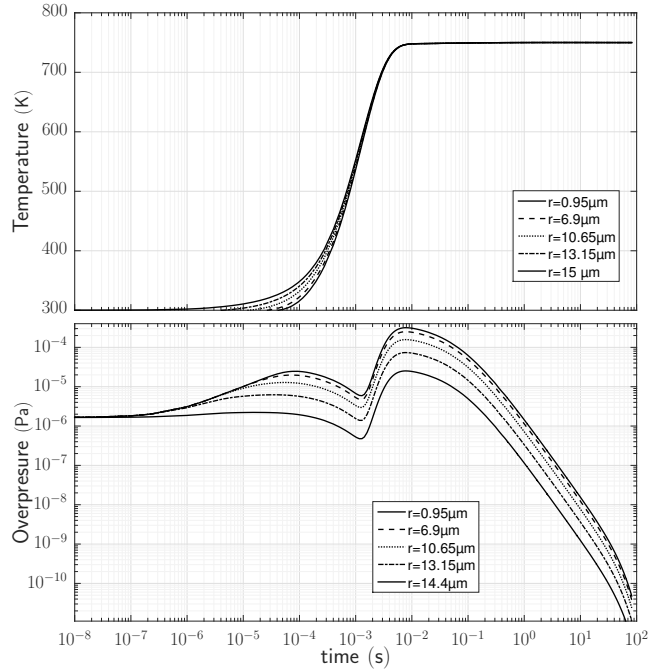

(a) Pressure and Temperature

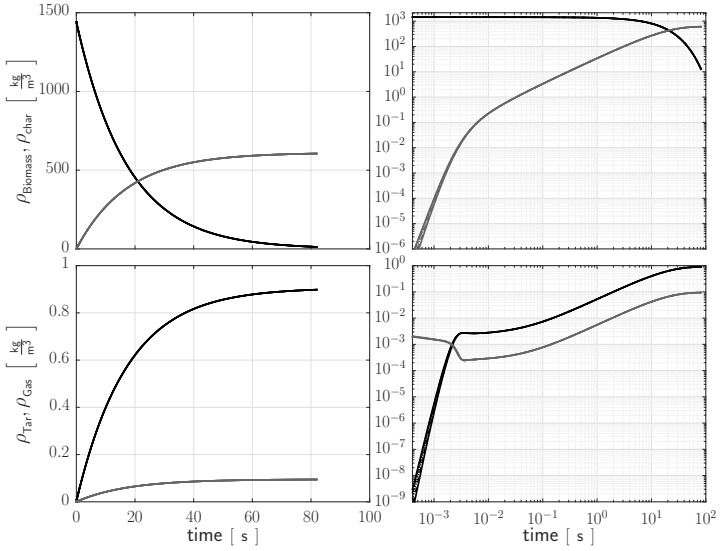

(b) Densities

Figure C.21. Pressure, temperature and densities profiles for a particle with $r = 15\,\mu\text{m}$ using Font kinetics and 750 K, external fluid velocity equal to $1\sigma_\text{p}$. Black lines represent biomass and tar densities whereas gray lines stand for char and gas

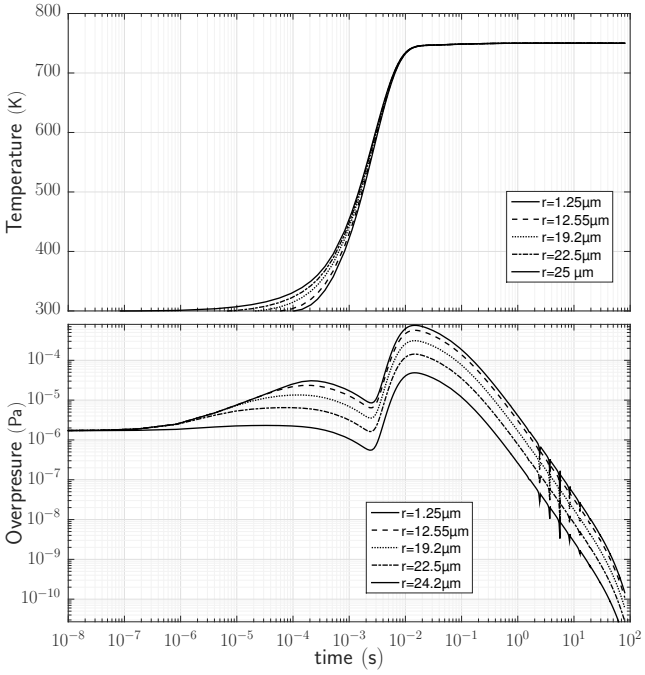

(a) Pressure and Temperature

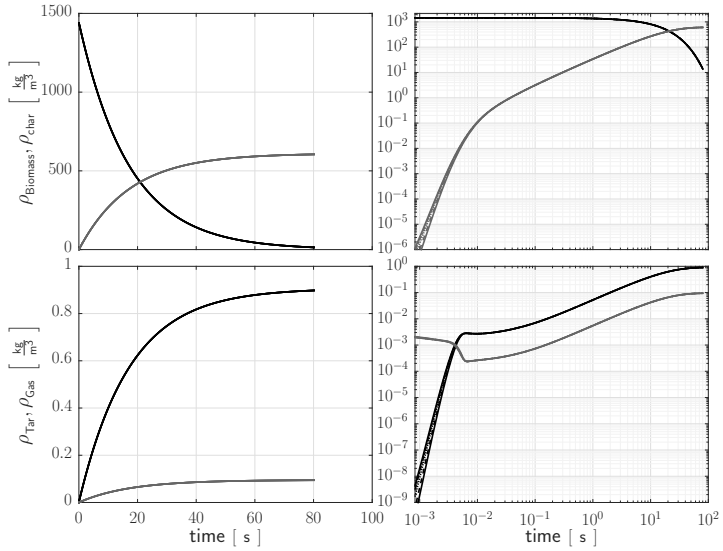

(b) Densities

Figure C.22. Pressure, temperature and densities profiles for a particle with $r = 25\,\mu\text{m}$ using Font kinetics and 750 K, external fluid velocity equal to $1\sigma_\text{p}$. Black lines represent biomass and tar densities whereas gray lines stand for char and gas

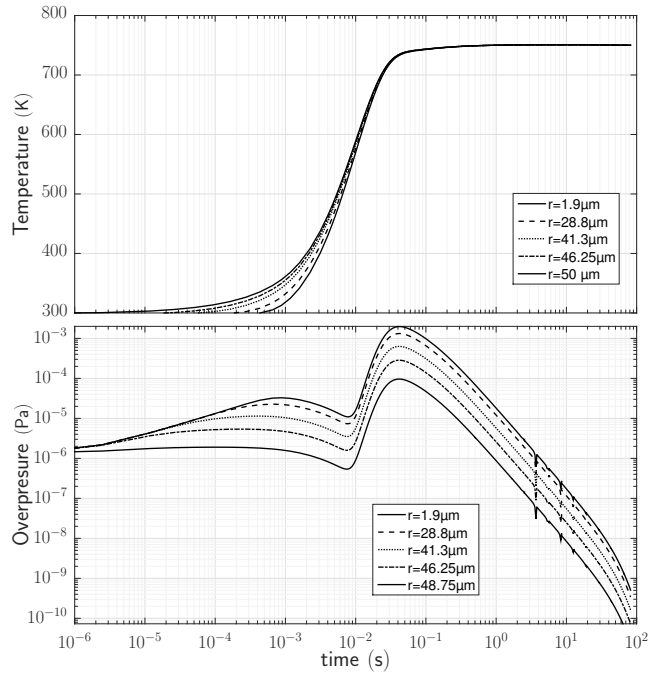

(a) Pressure and Temperature

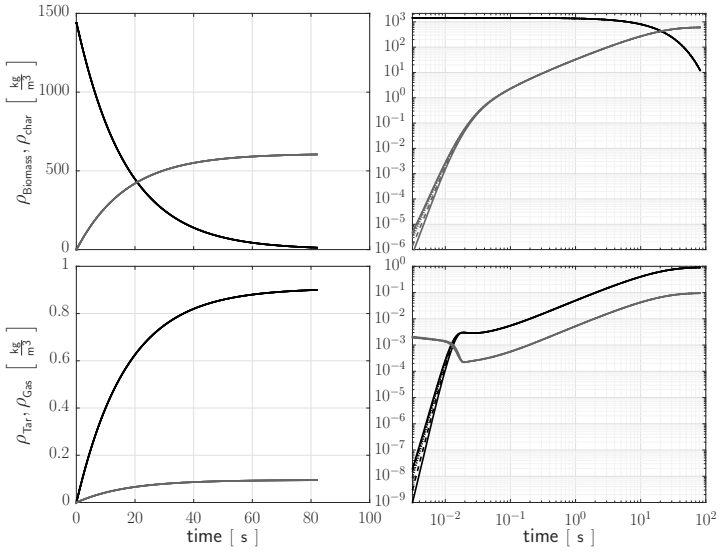

(b) Densities

Figure C.23. Pressure, temperature and densities profiles for a particle with $r = 50\,\mu\text{m}$ using Font kinetics and 750 K, external fluid velocity equal to $1\sigma_\text{p}$. Black lines represent biomass and tar densities whereas gray lines stand for char and gas

C.3.2. 1000 K

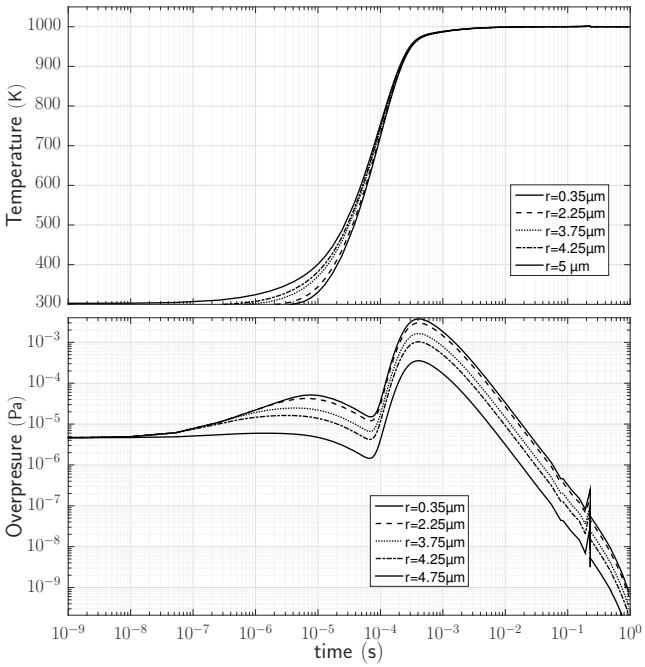

(a) Pressure and Temperature

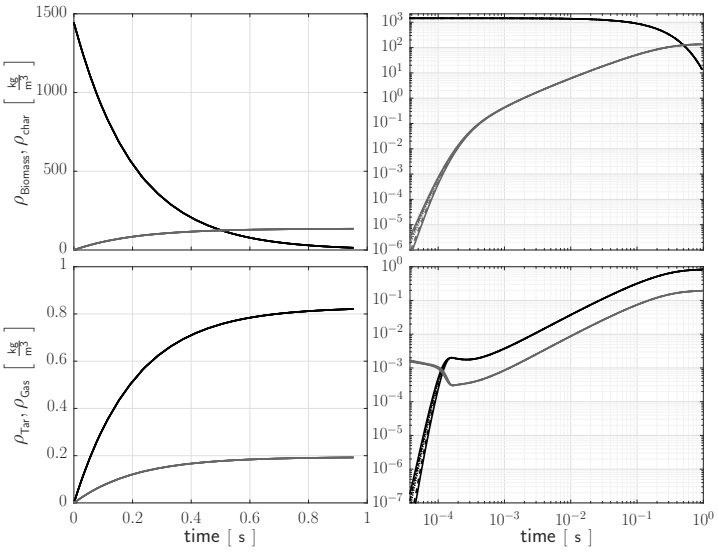

(b) Densities

Figure C.24. Pressure, temperature and densities profiles for a particle with $r = 5\,\mu\text{m}$ using Font kinetics and 1000 K, external fluid velocity equal to $1\sigma_\text{p}$. Black lines represent biomass and tar densities whereas gray lines stand for char and gas

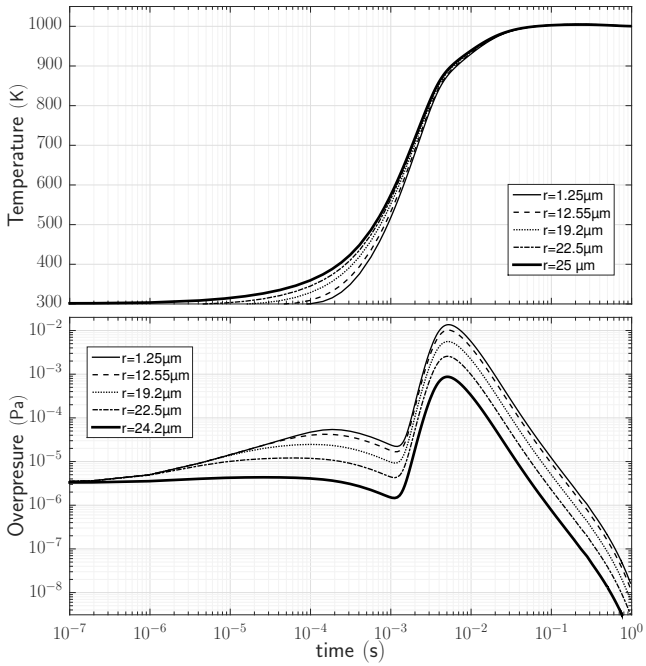

(a) Pressure and Temperature

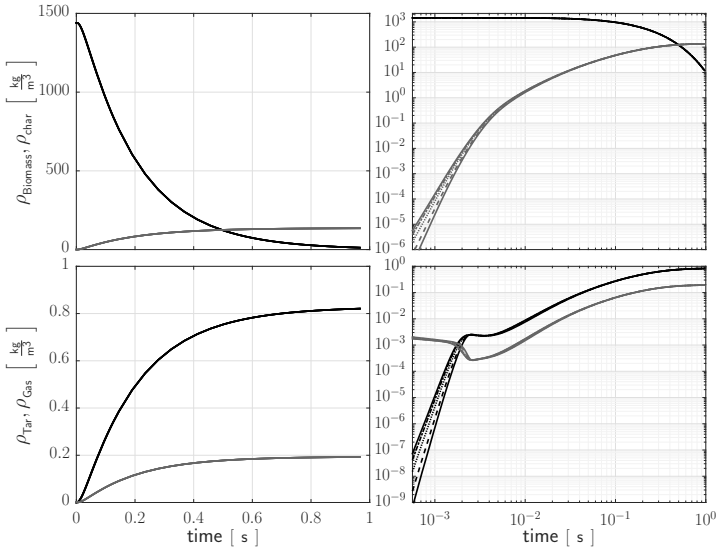

(b) Densities

Figure C.25. Pressure, temperature and densities profiles for a particle with $r = 25\,\mu\text{m}$ using Font kinetics and 1000 K, external fluid velocity equal to $1\sigma_\text{p}$. Black lines represent biomass and tar densities whereas gray lines stand for char and gas

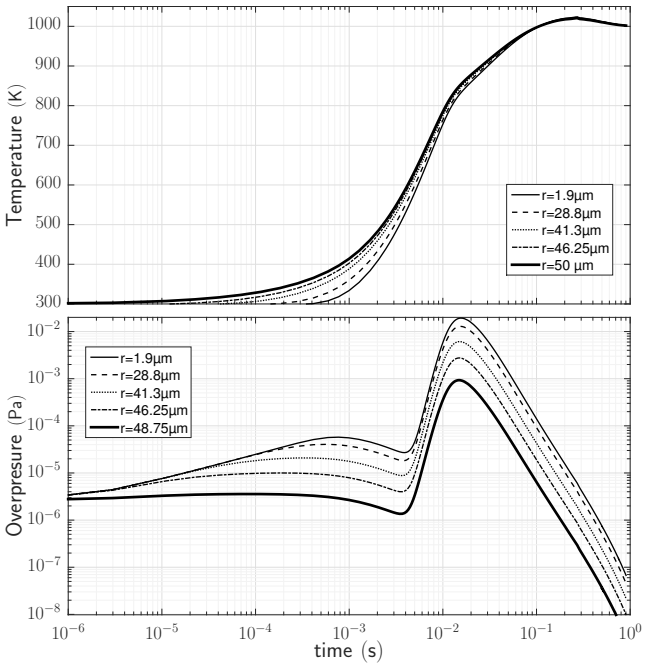

(a) Pressure and Temperature

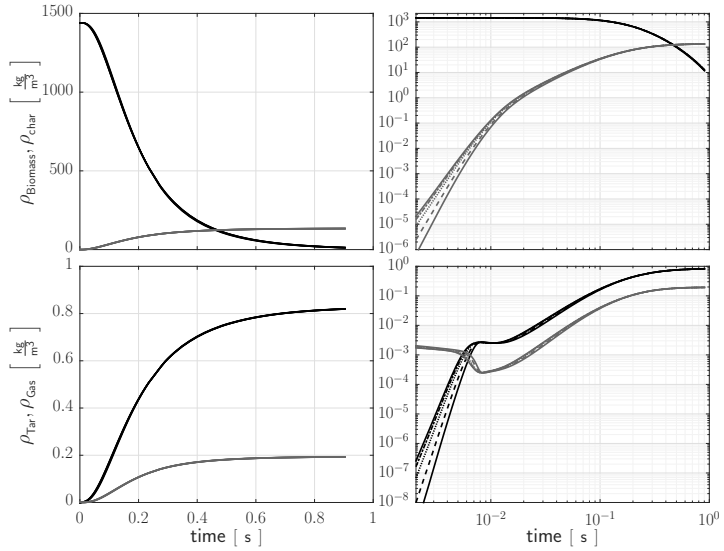

(b) Densities

Figure C.26. Pressure, temperature and densities profiles for a particle with $r = 50\,\mu\text{m}$ using Font kinetics and 1000 K, external fluid velocity equal to $1\sigma_p$. Black lines represent biomass and tar densities whereas gray lines stand for char and gas

C.3.3. Minimal C_{dust} to reach the LEL

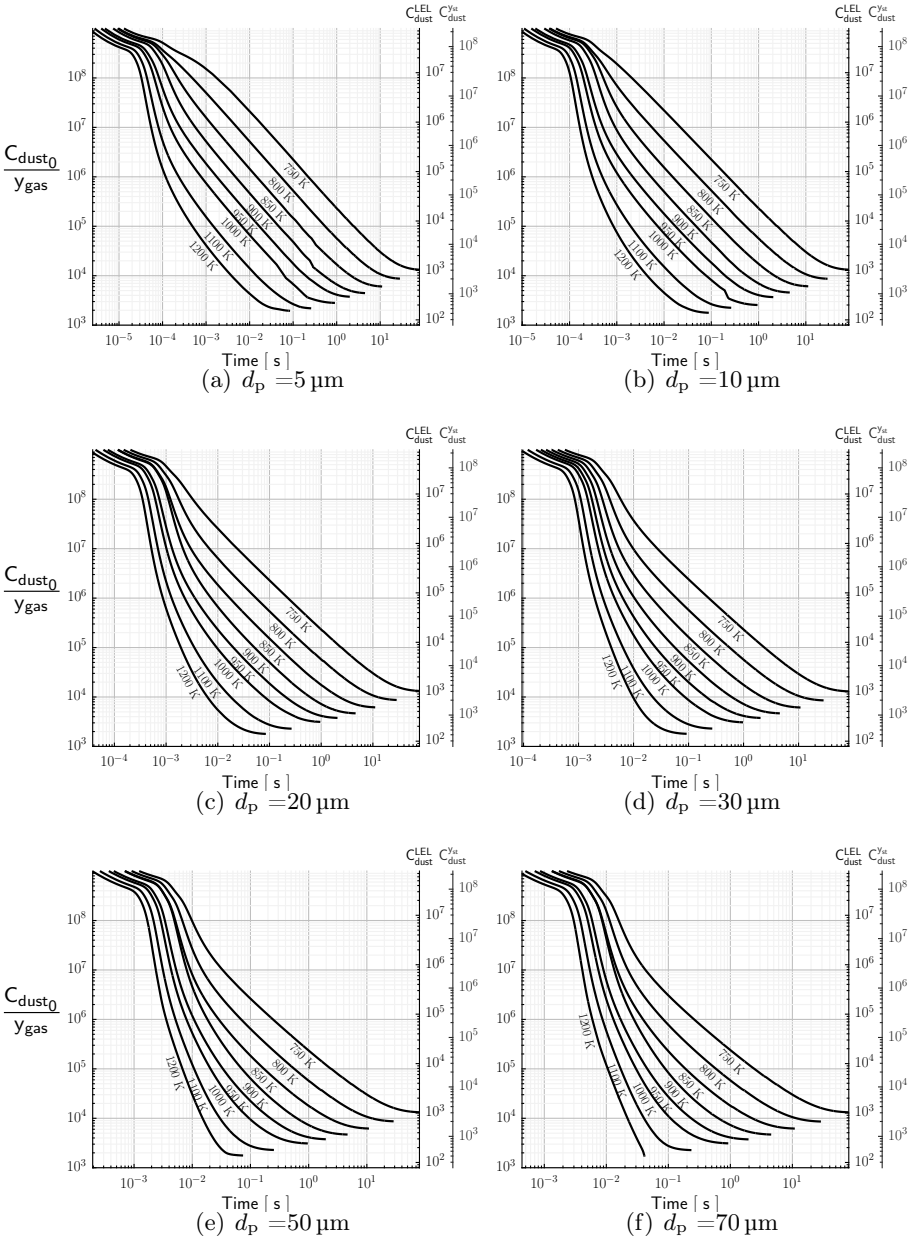

Figure C.27. Initial C_{dust} necessary to reach a concentration of y_4 in pyrolysis gases at time t using to **Font** kinetics, auxiliary axes on the left show the initial concentration necessary to reach the LEL =7.8% and the stoichiometric concentration (23%) of pyrolysis gases. Units for C_{dust} are in $\frac{\mathrm{g}}{\mathrm{m}^3}$

C.4. Chan

C.4.1. 750 K

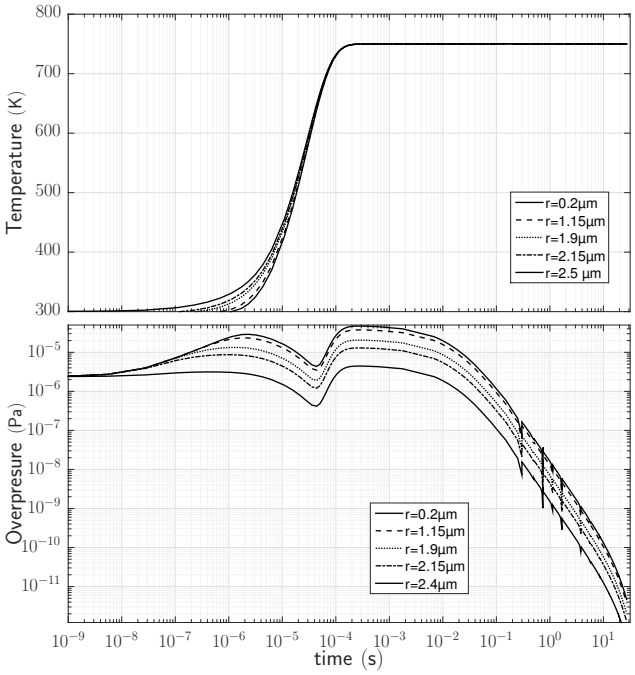

(a) Pressure and Temperature

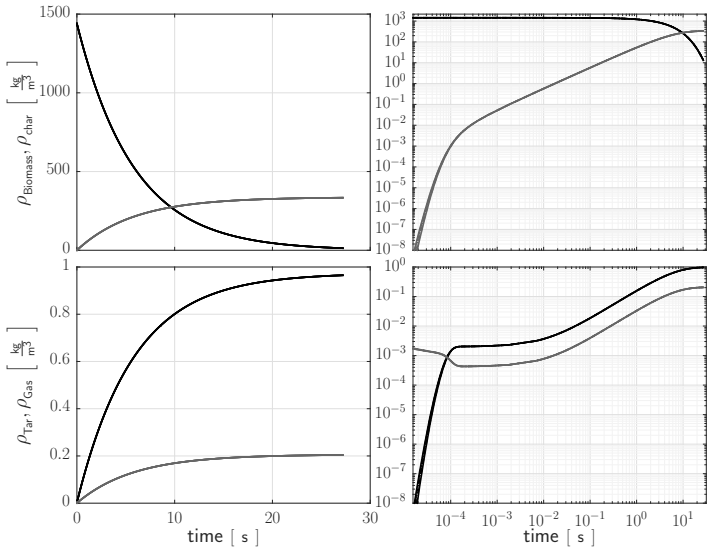

(b) Densities

Figure C.28. Pressure, temperature and densities profiles for a particle with $r = 2.5\,\mu\text{m}$ using Chan kinetics and 750 K, external fluid velocity equal to $1\sigma_p$. Black lines represent biomass and tar densities whereas gray lines stand for char and gas

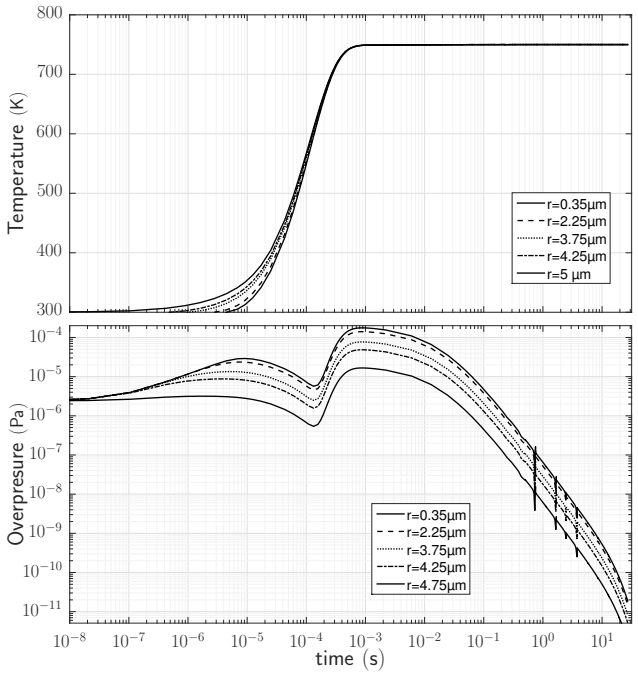

(a) Pressure and Temperature

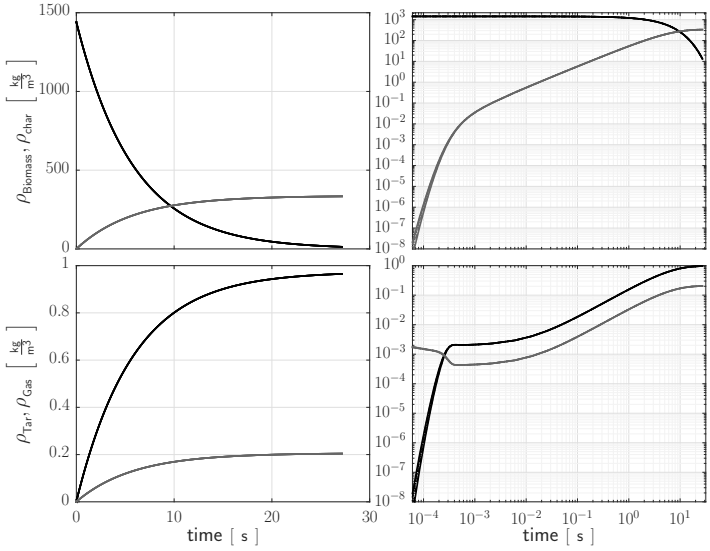

(b) Densities

Figure C.29. Pressure, temperature and densities profiles for a particle with $r = 5\,\mu\text{m}$ using Chan kinetics and 750 K, external fluid velocity equal to $1\sigma_\text{p}$. Black lines represent biomass and tar densities whereas gray lines stand for char and gas

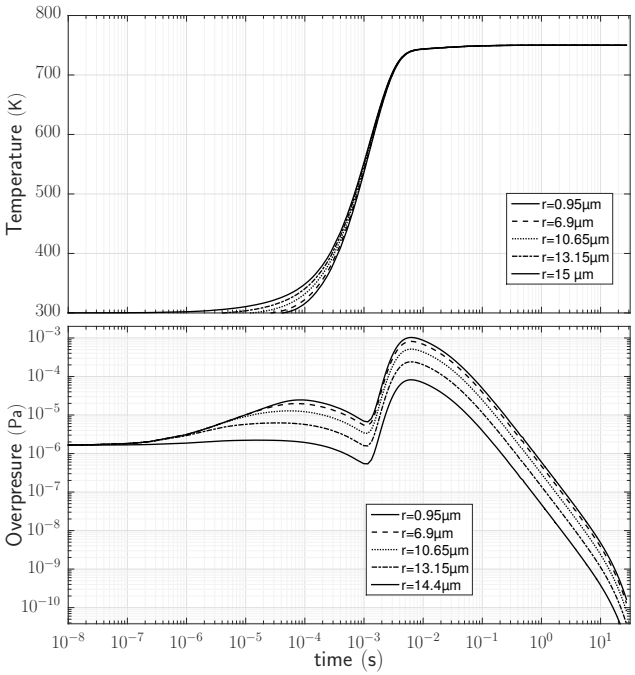

(a) Pressure and Temperature

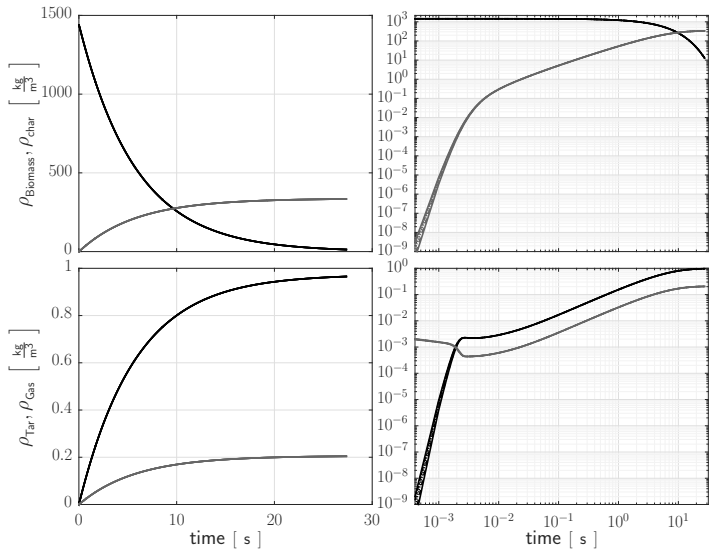

(b) Densities

Figure C.30. Pressure, temperature and densities profiles for a particle with $r = 15\,\mu\text{m}$ using Chan kinetics and 750 K, external fluid velocity equal to $1\sigma_\text{p}$. Black lines represent biomass and tar densities whereas gray lines stand for char and gas

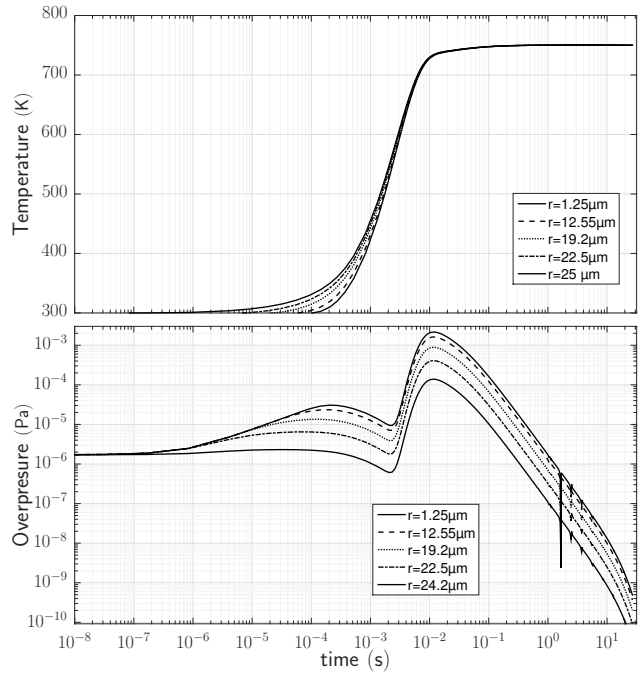

(a) Pressure and Temperature

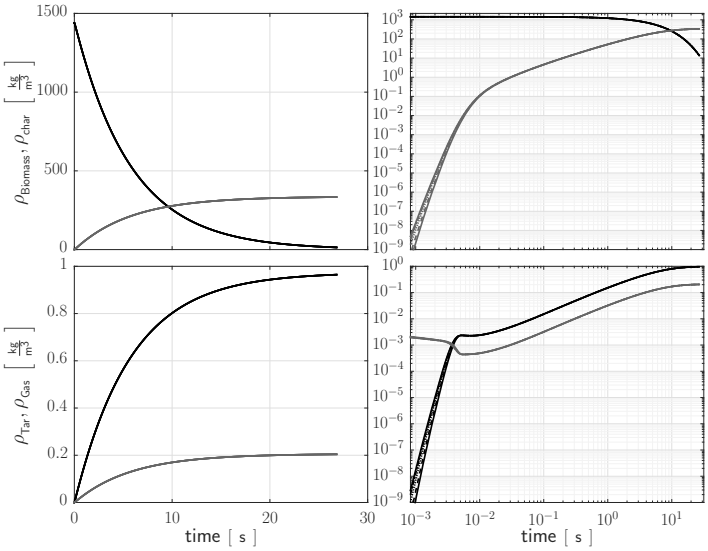

(b) Densities

Figure C.31. Pressure, temperature and densities profiles for a particle with $r = 25\,\mu\text{m}$ using Chan kinetics and 750 K, external fluid velocity equal to $1\sigma_\text{p}$. Black lines represent biomass and tar densities whereas gray lines stand for char and gas

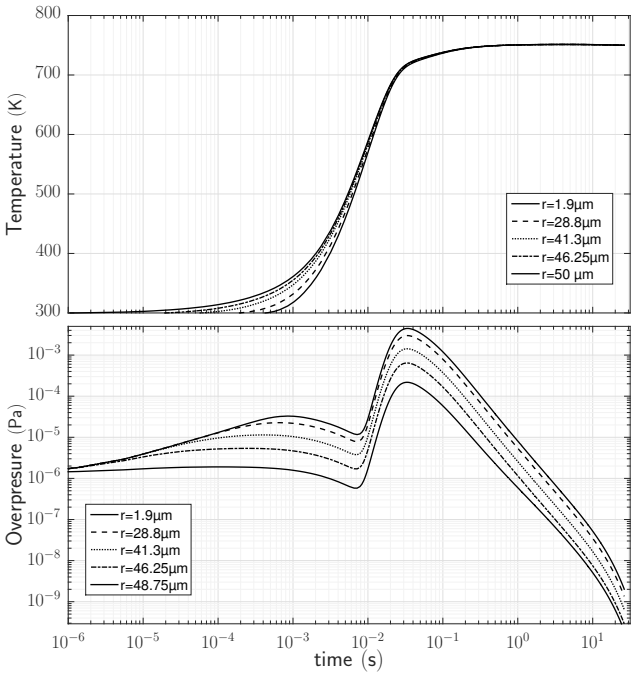

(a) Pressure and Temperature

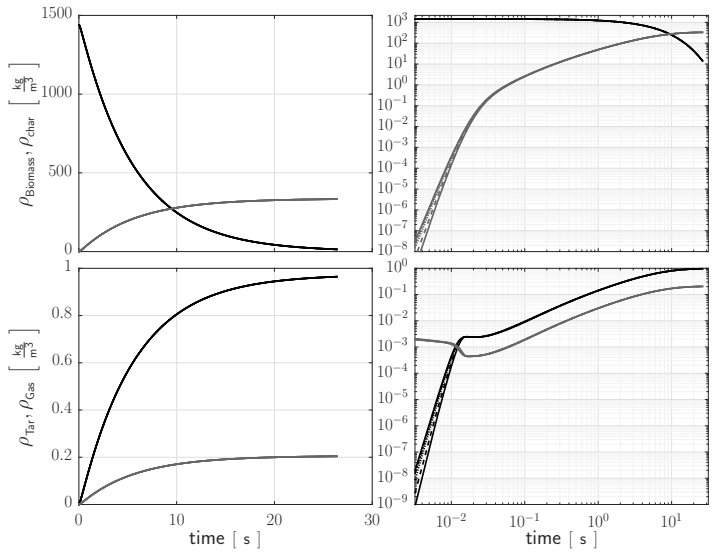

(b) Densities

Figure C.32. Pressure, temperature and densities profiles for a particle with $r = 50\,\mu\text{m}$ using Chan kinetics and 750 K, external fluid velocity equal to $1\sigma_p$. Black lines represent biomass and tar densities whereas gray lines stand for char and gas

C.4.2. 1000 K

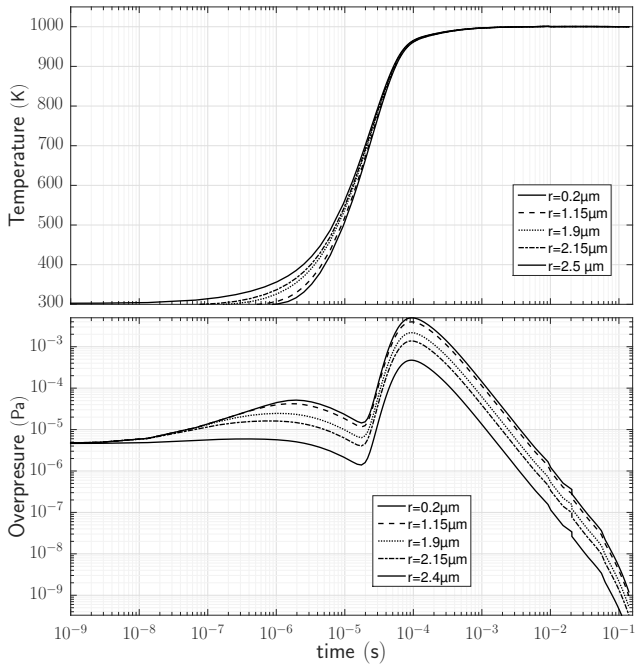

(a) Pressure and Temperature

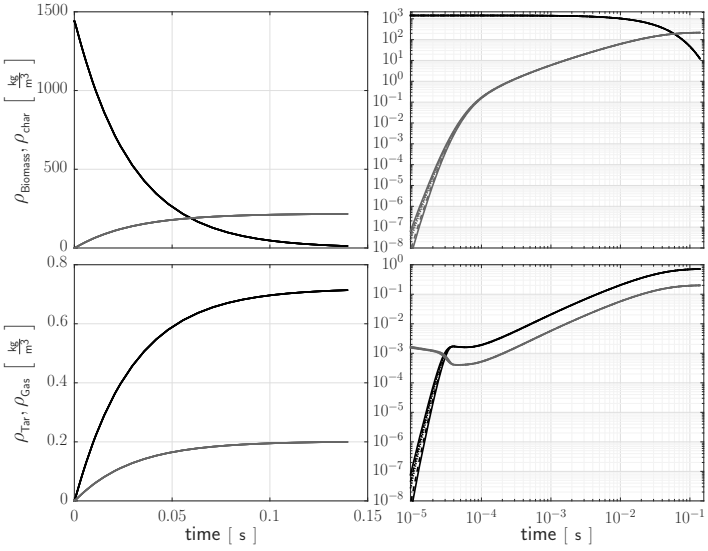

(b) Densities

Figure C.33. Pressure, temperature and densities profiles for a particle with $r = 2.5\,\mu m$ using Chan kinetics and 1000 K, external fluid velocity equal to $1\sigma_p$. Black lines represent biomass and tar densities whereas gray lines stand for char and gas

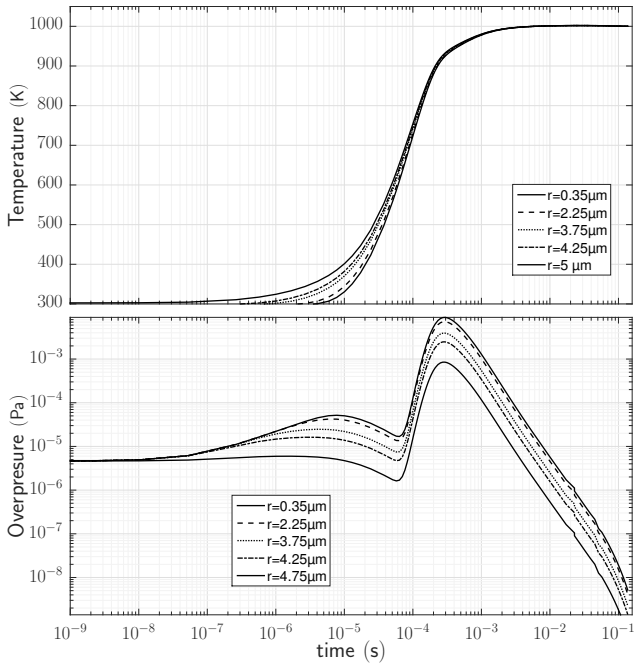

(a) Pressure and Temperature

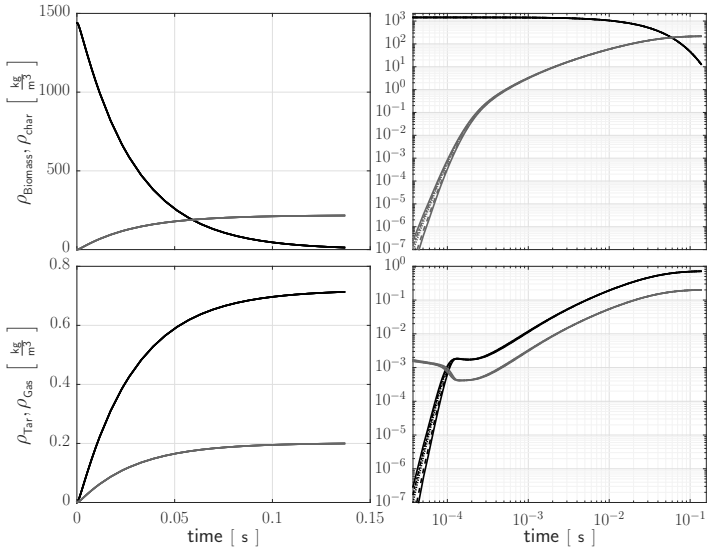

(b) Densities

Figure C.34. Pressure, temperature and densities profiles for a particle with $r = 5\,\mu\text{m}$ using Chan kinetics and 1000 K, external fluid velocity equal to $1\sigma_\text{p}$. Black lines represent biomass and tar densities whereas gray lines stand for char and gas

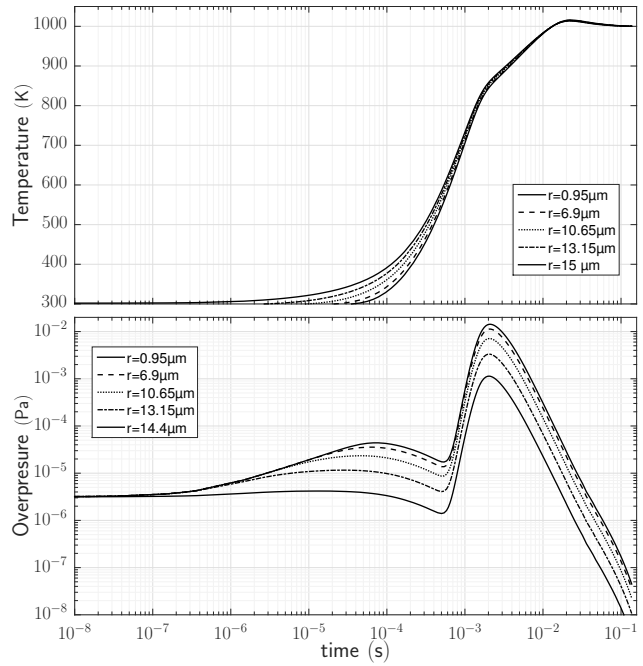

(a) Pressure and Temperature

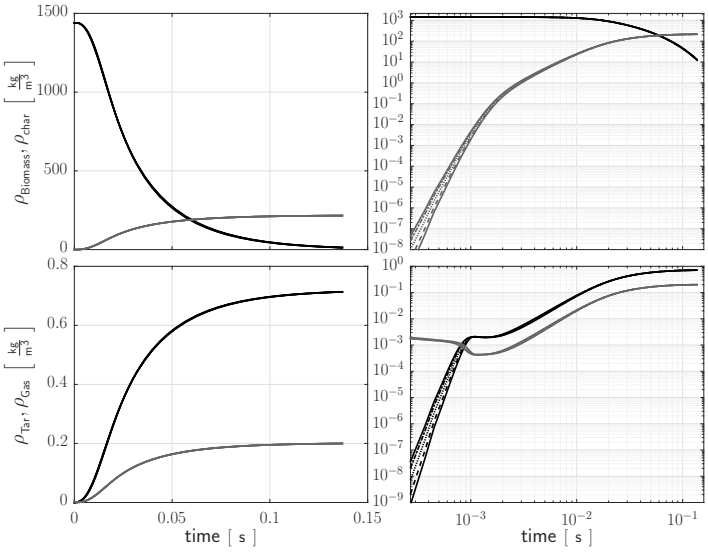

(b) Densities

Figure C.35. Pressure, temperature and densities profiles for a particle with $r = 15\,\mu\text{m}$ using Chan kinetics and 1000 K, external fluid velocity equal to $1\sigma_\text{p}$. Black lines represent biomass and tar densities whereas gray lines stand for char and gas

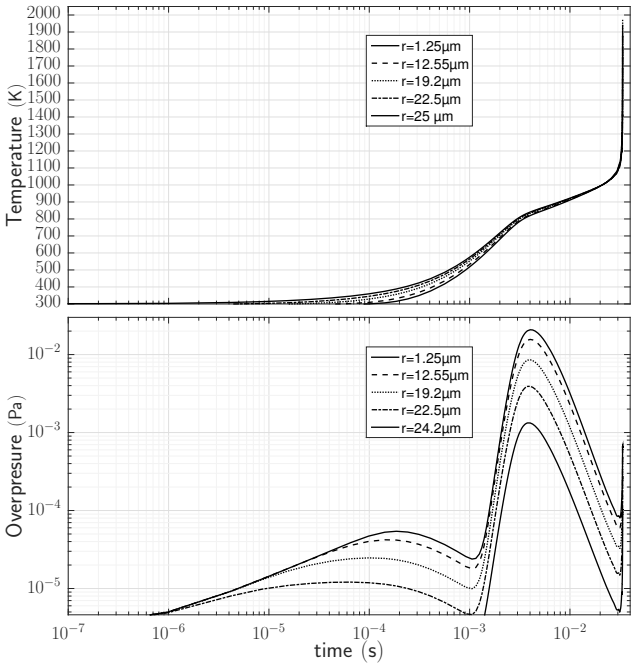

(a) Pressure and Temperature

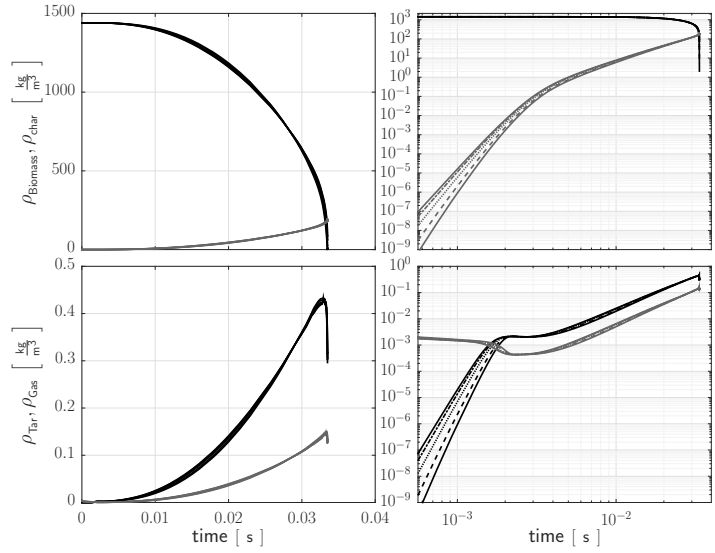

(b) Densities

Figure C.36. Pressure, temperature and densities profiles for a particle with $r = 25\,\mu\text{m}$ using Chan kinetics and 1000 K, external fluid velocity equal to $1\sigma_\text{p}$. Black lines represent biomass and tar densities whereas gray lines stand for char and gas

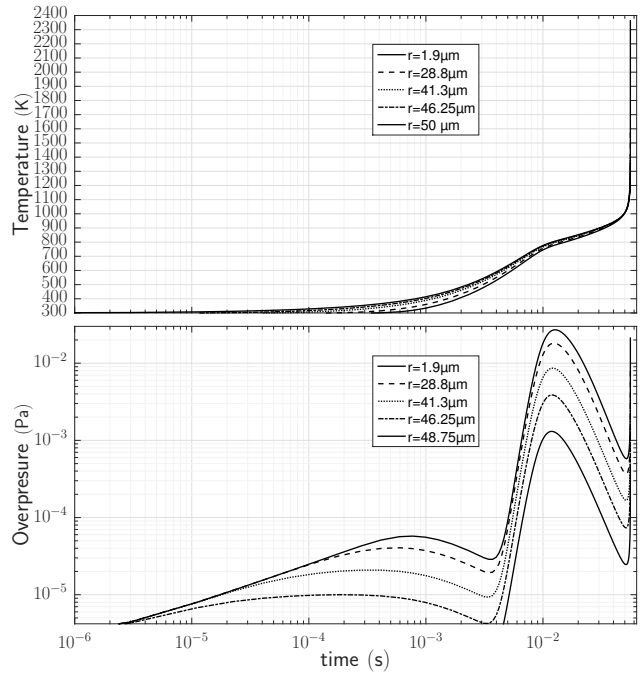

(a) Pressure and Temperature

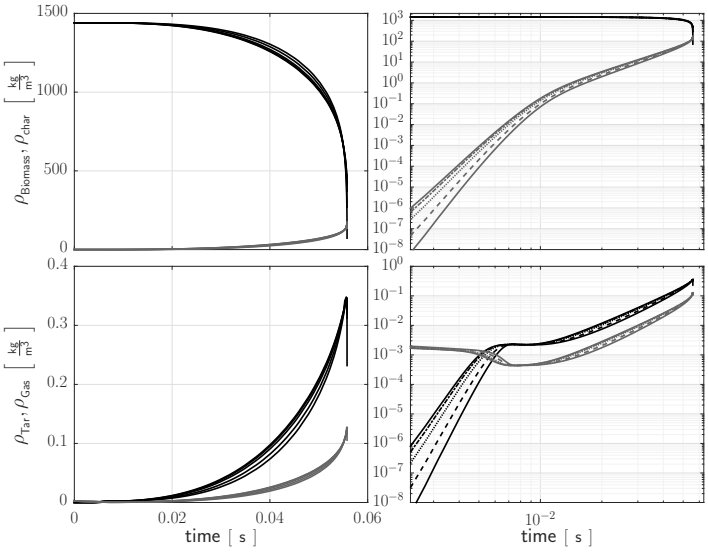

(b) Densities

Figure C.37. Pressure, temperature and densities profiles for a particle with $r = 50\,\mu\text{m}$ using Chan kinetics and 1000 K, external fluid velocity equal to $1\sigma_\text{p}$. Black lines represent biomass and tar densities whereas gray lines stand for char and gas

C.4.3. Minimal C_{dust} to reach the LEL

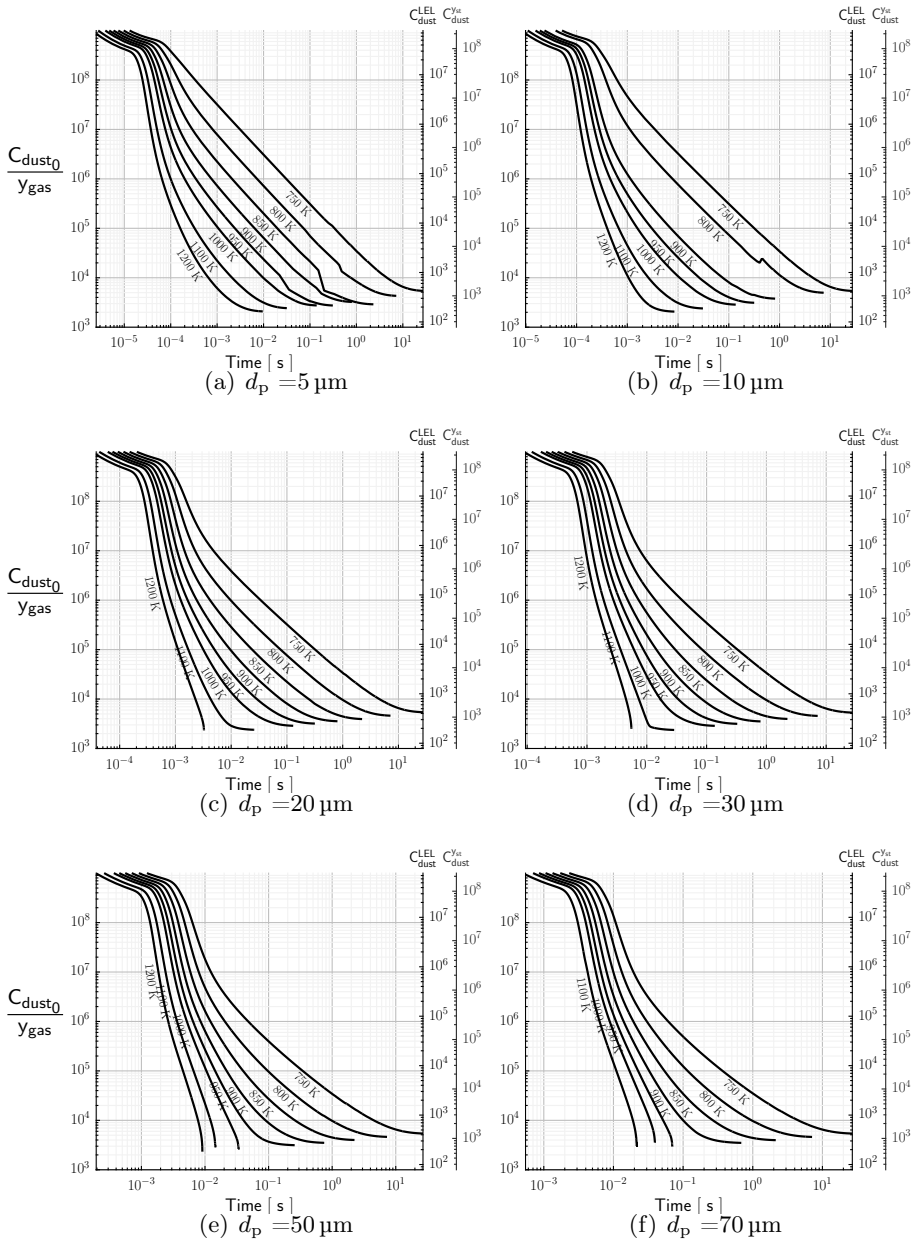

(a) d_{p} =5 µm (b) d_{p} =10 µm

(c) d_{p} =20 µm (d) d_{p} =30 µm

(e) d_{p} =50 µm (f) d_{p} =70 µm

Figure C.38. Initial C_{dust} necessary to reach a concentration of y_4 in pyrolysis gases at time t using to **Chan** kinetics, auxiliary axes on the left show the initial concentration necessary to reach the LEL =7.8% and the stoichiometric concentration (23%) of pyrolysis gases. Units for C_{dust} are in $\frac{\mathrm{g}}{\mathrm{m}^3}$

Appendix D
Three-dimensional estimation of the flame profile from two-dimensional data

Contents

Two methods were implemented to estimate the surface of a three-dimensional flame through the knowledge of its projection on a surface parallel to the direction of the movement of the flame. The first one has been named the "Method of Orthogonal Semi-Ellipses" (MOSES) and is designed for estimating the surface of a flame with a circular section, propagating inside a tube. The second one, is called "Perimeter Revolution Interpolation for Surface Approximation" (PRISA) and has a simpler foundation. It is used for flames propagating outwards in every direction.

D.1. Estimation of the surface of the flame front using the MOSES

Consider that the thick black line in **Figure D.1** represents the flame profile extracted from a frame in the video analysis of **Chapter 4**. If one circle is traced at the bottom of this flame profile with a diameter $2R$ equal to the width of the flame profile, then various ellipses can be traced from the circle to flame profile and back again to the circle as represented in **Figure D.1** between the points I, J and K. Thus, for any value of x in the domain of the flame's width, there is a unique orthogonal semi-ellipse for the flame front and its equation is:

$$z = \frac{c_x}{b_x}\sqrt{b_x^2 - y^2} \tag{D.1}$$

where c_x is the height of the two-dimensional flame front as a function of x, and b_x is the distance from the circumference to its central axis depending on the value x:

$$b_x = \sqrt{R^2 - x^2} \tag{D.2}$$

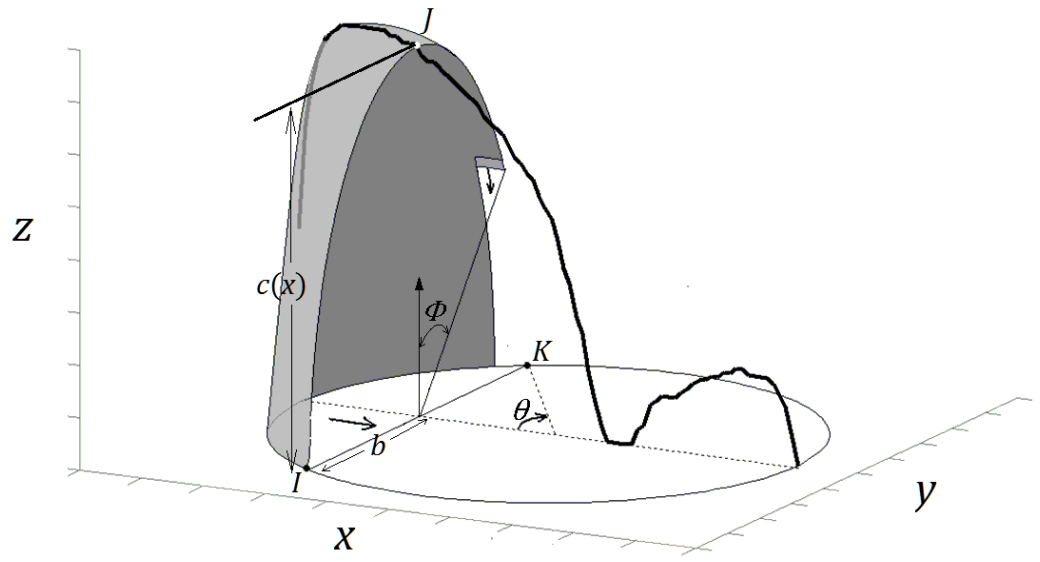

Figure D.1. Construction of the three-dimensional flame front from its two-dimensional profile

Provided c_x is known, the surface of the flame can now be estimated as:

$$S = \iint_D \sqrt{1 + \left(\frac{\partial z}{\partial x}\right)^2 + \left(\frac{\partial z}{\partial y}\right)^2}\,\mathrm{d}x\mathrm{d}y \tag{D.3}$$

where D represents the integration domain.

A change of variables becomes now convenient. Let x be defined in terms of θ and the radius R as:

$$x = R\cos\theta \tag{D.4}$$

and y in terms of R and the angles that generate the circle at the base θ and the corresponding orthogonal ellipse Φ:

$$y = R\sin\theta\sin\Phi \tag{D.5}$$

It can then be shown that $\frac{\partial z}{\partial x}$ and $\frac{\partial z}{\partial y}$ are expressed in therms of R, θ and Φ as:

$$\frac{\partial z}{\partial x} = \frac{\partial c_x}{\partial x}\cos\Phi - \frac{c_x\cos\theta\sin^2\Phi}{R\sin^2\theta\cos\Phi} \tag{D.6}$$

$$\frac{\partial z}{\partial y} = -\frac{c_x\sin\Phi}{R\sin\theta\cos\Phi} \tag{D.7}$$

Consequently:

$$\left(\frac{\partial z}{\partial x}\right)^2 = \cos^2\Phi\left(\frac{\partial c_x}{\partial x}\right)^2 - 2\frac{c_x\cos\theta\sin^2\Phi}{R\sin^2\theta}\frac{\partial c_x}{\partial x} + \frac{c_x^2\cos^2\theta\sin^4\Phi}{R^2\sin^4\theta\cos^2\Phi} \tag{D.8}$$

$$\left(\frac{\partial z}{\partial y}\right)^2 = \frac{c_x^2}{R^2}\frac{\sin^2\Phi}{\sin^2\theta\cos^2\Phi} \tag{D.9}$$

Equation D.3 can be now expressed in terms of **Equations D.8** and **D.9** and the angles θ and Φ As:

$$S = \iint_D \sqrt{1 + \left(\frac{\partial z}{\partial x}\right)^2 + \left(\frac{\partial z}{\partial x}\right)^2}\left|\begin{matrix}\frac{\partial x}{\partial\theta} & \frac{\partial x}{\partial\Phi}\\ \frac{\partial y}{\partial\theta} & \frac{\partial y}{\partial\Phi}\end{matrix}\right|\mathrm{d}\theta\mathrm{d}\Phi \tag{D.10}$$

where:

$$\left|\begin{matrix}\frac{\partial x}{\partial\theta} & \frac{\partial x}{\partial\Phi}\\ \frac{\partial y}{\partial\theta} & \frac{\partial y}{\partial\Phi}\end{matrix}\right| = R^2\sin^2\theta\cos\Phi \tag{D.11}$$

By defining the integration domain D in terms of Φ and θ as:

$$D = \begin{cases} 0 \le \theta \le \pi \\ \frac{\pi}{2} \le \Phi \le \frac{3}{2}\pi \end{cases} \tag{D.12}$$

Equation D.11 can be easily integrated with any numeric algorithm, assuming

that c_x, the height of the flame front as a function of x is known and differentiable so that $\frac{\partial c_x}{\partial x}$ can be calculated.

The construction of c_x is possible thanks to the video analyser, described in **Chapter 4**, that provides discrete points over c_x for each frame in the video. After scaling the pixel positions to the corresponding length dimensions c_x is calculated with a third-order polynomial, built by interpolation of the nearest five points to x. Therefore it is possible to differentiate c_x and more broadly to estimate the surface of flame front.

D.2. Estimation of the flame surface using the PRISA method

If the flame profile represented by the red line in **Figure D.2** is available, one could think that the flame surface can be estimated by constructing circles between its borders going in one arbitrary direction. This is certainly possible, and it may be useful to estimate the fundamental burning velocity and the flame thickness from recordings of turbulent flames. But before investing any time in developing such method, the PRISA[1] method was developed as a mean to verify if that time investment would be fruitful.

This is a simple method that considers that the surface of the flame can be approximated given that one has access to the perimeter P, the area A within P, the width a and the height b of the flame projected on a surface (All of these values are indeed available thanks to Simulink's "blob analyser" that is already used in the video analysis tool).

Consider the rectangle, the ellipse and the rhombus with the largest perimeter that can be drawn inside the box with dimensions $a \times b$, as portrayed in **Figure D.2**. It is conceivable that the surface of the flame contained inside that box is bounded by the surfaces of the revolution of those simpler figures around a vertical axis at $\frac{a}{2}$. The revolutions of the rectangle, the ellipse an the rhombus are respectively a cylinder a prolate ellipsoid and a double cone. Furthermore, the surfaces S_i of the solids, the perimeters P_i and the areas of A_i of the "polygons" can be easily calculated from the dimensions of the box a and b.

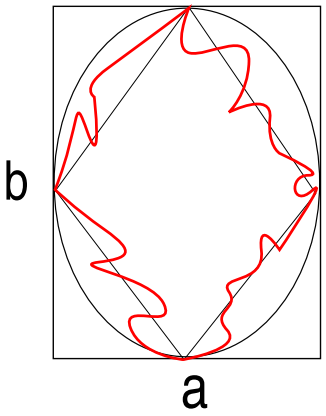

Figure D.2. Representation of the rectangle, the ellipse and the rhombus with equivalent height and width to that of the flame's profile

Consequently the PRISA method considers that the surface S of the flame divided by the area A of the projection of the flame, on the box $a \times b$ is a function of the perimeter P divided by $a + b$:

[1] *Prisa.* In spanish: rush, hurry.

$$\frac{S}{A} = f\left(\frac{P}{a+b}\right) \tag{D.13}$$

were the function $f\left(\frac{P}{a+b}\right)$ is the second order polynomial obtained from the points: $\left(\frac{P_{\mathrm{ra}}}{a+b}, \frac{S_{\mathrm{cy}}}{A_{\mathrm{ra}}}\right)$, $\left(\frac{P_{\mathrm{e}}}{a+b}, \frac{S_{\mathrm{e}}}{A_{\mathrm{e}}}\right)$ and $\left(\frac{P_{\mathrm{rh}}}{a+b}, \frac{S_{\mathrm{2c}}}{A_{\mathrm{rh}}}\right)$. The meanings the sub-indexes are the following: «ra» means rectangle, «cy» cylinder, «e» ellipse or ellipsoid, «rh» rhombus and «2c» double cone.

This method can be considered "not inaccurate" as long as the profile of the flame is not too complicated. Which is mostly the case for the initial stages of flames in the videos analysed. Furthermore it is certainly accurate for laminar flames in early stages that behave as ellipsoids with $\frac{a}{b}$ ratios close to 1.

Appendix E
Matlab and LaTeX codes

- Matlab code for building the severity maps presented in **Chapters 1 and 2**:

  `https://github.com/nicolascuervo/Severity`

- Matlab code for simulating the pyrolysis of one biomass particle:

  `https://github.com/nicolascuervo/Pyrolysis`

- Matlab code for estimating turbulence through PIV:

  `https://github.com/nicolascuervo/PIV`

- Simulink and Matlab code for extracting and analysing information from flame propagation videos:

  `https://github.com/nicolascuervo/Flame-Detection`

- LaTeXcode for this document:

  `https://github.com/nicolascuervo/Thesis-document`

- Powerpoint presentation for thesis defense:

  `https://github.com/nicolascuervo/Defense-Presentation`

Résumé

INFLUENCES DE LA TURBULENCE ET DES RÉGIMES DE COMBUSTION SUR LES EXPLOSIONS DE MÉLANGES HYBRIDES GAZ/POUSSIÈRE

Mots-clefs : Combustion, Flamme, Explosion, Turbulence, Mélanges Hybrides, Poussière, Pyrolyse

Prédire la propagation de la flamme lors d'une explosion de mélanges hybrides poudre/gaz dans des géométries complexes est un défi qui mobilise de multiples ressources. Une approche consiste à déterminer expérimentalement les caractéristiques inhérentes des mélanges poussière-air, comme la vitesse de flamme laminaire, et de les utiliser comme entrées dans les logiciels de Mécanique des Fluides Numérique (CFD). Néanmoins, la caractérisation expérimentale de la vitesse de combustion de suspensions turbulentes de poussières dans l'air est délicate de par notamment la variabilité des propriétés des poudres (taille des particules, humidité...), l'impossibilité de générer un nuage de poussière sans turbulence et l'impact de la poudre sur le rayonnement de la flamme. L'objectif de ce travail était de développer une approche permettant d'évaluer les propriétés fondamentales de propagation des flammes, à partir d'expériences en système fermé et des courbes d'évolution pression-temps, mais surtout grâce à l'analyse de la vitesse de flamme en fonction de son étirement et des instabilités hydrodynamiques. Dans une première étape, la turbulence du nuage de poussière avant inflammation a été étudiée. L'impact de la phase de pyrolyse sur l'explosion de poudres organiques a été aussi souligné expérimentalement et à l'aide d'un modèle de pyrolyse flash. Ensuite, le comportement de mélanges hybrides composés de gaz de pyrolyse et poudres organiques a été analysé, démontrant leurs particularités. Enfin, les interactions turbulence/combustion lors la propagation de la flamme ont été étudiés afin d'en extraire une vitesse de flamme 'pseudo' laminaire de la poussière ou des mélanges hybrides.

Abstract

INFLUENCE OF THE INTERACTIONS BETWEEN TURBULENCE AND COMBUSTION ON FLAME PROPAGATION OF HYBRID MIXTURES

Keywords: Combustion, Flame, Explosion, Turbulence, Hybrid mixtures, Dust, Pyrolysis

Predicting the flame propagation during a dust/gas hybrid mixture explosion in complex geometries is a challenge that mobilizes numerous resources. One approach consists on experimentally determining the inherent characteristics of dust-air mixtures, like the laminar flame speed, and using them as input for Computational Fluid Dynamics (CFD) simulation programs. Nevertheless, the experimental characterization of the burning rates of turbulent dust clouds in air still delicate due to the variability of the properties of powders (particle size distribution, moisture,...), the physical impossibility to generate a quiescent dust cloud and the impact of powder on the flame radiation among others. The ultimate goal of this work was to develop an approach to assess fundamental flame propagation properties, from closed vessel experiments and pressure-time evolution curves, but specially from the analysis of flame velocity as a function of its stretching and of the hydrodynamic instabilities. In a first step, the turbulence of the initial dust cloud has been studied. The impact of the pyrolysis phase on organic dusts explosion has also been highlighted both experimentally and by means of model for flash pyrolysis. Furthermore, the explosive behaviour of gas-dusts hybrid mixtures composed of pyrolysis gases and organic dusts has been analysed. Finally, the turbulence/combustion interactions during flame propagation have been studied in order to extract the "pseudo" laminar flame velocity of dusts clouds or hybrid mixtures.